

**THE LARGE HADRON COLLIDER AND THE EXPERIMENTS FOR RUN 3 —
ACCELERATOR AND EXPERIMENTS FOR LHC RUN3****LHC Upgrades in preparation of Run 3**

G. Arduini,^{1,*} V. Baglin, H. Bartosik, L. Bottura, C. Bracco, B. Bradu, G. Bregliozzi, K. Brodzinski, R. Bruce, M. Calviani, P. Chiggiato, P. Cruikshank, S. Claudet, D. Delikaris, S. Fartoukh,* C. Garion, M. Himmerlich, M. Hostettler, G. Iadarola, S. Kostoglou, S. Le Naour, A. Lechner, T. Lefevre, L. Mether, Y. Papaphilippou, V. Petit, M. Pojer, A. Poyet, S. Redaelli, F. Rodriguez Mateos, G. Rumolo, B. Salvant, F. Sanchez Galan, A. Siemko, M. Solfaroli-Camillocchi, G. Sterbini, M. Taborelli, L. Tavian, H. Timko, J.-Ph. Tock, A. Verweij, M. Wendt, J. Wenninger,^{1,*} D. Wollmann and Ch. Yin Vallgren

*European Organization for Nuclear Research, CERN,
Esplanade des Particules 1, 1211 Genève 23, Switzerland*

*E-mail: gianluigi.arduini@cern.ch, stephane.fartoukh@cern.ch,
jorg.wenninger@cern.ch*

ABSTRACT: The Large Hadron Collider (LHC) Long Shutdown 2 (2019–2021), following LHC Run 2, was primarily dedicated to the upgrade of the LHC Injectors but it included also a significant amount of activities aimed at consolidation of the LHC machine components, removal of known limitations and initial upgrades in view of the High-Luminosity LHC (HL-LHC) to favour the intensity ramp-up during Run 3 (2022–2025). An overview of the major modifications to the accelerator and its systems is followed by a summary of the results of the superconducting magnet training campaign to increase the LHC operation energy beyond the maximum value of 6.5 TeV reached during Run 2. The LHC configuration and the scenarios for proton and ion operation for Run 3 are presented considering the expected performance of the upgraded LHC Injectors and the proton beam intensity limitations resulting from the heat load on the cryogenic system due to beam-induced electron cloud and impedance.

KEYWORDS: Accelerator modelling and simulations (multi-particle dynamics, single-particle dynamics); Accelerator Subsystems and Technologies; Beam dynamics; Beam Optics

¹Editor.

*Corresponding author.

Contents

1	Introduction	1
2	Consolidation during LS2	4
2.1	DISMAC: motivation and achievements	5
2.1.1	The protection system of the LHC superconducting dipoles	6
2.1.2	Mechanism of electrical fault	7
2.1.3	The consolidation of the dipole diode insulation system	10
2.2	Consolidation and upgrade of the protection systems of the main magnet circuits	13
2.2.1	Controls and analysis software	13
2.2.2	Machine interlocks	14
2.2.3	Quench protection system	14
2.3	Beam dump consolidation	17
2.3.1	Beam dump block system	18
2.3.2	Upgrades of the dump block supporting system	19
2.3.3	Upgrade of the TDE dump block windows	19
2.3.4	Perspectives for Run 3 operation	21
3	HL-LHC upgrades	21
3.1	Collimation system	24
3.1.1	Staged collimation upgrade towards HL-LHC	27
3.1.2	Low-impedance upgrade of the collimation system and passive absorbers	28
3.1.3	Passive absorbers in IR7	30
3.1.4	Dispersion suppressors around ALICE	31
3.1.5	Dispersion suppressors around the betatron cleaning system	34
3.1.6	Crystal collimation system for ion beam cleaning	35
3.1.7	New layouts for wire collimators	37
3.2	Cryogenics	38
3.2.1	Point 4 cryogenic system upgrade during LS2	39
3.2.2	Achieved performance	39
3.3	Injection dump	40
3.3.1	Beam parameters and operational conditions	42
3.3.2	TDIS positioning and interlock logic	42
3.3.3	Aperture requirements	43
3.3.4	Impedance and electron cloud aspects	44
3.3.5	Spares	45
3.4	Machine-Detector Interface	45
3.4.1	Modifications in ATLAS forward shielding region	47
3.4.2	Modifications in CMS forward shielding region	49
3.4.3	Neutral absorber for IR8	49

4	Preparation for Run 3 and Run 3 operational scenario	50
4.1	Results of the magnet training campaign	51
4.2	Expected performance of the injectors during Run 3	56
4.2.1	Overview on the LHC injectors chain and beam production scheme before LS2	56
4.2.2	Upgrade of the LHC injectors during LS2	56
4.2.3	LIU proton beam performance	59
4.2.4	LIU ion beam performance	61
4.2.5	LIU beam commissioning plan in Run 3	63
4.2.6	Run 3 hardware options beyond the LIU baseline	66
4.3	Understanding of the observed heat-load in the Sectors during Run 2, upgrade of the instrumentation and expectations	67
4.3.1	Observed heat-load distribution during Run 2	68
4.3.2	Underlying mechanism	72
4.3.3	Beam-screen surface analyses	74
4.3.4	New laboratory diagnostic tools	78
4.3.5	New LHC diagnostic instrumentation	79
4.3.6	Expected limitations	81
4.4	LHC configuration and operational scenario for Run 3: protons	84
4.4.1	Beam parameters targeted for Run 3	84
4.4.2	LHC experiment requirements versus machine constraints	87
4.4.3	Beam physics considerations and LHC hypercycle in Run 3	96
4.4.4	Summary and outlook	103
4.5	Levelling techniques	105
4.5.1	β^* levelling in IP1 and IP5	106
4.5.2	Separation levelling in IP2 and IP8	109
4.5.3	Luminosity optimization	110
4.6	Beam beam long range compensation	110
4.7	LHC configuration and operational scenario for Run 3: ions	114
4.7.1	LHC heavy-ion operation	115
4.7.2	Beam parameters	115
4.7.3	LHC machine configuration	116
4.7.4	Predicted performance	117
A	Acronyms	120

1 Introduction

The Large Hadron Collider (LHC) [1, 2] consists of eight arcs and eight Long Straight Sections (LSS) as shown in figure 1. Each arc and its two adjacent half LSS compose an independent Sector. The two high luminosity experimental insertions are located at diametrically opposite straight sections: the ATLAS experiment is located at the Interaction Point 1 (IP1) and the CMS experiment at the

Interaction Point 5 (IP5). Two more experimental insertions are located around IP2 (for the ALICE experiment) and around IP8 (for the LHCb experiment), which also include the injection systems for Beam 1 (clockwise rotating) and Beam 2 (anti-clockwise rotating), respectively. Near-beam proton spectrometers based on detectors installed in so-called Roman Pots (RP) are installed in the Insertion Regions (IR) around IP1 (ALFA) and IP5 (CMS-PPS) for the measurement of p-p-scattering at very small angles. Two additional experiments (FASER and SND@LHC) have been installed during the last Long Shutdown LS2 (2019–2021) at approximately 480 m from IP1, one on each side. The beams are crossing in these four straight sections while the remaining four straight sections do not have beam crossings. Insertions at Points 3 and 7 host the collimation system. The insertion at Point 4 contains two Radio-Frequency (RF) systems: one for each LHC beam. IR6 contains the beam dumping system to extract the two beams from the machine using a combination of fast-pulsed ('kicker') magnets and septum magnets. Each beam features an independent abort system.

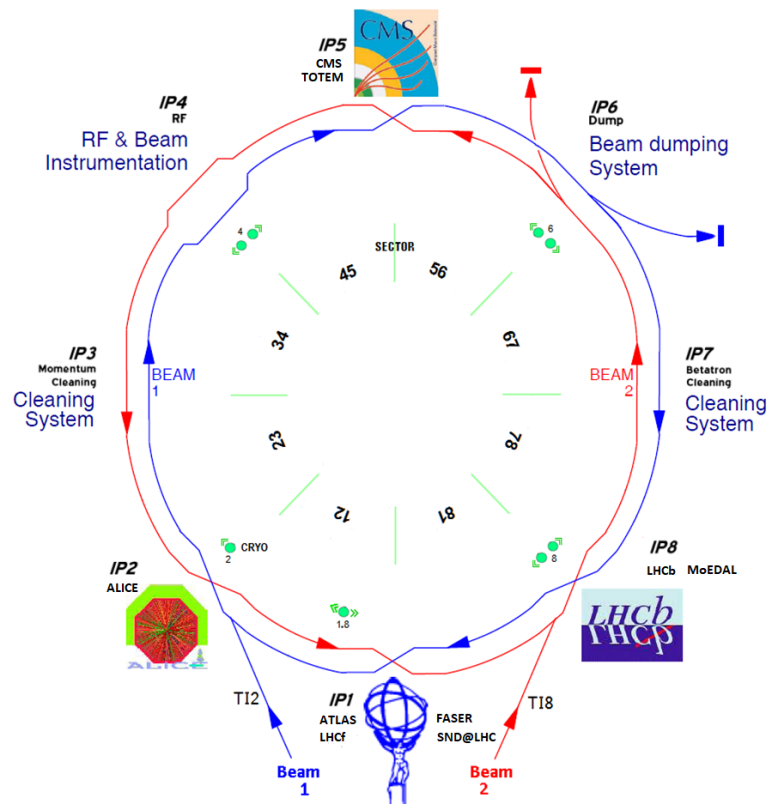


Figure 1. LHC schematic layout. The 8 sectors are indicated as well as the main functions of the eight Long Straight Sections. S12 is the Sector located between IP1 and IP2. A similar naming is used for the other sectors.

The LHC arcs consist of 23 regular arc cells. The arc cells are 106.9 m long and are made out of two 53.45 m long half-cells, each of which contains a Short Straight Section (SSS) assembly including twin-aperture superconducting quadrupoles and correctors, and three 14.3 m long 8.33 T twin-aperture superconducting dipole magnets. The two apertures of Ring 1 and Ring 2 are separated by 194 mm. The two coils in the dipole magnets are powered in series, and all dipole magnets of one arc form one electrical circuit. The quadrupoles of each arc form two electrical circuits: all focusing

quadrupoles (QF) in Beam 1 and Beam 2 are powered in series, and all defocusing quadrupoles (QD) in Beam 1 and Beam 2 are powered in series. The optics of Beam 1 and Beam 2 in the arc cells is therefore strictly coupled via the powering of the main magnetic elements.

During the first run of the LHC (Run 1: 2010–2013) proton-proton (p-p) collisions between bunches with a minimum spacing of 50 ns up to a centre of mass (c.o.m.) energy $\sqrt{s} = 8$ TeV were provided at IP1,2,5,8, Lead Ion-Lead ion (Pb-Pb) collisions at $\sqrt{s} = 2.76$ TeV/u were provided at IP1,2,5 and proton-Lead Ion (p-Pb) collision at $\sqrt{s} = 5.02$ TeV/u at IP1,2,5,8 [3]. Run 1 was followed by the first Long Shutdown (LS1: 2013–2014) in February 2013. LS1 was motivated by the need to consolidate the 13 kA splices between the superconducting magnets to allow the LHC to approach the design beam energy of 7 TeV in addition to the necessary regular maintenance of the equipment. The Superconducting Magnets and Circuits Consolidation (SMACC) project has principally covered the consolidation of more than ten thousands 13 kA splices but also other activities linked to the superconducting magnets such as the exchange of 18 main cryomagnets, the installation of additional safety relief devices, the repair of known helium leaks, and other consolidation activities [4]. The above modifications allowed to reach a proton beam energy of 6.5 TeV during the following Run 2 (2015–2018), after an extensive training campaign of the superconducting magnets. During Run 2, p-p collisions with beams with the nominal bunch spacing of 25 ns at $\sqrt{s} = 13$ TeV were achieved in all IPs and the nominal instantaneous luminosity of $1 \times 10^{34} \text{ cm}^{-2} \text{ s}^{-1}$ was exceeded. Pb-Pb and p-Pb collisions were provided at up to $\sqrt{s} = 5.02$ TeV/u and $\sqrt{s} = 8.2$ TeV/u, respectively, in IP1,2,5,8 [5, 6]

The main parameters achieved during Run 1 and Run 2 for protons and ion beams are summarized in tables 1 to 4.

Table 1. Evolution of the performance in regular proton operation during Run 1.

Parameter	2010	2011	2012
Beam energy at collision [TeV]	3.5	3.5	4
IP1/IP5 peak luminosity [$10^{33} \text{ cm}^{-2} \text{ s}^{-1}$]	0.2	3.5	7.7
Max. average event pile-up $\langle \mu \rangle$ [events/crossing]	4	17	37
Max. # bunches	368	1380	1380
Max. bunch pop. start of collisions N_b [10^{11} ppb]	1.2	1.45	1.6
Norm. transv. emittance start of collisions ϵ_n [μm]	≈ 2.2	≈ 2.3	≈ 2.5
β^* IP1/5 [m]	3.5	1.5 / 1.0	0.6
Half crossing-angle in IP1 and IP5 [μrad]	0 / 100	120	145
Max. stored energy [MJ]	24	112	143
IP1/IP5 integrated luminosity [fb^{-1}]	0.048	5.6	23.3
IP8 integrated luminosity [fb^{-1}]	0.047	1.2	2.2
IP2 integrated luminosity [pb^{-1}]	0.5	4.8	10

The evolution of the instantaneous luminosity and of the integrated luminosity during proton and ion operation in Run 1 and Run 2 are shown in figure 2.

Long Shutdown (LS) 2 (2019–2021), following Run 2, was primarily dedicated to the upgrade of the LHC Injectors (LHC Injectors Upgrade — LIU) [7, 8] but it included also a significant amount of activities aimed at consolidation of the LHC machine components, removal of known limitations

Table 2. Evolution of the performance in regular proton operation during Run 2. For 2017 the two figures for the maximum number of bunches refer to BCMS and 8b4e beams (see section 4.2.1). The emittance values for 2017 correspond to the BCMS beam.

Parameter	2015	2016	2017	2018
Beam energy at collision [TeV]	6.5	6.5	6.5	6.5
IP1/IP5 peak luminosity [$10^{34} \text{ cm}^{-2} \text{ s}^{-1}$]	0.5	1.4	2.1	2.1
Max. average event pile-up $\langle \mu \rangle$ [events/crossing]	22	45	66	64
Max. # bunches	2244	2220	2556 / 1868	2556
Max. bunch pop. start of collisions N_b [10^{11} ppb]	1.0–1.25	1.0–1.25	1.0–1.25	1.0–1.25
Norm. transv. emittance start of collisions ϵ_n [μm]	≈ 3.5	≈ 2.2	≈ 2.2	≈ 1.9
β^* IP1/5 [cm]	80	40	40–30	30–25
Half crossing-angle IP1/5 [cm]	145	185 / 140	150–120	160–130
Max. stored energy [MJ]	280	270	330	320
IP1/IP5 integrated luminosity [fb^{-1}]	4.2	39.7	50.6	66
IP8 integrated luminosity [fb^{-1}]	0.36	1.87	1.98	2.46
IP2 integrated luminosity [pb^{-1}]	9	13	19	27

Table 3. Evolution of the performance in heavy ion operation. While during the 2010 and 2011 runs both rings were filled with lead ions for Pb–Pb collisions, the 2013 run featured mixed operation of proton and lead beams.

Parameter	2010	2011	2013
Beam energy at collision [Z TeV]	3.5	3.5	4
Beam type	Pb-Pb	Pb-Pb	p-Pb
Peak luminosity [$10^{27} \text{ cm}^{-2} \text{ s}^{-1}$]	0.03	0.5	110
Max. # ion bunches	137	358	338
Ion bunch spacing [ns]	500	200	200
Ion bunch population N_b [10^7 ppb]	11	13	15
IP1/IP5 integrated luminosity [μb^{-1}]	9.5	155	31800
IP2 integrated luminosity [μb^{-1}]	9.3	144	31200

and initial upgrades in view of the High Luminosity LHC (HL-LHC) [9] to favour the intensity ramp-up during Run 3 (2022–2025).

2 Consolidation during LS2

Major work was devoted to the consolidation of all 1232 dipole bypass diodes as part of the Diode Insulation and Superconducting MAGnets Consolidation (DISMAC) project [10] (see section 2.1). The main activities on the LHC superconducting magnets occurred during LS2 are schematically represented in figure 3. These included the replacement of 22 superconducting magnets (19 dipoles and 3 quadrupoles) to resolve non-conformities revealed after LS1 (e.g. excessive internal splice resistance, damaged quench heaters) or to re-establish the nominal configuration of the correction circuits after the sector 34 incident in 2008, when four non-fully compliant magnets were installed and only two of them could be replaced during LS1. Within the DISMAC Project about 2800

Table 4. Evolution of the performance for heavy ion operation in Run 2. While during the 2015 and 2018 runs both rings were filled with lead for Pb-Pb collisions, the 2016 run featured mixed operation of proton and lead beams.

Parameter	2015	2016	2018
Beam energy at collision [Z TeV]	6.37	6.5	6.37
Beam type	Pb-Pb	p-Pb	Pb-Pb
Peak luminosity [$10^{27} \text{ cm}^{-2}\text{s}^{-1}$]	3.6	890	7.4
Max. # ion bunches	518	540	733
Ion bunch spacing [ns]	100	100	75 / 100
Ion bunch population N_b [10^7 ppb]	16	21	20
IP1/IP5 integrated luminosity \mathcal{L}_{int} [nb^{-1}]	0.58	190	1.8
IP2 integrated luminosity [nb^{-1}]	0.43	43	0.9

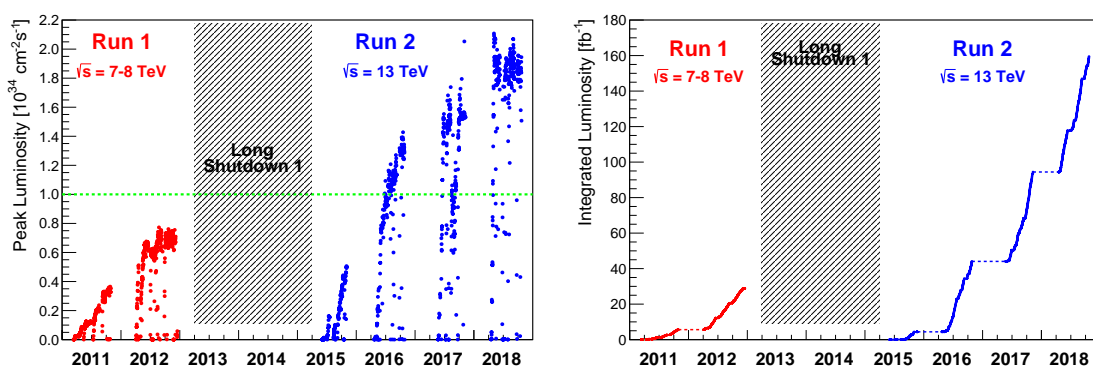


Figure 2. Evolution of the LHC peak (left) and of the integrated (right) luminosity (average of ATLAS and CMS) during Run 1 and Run 2. The green line on the peak luminosity plot indicates the design luminosity.

current leads were verified, as part of a regular maintenance campaign, and additional cryogenic instrumentation has been added to allow more detailed measurements of the beam-induced heat load in the LHC beam screens (see section 4.3.5).

A refurbishment and upgrade of the protection system of the main magnet circuits took place in view of training the magnets to 7 TeV (see section 2.2) and the two beam dump absorbers have been replaced with modified spares and the connection to the corresponding dump lines departing from IR6 have been modified (see section 2.3) to address performance issues observed during Run 2 and described in [11].

2.1 DISMAC: motivation and achievements

At the end of 2016, sectors 34 and 45 were trained (see section 4.1) with the aim to gather more information on the main dipole training behaviour for operating at energies higher than 6.5 TeV achieved after LS1 and corresponding to a main dipole current of 11 080 A [12, 13]. The training in sector 45 was stopped, for time reasons after 24 quenches, after having reached a maximum current of 11 540 A, equivalent to a beam energy of 6.82 TeV. In sector 34, training was stopped at 11 420 A (corresponding to a beam energy of 6.75 TeV) after 8 quenches and following the detection of a short



Main work on the LHC superconducting magnets during LS2 (2019-20)

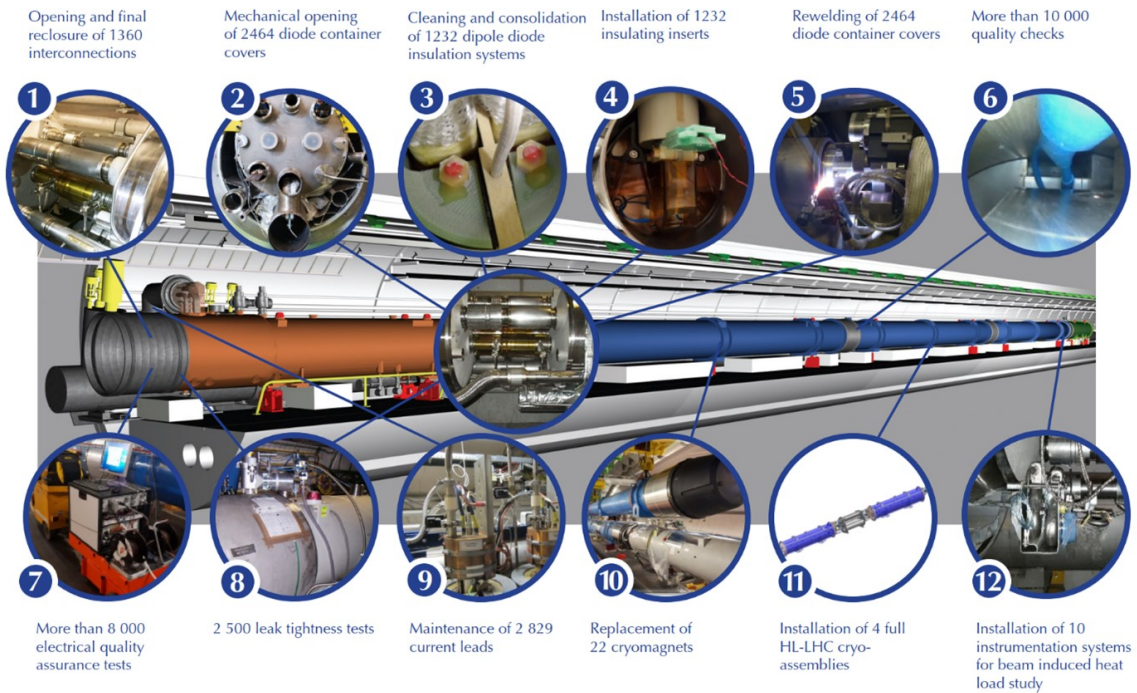


Figure 3. Main work on the LHC superconducting magnets during LS2.

circuit to ground [14]. This short was located in the part of the cold mass containing the protection diode (see section 2.1.1) and was associated to the effect of the transient triggered by each training quench. The limited training experience, combined with the data acquired so far, is compatible with the fact that the main dipoles have to be, at least partially, retrained after each warm-up and cool-down cycle [12, 13] (see section 4.1). This triggered a reflection on the origin of the short and risk associated with training, leading to the decision of launching a specific consolidation of the circuits to decrease such risk.

2.1.1 The protection system of the LHC superconducting dipoles

In each of the 8 LHC sectors, 154 dipoles are powered in series (see figure 4), forming a 3 km long string. At nominal current, the magnetic stored energy in one sector is in excess of 1 GJ. This is a significant stored energy, and requires appropriate quench management to avoid that a quenching magnet may be damaged by excessive temperature or voltage resulting from dumping even a small fraction of this energy in it.

Drawing also on extensive previous experience in superconducting accelerators of comparable dimensions, the quench protection system of the superconducting LHC dipole [15] is based on the principle of by-pass diodes. In the LHC each dipole magnet is equipped with “cold diodes” connected in parallel to the magnet itself. In case of a magnet quench, the resistive voltage is detected (typical threshold of the order of 100 mV) and causes firing of a set of “quench heaters”

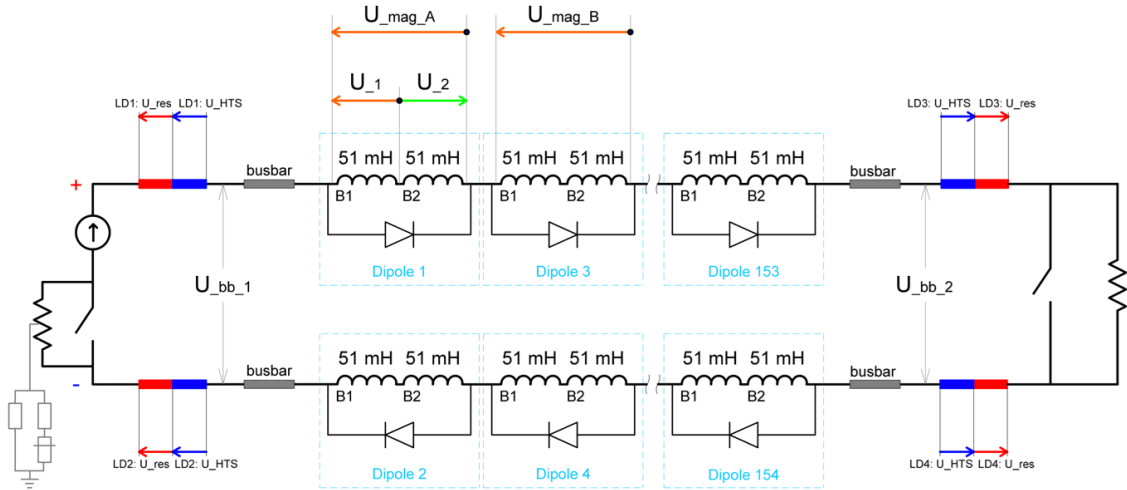


Figure 4. Schematic of a Main Dipole (RB) circuit in the LHC.

that initiate a transition to normal (resistive) state over a large part of the magnet. The developing coil voltage causes the “opening” of the diode (typical opening voltages of the order of 6–7 V), thus by-passing the quenching magnet during a free-wheeling discharge of the whole main dipole circuit that typically lasts a few hundreds of seconds. During this time the by-pass diode can transport the large current under limited terminal voltage, of the order of 500 V to ground. This well-established protection technology ensures safe operation of the main accelerator magnets (the main quadrupoles in the LHC are protected in a similar way), and depends critically on good dielectric strength of the whole circuit.

The cold diodes connected in parallel to the magnet coils are shown in figure 5. They are housed in a container directly connected to the cold mass superfluid helium volume, therefore operating at 1.9 K. For accessibility reasons, the diode container is located at the extremity of the cold mass, allowing to access it from the interconnection. This design was developed so that, despite the tight available space, it is possible to exchange a diode without disconnecting the whole magnet.

The electrical connection of the diode to the magnet is a bolted “half-moon” splice between an extension of the main busbars powering the main dipoles and the LHC bypass diodes. This is shown schematically in figure 6. The busbar extension is insulated by a flexible sock all the way to the half-moon. The top of the half-moon connection should also be insulated with G10 pieces (see figure 7). Because of practical assembly limitations, however, only a fraction of approximately 15 % of the connections were insulated, while the rest present bare half-moon connections, though surrounded by an insulating G10 cylinder.

2.1.2 Mechanism of electrical fault

It became soon evident that debris, coming from the production of the cold mass and its electrical/hydraulic connection in the arc chain, could collect in the diode container and the vertical half-moon assembly because of their geometry and being located in the lowest part of the magnet. In fact, since 2006, nine short circuits to ground were localised in the LHC dipole diode containers, similar to the one shown in figure 8, where a few-centimetre-long piece of metal (coming from

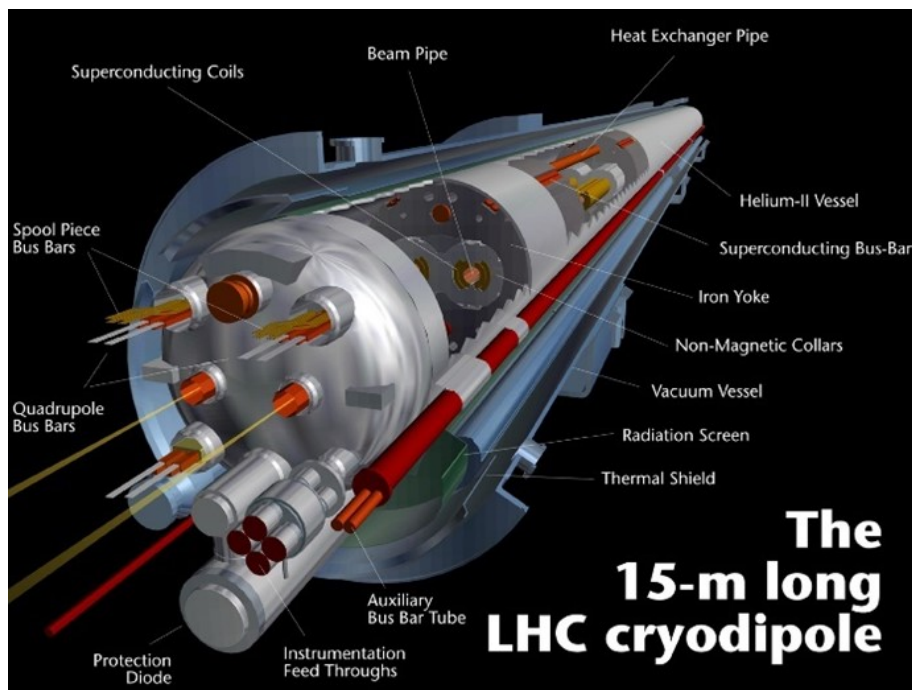


Figure 5. The LHC dipole magnet. The Protection Diode is shown in the lower part of the figure.

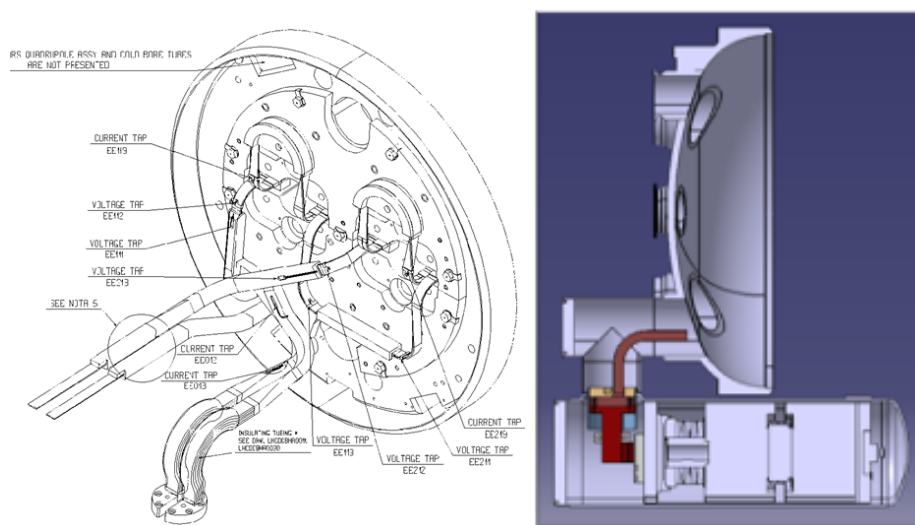


Figure 6. Schematics of connection of the diode to the magnet busbars.

the deburring after production) is touching the half-moon and the metallic pipe supporting the diode container, generating a fault to ground. This kind of residues were present in the cold masses since the manufacturing of the magnets, and can be transported by large helium flows occurring during cool-down and warm-up phases, flushing sequences after an intervention and also in case of quenches, especially at high current. In the seven first cases (of the nine mentioned above), the LHC was at, or very close to, room temperature. They were solved by cutting the metallic enclosure and removing the metal debris at the origin of the short, with a minimum impact on the schedule. At the



Figure 7. Top view of a diode insulated connection.

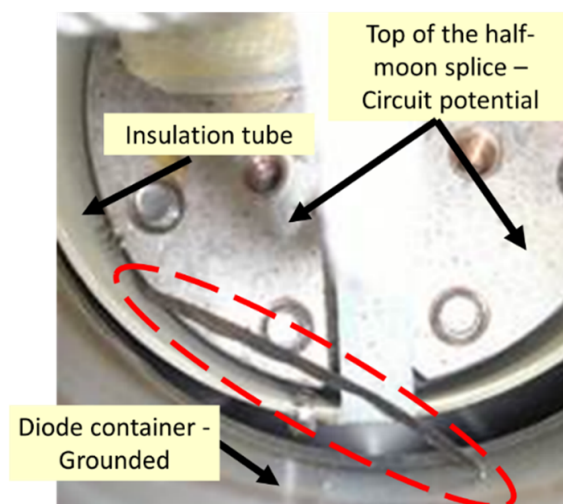


Figure 8. Bare half-moon splices and metal shaving creating an earth fault.

end of LS1, during the long sequence of powering of the superconducting circuits (to recommission them before operation with beam), a fault to ground developed in the dipole line of one of the sectors and the tests were suspended. All protection mechanisms worked properly, whilst in-situ electrical measurements localised the fault in the diode vicinity. X-ray images were acquired: even if not fully conclusive, all data pointed to the same origin as in the previous cases.

As the LHC was in operating conditions, i.e. at 1.9 K, giving access to the diode container to remove the debris would have taken more than three months, mostly required for the warm-up and cool-down. In addition, submitting a large cryogenics system such as the LHC to a thermo-mechanical cycle is not risk-free: this could generate other short circuits, damage to instrumentation or leaks due to the thermally induced movements. Therefore, an alternative method was devised, analysed and applied to eliminate the short circuit [14]: the application of a capacitive discharge across the short circuit, the so-called Earth Fault Burner (EFB). The principle is to send a high current pulse

(up to 1 kA) through the fault, by means of the closest voltage taps. This can clear the fault relying on three mechanisms:

- melting of the metal piece, breaking it into several smaller parts,
- displacing the metal piece under electromagnetic forces,
- boiling helium and displacing the part.

This was also successfully applied in the LHC in 2016 in sector 34, when the fault mentioned in the introduction appeared. Nevertheless, this process could lead to damage on one of the voltage taps or even puncture the cryogenic envelope, if not properly controlled and it takes a certain time, most of which is necessary for the earth-fault localisation. Considering the risk associated to a short to ground and the statistical estimate of the appearance of such faults during the training campaign, the DISMAC project was set-up to develop and implement a mitigation plan during LS2.

2.1.3 The consolidation of the dipole diode insulation system

The functional specifications for the consolidation of the LHC dipole diode busbar insulation [16] take into account the following requirements:

- compatibility with the existing configuration, especially the present insulation system,
- electrical requirements [17],
- mechanical requirements,
- hydraulic impedance,
- radiation resistance [18],
- assembly and disassembly rates.

Figure 9 illustrates the list of macro-tasks that were identified and performed for the consolidation of the insulation of the 1232 dipole diodes. Quality Assurance (QA) and Quality Control (QC) tasks had a prominent role in the whole consolidation process.

After the preparatory work to give access to the interconnection and the diode container, the consolidation included several tasks, listed below:

1. Cutting of the two covers to access the diode and the magnet end to give access to the magnet end cover, to the half-moon connection and to the diode (see figure 10). The visual inspections that followed revealed an issue with many existing welds (lack of fusion/penetration of some welds and root porosities) for which an extensive investigation was launched. After many metallographies, micro tomographies, burst test and tensile test, the replacement of 8 diode boxes was deemed necessary. The same team who opened the covers was responsible of re-welding them after the interventions.
2. Removal of the reasonably accessible debris and other contaminants from the half-moons, the dipole cold mass end cover, the diode container and venting channel. Few examples of the objects removed from the end covers and half-moons are shown in figure 11.

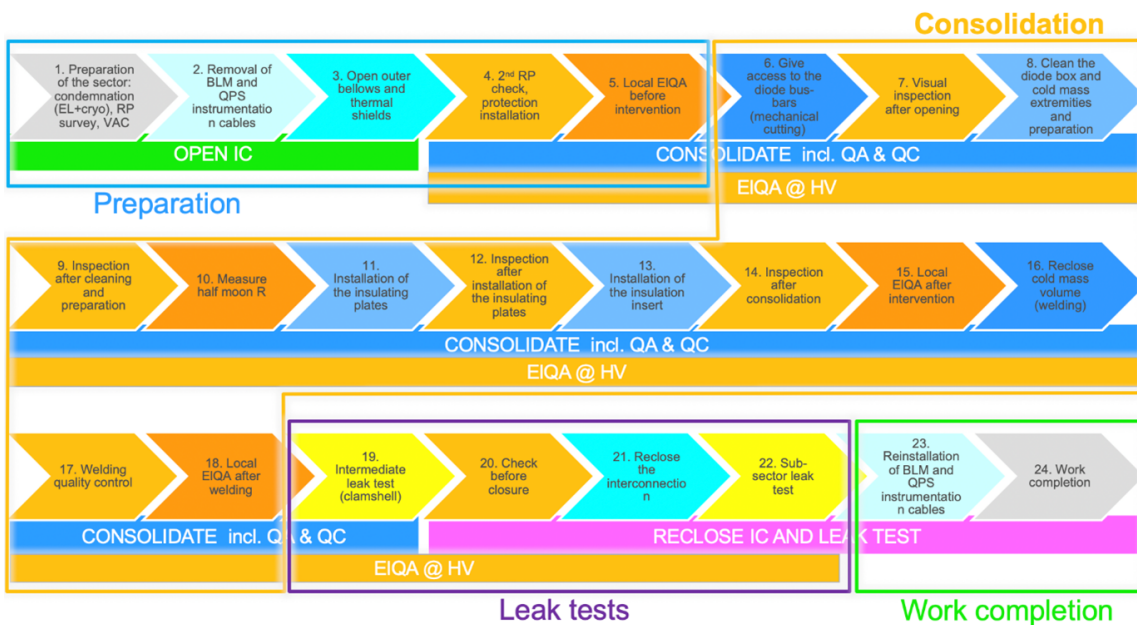


Figure 9. The list of the tasks for the consolidation of the diode insulation.

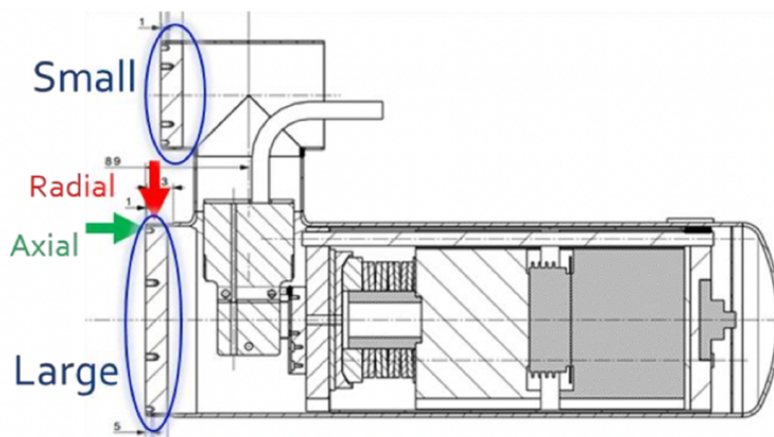


Figure 10. Covers to be cut for the consolidation.



Figure 11. Examples of the debris removed during the cleaning process.

- Consolidation of the insulation of the half-moon splices with newly designed insulation plates that can be installed without opening the half-moon splices also in case the busbars are misaligned or deformed. The half-moon splice electrical insulation is mainly assured by insulation sheets that are kept in place by the insulation G11 plates (see figure 12).

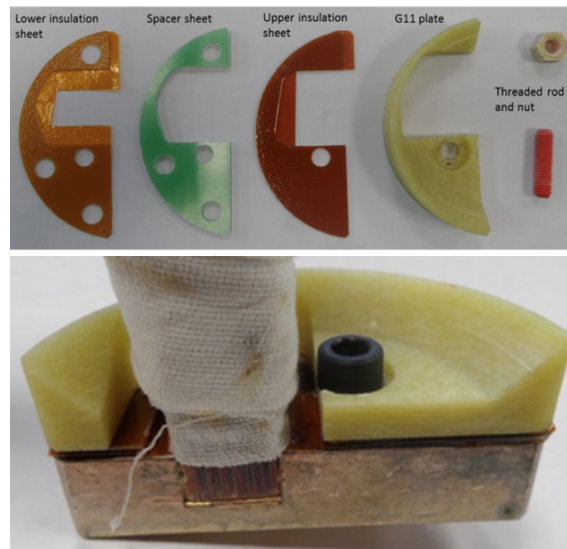


Figure 12. The new insulation pieces separate (top) and assembled in the final configuration (bottom).

- Installation of a new insert to cover the blank busbars and to protect the diode venting channel from metal chips. This insert is shown in figure 13.

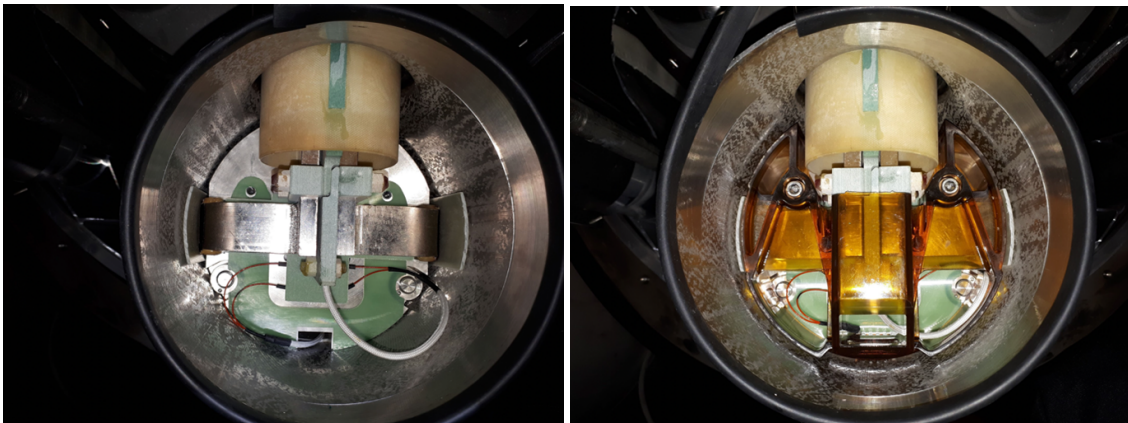


Figure 13. Before (left) and after (right) the installation of the insulation insert in front of a diode.

- Reinforcement of fissured or broken vetronite tubes insulating the half-moons from the stainless-steel tube containing them. Whenever the extent of the damage was not too big, the tube was reinforced with epoxy while in case of significant damage the tube was additionally reinforced with a thin vetronite layer.

6. Quality Assurance and Control to validate the interventions and avoid the appearance of collateral damages. Visual inspections aimed at checking the level of cleanliness and the correct assembly of the different components. Electrical checks were assessing the integrity of the insulation and the continuity of the voltage taps connections (delicate and therefore critical for the final electrical integrity). Vacuum tests assessed the integrity of the vacuum system after the opening and re-welding of several tubes and lines and the opening and re-closure of the external envelopes.
7. Digital documentation of the various steps to ensure the coordination of the activities, with signature and unblocking of the next actions, and to record all data (photos and QA/QC steps).

The diodes consolidation started in April 2019, and, even if it encountered a huge number of non-conformities (mainly not related to the consolidation itself) and was affected by the impact of the COVID-19 pandemics, it was finally declared completed with the last vacuum validations in October 2020.

2.2 Consolidation and upgrade of the protection systems of the main magnet circuits

A substantial effort has been dedicated during LS2 in order to consolidate and/or upgrade the protection systems of the main magnet circuits for Run 3. We will focus here on the most relevant aspects which could have an impact on the commissioning with beam and operation of the LHC.

2.2.1 Controls and analysis software

The energy stored in the beam and the magnets of the LHC is by far larger compared to other existing accelerators. The LHC machine interlock systems manage the interlock conditions and trigger safe extraction of the energy stored in the electrical circuits and in the beams. To operate the machine in the presence of such large interlock systems requires powerful diagnostics to trace back the origin of power and beam related problems. This diagnostics tool, called the Post-Mortem (PM) system [19], has the role of organizing the collection and analysis of transient data recorded around a beam or power abort by all relevant LHC equipment systems. During LS2 the PM system has been subject to a complete renovation, including new storage and protocols, while preserving similar interfaces and workflows for the existing use cases. The adaptation to the clients has been done in a way to minimize impact by keeping the same interfaces and workflows. More user applications can make usage of the service (other than Java and Labview, e.g. Python).

The AccTesting framework [20], developed to orchestrate the thousands of tests for electrical circuits of the LHC during its commissioning, and the applications required for the preparation for the 2021 LHC Powering Tests campaign were validated months ahead of the actual powering tests and training campaign. For this purpose the Powering & Protection Test-bed was used extensively. This test-bed, a facility installed in a surface building, mimics representative parts of the systems present in the LHC in terms of controls infrastructure and underlying hardware.

New analysis notebooks using data from the logging and PM databases have been created to improve the data analysis of powering tests and circuit events during Run 3 (quenches, powering faults of various kinds, etc). The new data extraction interface is open to more users. The advancement is close to completion of all the required PM analysis modules.

Numerous models of the LHC superconducting magnet circuits have been prepared and simulations performed using STEAM [21] in order to better understand their behaviour, especially in case of transients for certain failure scenarios (inter-turn shorts, missing parallel resistor in the undulators, etc).

2.2.2 Machine interlocks

The LHC Global Protection Mechanism is a functionality implemented within the Power Interlock Controller [22]. It was designed to trigger a preventive discharge of magnet circuits located in the same powering sectors of a quenching main magnet to reduce the likelihood of secondary quenches due to heat propagation. During LS2, this function has been automatically disabled while a sector is powered at low currents (i.e. the current in all main magnets is below 1 kA), since no quench propagation has been observed at these current levels. This change preserves safety of LHC operation, while improving machine availability and reducing the wear of protection components.

The LHC has 202 operational Energy Extraction Systems for the protection of 600 A corrector circuits. Considering the required operational currents up to LS3, several extraction systems have been by-passed to increase the system lifetime in view of limited spare availability while at the same time decreasing maintenance efforts and increasing the overall availability of the LHC protection system. The systems that have been by-passed (16 connected to the skew-sextupole spool pieces circuits) remain installed and powered and can, if required, be re-inserted into the circuits during e.g. technical stops.

To limit the risks when masking interlocks while providing flexibility for machine setup, the LHC ‘Set-up Beam Flag’ [23] allows masking only when operating below a defined threshold in beam energy and intensity. A few configurations are available for the threshold as a function of the beam energy. A new Set-up Beam Flag configuration has been defined to improve the efficiency of optics measurements. This new configuration limits interlock masking to a total beam population of 4×10^{10} protons independently of beam energy. Three pilot bunches (pilot bunches have a population of $N_b = 5\text{--}10 \times 10^9$ protons) can be used for optics measurements provided the overall β -beating is not larger than 20 %. The efficiency for optics measurements is improved as three bunches can be measured at the same time, reducing the measurement uncertainties.

Since LIU beam intensities cannot be safely dumped on the beam stoppers (TEDs) in the SPS-to-LHC transfer lines TI2 and TI8, a new protection logic has been implemented such that when TEDs are inserted in the beam path, the SPS extracted beam population is limited to 3.5×10^{13} protons. This has been introduced within a new set of Safe Machine Parameters (SMP). The SMP System [22] provides a set values, related in particular to beam energy and intensity, to the Beam Interlock System (BIS) as well as to other clients. The values are transmitted via optical fibres or over the general timing network.

2.2.3 Quench protection system

The 392 operational racks which are responsible for the protection of the Main Quadrupole magnets (MQ) in the LHC have been upgraded during LS2 to ensure their maintainability and improve their dependability (figure 14) [24].

The system was fully qualified during Individual System Tests, and subsequently during the commissioning and powering tests in 2021, which included a few MQ magnet circuit training quenches. The system has proved excellent stability. Moreover, the improved functionalities of the



Figure 14. Quench Protection Racks for the LHC Main Quadrupole Magnets in position in the tunnel (left), during the upgrade at the Laboratory (center) and at temporary storage (right).

DQLPU type B (the quench detectors within the racks) have shown already to be very useful for diagnostics, tests, and maintenance.

The quench detection boards of the LHC Main Dipoles (MB) have normally a voltage threshold of 100 mV. After a quench of one of the MB magnets in the RB circuit, the boards connected to adjacent magnets pick up signals due to electromagnetic coupling. The origin is most likely a voltage induced in the voltage tap loop due to the fast transfer of the current from the quenching magnet into the cold bypass diode. This voltage pick-up often exceeds the 100 mV threshold, hence resulting in the so-called ‘fast secondary quench triggers’ in one or more adjacent magnets. The effect is hardly present below 10 kA and becomes more pronounced at higher currents.

In order to avoid these unnecessary quenches during the magnet training campaign, modified or new 200 mV quench detection boards were installed prior to the training campaign leading to an important decrease of high current MB quenches. About 1200 boards were modified at CERN, 100 boards newly made at CERN, and 650 boards made in industry. The original 100 mV boards have been reinstalled at the end of the training campaign before restarting beam operation.

Undulators are installed in IR4 to enhance synchrotron radiation emission at low energy for beam profile measurements. The measurement chain within the quench detection system for these magnets has been upgraded with the installation of a new closed-loop Hall current sensor. Perturbations observed in the signals from this magnet are due to the fast change in inductance as a function of the current. Validation of the current sensor’s efficiency was successfully completed during the powering tests campaign in 2021.

The 13 kA energy extraction systems of the main dipole and quadrupole circuits [25] have undergone a complete revision and maintenance process in all their components during LS2. All the 256 switches have been disconnected and removed from the tunnel (figure 15). Switches have been fully disassembled, inspected and overhauled for the critical parts like the driving mechanism and the arcing contacts. At the same time, 32 new switches were installed as a first phase of consolidation, therefore creating new spares once the replaced units are refurbished.

All electrical contacts of the 13 kA energy extraction systems were checked, cleaned and in many cases the surfaces were fully redone (e.g. silver coating of the dump resistors’ contacts, refurbishment of multi-lamellar contacts, etc). Verifications were carried out on the electrical parts and insulators.



Figure 15. Switches of the 13 kA energy extraction systems in the laboratory.

Some of the electronics boards related to the control of the systems have been upgraded to tackle obsolescence of components and number of spares.

During the short circuit tests (i.e. the validation of the room temperature part of the circuits, from the power converter to the extremity of the water-cooled cables, before the connection to the current leads) and the powering tests (i.e. the Hardware Commissioning — HWC — of the circuits after LS2), the function of each of the energy extraction systems was verified at different current levels. This process is part of the mandatory qualification tests required after any hardware modification. These tests include the validation of the so-called conical joints (i.e. the main terminals of the extraction systems — see figure 16).

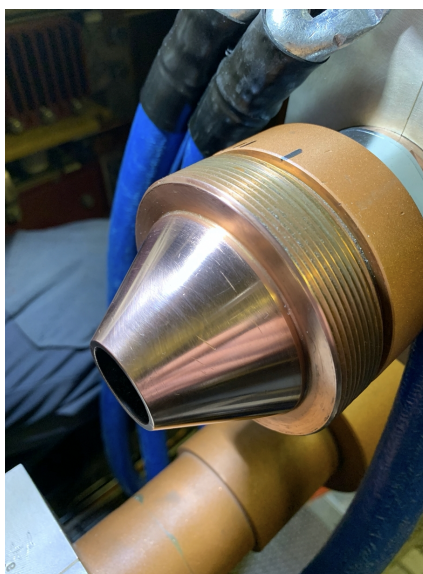


Figure 16. Conical joint as terminal of the 13 kA energy extraction systems.

2.3 Beam dump consolidation

The two LHC beam dump blocks have to withstand arduous operating conditions and are essential for the safe and reliable operation of the collider. Their function is to absorb the energy of the two counter-rotating beams that circulate inside the LHC vacuum chambers under all foreseeable circumstances, including abnormal operation conditions of the machine.

During LS2 and following the operational challenges encountered during Run 2 (see [11] for more details), extensive work was carried out to consolidate the dumps to cope with the more demanding future operating conditions of the LHC Run 3. The main changes implemented are listed below and visually presented also in figure 17:

- uncoupling of the dump block from the LHC vacuum line to avoid generation of high reaction forces between dump, connecting line and extraction line and consequently to avoid transmission of vibrations to the upstream components;
- design of a new upstream window for the dump block and upgrade of the downstream one;
- design of a new dump block support system able to cope with the dump block vibrations and prevent long-term physical displacement of the dump;
- installation of a new instrumentation system suite to monitor the dump block behaviour.

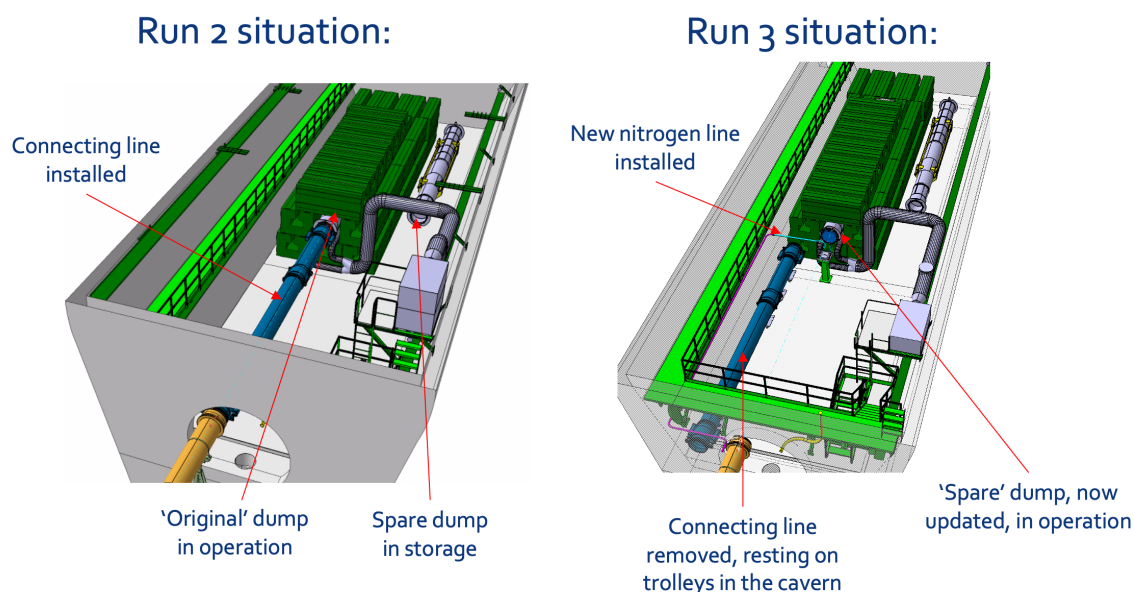


Figure 17. Scheme of the LHC beam dump cavern during Run 2 (left) and Run 3 (right), showing the dump block and the different subsystems.

A detailed and exhaustive analysis of the engineering studies and background information is available in [26, 27].

2.3.1 Beam dump block system

The two external dumps of the LHC, also known as Target Dump External (TDE), are essential devices for LHC operation. Each of them is installed in an underground cavern located at the end of a tunnel departing from IR6 (see figure 1). Their function is to absorb the energy of the two intense counter-rotating beams that circulate inside the LHC vacuum chambers under all foreseeable circumstances, including abnormal operation conditions of the machine. Each dump is installed inside a purpose-built cavern and is surrounded by iron shielding. The dump blocks are 8.5 m long and 722 mm in diameter, constituted by a vessel of duplex stainless steel, 12 mm thick, containing a mix of graphite blocks and plates of different densities, in order to progressively absorb the proton beam (see figure 18).

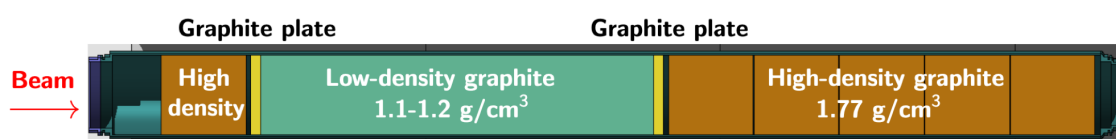


Figure 18. Schematic section of the TDE dump block showing the regions of high density and low-density graphite. The yellow segments are 80 mm thick extruded graphite plates containing the low-density graphite disks.

At the beginning of Run 3 with a bunch population of 1.4×10^{11} ppb, the total energy stored by each beam will reach 418 MJ. At the highest envisaged Run 3 bunch population (1.8×10^{11} ppb), it will increase to 539 MJ, exceeding the LHC ultimate value (535 MJ). The dump absorber blocks, vessel and windows absorb about 78 % of the beam energy, while the remaining energy fraction escapes in the form of secondary particles (19 %) or is consumed in nuclear collisions (3 %). The particles leaking from the dump deposit their energy in the surrounding shielding, air, cavern walls and surrounding bedrock, with the exception of neutrinos, which have a very low interaction cross section and can travel much longer distances.

Prior to the LS2 upgrades, each dump was installed on two steel cradles – they were not clamped or bolted down, instead relying on friction and the connection to the rest of the beam line to stay in place. Four dumps were initially built: two of them have been installed in the machine and have operated during the first and second runs of the LHC; the other two were kept as spares. The dumps were connected to the LHC beam pipe via the “connecting line”, a 10.5 m long, 606 mm diameter stainless steel tube [11, 28]. Both the connecting line and the dump were isolated from the vacuum in the LHC beam pipe by a beam window, and they were filled with nitrogen at 0.15 bar above atmospheric pressure. The purpose of the nitrogen is to create an inert atmosphere, free of oxygen, to avoid the oxidation of the graphite at the high temperatures generated by the beam impact.

During LHC Run 2, nitrogen leaks were detected around the seals. A series of interventions were necessary in order to fix these leaks. Finite element simulations were performed in order to simulate the behaviour of the dump after a beam impact. It was found that the tens of MJ deposited in the steel vessel produced adiabatic temperature rise in the order of 100 °C, generating very fast and large vibrations [26], which were not considered in the initial design of the dump. The amplitude of these vibrations is proportional to the total beam kinetic energy. Thus, it makes sense that the leaks and problems started around the same time as the intensity in the LHC was increased. The detailed analysis of the dump “fast” and “slow” behaviour is described in [26, 27].

In order to prepare the dumps for the increased intensity expected in Run 3, it was decided to remove the connecting line, thus disconnecting the dump from the rest of the LHC beam pipe as to avoid the appearance of leaks in the Ultra-High Vacuum (UHV) section of the LHC as shown in figure 17. This required the design of a new dump support frame, new upstream window, and new nitrogen connection. In turn, these changes required modification to the dumps to make them compatible with the new dump support frame. Due to the residual dose rate of the operational dumps (almost 10 mSv h^{-1} at contact), it was decided to modify the two spare dumps and install them. The two used, activated dumps were removed from the caverns to allow examination in the future.

2.3.2 Upgrades of the dump block supporting system

In the context of the LS2 upgrades, it was decided to physically separate the dump blocks from the extraction lines (figure 17). This change required the development of an ad-hoc support system for the dump block system. Since the vibrations are intrinsic to its thermo-mechanical behaviour, they cannot be eliminated but only mitigated. The objectives of the new support system were to allow the dump to vibrate freely, expand and retract without migrating and without transmitting its vibrations or movements to other beam line components.

The system is based on two steel wire rope loops that suspend the dump block inside a frame. This design provides freedom to accommodate vibrations and at the same time avoids any accumulative movement of the dump over repeated expansion and retraction cycles as the dump is brought back to its original position by gravity. The wire ropes¹ are supported at each end by a steel S460ML (1.8838) cradle structure that fits around the dump block (see figure 19). The new support was designed to fit in the restricted space inside the shielding blocks around the dump block and to be compatible with the remote handling equipment. The ropes (diameter, material, winding) were selected based on the expected dump vibrations, including fatigue analysis and tests to validate the analysis. The original grease that the rope contained was exchanged for a radiation-tolerant grease that is able to withstand the expected dose during Run 3.

2.3.3 Upgrade of the TDE dump block windows

The upstream and downstream windows were exchanged as part of the LS2 upgrade. New Ti-Grade 5, Con-Flat (CF)-flange downstream windows had been designed and manufactured prior to LS2, as it was known that the old Ti-grade 2 windows could not withstand the operating conditions of Run 3.² This change was implemented by welding a new extension to the dump block with a bolted flange interface, so that the new window could be bolted and sealed via a copper gasket, to the downstream end of the dump vessel.

The decision to exchange the upstream window (see figure 20) was taken during LS2, as a consequence of deciding to remove the connecting line. A new Ti-Grade 5 upstream window was designed so the dump could be sealed and a nitrogen line could be connected to it. The upstream window was sealed to the main dump block with a specific radiation tolerant Ethylene Propylene Diene Monomer (EPDM) O-ring and a chain clamp. The interface was studied so it would not leak

¹A 21 mm diameter galvanized high strength steel wire rope, manufactured by DIEPA, was selected for the application.

²In some Run 3 beam dilution failure scenarios the maximum temperature and stresses reached were 203 °C and 209 MPa respectively, possibly leading to yielding in this material [26].



Figure 19. Photo of the two LHC spare dump blocks being equipped in the underground cavern at Point 6 in order to become the new operational dumps. In the figure one could see the dump blocks being inserted in the new cradle as well as the new dump block upstream Ti-Grade 5 window (CERN-PHOTO-202009-112).

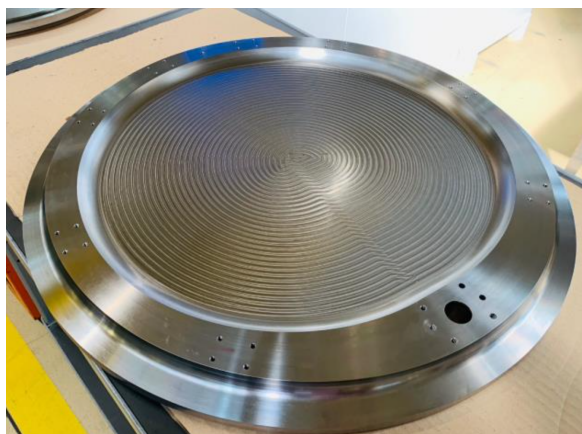


Figure 20. Photo of the Ti-Grade 5 window after the completion of the final machining; the N_2 injection opening is also visible.

due to the beam induced vibrations. The EPDM O-rings were selected based on their radiation resistance to the expected dose in their location.

As discussed in [26] the new dump windows must withstand three different types of loads, occurring at different times scales after the dump and generated by different dynamic sources: 1) thermal stresses induced by the energy deposition of the proton beam, occurring in roughly $90 \mu\text{s}$, 2) mechanical loads induced by the N_2 atmosphere at 0.2 bar of over-pressure inside the dump block vessel and 3) dynamic vibration loads derived from the dump block longitudinal vibrations induced by the energy deposition of the beam shower in the vessel, roughly at 200 Hz. It is worth reporting that the oscillatory stresses on the windows due the vibration load are the highest ones amongst the three types of loads listed [26].

2.3.4 Perspectives for Run 3 operation

During the technical execution of these updates, an opportunistic endoscopy was executed inside the core of the dump for the clockwise rotating beam located in the underground cavern UD68. The extruded graphite disks retaining the low density sector in the UD68 dump (see figure 18) were found to be fully cracked along the diameter [29] (see figure 21). Several hypothesis were raised to explain the observations, mainly pointing to the dynamic behavior of the dumps.

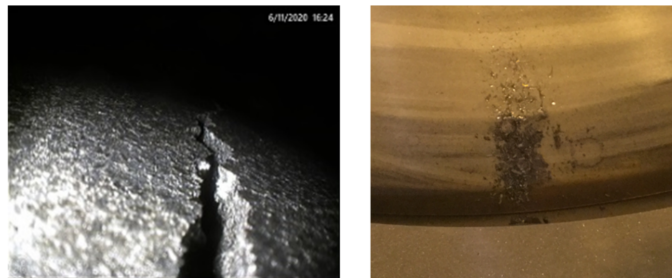


Figure 21. Endoscopic image of the upstream extruded graphite block of the UD68 dump block (left) and powder found in the dump before dump disconnection and removal (right).

Moreover, previous experiments conducted at the CERN HiRadMat facility indicated serious damage on a low density graphite disk, of the same type of those installed on the LHC beam dumps [29] (see figure 22).

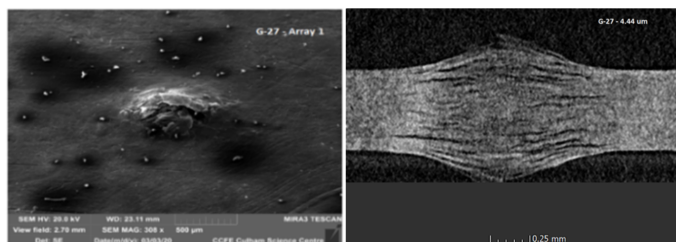


Figure 22. Scanning Electron Microscopy (SEM) results (left) and CERN micro-CT scan (right) on a low density graphite sample installed in the HRMT43 experiment.

In order to assess the impact of these observations on Run 3 LHC operational scenarios as well as for the future HL-LHC beam dump upgrade, a dedicated HiRadMat experiment was executed in November 2021, with essential post irradiation analyses to follow in 2022. Similarly, a complete autopsy of an operational LHC beam dump will be executed in early 2022.

3 HL-LHC upgrades

The HL-LHC Project has been established at the end 2010 [30] to fully exploit the physics potential of the LHC with the following targets:

- A peak luminosity of $5 \times 10^{34} \text{ cm}^{-2} \text{ s}^{-1}$ with levelling operation (corresponding to an average event pile-up (PU) $\langle \mu \rangle$, i.e. the number of events per bunch crossing in the detectors, of ≈ 140)

with the possibility to reach a peak levelled luminosity of $7.5 \times 10^{34} \text{ cm}^{-2}\text{s}^{-1}$ (corresponding to $\langle \mu \rangle > 200$).

- An integrated luminosity of 250 fb^{-1} per year, with the goal of 3000 fb^{-1} in the decade following the upgrade with an almost tenfold increase with respect to the expected luminosity reach by the end of Run 3.

The key elements for optimizing the luminosity performance [9] are:

- The beam brightness, the ratio of the bunch population to its transverse emittance will be increased thanks to the upgrade of the injectors.
- The number of bunches will be maximized by maintaining the bunch spacing of 25 ns.
- Reduction of β^* requiring doubling the aperture of the triplet magnets and of the first separation dipole (D1) and additional modifications of the matching section (including a new larger aperture recombination dipole — D2). The reduction of β^* down to 15 cm is achieved thanks to an innovative optics concept, the Achromatic Telescopic Squeeze (ATS) [31]), allowing, among others, to compensate the strong chromatic aberrations coming from the larger β -functions inside the triplet magnets with the available arc correction circuits.
- Compensation of the luminosity reduction factor, due to the large crossing angle required to minimize Beam-Beam Long-Range (BBLR) effects, by means of special superconducting RF crab cavities, capable of generating transverse electric fields that rotate each bunch longitudinally such that they effectively collide head-on at the collision points.
- The so-called dynamic β^* squeeze will be used as levelling mechanism to vary the transverse beam size at the IP and maintain the luminosity and therefore the event PU at acceptable levels for the experiments throughout the whole fill length.

A schematic view of the high luminosity insertion region (IR1 and IR5) before and after the HL-LHC upgrade is presented in figure 23.

Table 5 shows the beam parameters in collision and compares them with the design LHC parameters.

The main equipment upgrades and layout modifications for HL-LHC will be carried out by the end of LS3 (2026–2028) in LSS1 and LSS5 but other parts of the LHC need to be modified to deal with the upgraded performance. A non-exhaustive list includes:

- Upgrade of the insertion regions IR1 and IR5 from the present collision debris absorber (TAS) to the Q4 quadrupole and in particular the replacement of the existing NbTi triplet magnets with Nb₃Sn magnets.
- Installation of one new large 1.9 K refrigerator unit at both P1 and P5 to provide the cooling power needed to absorb the larger heat load due to collision debris and, with the adoption of a new cryogenic distribution line, to allow the cooling-down or the warming-up of IR1 and IR5 independently from the arcs.

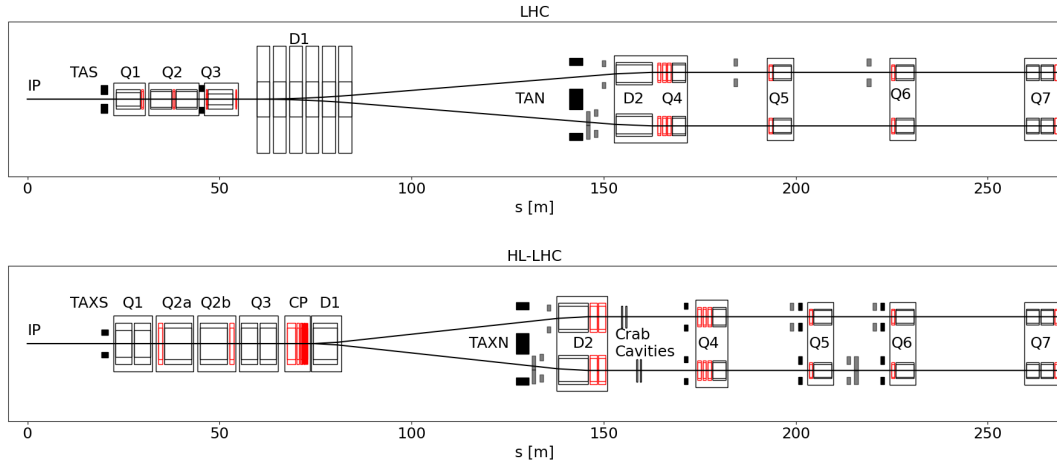


Figure 23. Schematic view of one side of the high luminosity insertions IR1 and IR5 in the LHC (top) and HL-LHC (bottom). The IR collimators are shown in gray. (Courtesy R. De Maria, CERN).

Table 5. HL-LHC nominal parameters for 25 ns operation for two production modes of the LHC beam in the injectors [32] (see section 4.2.1) compared to the LHC design parameters [2].

Parameter	Nominal LHC (design report)	HL-LHC (standard)	HL-LHC (BCMS)
Beam energy in collision [TeV]	7	7	7
Particles per bunch N_b [10^{11} ppb]	1.15	2.2	2.2
# bunches per beam	2808	2760	2744
# colliding bunches in IP1 and IP5	2808	2748	2736
Total beam population N_{tot} [10^{14}]	3.2	6.1	6.0
Beam current [A]	0.58	1.10	1.10
Half-crossing angle in IP1 and IP5 [μ rad]	142.5	250	250
Minimum β^* [m]	0.55	0.15	0.15
Norm. transverse emittance start of collisions ϵ_n [μ m]	3.75	2.50	2.50
Longitudinal emittance ϵ_L [eVs]	2.50	3.03	3.03
Levelled luminosity in IP1/5 [10^{34} cm $^{-2}$ s $^{-1}$]	–	5.0	5.0
Max. average event pile-up $\langle\mu\rangle$ [events/crossing]	27	131	132
Levelling time [h]	–	7.2	7.2
# collisions in IP2/IP8	2808	2492/2574	2246/2370
N_b at injection [10^{11} ppb]	1.20	2.30	2.30
Maximum # bunches per injection N_{SPS}	288	288	240

- Upgrade of the cryogenic system in P4 to increase the cooling power available, considering the presence of the superconducting RF system and the future installation of the Hollow Electron Lenses (HEL).
- Installation of new collimators in IR1 and IR5 as well as the upgrade of most secondary collimators and a few primary ones for impedance reduction.

- Insertion of crab cavities in IR1 and IR5.
- Installation of collimators in the cold Dispersion Suppressors regions, DS2 and DS7, in DS7 via the insertion of 11 T dipoles to create the necessary space. Crystal-assisted collimation for ion beams has been also designed as a possible means to enhance collimation efficiency and as a back-up solution in case of issues with the installation of the 11 T dipoles.
- Modification of the Machine-Detector Interface (MDI) at the ATLAS and CMS experiments with new collision debris absorbers (TAXS and TAXN) in IR1 and IR5 and the installation of a new neutral collision debris absorber (TANB) in IR8 for coping with the increased luminosity expected at IP8 in Run 3, after the LHCb upgrade.
- Modification of the injection systems, in particular installation of new upgraded injection absorbers (TDIS) and injection transfer line absorbers to cope with injection failures.
- Major underground and surface civil engineering works in P1 and P5, to host the technical infrastructure, the refrigerators as well as the powering and protection equipment for magnets and cavities.
- Hollow Electron Lenses for generating an enhanced particle diffusion in the beam halo and favour its depletion, considering that it could account for a total stored energy of 35 MJ, based on the experience during Run 2 operation.
- Upgrade of the LHC Beam Dump Kicker system and of the main beam dump absorbers (TDE).

Some of the above upgrades have been implemented during LS2 and they will benefit the performance during Run 3. They are described in the following sub-sections.

3.1 Collimation system

The safe and efficient operation of the LHC relies on a complex beam collimation system that protects the machine against unavoidable beam-halo losses [33–38]. An immediate limitation at the LHC is represented by possible quenches of the superconducting magnets while operating beams with stored energies in excess of 300 MJ. With quench limits of the order of 20–30 mW cm⁻³, a collimation cleaning efficiency above 99.99 % is required to avoid quenches with operational losses that can reach levels of several hundreds kW [2]. The collimation system must fulfil other important roles [39]. It provides passive protection to any LHC aperture bottleneck, in particular the triplet magnets around the experiments. It also helps concentrating the radiation dose and activation to confined areas designed for this purpose, and provides local protection of equipment to improve its lifetime. In addition, dedicated collimators, on the outgoing beam side of each high-luminosity experiment, clean collision-debris products. Furthermore, collimation plays a crucial role in keeping machine- and halo-induced experimental backgrounds under control [40, 41].

For these requirements, the LHC collimation system features an unprecedented complexity compared to previous particle accelerators. The performance of the system has been continuously monitored and improved since the first operation in the Run 1. The first deployment of the collimation system consisted of 108 movable collimators and 10 fixed-aperture absorbers, and provided an excellent cleaning efficiency above 99.99 % [42], i.e. less than 10⁻⁴ of the primary beam losses

reached the superconducting magnets. The highest losses in this type of equipment occur in the Dispersion Suppressors (DS) around IR7.

An important upgrade that took place for Run 2 involved the replacement of critical collimators with a new design embedding Beam-Position Monitors (BPM), which enable a faster system setup with beam and better control of abnormal orbit conditions at collimators. This upgrade was one of the ingredients that enabled reaching record-low β^* values in Run 2 [43]. Additional collimators for an improved physics debris collimation system around ATLAS and CMS and new passive absorbers in IR3 were also deployed.

The system must be upgraded further in order to cope with the new HL-LHC challenges [9, 44]. During LS2, the first steps of the HL-LHC collimation upgrade took place. There are multiple reasons for the staged implementation of the HL-LHC collimation upgrade. First of all, the upgrades to increase the performance of the LHC with heavy-ion beams take place already in LS2: the ALICE detector upgrade (see section 4.7.1) and the increase of Pb ion beam intensities resulting from LIU (section 4.2.4). The Run 3 collimation system must be able to cope with this increased intensity and luminosity. The progressive availability of LIU proton beams also requires LHC upgrades that enable higher stored intensities. In particular, a reduction of the collimation system impedance enables larger beam currents, and thus the possibility to study unexpected possible future limitations in view of the final HL-LHC upgrade. Finally, a staged deployment of collimation upgrades will allow reducing the workload for LS3 and at the same time deploying some key technologies that can be fully validated with beam before the full-scale implementation in LS3.

Figure 24 shows the final collimation system for Run 3. It comprises 114 ring collimators, including dump and protection devices, that fulfil the different roles introduced above. A total of 22 new collimators were built in LS2, including 5 operational spares.

The backbone of the LHC collimation system is the betatron (IR7) and momentum (IR3) multi-stage cleaning systems installed in two separated warm insertions. The functioning principle of the multi-stage collimation hierarchy, deployed both in IR3 and IR7 and required to achieve a very efficient halo cleaning, is illustrated in figure 25 [45].

Primary (TCP) and secondary (TCS) collimators are placed closest to the beam. Active shower absorbers (TCLA) catch the showers produced upstream, before they reach cold elements. Robust materials are typically required for TCP and TCS collimators, more susceptible to beam losses, while for TCLA that are further retracted, less robust but more efficient materials are used. At the LHC, a Carbon-Fibre Composite (CFC) is used for the former while a heavy tungsten alloy called INERMET[®] 180 is used for the latter.

A dedicated collimation scheme is used to protect the experimental regions against incoming beam losses. A pair of tertiary (TCT) collimators, made of INERMET[®] 180, are installed upstream of the triplet quadrupoles in the final-focus system to protect them from horizontal and vertical beam losses. The high-luminosity regions IR1 and IR5 also use dedicated physics-debris collimators (TCL) to efficiently dispose of the collision products and minimise the impact of losses on the downstream matching section and cold arc.

Table 6 summarises the used collimator families in Run 2 and in Run 3. Collimator family names, collimation plane, jaw material and the planned operational settings in Run 3 are also given. Dump protection devices, which are also part of the collimation hierarchy, are listed as well.

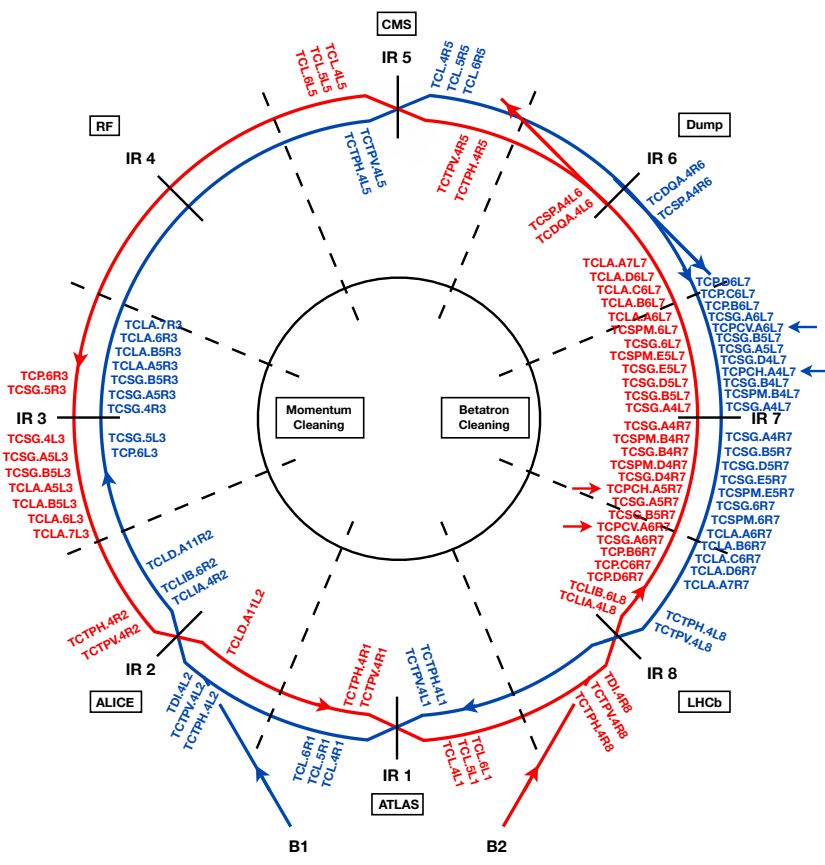


Figure 24. Graphical illustration of the LHC collimation system in Run 3.

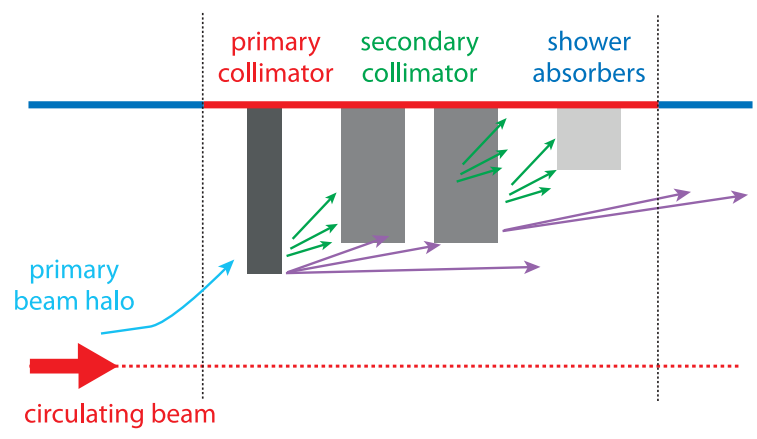


Figure 25. Schematic view of the multi-stage collimation scheme deployed in the betatron (IR7) and momentum (IR3) cleaning insertions of the LHC. Primary and secondary collimators are closest to beam and are made of robust CFC. Shower absorbers sit at larger apertures and are made of a tungsten alloy to improve absorption, in the shadow of protection devices. Additional layers of the collimation hierarchy include tungsten tertiary collimators in the experimental regions and robust protection devices, not shown in the scheme.

Table 6. List of operational movable and fixed-aperture collimators for the LHC Run 3 collimation system, including their abbreviated names, plane (H = horizontal, V = vertical, S = skew), the material (CFC = carbon-fibre composite, W = heavy tungsten alloy — INERMET® 180 —, MoGr = Molybdenum carbide-Graphite, Mo-MoGr = Mo-coated MoGr), the number of installed units, and the operational openings in collision in units of beam σ . The LHC settings are given for p-p operation at $\beta^* = 30$ cm, using a reference normalized emittance $\epsilon_n = 3.5 \mu\text{m}$. The IR2 TCLD's and the crystal primary collimators are used only in ion operation.

Functional type	Name	Plane	Material	#	#	Settings
				Run 2	Run 3	Run 3 [σ]
Primary IR3	TCP	H	CFC	2	2	15.0
Secondary IR3	TCSG	H	CFC	8	8	18.0
Absorber IR3	TCLA	H, V	W	8	8	20.0
Passive absorber IR3	TCAP	–	W	4	4	–
Primary IR7	TCP	H, V, S	CFC	6	2	5.0
Low-impedance primary IR7	TCPPM	H, V	MoGr	0	4	5.0
Primary crystal IR7	TCPC	H, V	Si	4	4	–
Secondary IR7	TCSG	H, V, S	CFC	22	20	6.5
Low-impedance secondary IR7	TCSPM	H, V, S	Mo-MoGr	0	8	6.5
Absorber IR7	TCLA	H, V, S	W	10	10	10.0
Passive absorber IR7	TCAP	–	W	8	8	–
Passive absorber mask IR7	TCAPM	–	Steel	0	2	–
Dispersion suppressor IR2	TCLD	H	W	0	2	–
Tertiary IR2/IR8	TCTP	H, V	W	8	8	37/15
Tertiary IR1/IR5	TCTP	H, V	W	6	2	8.5
Tertiary IR1/IR5 with wires	TCTW	H, V	W	2	4	8.5
Physics debris IR1/IR5	TCL	H	Cu / W	12	12	17–40
Dump protection IR6	TCDQ	H	CFC	2	2	7.3
	TCSP	H	CFC	2	2	7.3

3.1.1 Staged collimation upgrade towards HL-LHC

Three main pillars of the HL-LHC collimation upgrade can be identified [44]:

- Improved protection of the DS around IR7 and IR2 particularly for ion operation.
- Reduction of the collimator-induced impedance to allow operation with higher-brightness beams.
- Improvement of the collimation of incoming and outgoing beams in the experimental insertions IR1 and IR5.

A detailed description of these upgrades can be found in [44]. The proposed staged collimation upgrade involved several important HL-LHC activities to take place already in LS2 as well as some consolidation activities:

- the DS cleaning upgrades around IR2 (2 TCLD collimators);

- the first phase of the low-impedance upgrade of the system, involving the installation of 8 new secondary collimators (TCSPM) and 4 primary collimators (TCPPM) in IR7;
- the improvement of the protection of warm magnets in IR7 against radiation effects by means of two new passive absorbers (TCAPM);
- the deployment of crystal collimation for ion beams in IR7.

These items are described in detail in the following section. The tunnel activities during LS2 were primarily concentrated in the straight section of IR7 and on the DS regions around IR7. In addition to these major interventions, a reshuffling of the collimators with embedded wires for BBLR compensation studies was carried out in IR1 and IR5 (as discussed in section 3.1.7).

The installation of the TCLDs in IR7 was also initially planned to mitigate the risk of quenches during ion operation in Run 3. That requires the replacement of one LHC main 8.33 T dipole with two shorter 11 T dipoles to liberate some space for the installation of the collimator. A scheme with the TCLD collimator installed between two cold dipoles is shown in figure 26 (the same design and integration is used for the IR2 TCLDs without 11 T dipoles). The IR7 installation could not take place during LS3 because of the project decision to defer the installation of the 11 T dipoles [46, 47]. Crystal collimation will be used instead in IR7 during ion operation in order to increase the cleaning efficiency and to lower the losses in the DS regions around IR7. The full crystal collimation scheme required 4 TCPCs, one per beam and plane. Because of the late decision to defer the 11 T dipole installation (Nov. 2020), only two new TCPCs could be built in time for installation before the start of Run 3 in 2022. The test TCPC units built and installed in Run 2 for crystal collimation tests will be kept operational and used for the ion run at the end of 2022. The fully-upgraded Run 3 system will be completed with the installation of two more new TCPCs at the end of 2022.

3.1.2 Low-impedance upgrade of the collimation system and passive absorbers

The LHC impedance budget is largely dominated by the contribution of the LHC collimators [48]. In particular, the primary and secondary collimators are the largest contributors because they are the closest collimators to the circulating beam and they are made of robust CFC, with typical resistivity values of 5000–5500 nΩ m.

This potential limitation was known already at the LHC design stage [2]: the robustness of the first collimation stages was favoured for the first LHC runs as solutions could not be found to withstand the design loss scenario while ensuring a sufficiently low resistivity [2]. The robustness requirement rules out the possibility to deploy high-Z metals because of their relatively low melting point and comparatively large thermal expansion that impairs their resistance to thermal shocks [49]. The collimation system was however prepared for a future impedance upgrade. Every TCS slot in IR3 and IR7 features a companion slot for the future installation of a low-impedance secondary collimator [2], for a total of 22 cabled slots in IR7 and 8 in IR3. Simulations predict that beam stability can be guaranteed for the HL-LHC operational scenarios if the CFC of present TCSGs is replaced, at least in the betatron cleaning insertion, with a material having an electrical conductivity a factor of 50 to 100 higher than CFC [50]. However, the TCSGs should also maintain a sufficient robustness against beam impacts and a high cleaning efficiency.

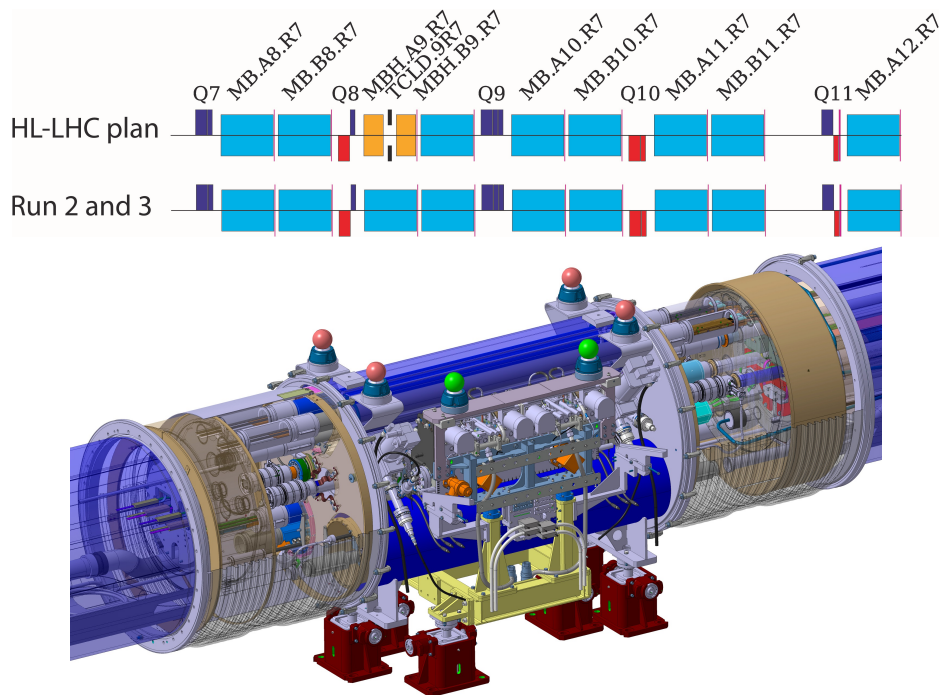


Figure 26. Top: scheme with the HL-LHC planned upgrade of the DSs around IR7 and of the Run 3 layout, which remains unchanged from Run 2. Bottom: 3D drawing of the TCLD collimator and the new cryogenics bypass between two 11 T dipoles (IR7) or connection cryostat (IR2). (Courtesy of L. Gentini, CERN).

The upgrade of primary and secondary collimators relies on a novel carbon-based material, the Molybdenum carbide-Graphite (MoGr). This is a ceramic composite, jointly developed by CERN and Brevetti Bizz (IT) [51], in which the presence of carbides and carbon fibres strongly catalyses the graphitic ordering of carbon during high temperature processing. This enhances its thermal and electrical properties [49]. To further improve their surface electrical conductivity, these materials will be coated with 5 μm pure molybdenum. The coating is only planned for the secondary collimators, to minimise the risk of direct exposure to primary beam losses. An extensive literature is available on the R&D for the development of this material [52] and on the key validation steps prior to the deployment for accelerator applications [53–56]. This includes the installation in the LHC of a full-scale secondary collimator prototype made of MoGr that was tested extensively with beam in 2017–2108 [48]. For the LS2 production (see below), the first industrial production of MoGr was successfully setup, involving material procurement for 15 new collimators (12 for installation and 3 spare units). Figure 27 shows the achieved electrical performance of every production batch of coated MoGr blocks, as measured on coating samples. The acceptance limit was set to 100 $\text{n}\Omega\text{ m}$, i.e. about a factor two larger than the pure-Mo resistivity. The limit was respected well throughout the production. The resistivity of uncoated MoGr was measured to about 1000 $\text{n}\Omega\text{ m}$ [57]. A photograph of the MoGr blocks for a full TCPPM jaw, prepared for thermal treatments, is shown in figure 28.

The foreseen HL-LHC upgrade consists of the installation of Mo-coated MoGr collimators in 9 out of 11 TCS slots per beam. In addition, the replacement of 4 IR7 primary collimators (horizontal and vertical ones for each beam) with new TCPPM made of uncoated MoGr is also planned. It is

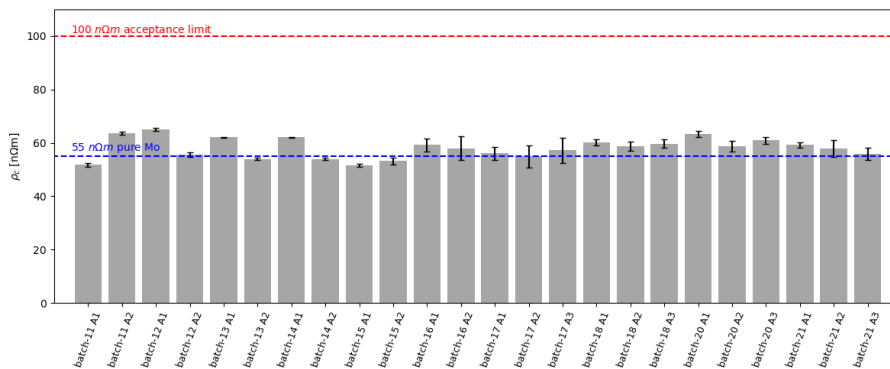


Figure 27. Measured resistivity of Mo-coated MoGr production batches for the LS2 collimation low-impedance upgrade. (Courtesy of N. Biancacci, CERN).

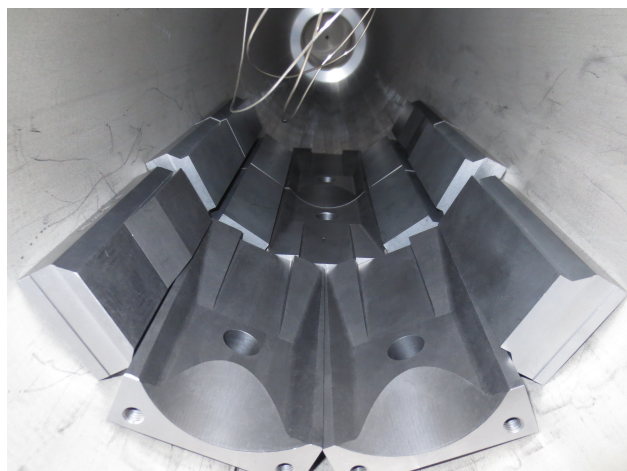


Figure 28. MoGr for a TCPPM jaw ready for thermal treatment. (Courtesy of F. Carra, CERN).

noted that all new collimator have in-jaw BPM to improve significantly the alignment of the system. This low-impedance upgrade will take place in two stages: the first installation of 4 TCPPMs and 8 TCSPMs has taken place in LS2. It will be followed by a second installation in LS3, when the remaining 10 secondary collimators will be installed. This schedule gives already an impedance reduction and operational experience with the new collimators in Run 3, while allowing possible further iterations on the collimator design for the last units. Photographs of a new primary collimator made of MoGr are shown in figure 29.

The choice of the slots for installation during LS2 [58] was mainly driven by maximising the impedance reduction for the first upgrade phase, while avoiding installation slots with the highest expected thermo-mechanical loads, as an extra safety measure for validating the first-phase design. A photograph with the tunnel view of a TCPPM collimators, as installed in IR7, is shown in figure 30.

3.1.3 Passive absorbers in IR7

Two new passive absorbers were also installed in IR7. Figure 31 shows a photograph of the one installed for beam 2 on the right side of IR7. These devices, called TCAPM, have a fixed elliptical

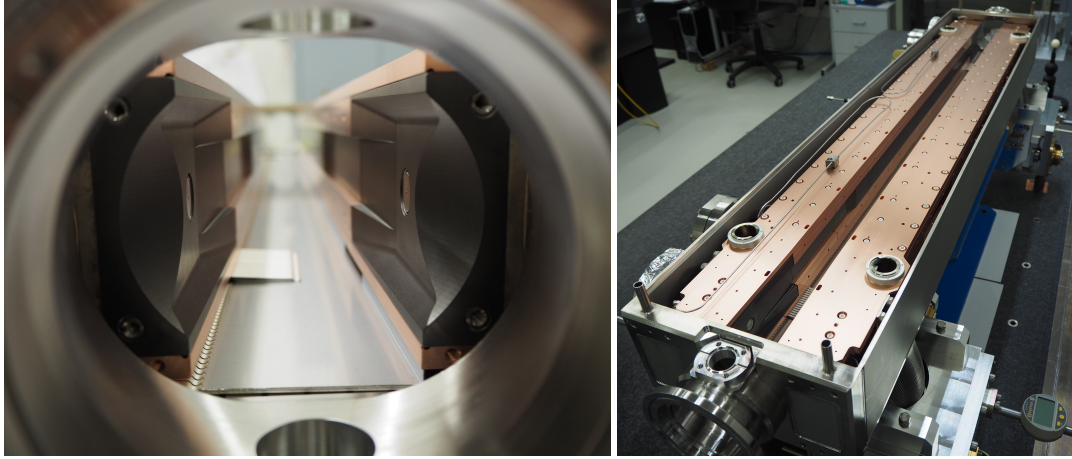


Figure 29. Photographs of a low-impedance primary collimator, TCPPM, with the vacuum tank opened before final welding: front view (left) and top view (right). The BPMs embedded in the jaw’s tapered part are also visible. (Courtesy of F. Carra, CERN).

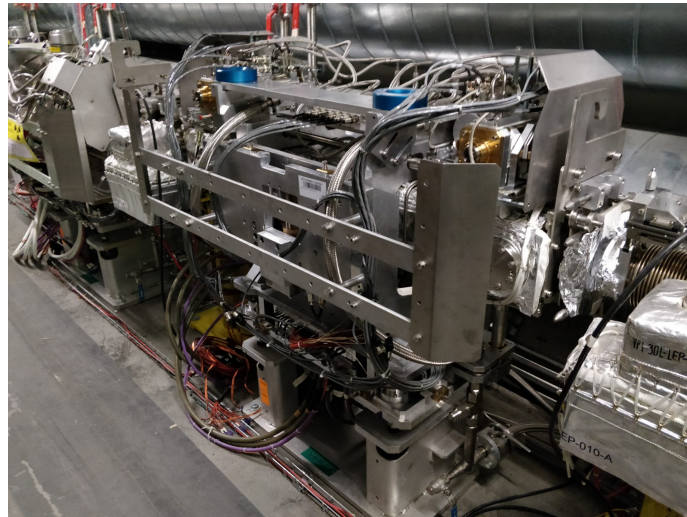


Figure 30. Horizontal primary collimator, TCPPM, installed in IR7 on Beam 2. (Courtesy of I. Lamas, CERN).

aperture that matches the one of the downstream magnet. A steel structure shields the magnet coils and protects from radiation damage the epoxy insulator used for the coils. It is expected that, with this upgrade, the warm magnet lifetime is compatible with the full HL-LHC programme [59].

3.1.4 Dispersion suppressors around ALICE

When two Pb ion beams collide, secondary ion beams with different magnetic rigidity are created, which are lost in the downstream DSs at both sides of the interaction point [60–65]. These ions represent a source of local heat deposition in the impacted magnet. The dominating processes are Bound-Free Pair Production (BFPP), where electron-positron pairs are created and one (BFPP1) or two (BFPP2) electrons are captured in a bound state of one of the colliding nuclei, thus changing

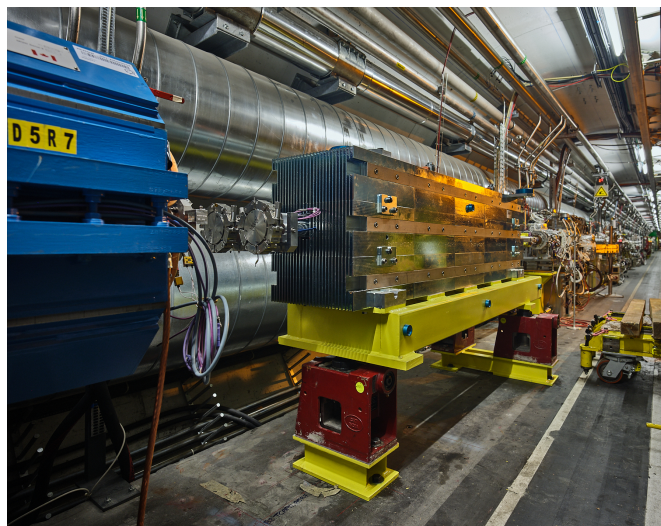


Figure 31. Passive radiation absorber, TCAPM, installed just upstream of the IR7’s warm quadrupole (blue magnet in the photograph) to minimize the effect of radiation on sensitive components. (Courtesy of I. Lamas, CERN).

its charge, and electromagnetic dissociation (EMD), where one nucleus predominantly emits one (EMD1) or two (EMD2) neutrons, thus changing mass. Further photon-induced processes also take place, but the four mechanisms mentioned here have the highest cross sections. An example of BFPP1 ion beams produced in collisions of $^{208}\text{Pb}^{82+}$ nuclei in IR2 is given in figure 32. At the upgraded ALICE luminosity of $6.4 \times 10^{27} \text{ cm}^{-2}\text{s}^{-1}$ (see section 4.7), at 7Z TeV the BFPP1 beam can carry up to 165 W, well above the superconducting magnet quench limit.

Downstream of ATLAS and CMS, these losses are mitigated by redirecting them with a local orbit bump into a connection cryostat without a magnet, which alleviates the risk of quenches at the luminosities considered for Run 3 and Run 4. Downstream of ALICE and LHCb, this technique does not work because of the opposite quadrupole polarities, causing the off-momentum orbit of the BFPP ions to be at a minimum at the connection cryostat [65]. Therefore, new collimation solutions had to be found.

Dispersive losses cannot easily be prevented with collimators in the straight sections, where the single-pass dispersion remains small. This calls instead for a local collimation in the cold regions, where the dispersion is large enough for the particles with changed rigidity to be well separated from the main circulating beam. A new collimation scheme in the DSs is based on the novel TCLD collimator design that is very compact and can be integrated in the cold region thanks to a special connection cryostat, as illustrated in figure 33. The TCLD remains at room temperature and it is installed in a vacuum-sectorized area adjacent to the cold element immediately upstream and downstream of the collimator. In the DSs around IR2, the BFPP1 beam produced in Pb-Pb collisions can be steered at the location of a magnet-free connection cryostat in cell 11, enabling the installation of the TCLD collimators. The schematic view of this regions, in the Run 2 and Run 3 layouts, is shown in figure 34. This installation required a new cryogenics by-pass (see right scheme of figure 33) and two, shorter connection cryostat. This assembly replaces the present, about 15 m-long, connection cryostat.

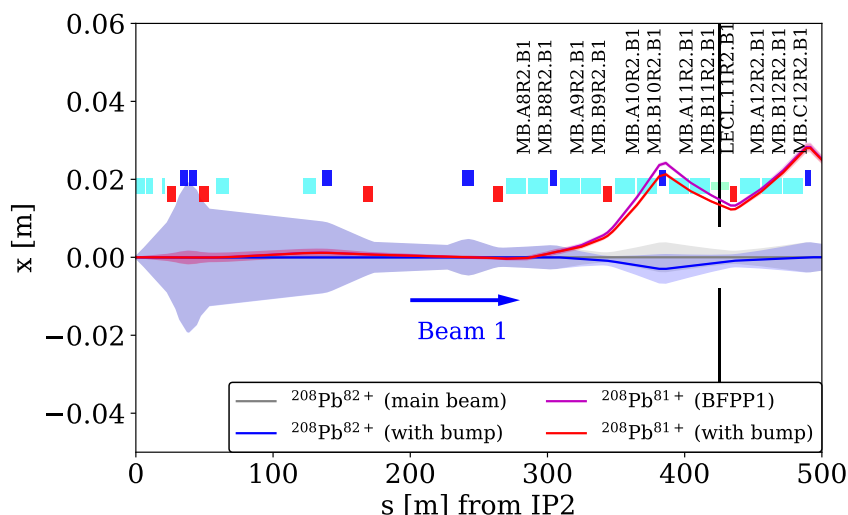


Figure 32. The Beam 1, 12σ envelope of the main $^{208}\text{Pb}^{82+}$ beam (light gray) together with the dispersive trajectory of ions undergoing the BFPP1 process, coming out of the ALICE experiment (IP2), without (magenta) and with (red) a correction orbit bump used to steer the BFPP1 ions out of the machine aperture in cell 10 and onto the jaw of the new TCLD collimator. The envelope of the main beam with bump is also shown (light blue). The collimator jaws appear as black lines. Figure taken from [65] (CC BY 4.0).

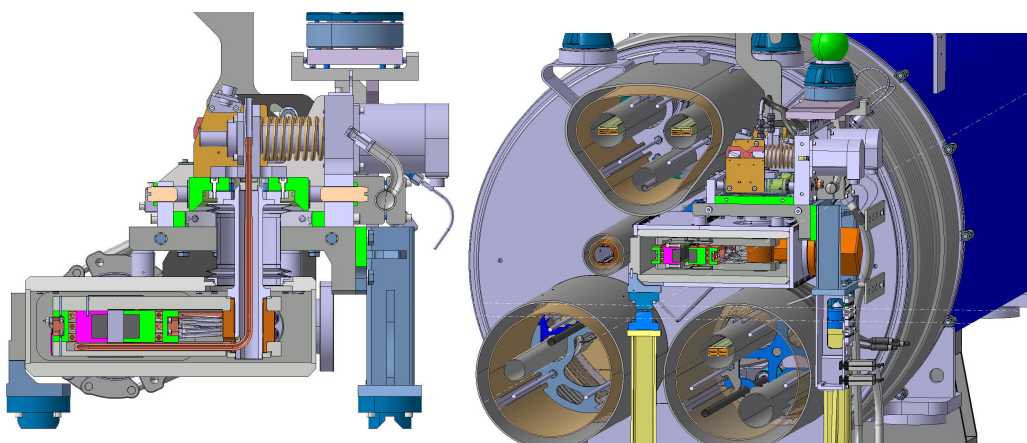


Figure 33. Drawing of the TCLD collimator (left) and cross section of its 3D integration in the cryogenics by-pass specially designed to fit the compact TCLD design between the cryogenics connections. The same designs for the collimators and for the by-pass are used for the installations without (IR2) and with (IR7) 11 T dipoles. (Courtesy of L. Gentini, CERN).

The installation of the two connection cryostats and of the TCLD collimators around IR2 was successfully completed in 2020. A photograph of the TCLD collimator, as installed on the right side of IR2, is given in figure 35. The TCLD is integrated in a specially designed assembly, containing a beam pipe for the other beam, as well as a cryo-by-pass. The system design is particularly complex due to the very limited space imposed by the surrounding cryogenic equipment. Therefore, the active length of the collimator jaw material had to be reduced to only 60 cm compared to 100 cm adopted for most other LHC collimators.

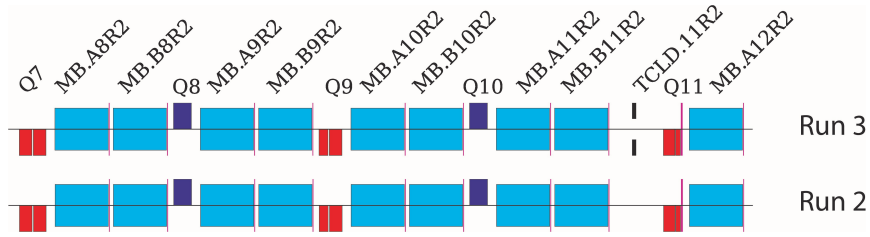


Figure 34. Schematic layout of the DS region on the right side of ALICE. The TCLD collimator is installed on the connection cryostat (top layout), in a region where there were no collimators or magnetic elements (bottom) in Run 2.

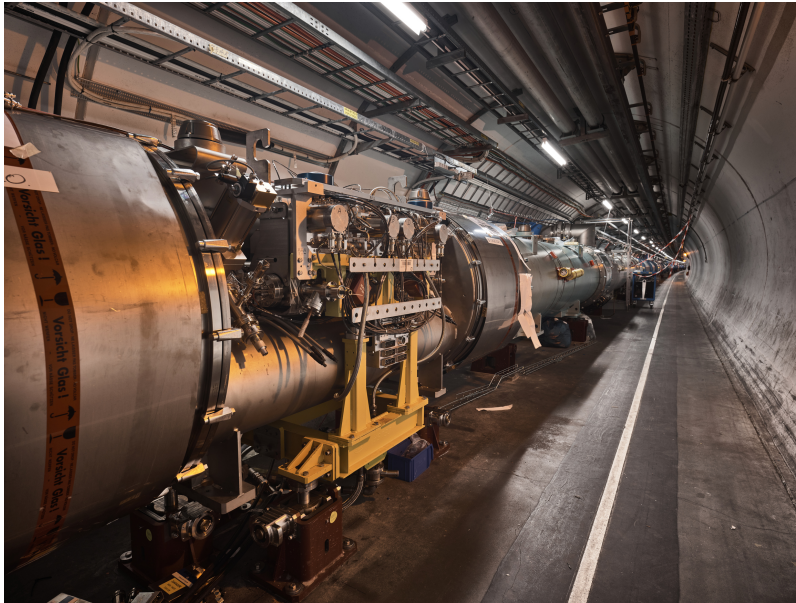


Figure 35. TCLD collimator as installed in the LHC tunnel, in the right side of IR2.

The combination of TCLD collimators and orbit bumps will enable reaching the luminosity of $6.4 \times 10^{27} \text{ cm}^{-2}\text{s}^{-1}$ at ALICE. At LHCb, no collimator installation is presently foreseen and the luminosity will hence be levelled at a lower value of $1 \times 10^{27} \text{ cm}^{-2}\text{s}^{-1}$ to avoid quenches. This value was used for ALICE in Run 2 and is lower than the luminosity at which a quench has been observed close to CMS [65]. This approach is motivated by differences in local geometry and impact distribution, but further detailed studies could be carried out to investigate if the LHCb levelling target could be increased.

3.1.5 Dispersion suppressors around the betatron cleaning system

The cleaning upgrades in DS regions around IR7 are primarily driven by the increased risk of quenches from off-momentum losses following the interactions of halo particles with the collimator jaws. A small fraction of protons or ion fragments interacting with the collimators in IR7 escape from the betatron system with a different magnetic rigidity. These are mainly single-diffractive protons emerging from the TCPs or ions having experienced fragmentation or electromagnetic

dissociation. They are typically lost in the cold DS magnets, where the dispersion starts to increase and where they represent a source of local heat deposition.

Although the intensities of heavy-ion beams are lower than those of proton beams, they undergo numerous nuclear and electromagnetic interactions with the material of the primary collimators, creating an abundance of secondary ions with different mass and charge. Collimation of heavy-ion beams is therefore much less efficient than that of proton beams [66, 67]. In Run 3 the cleaning system will have to sustain a higher power loss due to the higher beam intensity than in Run 2, in particular for Pb ions where the stored beam energy will be nearly doubled (see section 4.2.4 and 4.7).

Simulations have been performed for protons and Pb ions indicating a potential intensity limitation for the latter already in Run 3. The peak power load in the superconducting coils in the DS, averaged over the cable width, is estimated for the HL-LHC 7 TeV target parameters at around 21 mW cm^{-3} for protons and 57 mW cm^{-3} for Pb ions in case of a beam lifetime drop to 0.2 h [44]. This should be compared with a quench limit of around 20 mW cm^{-3} , inferred from quench tests and corresponding simulations [68]. The power load due to proton losses exceeds the quench limit for HL-LHC beam parameters, while in Run 3 it could reach at most about 16 mW cm^{-3} . The upgraded collimator material used in primary collimators improves, according to simulations, the DS losses by about 20–25 %, bringing them to the level of $10\text{--}12 \text{ mW cm}^{-3}$ in Run 3, comfortably below the assumed quench limit. The power load due to Pb ion losses exceeds it by almost a factor 3 already for Run 3, calling for an upgrade during LS2.

In IR7 this is only feasible with a major change of the superconducting magnets layout. In order to make space for the new collimators, it was initially envisaged to replace, for each TCLD in IR7, an existing main dipole with two shorter, higher-field 11 T dipoles. The 60 cm long TCLD, made of the tungsten alloy INERMET[®] 180, were to be located in the new connection cryostat between two 11 T magnets. It is important to note that the collimator and by-pass design are the same for the integration in around IR2 and IR7, in order to minimize the impact on the production. The TCLD collimators were successfully produced during LS2 and prepared for installation. On the other hand, in Nov. 2020 the decision was taken not to install the 11 T dipoles during LS2 [46]. While this deferral of the planned upgrade does not pose obvious risks to the proton operation targets in Run 3, an alternative upgrade had to be found to improve the cleaning performance for the upgraded ion beams.

3.1.6 Crystal collimation system for ion beam cleaning

Following the decision not to install the 11 T dipoles during LS2, and the subsequent deferral of the TCLD collimator installation, the upgrade of collimation of heavy-ion beams in Run 3 relies on the crystal collimation scheme. It is shown schematically in figure 36, and can be compared with the multi-stage system of figure 25. While the latter requires several secondary collimators and absorbers, one single absorber per collimation plane would instead be sufficient, in theory, in a crystal-based collimation scheme. A bent crystal replaces the primary collimator and steers the impinging halo coherently on a single spot [69, 70]. Nuclear interactions are much reduced in this case, which translates into a reduction of dispersive losses downstream of the cleaning insertion. The focus of crystal R&D for collimation upgrade studies has been put on the betatron cleaning and this technique has been studied as an alternative to the solution based on local TCLD collimators in the DS. Simulations indicate a possible gain in cleaning efficiency of proton beams between a factor 5 and 100 compared to the Run 2 system [71], for a layout that uses existing secondary collimators

as absorbers. This configuration is currently not possible for protons as we do not have a validated solution for the design of a collimator absorber capable of disposing of the 1 MW power extracted by the crystal for the design loss scenario with 0.2 h beam lifetime in nominal HL-LHC proton operation. The crystal collimation option is, however, directly applicable for collimating heavy-ion beams, which have a much lower intensity. The extracted power for design failures is more than 30 times lower than for protons and the present secondary collimators are adequate as absorbers of channelled ions. Crystals can be integrated into the present ion collimation hierarchy without further modifications or major changes of the collimators that are used for proton operation.

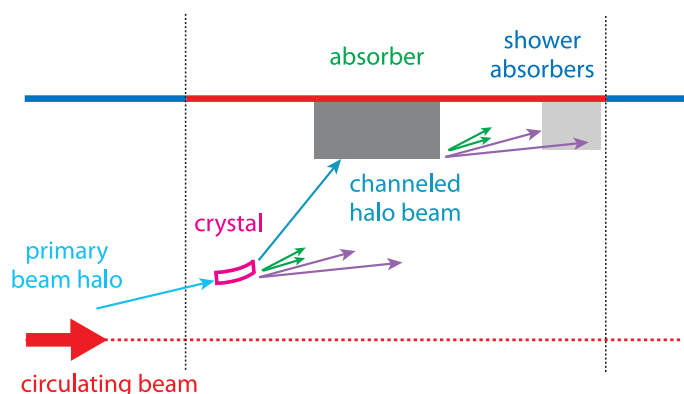


Figure 36. Schematic view of a crystal-based multi-stage betatron cleaning system where the primary collimator use bent crystals to steer the halo particles onto dedicated halo absorbers. Compared to the standard collimation scheme of figure 25, fewer — ideally one — absorbers are needed instead of the several secondary collimators used in the present collimation system.

Four crystal primary collimators of different designs were installed in IR7 in different campaigns between 2015 and 2017 [72]. These are test devices which are however not considered sufficiently reliable for standard long-term operation. It is planned to upgrade this system by replacing all the four present TCPCs with new devices. Because the decision to defer the 11 T dipole installation was only taken at the end of 2020, only two new TCPCs could be built during 2021 and installed before the start of Run 3. Four additional units (including two spares) will be built in 2022 and the final layout will be deployed for 2023. The first ion run in 2022 will therefore still rely partly on old devices. The two best-performing TCPC assemblies, i.e. the horizontal ones for each beam [72], will be kept operational. The risk associated to this strategy is considered acceptable.

The final design is shown in figure 37: it features a replacement-chamber consisting of an ‘O’-shaped pipe that is moved into the beam when crystals are not needed, to minimize the effect of the TCPC on the circulating beams. This is the case, typically, for proton operation when the crystal collimators are not used. This chamber is moved out — as shown in figure 37 — to enable linear movement of the crystal into the beam. A custom-design goniometer based on an interferometer, capable to achieve sub- μm angular accuracy [73–75], is used for setting the crystal to its optimum-channeling orientation. Channeling of high-energy LHC beam was reliably achieved for proton [76] and ion [71, 77] beams. Details of the crystal setup procedure can be found in [71]. A review of the crystal-based collimation performance with Pb beams can be found in [72, 78]. See also [79] for an example of other recent applications of crystal collimation at the LHC.

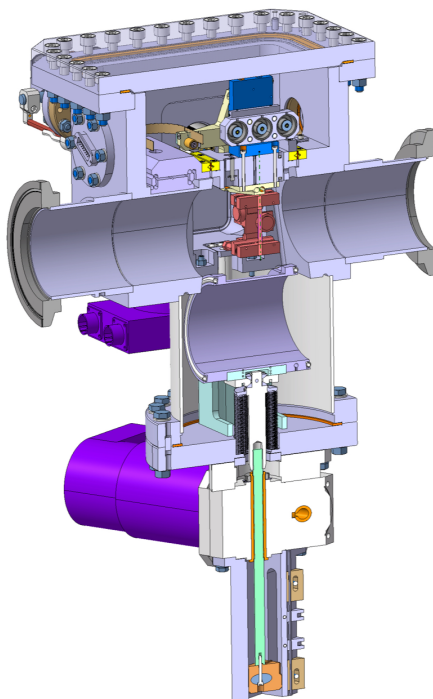


Figure 37. Drawing of the TCPC, crystal primary collimator, assembly. The design is based on a replacement-chamber concept: when crystals are not needed, specifically during high-intensity proton operation, this chamber is moved into the beam to shield the crystal. In crystal operation, shown in the figure, the chamber is moved out of the beam to allow crystal movement into the beam. (Courtesy *L. Gentini, CERN*).

3.1.7 New layouts for wire collimators

As a part of the HL-LHC studies, four special collimators with embedded powered wires, called TCTW, were built to assess BBLR compensation schemes at the LHC. A copper wire that can carry up to 350 A is integrated in each INERMET[®] 180 jaw, as shown in the drawing of figure 38. The two wires in each collimator can be powered individually, in series or with currents of opposite signs, depending on the required configuration. Otherwise, the collimator uses the standard TCTP design, it includes BPMs and can be used as a standard tertiary collimator. The operation of these devices with beam at the design current was validated in various studies during Run 2 [80].

Initial studies aimed at demonstrating the feasibility of the BBLR compensation scheme [81], starting with low-intensity beams (see also section 4.6). To this end, the four available collimators were installed on Beam 2, one upstream and one downstream of IR1 (vertical crossing) and IR5 (horizontal). This is illustrated in the left graph of figure 39. The upstream TCTWs occupied slots of standard tertiary collimators and were used in operation for this purpose, with wires off. Following the promising beam tests [80], and the observation that the upstream TCTW are more efficient than the downstream ones because of optics constraints, it was then decided to reconfigure the TCTW layouts during LS2. One TCTW per beam and per collision point, as shown in the right scheme of figure 39, is installed for each incoming beam. This new layout opens the possibility to use these collimators for BBLR compensation during physics fills at the LHC in Run 3.

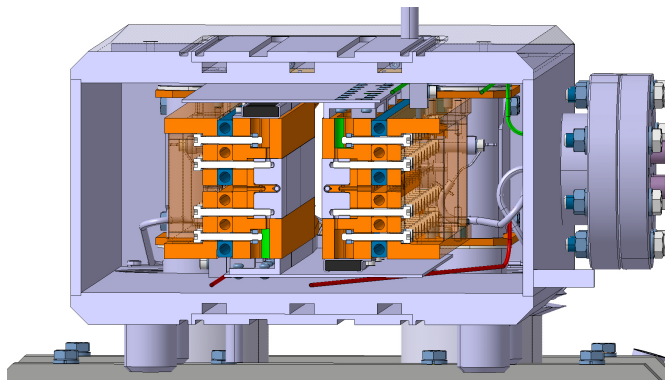


Figure 38. Transverse cross section of the tertiary collimators with current-carrying wires embedded in the jaws. (Courtesy L. Gentini, CERN).

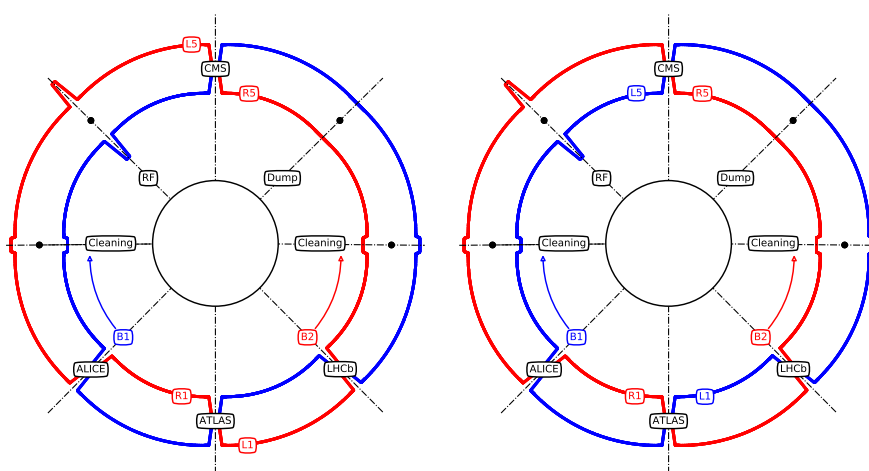


Figure 39. Schematic layout of the LHC ring showing the TCTW layouts: 2018 configuration with 4 TCTW on beam 2 (left) and 2022 configuration with 2 TCTW per beam, at the most efficient locations upstream of IR1 and IR5 (right). (Courtesy A. Poyet, CERN).

3.2 Cryogenics

The LHC sectors are cooled by 8 similar helium refrigerators. The architecture of the LHC cryogenic system is shown in figure 40 [1, 2]. As part of the HL-LHC project the following upgrades are going to be implemented [9]:

- the installation of two new cryogenic plants at Point 1 and Point 5 for the high-luminosity insertions. This upgrade will be based on a new sectorization scheme aimed at separating the cooling of the magnets in these insertion regions from the arc magnets and considering the new feed-boxes and superconducting links located in underground infrastructures;
- the installation of new cryogenic distribution lines (QXL) at Point 1 and Point 5 in the LHC tunnel and in new underground service galleries;
- the upgrade of the existing cryogenic plant (QSRA and QURA) cooling the LHC sector 34 located at Point 4.

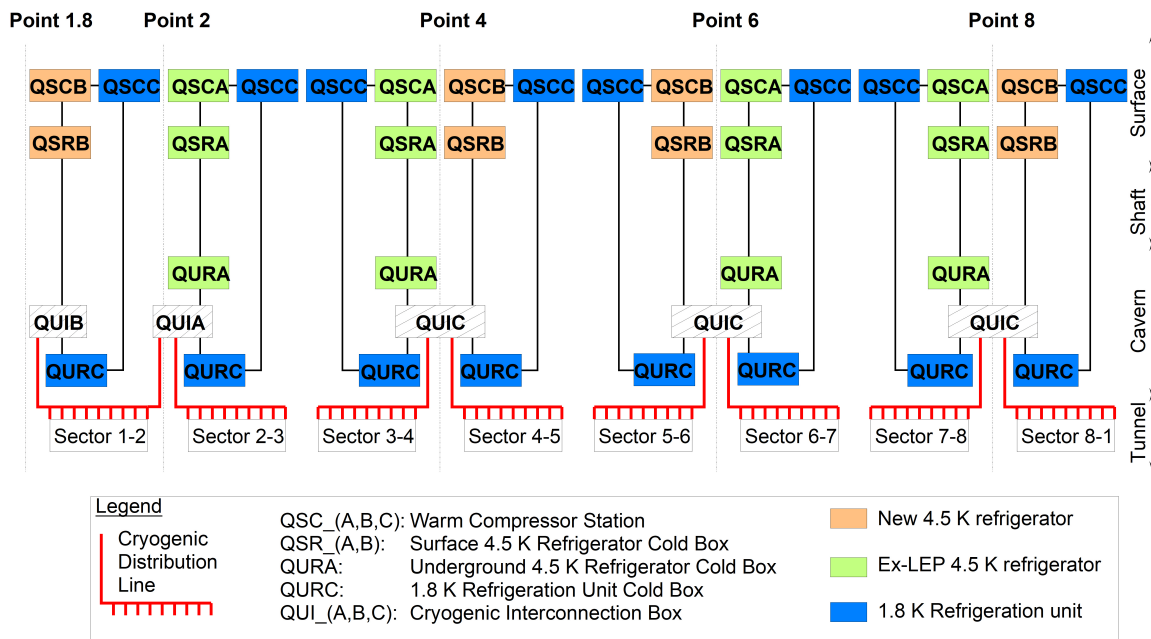


Figure 40. Architecture of the LHC cryogenic system.

Point 4 needs more cooling capacity due to the presence of the superconducting RF system installed in LSS4. This has not limited LHC so far, but would be a bottleneck for the HL-LHC era and even during Run 3 taking into account the expected higher circulating beam intensity (see section 4.3). Following conceptual studies ranging from completely new cryogenic infrastructure to partial modifications, it was decided to upgrade the existing refrigerator of sector 34 without touching the working and not limiting cryogenic distribution, while sector 45 will recover cooling capacity with its extremity situated in Point 5 and cooled by the new HL-LHC infrastructure.

3.2.1 Point 4 cryogenic system upgrade during LS2

The upgrade of the cryogenics system in Point 4 has taken place during LS2. More efficient expansion turbines have replaced the original ones, thus allowing to provide the required higher cooling capacity (+12%) with the same original compressors and identical power consumption. The upper and lower cold boxes (QSRB and QURC, respectively) have been modified. For the upper cold box at the surface, it was necessary to enter inside the box for cutting pipes and welding larger housing (see figure 41).

For the lower cold box, specific adapters were engineered as access inside the box was not possible (see figure 42).

3.2.2 Achieved performance

After cool-down, it was only possible to operate the upgraded cryogenic plant in stand-alone mode with limited load, allowing to demonstrate the full operating range of the new turbines as well as its global correct performance. Once the LHC sectors were cooled at nominal temperature in Spring 2021, it was possible to have representative loads on all temperature levels (thermal shield between 50 K and 75 K, cold masses at 1.9 K, beam screens between 4.5 K and 20 K and liquefaction load in

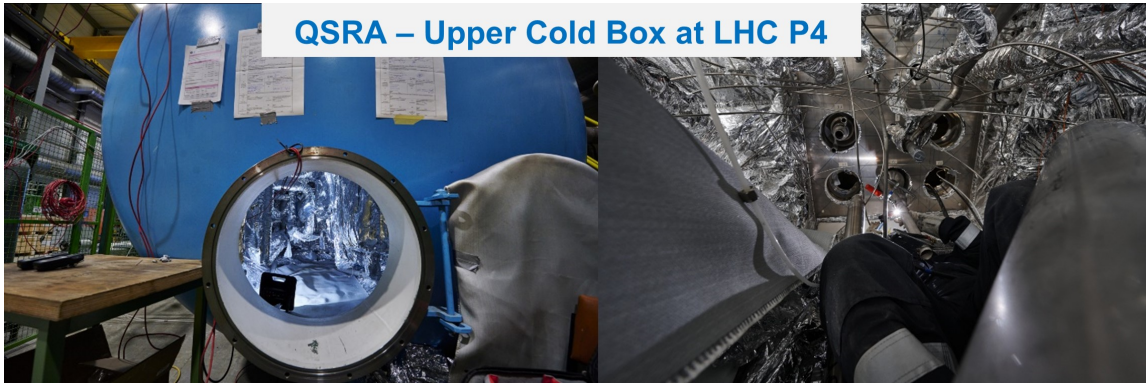


Figure 41. Modification of the Upper Cold Box (QSRA) at Point 4 of the LHC.

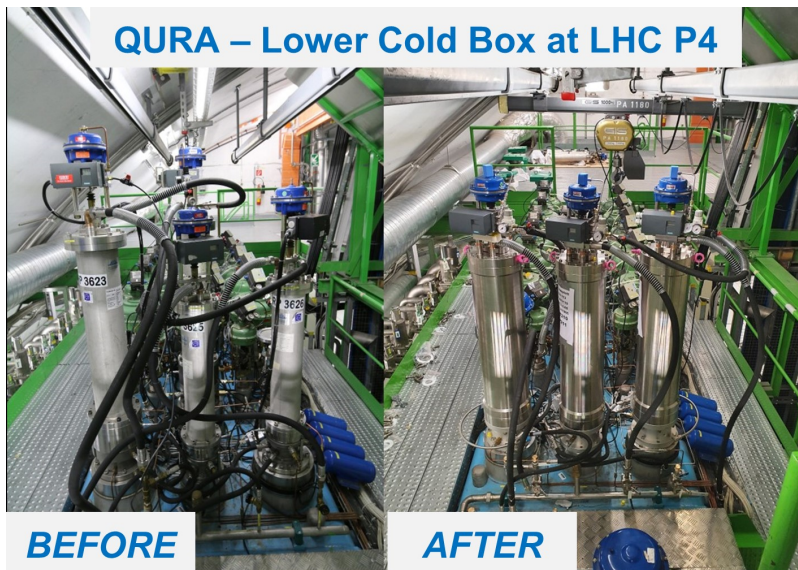


Figure 42. Modification of the Lower Cold Box (QURA) at Point 4 of the LHC.

current feed-boxes) and to compare with a similar reference test performed during Run 2. Although the absolute value differs from original LHC performance values, we could observe the expected gain in capacity of 2.4 kW at 4.5 K. Since the start-up in autumn 2020, the new turbines have been operated without any failure nor induced perturbation.

3.3 Injection dump

A movable two sided injection dump is installed at about 90° phase advance from the LHC injection kickers (MKI) [82] to protect downstream machine elements in case of MKI malfunctions. This dump is also used to intercept pilot bunches during the setup or commissioning of the injection system. The original design (TDI) consisted of a single module with 4.185 m long jaws accommodating absorber blocks of different materials (2.885 m hexagonal Boron Nitride — hBN —, 0.6 m Al and 0.7 m Cu) [83]. During the first LHC Physics Runs, the TDIs in both IR2 and IR8 were affected by several anomalies including out-gassing, structural damage of the beam screens and elastic deformation of the jaws due to beam induced RF heating. This imposed limitations in the maximum number

of bunches per injection and thus also in the total stored intensity. Several hardware changes were applied during LS1 and the following Year-End Technical Stop (YETS) to mitigate the encountered problems [84]. Despite a visible reduction of the beam induced deformation and of the vacuum activity, it was decided to develop a new design to improve robustness, reliability, setup accuracy, to reduce impedance and to streamline operational procedures in view of operation with higher beam intensity and brightness after LS2.

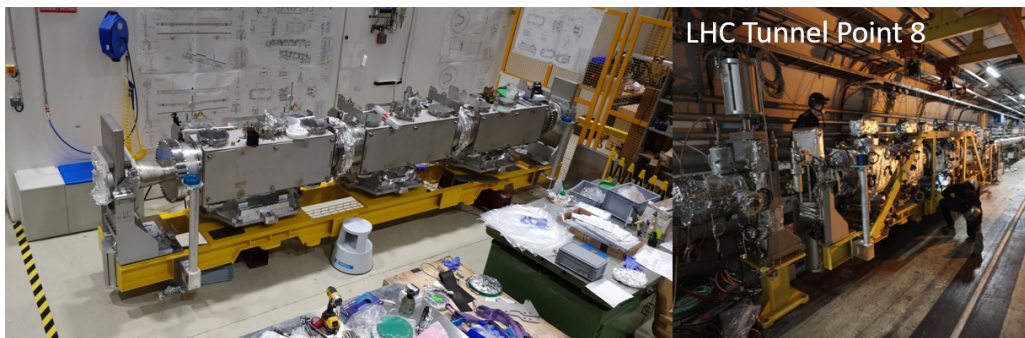


Figure 43. The three modules of the TDIS installed on the common girder (left) and the final installation in Point 8 of the LHC are shown.

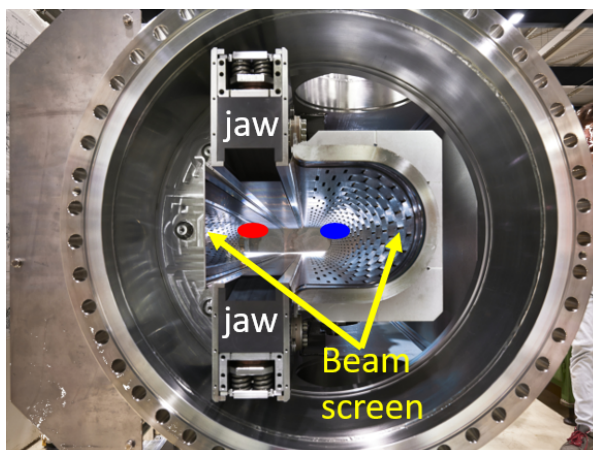


Figure 44. Cross section of one of the first two modules of the TDIS: the two circulating beams, top and bottom jaws and the beam screen are indicated.

The newly installed injection dump (TDIS) consists of three modules of equal length (1.6 m) (figure 43). The jaws of the first two modules are made of low-Z absorber blocks (SIGAFRENE[®], 1.83 g cm^{-3}) while the last module consists of a sandwich of higher-Z materials ($\text{Ti}_6\text{Al}_4\text{V}$ and CuCr_1Zr) (figure 44).

The jaws of each module can be moved independently in order to be aligned with respect to the circulating beam. The shorter jaws and the improved mechanics allow a more precise beam based alignment, less affected by deformation due to beam induced heating and less sensitive to mechanical offsets and angles.

3.3.1 Beam parameters and operational conditions

A fault of the MKI can lead to the whole injected train of bunches (a.k.a. batch) impacting the TDIS with different impact parameters. The survival of the TDIS has to be granted together with the protection of the downstream machine elements from damage. The new injection dump is designed to withstand any MKI failure when operating with the baseline beam parameters shown in table 7. The possibility of operating with the so called “high performance” beams, consisting of four bunch trains of 80 HL-LHC standard bunches (see section 4.2.1), was also considered.

Table 7. Bunch population, number of bunches per injection, normalized transverse emittance (ϵ_n) and vertical r.m.s. beam size at the front face of the TDIS (σ_y) for the HL-LHC baseline (HL-LHC standard and BCMS) and “high performance” (320 bunches) beams (see section 4.2.1 for a description of the different beam types).

	Bunch population [10^{11} ppb]	# bunches/inj.	Total beam population [10^{13}]	ϵ_n [μm]	σ_y [mm]
HL-LHC standard	2.3	288	6.68	2.1	0.42
HL-LHC BCMS	2.3	288	6.68	1.7	0.37
High Performance	2.3	320	7.42	2.1	0.42

Beside protecting from damage, also the risk of quench of the downstream superconducting magnets, induced by losses at the TDIS, has to be minimised. For the expected load cases during routine injection, the superconducting separation dipole D1 and the downstream magnets are not expected to quench. This includes the impact of a pilot bunch with any impact parameter as well as intermediate and full population bunches on the TDIS with large impact parameters (the limit case being a batch of 288 injected bunches of 2.3×10^{11} ppb not kicked by the MKI). The number of nominal bunches which can hit the TDIS without inducing a quench in the downstream magnets strongly depends on the impact parameter. Quenches can be admitted for rare failures like MKI flashovers, determining a grazing incidence, or a beam sweep induced by an MKI timing error. The continuous load from the secondary beam halo is also not supposed to cause any quench (assuming 0.2 h lifetime and 5.6×10^{10} p/s reaching the injection dump).

3.3.2 TDIS positioning and interlock logic

Each jaw of the TDIS has to be aligned with respect to the circulating beam once the reference orbit has been established in the machine. The nominal optics foresees crossing and separation bumps at injection in IR2 and IR8 to avoid parasitic collisions between the two counter-rotating beams. These bumps translate into a closed orbit with an offset and an angle with respect to the machine axis at the TDIS. In particular, the vertical offsets and angles at the TDIS are of the order of:

- IR2: -3.5 mm and -60 μrad
- IR8: 1.5 mm and -15 μrad

The difference in r.m.s. vertical beam size (σ_y) along the module is $< 5\%$ determining a beam divergence that can be neglected for the TDIS setup. Past experience showed that angles smaller than 100 μrad are hardly measurable through beam based angular alignment (in particular for short

jaws) [85]. For this reason and since a maximum offset of $\pm 100 \mu\text{m}$ (i.e. $\pm 0.3\sigma_y$ in the worst case of BCMS beams) is expected between the upstream and downstream jaw corners of each module, the present strategy consists in aligning all the TDIS jaws parallel with respect to the machine mechanical axis and using the same procedure as for all the other ring collimators [86]. The protection of the LHC aperture in case of an MKI failure requires setting the first two TDIS modules at about $\pm 4 \text{ mm}$. The last high-Z module has to be kept further retracted by 2.0 mm to avoid any direct impact of the beam. The validation of the correct positioning is obtained by simulating the failure of the MKIs with an orbit bump and checking that the TDIS cuts any beam with an amplitude larger than the expected settings. Beam Loss Monitors (BLM) consisting of ionisation chambers are installed at the TDIS for the beam based alignment and the validation process, to monitor the quality of the injections during the filling period and in general local losses during the full machine cycle. Diamond BLMs are used to examine the longitudinal structure of the losses.

The TDIS jaw position is checked and interlocked. Linear Variable Differential Transformer (LVDT) transducers are installed at the upstream and downstream extremity of each jaw and provide a direct readout of the position of each motor axis. A system of interlocks is set up based on the LVDT readings. Contrary to the LHC collimators the thresholds of the TDIS are never modified during the machine cycle to discard any risk of injecting the beam with the jaws at the wrong settings. Inner and outer limits are defined for each jaw corner. Generally the dump thresholds is set to $\pm 0.25\sigma_y$ around the injection position and the warning thresholds to half of it. The TDIS jaws can be moved across the outer limit to be sent to parking before the start of the energy ramp. In this case the beam injection is inhibited but no beam dump is requested. The movement of the jaws is instead blocked when the inner limits are overcome and a beam dump request is triggered. Two fully independent and redundant systems are used to check the TDIS gap with respect to the limits defined as a function of the energy. The first is the conventional collimation control system [87] which uses the LVDT readings to calculate the upstream and downstream gap. Only an outer limit, generally corresponding to the measured gap plus $1\sigma_y$, is defined. No jaw blockage or beam dump is triggered by crossing this limit but injection is inhibited. The TDIS gap is also surveyed by the Beam Energy Tracking System (BETS) [88]. Inner and an outer limits are defined (measured gap $\pm 1.5\sigma_y$) and the BETS checks the TDIS gap and the operational energy. Also in this case injection is possible only if the jaws are within the gap limits and the energy corresponds to injection energy (450 GeV).

3.3.3 Aperture requirements

The requirements due to the angular acceptance of the ALICE Zero Degrees Calorimeter [89] (ZDC) impose a lower limit on the inner beam screen dimension and the position of the jaws during physics. The neutrons emerging from the collisions in ALICE must not be intercepted by any aperture restriction when travelling on a straight line towards the ZDC. Vertically, a symmetric opening is required in order to allow for the polarity change of the crossing angle in ALICE (figure 45). For this purpose, the jaws of the TDIS, after injection, can be opened to a parking position of $\pm 55 \text{ mm}$.

Horizontally, the ZDC poses a limitation on the minimum aperture only towards the internal side of the ring (aperture $\geq 138 \text{ mm}$), while the beam screen dimension on the external side were defined by impedance reduction considerations. This is the reason why the beam screen is not symmetric, as shown in figure 44.

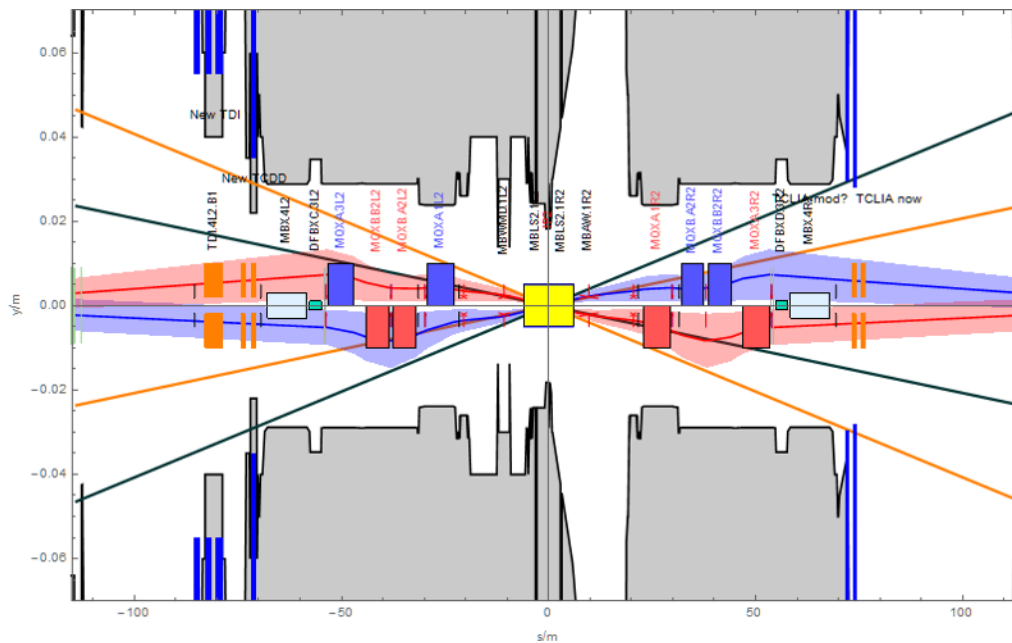


Figure 45. Schematic view of the machine vertical aperture and the trajectories of the neutrons emerging from the collisions in ALICE and travelling towards the ZDC in case of vertical crossing angles of $\pm 100 \mu\text{rad}$ (orange and black lines). Blue lines define the aperture of the injection protection collimators, when at parking position during collisions.

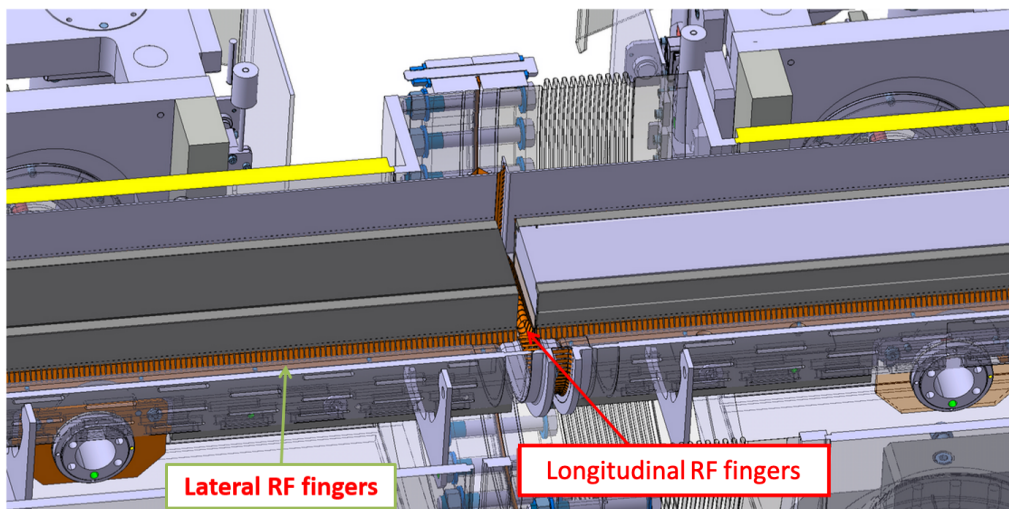


Figure 46. Schematic view of lateral and longitudinal RF fingers between consecutive modules of the TDIS.

3.3.4 Impedance and electron cloud aspects

A large campaign of impedance studies was done for the TDIS [90–94] and the design finalised accordingly. Longitudinal and transverse RF fingers are implemented to maintain a good electrical contact between the jaws and the beam screen (figure 46).

This allows to reduce the low frequency resonant modes. The jaws are machined with a 100 mm long and 10° angle tapering at the entrance and exit of the TDIS assembly to further reduce

the transverse impedance. The beam screen geometry for the circulating beam is smooth to minimise beam-induced wake-fields and conical transition flanges are installed at the extremities of the TDIS tank. Despite applying a high conductivity coating on top of the low-Z material would have reduced the heating to the jaws by a factor of 10 and the vertical impedance of the overall LHC at injection by 10 to 20 %, it was decided to install bare graphite blocks. The reason is to avoid the possible damage of the coating in case of grazing impact and because of other drawbacks related to the coating process itself. The cooling system is designed to cope with the estimated resistive wall beam-induced heating (expected to be < 800 W), the heat load due to trapped High Order Modes (HOM) and electron cloud for non-coated graphite blocks (in total 2400 W in case of bad or no contact of the lateral and/or longitudinal RF fingers and 5 mm half-gap [95]).

In order to minimise the background in ALICE, a static pressure $< 5 \times 10^{-9}$ mbar is required at the TDIS during injection. A dynamic pressure rise of about 2×10^{-7} mbar is estimated for a Secondary Electron Yield (SEY) of 1.6 and a half-gap of ± 4 mm (injection position). Electron cloud studies performed on the TDIS allowed identifying that the electron flux increases when opening the TDIS gap and reaches a maximum at around 40 mm half-gap. The strongest multipacting occurs on the surface of the metallic jaws and of the flat parts of the beam screen [96]. Carbon coating is applied to the beam screens to strongly suppress multipacting. No coating is instead applied to the metallic blocks since, according to vacuum dynamics simulations, the target pressure of $< 5 \times 10^{-9}$ mbar can still be achieved while several drawbacks related to coating (costs, manufacturing complexity and risk of potential peel-off/UFO³ in case of unexpected coating degradation) can be avoided. A maximum heat load of < 250 W is expected for the worst case of 40 mm half-gap and SEY = 1.6 (partially conditioned surface). TDIS transitions are also coated with Non-Evaporable Getter (NEG) to improve the performance compared to bare stainless steel. The NEG coating will provide SEY < 1.2 [98] and additional pumping. All these measures will allow keeping the maximum pressure of 2×10^{-9} mbar compatibly with the background requirements at the experiments both in IP2 and IP8.

3.3.5 Spares

Two full spare modules (one per IR) are built and equipped with sector valves to avoid bake out in the tunnel and thus reduce the intervention time in case of replacement. No aging effects are expected which would require replacing the TDIS before the end of the HL-LHC operation. Spares are needed for replacement in case of damage or major failures of the equipment. A regular yearly inspection and maintenance, at every YETS and Extended Year-End Technical Stop (EYETS), has to be envisaged.

3.4 Machine-Detector Interface

In all IPs the p-p collisions produce a shower of forward particles, namely of neutrals (mostly neutrons and photons) and charged particles (mostly pions and protons), that leave the interaction point and deposit energy in the machine elements. Because of the increase in the instantaneous and integrated luminosity at IP1 and IP5 expected for HL-LHC, a significant increase of the energy deposited by

³Events nicknamed as “Unidentified Flying Objects” (UFO) are due to dust particles of around 10 μm diameter that fly into the beam generating localized beam losses [97].

the collision debris in the superconducting magnets close to the Interaction Point (IP) is anticipated, requiring a redesign of the protection elements. Activation levels will also increase in such a way that the residual dose rates will affect the reliability of equipment and associated services (i.e cabling, electronics) and the ability from personnel to perform routine maintenance operations on them [99].

The TAS absorbers, located in front of the first Inner Triplet (IT) quadrupole (Q1), on the IP side, and shielding the downstream elements from the secondary particles generated from at the IP at large angles [100], are among the most activated LHC machine elements. They are surrounded by a massive shielding in the experimental cavern to reduce the background radiation generated in the detectors by the interactions taking place in the TAS, the section cut of the Forward Shielding is shown in figure 47.

The region extending from Q1 to the start of the TAS (located between 20.8 m and 22.1 m from the IP) is a dead-end zone and due to the shielding requirements, the access to that area is very narrow (40 cm wide passage for personnel from the tunnel wall to the elements belonging to the LHC machine and auxiliary beam line equipment), and the space surrounding is limited in all directions with a maximum height below 1.8 m. Furthermore, only 1.3 m are available longitudinally to house multiple pieces of equipment essential for operation. The access to these elements for operations such as alignment and bake-out (BPM, sector valves) is also difficult and it implies non-negligible radiation doses to the personnel.

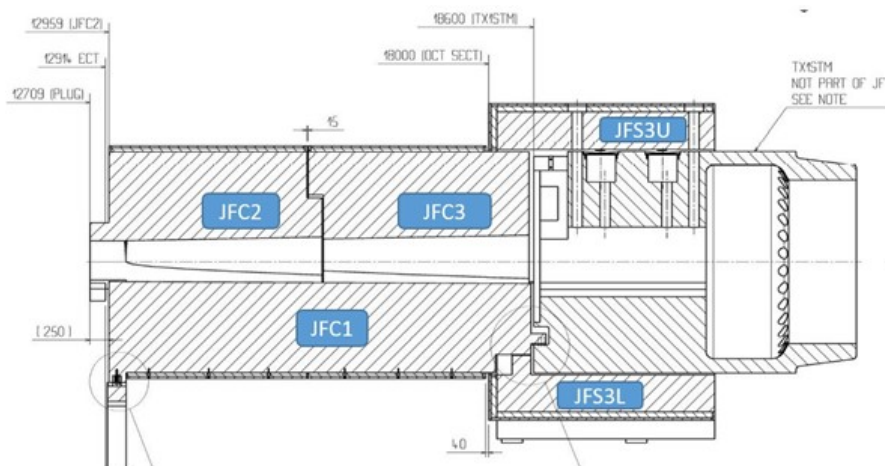


Figure 47. 2D side-view cut of the ATLAS Forward Cylindrical Shielding (JFC) structures showing the TAS housing (TX1STM, inside JFS3U and JFS3L) and the machine-interface space (right of the picture). The VAX will be relocated to the JFC region in LS3. JFC1 and JFC2 modifications were completed in LS2, while JFC3 modifications are partially completed.

For the above reasons, the shielding structures located in the experimental caverns and surrounding the TAS absorber will be modified for HL-LHC. The TAS will be replaced by a new larger aperture absorber TAXS (60 mm instead of the present 34 mm diameter). The modifications will allow the future relocation of the assembly module containing vacuum equipment (Vacuum Assembly for eXperimental areas — VAX) now installed between Q1 and TAS, and adopting a remote handling approach. A number of subsystems in this area were already modified in LS2 in view of the HL-LHC upgrade to reduce the dose to personnel and relax the LS3 schedule.

The LHCb detector at IP8 was upgraded during LS2 to operate at an instantaneous luminosity of $2 \times 10^{33} \text{ cm}^{-2}\text{s}^{-1}$, a factor five more than in Run 2 configuration. The power deposited by neutral particles in the IP8 D2 recombination superconducting dipoles could trigger magnet quenches. For that reason a new Target Absorber for Neutrals (TANB) has been designed and installed on each side of IP8 in front of the D2 dipoles. The design of the TANB absorber (shown in figure 48) is extremely compact, it is the result of an optimization taking into account both space integration and performance constraints [101–103].

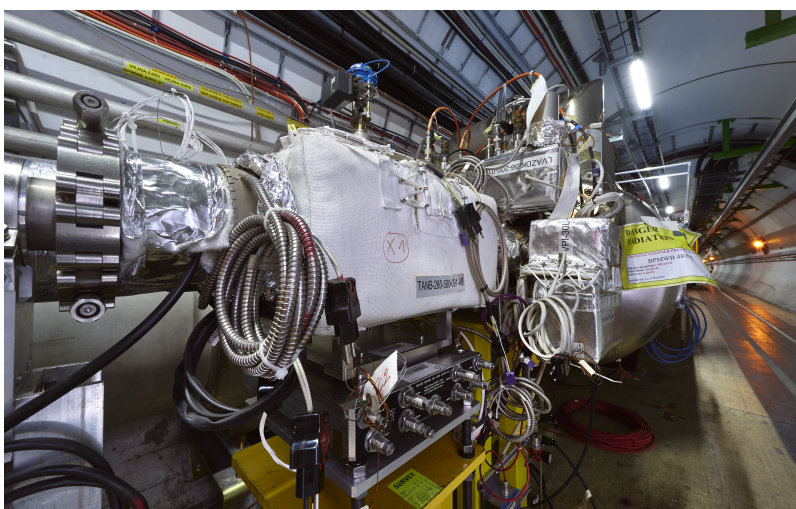


Figure 48. The TANB absorbers were installed in the LHC tunnel to protect the accelerator components from particles produced by collisions occurring in the LHCb experiment.

3.4.1 Modifications in ATLAS forward shielding region

In view of the relocation of the equipment installed between Q1 and TAS from its present location to the ATLAS experimental cavern during LS3, it is necessary to modify the forward shielding structures [104] to gain space and to be compatible with experiment opening configurations. During LS2 both Toroidal Tube Shieldings (JTT), one per side, were replaced by new ones while the Forward Cylindrical Shielding structures (JFC1, JFC2 and JFC3, shown in figure 47) were modified.

The machining of the structures was done remotely using an industrial Kuka 120 robot [105] with a special tooling head adapted for the task. Due to the activation and the nature of the materials, the work was performed inside a special depressurized cabin with a top-opening roof for handling and dry machining. The Kuka robot was purchased by CERN and will be used for the remaining shielding modifications in LS3. In the meanwhile, it is available for multiple purposes.

The JTT shown in figure 49 is a cylindrical structure made of ductile cast iron that surrounds the beam pipe in the ATLAS End-Cap Toroids (ECT). The shielding consists of four pieces called plug pieces. The non-IP piece has a large hole in the center into which the JFC2 shielding is inserted, and which will surround the VAX in HL-LHC during standard opening of the ATLAS detector. Due to the “modest” weight of the shielding (10 t) and its activation, the decision was to manufacture a new plug, keeping its external dimensions unchanged and adapting the inner hole to a square shape to leave sufficient space for the VAX when ATLAS opens the ECT without removing the vacuum

chambers, a configuration adopted in every YETS. On the outside of the cast iron, the polyethylene layer, doped with B_2O_3 (0.05 by weight) acting as neutron shielding, was reinstalled. The photons created in the polyethylene layer are stopped by the stainless steel ECT bore-tube that supports the shielding. Figure 50 shows the installation of the new JTT and the support of the Vacuum Toroidal chamber (VT) inside the JTT, also upgraded in LS2 with new mechanical stops and an adapted dogleg shape, already compatible with HL-LHC operation [106]. To keep the shielding material budget unchanged, a new shielding was also manufactured and attached to the JFC2 structure, providing an equivalent protection to the one provided by the old JTT plug.



Figure 49. Left: view of the new JTT shielding before installation of the borated polyethylene plates. Right, the old JTT after removal. Note the small cylindrical opening vs. the new square shape and the slots for the supports of the VT chamber in both pieces.

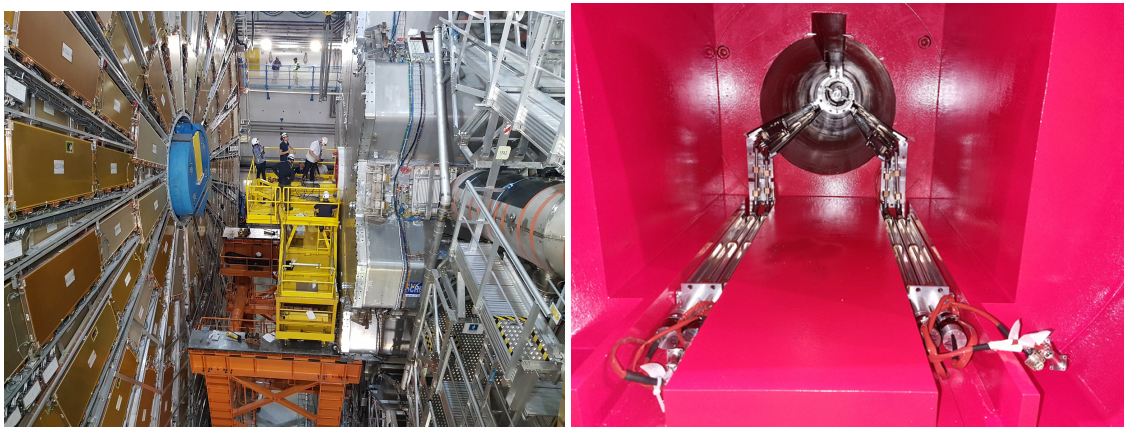


Figure 50. View of the installation of new JTT shielding inside the ATLAS ECT and the new VT chamber supports after installation. The dogleg system is compatible with the ATLAS standard YETS opening during HL-LHC operation.

3.4.2 Modifications in CMS forward shielding region

In CMS, the forward shielding [107] surrounding the TAXS and the experimental beam pipe is composed by two cantilevered parts that can be opened using a “classical” hinged system. Also in this case the future VAX relocation to the experimental cavern needs a series of modifications of the forward shielding in order to create space and to be compatible with the volume of the different modules containing the two vacuum sector valves and the VAX. In order to reduce constraints due to material activation, and profiting from the CMS Phase II-tracker project requiring the replacement of the central vacuum chamber and the majority of the vacuum layout made of stainless steel, the new Al-6065 VAX support structure was installed during LS2 replacing the Stainless Steel cylindrical forward beam pipe support, as shown in figure 51. The shielding inserts inside the Rotating shielding were also replaced by new ones compatible with the newly installed VAX support and future HL-LHC VAX vacuum modules. Future material activation in that region is reduced with the change of material (Aluminium instead of Stainless Steel). Detailed information about the vacuum layout changes inside the experiment can be found in [108].

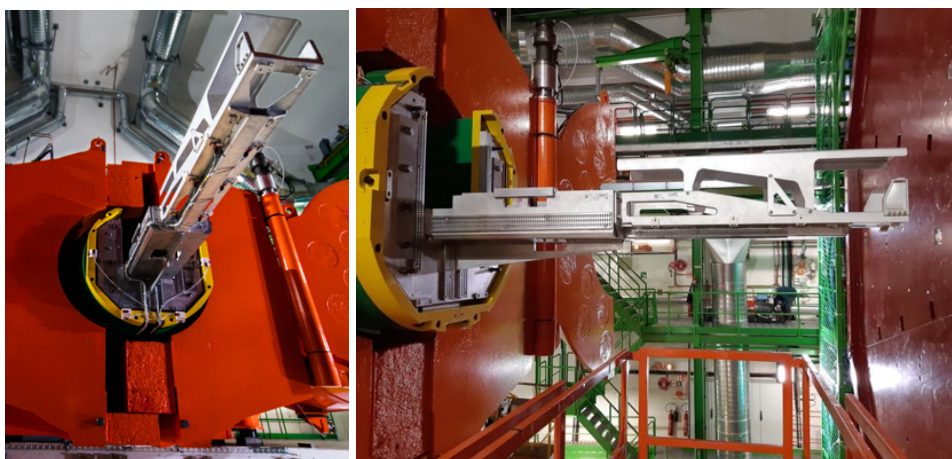


Figure 51. View of the new aluminium VAX support installed in front of the TAS, inside the CMS cavern. The structure is now compatible with the HL-LHC configuration.

3.4.3 Neutral absorber for IR8

The new TANB is composed of two blocks of high density material (in this case tungsten) clamping the two SS316LN beam vacuum chambers approximately 1.9 m upstream of D2 on the IP side to create a static mask around the beam pipes to stop the forward neutral particles. The TANB blocks include temperature sensors, are clamped with tungsten rods and are surrounded by a heating jacket to allow bake-out at a maximum temperature of 250 °C.

The peak power density expected during operation in the TANB was estimated with FLUKA simulations [109] for two different crossing angle configurations and for the nominal instantaneous luminosity of $2 \times 10^{33} \text{ cm}^{-2} \text{ s}^{-1}$ (see figure 52) showing an adequate level of protection for D2 [110]. The power deposition on the TANB is not expected to exceed 25 W and, based on the results of a thermo-mechanical analysis [111], there will be no need of water cooling for this device [111].

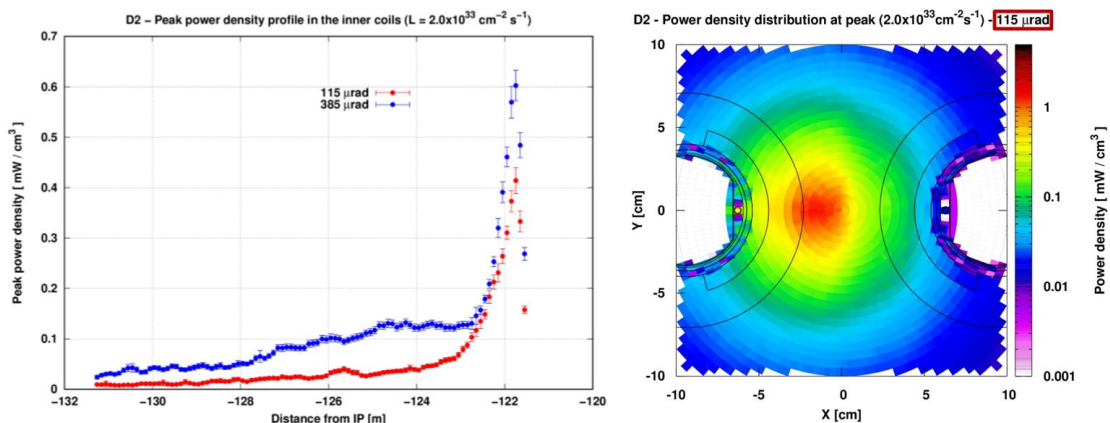


Figure 52. FLUKA simulations of peak power density (left graph) and section view at peak power (right plot) in the IP8 D2 coils for 115 μrad half crossing angle using a tungsten absorber. (Courtesy of A. Tsinganis and F. Cerutti, CERN) [110].

The continuous energy deposition during operation will activate the TANB. In compliance with the ALARA (As Low As Reasonably Achievable) principle a new alignment platform was engineered to improve the ergonomics of the alignment operations and minimize the amount of time spent close to the equipment during these activities.

The innovative 6-Degree-Of-Freedom (DOF) alignment table called WEPLATE [112], shown in figure 53, acts as a standard mechanical alignment table (no electronics), but the ergonomics has been adapted to regions with difficult access. All alignment operations can be performed from the front plate on the transport side of the tunnel. Results and steps followed to produce the installed version are documented in [113].

Four units are currently installed in IR8, one per TANB and one for each pair of BPMs located in the vicinity of the absorber. The WEPLATE was designed for the HL-LHC baseline requirements for survey and alignment, considering the requirements from other systems (e.g. vacuum, collimators, beam monitors, etc.). The service load of the WEPLATE on the other hand was specifically defined for the TANB, which amounts to 600 kg.

4 Preparation for Run 3 and Run 3 operational scenario

Following the consolidation of the main dipole diode boxes by the DISMAC project described in section 2.1, the LHC main dipoles were ready for the long training campaign to the design beam energy of 7 TeV. After two incidents forcing warm-up to room temperature and repair of sectors 23 and 78, the LHC target energy was lowered to 6.8 TeV which has become the nominal operation energy for Run 3 as explained in section 4.1.

The successful upgrade of the LHC Injector chain, see section 4.2, promises bunch populations of 1.8×10^{11} ppb for the 25 ns LHC beam in the second year of Run 3, boosting the LHC peak luminosity for the lowest values of β^* well above the maximum luminosity of $2 \times 10^{34} \text{ cm}^{-2} \text{ s}^{-1}$ which is defined by the cryogenic cooling capacity of the triplet magnets. Such large bunch populations represent a challenge for many LHC systems whose upgrades are described in this article. Heat load

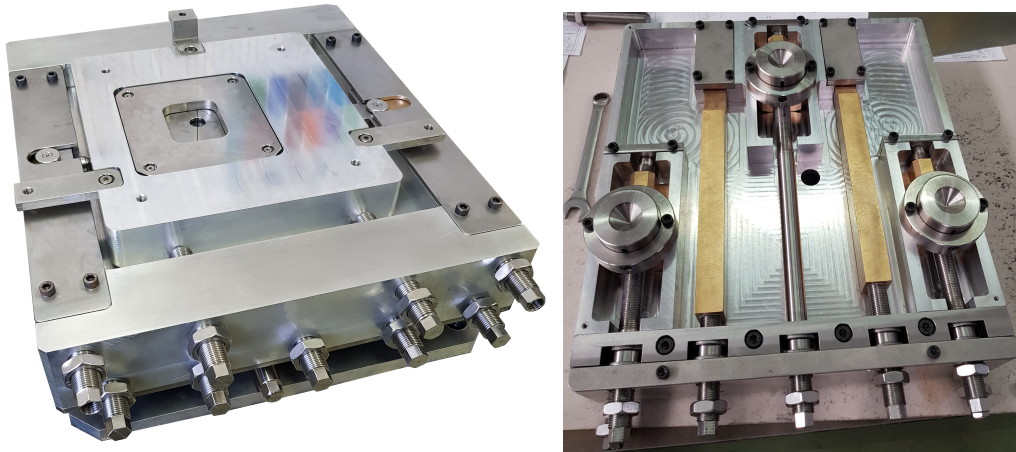


Figure 53. View of the new alignment table (WEPLATE) installed below the TANB absorber in IR8, all the alignment operations can be performed from the machine side.

due to beam-induced electron clouds is one of the potential limitations and it has been thoroughly studied during Run 2 and LS2, leading to a deeper understanding of the observations made and to the identification of possible mitigation measures (see section 4.3).

The operational scenarios of the LHC had to be revised for Run 3 to make best use of the high beam currents, implying luminosity levelling by β^* with levelling times of up to 12 h with a reduction of β^* by a factor 4 over the course of a fill. The full flexibility of the ATS optics will be deployed for operation in Run 3 as detailed in section 4.4. The integrated luminosity at ATLAS and CMS during Run 3 could approach 290 fb^{-1} , provided the crossing angle polarity in IR1 is varied to keep the total integrated radiation dose at the triplets below 30 MGy (see section 4.4.2). The integrated luminosity in ALICE and LHCb could reach 0.19 fb^{-1} and 30 fb^{-1} , respectively [114].

To anticipate the technical challenges associated to such operation scenarios, first tests of β^* levelling were already performed during regular operation at the end of fills in 2018, as described in section 4.5. In addition, BBLR wire compensators, tested during machine development sessions in Run 2, have been reconfigured during LS2 and could allow to operate at smaller crossing angles for the same bunch population (see section 4.6).

Finally, the upgrades of the SPS RF system with slip stacking of ion batches to reduce the ion bunch spacing to 50 ns also bring a significant increase of ion performance which reaches HL-LHC targets already in Run 3.

4.1 Results of the magnet training campaign

An increase in beam energy beyond the Run 2 value of 6.5 TeV implies that many superconducting circuits will also have to run at slightly higher currents. Except for the main dipole circuits, all other circuits have already been commissioned to 7 TeV equivalent during previous HWC campaigns. Those circuits had to be retrained after LS2, a normal phenomenon for superconducting magnets that experienced a thermal cycle. The 8 main dipole circuits, however, had to be retrained to 10 980 A (corresponding to 6.5 TeV) and then further trained to 11 850 A (corresponding to 7 TeV). Note that, for operational stability, the magnets are trained to a current that is 100 A higher than the operational

current, so the initial target for the training campaign in preparation of Run 3 was set to 11 950 A. Each circuit contains 154 dipole magnets in series, assembled by 3 different firms, and containing superconducting cables produced by several companies [1]. Each sector contains different fractions of magnets assembled by the three firms, which affects strongly the required training time.

Training of the dipole magnets depends not only strongly on the magnet assembler but also on training campaigns in previous years. All the superconducting magnets have been tested upon delivery. All the 1277 dipole magnets (including 45 spare magnets) have reached at least 12 000 A, and about 60 % of them reached at least 12 850 A, corresponding to the ultimate energy of 7.5 TeV, in the magnet test-stand before installation [115]. Different sectors have experienced a different number of thermal cycles and therefore also a different number of training campaigns. Furthermore, also the final current reached during a campaign varies between the sectors. Therefore an overview is given of the past training campaigns, before presenting the data of the training campaign in 2021–2022.

Table 8 shows the number of training quenches required to reach a current of 11 080 A in the main dipole magnets in 2014–2015 (after LS1). Note that the number of training quenches varies strongly among the 8 sectors and that S56 was already trained to 11 173 A in 2008, requiring 29 quenches. [116, 117].

Table 8. Number of quenches needed in 2014–2015 to train the 8 dipole circuits to 11 080 A.

Sector	# quenches
S12	7
S23	17
S34	16
S45	51
S56	18
S67	22
S78	19
S81	29

In December 2016, sectors 34 and 45 have been pushed to higher currents to assess the number of required quenches for operation at higher energy. S34 needed 8 quenches to train from 11 080 A to 11 416 A and S45 needed 24 quenches to train from 11 080 A to 11 536 A. The training was not pursued until 11 600 A, as initially planned, due to time limitations. At the end of Run 2, in December 2018, another attempt was done to assess the number of quenches needed to prepare the LHC for high-energy operation. A week was dedicated to train S12 to higher current. A current of 11 436 A was finally reached, after 17 training quenches.

After LS2 all sectors were retrained to 11 080 A and then trained further with the aim of reaching the current of 11 950 A necessary to guarantee stable operation at 7 TeV.

However, during the main dipole training of S78 and S23 two unexpected events occurred, which had a non-negligible impact on the training campaign:

1. An inter-turn short occurred during a training quench at 11 600 A in the dipole B28L8 in S78. The sector was warmed up and the damaged magnet was replaced.

2. A problem with a cold bypass diode in S23 occurred during a quench of dipole A23R2 at about 8500 A. During the current discharge of the circuit, the diode went into short. This issue had no consequences on the circuit discharge itself, but since the diode remained in short, only part of the current would flow through the magnet. At the moment of the diode failure S23 was only partially trained, reaching 11 537 A in 34 quenches. Therefore, also sector 23 had to be warmed up in order to exchange the diode.

The two events mentioned above triggered an evaluation of the risk associated with training to 7 TeV as compared to the benefits of operating at that energy. As a result of this analysis [118], it was decided to set the target energy for Run 3 to 6.8 TeV, corresponding to a training current of 11 600 A (including the operational margin of 100 A).

After cooling down following the replacement of the dipole B28L8, S78 needed a single quench to reach 11 080 A and another 20 training quenches to re-train to 11 600 A, so significantly less than the 71 quenches needed before. For sector 23, only 3 training quenches were performed (at 10 920 A, 11 041 A, and 11 062 A) after the cool-down following the diode replacement. Unfortunately an issue with a deformed RF finger in a PIM required another warm-up of the sector. After replacement of the PIM and cool-down of S23 the training to 11 600 A was resumed. After two quenches a current of 11 080 A was reached, but it took another 62 quenches to reach 11 600 A, surprisingly many more as compared to the 34 quenches that were needed to reach 11 537 A before the bypass diode failure. The reason for that remains to be understood.

Table 9 lists the number of quenches per sector required to reach the current level of 11 080 A and the additional number of quenches required to reach 11 600 A during the 2021–2022 training campaign. The maximum current reached during the training campaign, the corresponding beam energy considering the operational margin of 100 A and the total number of quenches required to reach the maximum current are also listed.

Table 10 shows the number of magnets that had 1, 2, 3, 4, 5 training quenches since the completion of the LHC installation in 2008 till the end of the 2021-2022 training campaign. Note that 562 of the 1232 magnets (so 46 %) never experienced a training quench in the LHC, yet.

During the dipole magnet reception tests on average 0.29 training quenches per magnet were needed to reach 11 080 A. In the LHC we find a number which is about 2 times smaller, namely $179/1232 = 0.15$, where 179 is the sum of all quenches in table 8. A similar comparison can be done for the current level of 11 600 A. During the reception tests on average 0.51 training quenches per magnet were needed to reach 11 600 A. In the LHC we find only a slightly smaller number, namely $541/1232 = 0.44$, where 541 is the sum of all quenches in the second column of table 8 and the third column of table 9 (using the first data sets for S23 and S78, even though S23 was only trained to 11 537 A). The retraining of S78 after the thermal cycle in 2021 was much faster than foreseen: only 1 quench was required to reach 11 080 A as compared to 19 in the first training campaign (see table 8) and only 20 training quenches more to reach 11 600 A as compared to 71 in the previous campaign.

So in general we can conclude that re-training to reach a given current level after a thermal cycle is faster than the previous training, though the behaviour of sector 23 after the two consecutive thermal cycles remains unexplained. Quantitative conclusions cannot be drawn at this moment, and could very well depend on the duration and number of consecutive thermal cycles, the magnet manufacturer and the current level.

Table 9. Summary of the main results of the 2021–2022 training campaign for each of the eight LHC sectors. Note that for S23 two sets of data are presented: the first set shows the data of the initial training performed after LS2; the second set shows the data of the training performed after two thermal cycles, one needed to replace the bypass diode and the other to replace the PIM. Also note that for S78 two sets of data are presented: the first set shows the data of the initial training performed after LS2; the second set shows the data of the training performed after the thermal cycle required to replace the dipole magnet B28L8.

Sector	# quenches to 11 080 A	# quenches to 11 600 A	Max. current [A]	Beam Energy [TeV]	Total # quenches
S12	1	27	11950	7.0	92
S23	3	31 [†]	11537	6.75	34
	2	62	11600	6.8	64
S34	6	22	11950	7.0	81
S45	3	28	11950	7.0	102
S56	6	85	11600	6.8	91
S67	18	52	11600	6.8	70
S78	11	71	11600	6.8	82
	1	20	11600	6.8	21
S81	18	46	11600	6.8	64

[†] # of quenches required to reach the maximum current of 11 537 A.

Table 10. Number of dipole magnets that had 1,2,3,4, or 5 training quenches since the start of the LHC.

# training quenches	# magnets
1	446
2	154
3	56
4	11
5	3

Training of the main dipole circuits is usually characterized by a continuous increase of the current at which quenches occur. This can be seen in the plots in figure 54. However, in the same plots some scattered points at lower current can also be observed. While the magnets are being trained, in fact, some quenches at a current lower than the previous training level are observed. This effect is called de-training. The de-training is a known phenomenon, which does not affect the general training behaviour of the circuit. As it can be observed in figure 54, indeed, despite of this lower single points, the current of the circuit increases again at the next attempt.

Another interesting effect is that all circuits experienced flat-top quenches. When the target current is finally reached, the circuit is maintained at stable current for four hours, in order to establish a stable situation. However, a few quenches occur during this plateau, forcing to repeat the operation, until the circuit can be steadily maintained at the target current for several hours. For each circuit, between one and nine quenches at flat-top were needed. The larger number of flat-top quenches occurred in the two circuits which were trained to 11 950 A, equivalent to 7 TeV beam energy.

4.2 Expected performance of the injectors during Run 3

4.2.1 Overview on the LHC injectors chain and beam production scheme before LS2

The 450 GeV beams injected into the two rings of LHC are produced through a long chain of accelerators as illustrated in figure 55.

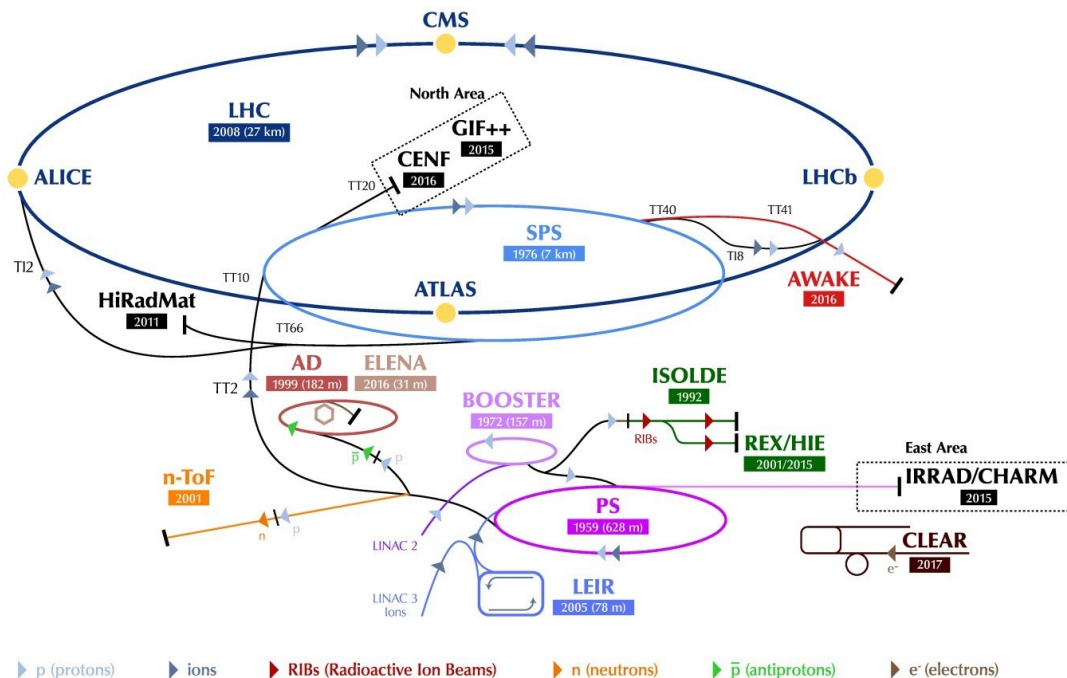


Figure 55. Overview on the LHC injectors chains, both for protons and heavy ions before LS2.

Before LS2, the protons produced at the source were accelerated in Linac 2 to a kinetic energy of 50 MeV and then injected into the four rings of the Proton Synchrotron Booster (PSB) through a classical multi-turn injection process. In the PSB, six proton bunches were accelerated to a kinetic energy $E_{\text{kin}} = 1.4$ GeV and then extracted to the Proton Synchrotron (PS) over two subsequent cycles (4 bunches, or one per ring, over the first cycle and 2 bunches over the second cycle, 4 + 2). In the PS, the six bunches were then triple split into 18 bunches on an intermediate plateau at 2.5 GeV and then accelerated to $E_{\text{kin}} = 25$ GeV to be further split into 72 bunches by means of two subsequent processes of double splitting, and sent to the Super Proton Synchrotron (SPS) over 4 subsequent cycles. The SPS would finally accelerate the four trains of 72 bunches (25 ns spacing between bunches, 200 ns spacing between trains) to $E_{\text{kin}} = 450$ GeV and extract them to the LHC (see figure 56).

4.2.2 Upgrade of the LHC injectors during LS2

During LS2, the great majority of the modifications related to the LIU project were implemented in the CERN accelerator complex. The aim of the LIU project was to increase the beam intensity and brightness in the LHC injectors in order to match the HL-LHC requirements for both protons and lead (Pb) ions [119], while ensuring high availability and reliable operation of the injector complex up to the end of the HL-LHC era in synergy with the Accelerator Consolidation project [120].

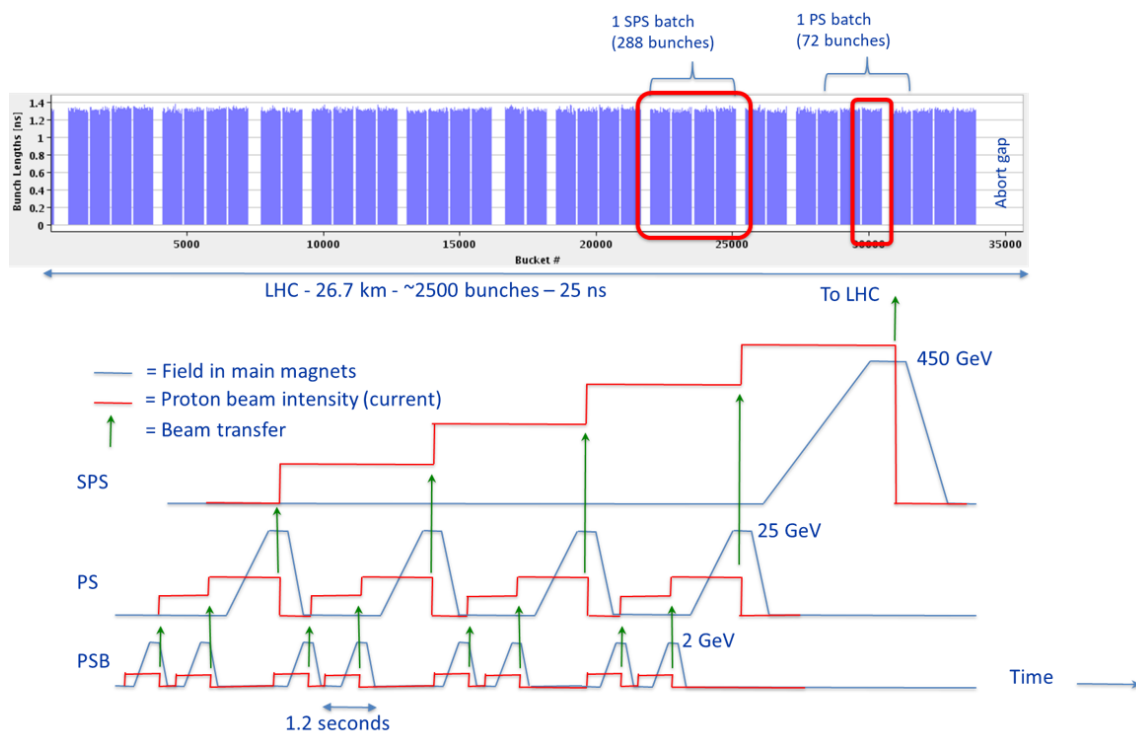


Figure 56. Production scheme of the LHC beam in the injectors.

For this purpose, a series of major upgrades were identified and had to be put in place in all the accelerators of the LHC injectors chain, which are detailed in [7, 8]. The main items relevant to the achievement of the desired beam performance are listed here below.

- Connection of PSB to the newly commissioned Linac 4. The H^- charge-exchange injection into the four rings of the PSB at 160 MeV was designed to produce beams with twice higher brightness than with Linac 2. Doubling of $\beta\gamma^2$ at 160 MeV with respect to the previous injection energy of 50 MeV allows doubling the beam brightness at constant space charge tune spread.
- Increase of the PS kinetic energy at injection from 1.4 to 2 GeV. In combination with optimized longitudinal beam parameters at the PSB-PS transfer, this was the key to reach in the PS the LIU beam brightness target at unchanged space charge tune spread. The higher PSB extraction energy required the replacement of its main power supply and RF systems.
- Installation of a longitudinal feedback, reduction of the impedance of the 10 MHz RF system and implementation of the multi-harmonic feedback systems on the high frequency RF systems in the PS. These interventions were needed to increase the threshold of the longitudinal coupled bunch instabilities that used to limit the LHC beam intensity in the PS.
- Upgrade of the SPS 200 MHz RF system. The RF power was increased by adding two new 200 MHz solid-state power-plants, changing to pulsed operation mode, and rearranging the 200 MHz cavities to reduce their impedance and the beam loading effect with LHC-type

beams. A further reduction by a factor 3 of the HOM of the 200 MHz Travelling-Wave Cavities was also pursued through the installation of specially designed couplers. A new low-level RF for the 200 MHz RF system was also implemented to allow for more flexibility, beam loss reduction and new RF beam manipulations.

- SPS impedance reduction and electron cloud mitigation through shielding of the focusing quadrupole (QF) flanges and a-C coating of the corresponding vacuum chambers. The goal was to increase the threshold for longitudinal beam instabilities as well as alleviate electron cloud effects and transverse instabilities.
- Upgrade of injection protection and beam dump devices to cope with the increased beam intensity and brightness. The SPS extraction protection, transfer line stoppers and collimators also had to be renovated.
- Upgrade of the beam instrumentation, vacuum systems, and general services to comply with the performance and reliability targets.

After LS2, H^- ions are accelerated in Linac 4 [121] to 160 MeV. Through an H^- charge-exchange process, these negative hydrogen ions are then double stripped with high efficiency and thus converted into protons, which are subsequently injected into the four rings of the PSB. In the PSB, six proton bunches are accelerated to $E_{\text{kin}} = 2$ GeV and then extracted to the PS over two subsequent cycles (4+2). In the PS, the six bunches are then split into 18 bunches on an intermediate plateau at 3.1 GeV and then accelerated to $E_{\text{kin}} = 25$ GeV to be further split into 72 bunches (see figure 57) and sent to the SPS over 4 subsequent cycles. To be noted that it could be possible to inject into the PS seven bunches from the PSB (4+3), voluntarily lose one bunch at 3.1 GeV after the triple splitting (e.g. using the transverse damper) and end up at 25 GeV with a train of 80 bunches (the so-called “high performance” beam mentioned in section 3.3.1) and a gap of 4 empty buckets, which is sufficient for the rise time of the PS extraction kicker. As before LS2, the SPS finally accelerates the four trains of 72 bunches (25 ns spacing between bunches, 200 ns spacing between trains) to $E_{\text{kin}} = 450$ GeV and extracts them to the LHC.

Alternatively to the scheme described above, a different scheme of LHC beam production is based on injecting twice 4 bunches from the PSB to the PS (4+4), merging and triple splitting them on the intermediate energy plateau of the PS, and accelerating the 12 resulting bunches to $E_{\text{kin}} = 25$ GeV. Here trains of 48 bunches are obtained after a double process of double splitting. Four or five trains of 48 bunches can then be injected into the SPS, where they are accelerated to $E_{\text{kin}} = 450$ GeV. This scheme is called Bunch Compression, Merging and Splitting (BCMS) [122] and is of interest because of its potential to produce brighter beams at the expense of the lower number of bunches per SPS train. It is currently the default production scheme for Run 3, as is explained further below.

Another interesting alternative to the standard production for LHC beams is the so called 8b+4e scheme [123]. This scheme is basically the same as the standard one, except that the triple splitting at intermediate energy in the PS is replaced by an unbalanced double splitting, so that the train of 18 bunches with 100 ns bunch spacing that one would obtain with the

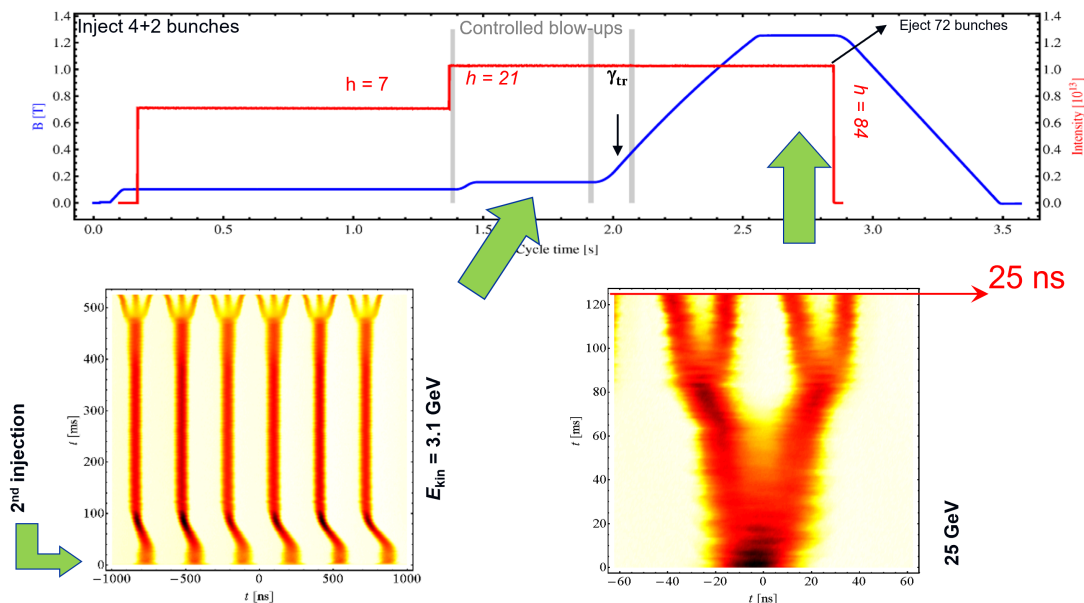


Figure 57. Bunch splitting schemes in the PS: triple splitting at 3.1 GeV and two consecutive double splittings at 25 GeV.

standard scheme is replaced by a train of 12 bunches arranged in 6 sequences composed by two bunches spaced by 100 ns and a gap of 200 ns between pairs, as illustrated in figure 58. After the two double splittings at top energy, this train will eventually result in a train of 48 bunches arranged in 6 mini-trains of 8 bunches spaced by 25 ns with gaps of 200 ns between them, as can be seen by the sketches above the plots in figure 58. Besides, since the gap of 200 ns between mini-trains is sufficient to accommodate the rise time of the PS extraction kicker, in this scheme it is also possible to inject initially 7 bunches from the PSB (4+3) and obtain finally a train of 56 bunches. This scheme has the advantage of preserving the basic 25 ns structure, as desired by the LHC experiments, while creating the potential to suppress the build-up of the electron cloud in the SPS and LHC thanks to the presence of the gaps. In fact, this alternative is under consideration if electron cloud limitations arise in the LHC and limit operation at high bunch population (see section 4.3.6).

Table 11 summarises the main target parameters at the SPS exit (or equivalently, LHC injection) for both protons and Pb ions, as well as the values achieved prior to the upgrades. From this table, it is clear that, while for protons the main challenge lies in reaching the target single bunch parameters (double population and roughly double brightness), in the case of the Pb ions the single bunch parameters have been already demonstrated, but the total number of bunches in the LHC will only become accessible through a novel production scheme based on the LIU upgrades.

4.2.3 LIU proton beam performance

After the implementation of the LIU upgrades, the proton beam parameters expected at LHC injection will match the HL-LHC target values reported in table 11 for the LHC standard beam (trains of 72 bunches at the PS exit). This can be illustrated visually in a so-called *limitation diagram*, as

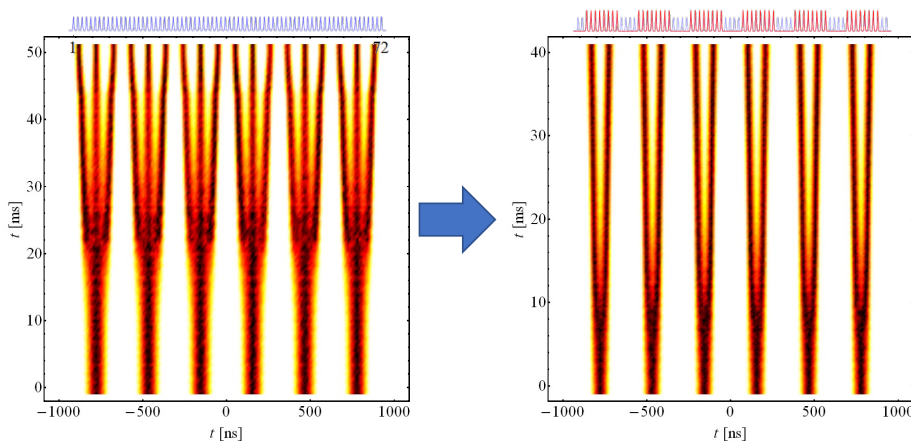


Figure 58. The triple bunch splitting schemes at 3.1 GeV in the PS of the standard production scheme (left plot) is replaced in the 8b+4e scheme by an unbalanced double splitting resulting in 100 ns spaced doublets with 200 ns between doublets (right plot). The final train structure extracted from the PS after the two double splittings at flat top is shown above the plots (blue is the standard, red is the 8b+4e).

Table 11. Beam parameters at LHC injection for protons and Pb ions, HL-LHC target and achieved in Run 2. A line with the achievable BCMS parameters after LIU is also included for the protons.

	N_b [10^{11} ppb]	$\epsilon_{n(x,y)}$ [μm]	bunches @SPS extraction	bunches in LHC
HL-LHC	2.3	2.1	288 (4×72)	2760
LIU BCMS	2.3	1.7	240 (5×48)	2760
Achieved Run 2	1.15	2.5	288 (4×72)	2760
	N_b [10^8 ppb]	$\epsilon_{n(x,y)}$ [μm]	bunches @SPS extraction	bunches in LHC
HL-LHC	1.9	1.5	56 (14×4)	1240
Achieved Run 2	2.0	1.5	36 (9×4)	648

shown in figure 59: in the beam parameter space of normalised transverse emittance versus bunch population at SPS extraction, all the boundaries for population and brightness limitations in the PSB, PS and SPS are plotted and the inaccessible regions are shaded. The population limitations appear as straight vertical lines, while the brightness limitation curves are determined by space charge at injection of the various machines. In particular, in the PSB the brightness line is due to both the injection process (proton multi-turn before LS2, H^- charge exchange after LS2) and space charge and comes from both measurements and simulations, while the brightness curves in the PS and SPS have been calculated assuming the known empirical limits on the maximum tolerable space charge tune spread (0.31 in the PS and 0.21 in the SPS). The best achievable parameter set corresponds to the point with the highest population and lowest emittance in the non-shaded area. As can be seen, the achievable beam parameters for the LHC standard beam match exactly the HL-LHC target values. The measured points from Run 2 are also plotted, highlighting the important challenge for the LIU project [124].

In addition, due to the LIU improvements, also different LHC beam types will benefit and see their performance improved in post-LS2 operation. The BCMS scheme described in the previous section, which results in trains of 48 bunches out of the PS, will be produced with ca. 20 % higher

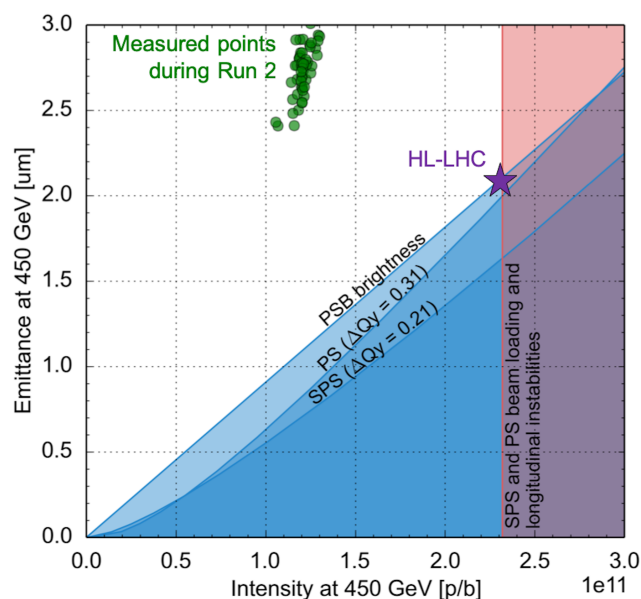


Figure 59. Limitation diagram for LHC standard 25 ns beam. The HL-LHC target (purple star) matches the best achievable LIU parameters. Measured points from Run 2 are also displayed (green).

brightness with respect to the standard beam (see figure 60, left plot). Just like the standard 25 ns beams, its bunch population reach will be limited by the SPS longitudinal instabilities. Its brightness, instead, will be equally limited by space charge in the PS and in the SPS, which is why this beam will not fulfil its potential of double brightness from the PSB brightness line. Due to the increased brightness, special care had to be taken to validate the robustness of the extraction/transfer/injection protection devices for this beam. The BCMS beam is considered by HL-LHC an interesting alternative in case mitigation against uncontrolled emittance blow-up is needed. However, due to its potential to accumulate almost the same number of bunches in LHC as the standard beam, it has been chosen as the most likely baseline beam for Run 3 operation [125] (see section 4.4.1). The 8b+4e beam, made of trains of 56 bunches sent from the PS to the SPS in alternating sequences of 8 bunches and 4 gaps as described above, has basically the same performance reach as the BCMS beam, as shown in the limitation diagram at the right side of figure 60. SPS space charge and longitudinal instabilities are the limitations for this type of beam. This beam, or any combination of its pattern with a pure 25 ns beam, is considered by HL-LHC an alternative in case mitigation against electron-cloud effects (e.g. beam-induced heat-load in the beam screen of the cold arc) is needed. For the same reason, it could also become the operational beam during Run 3 for physics production.

4.2.4 LIU ion beam performance

Concerning the Pb ions (see figure 55 for the scheme of the LHC Ion Injector chain), thanks to an intensive campaign of machine studies and additional instrumentation installed in Linac 3 and the Low Energy Ion Ring (LEIR), the single bunch parameters achieved in 2018 at the SPS extraction already matched the HL-LHC desired values, even including a 5% margin for the additional losses expected with the future RF manipulations. As a consequence of the higher current from Linac 3, after the removal of an aperture limitation at the source, optimised transfer and injections into LEIR,

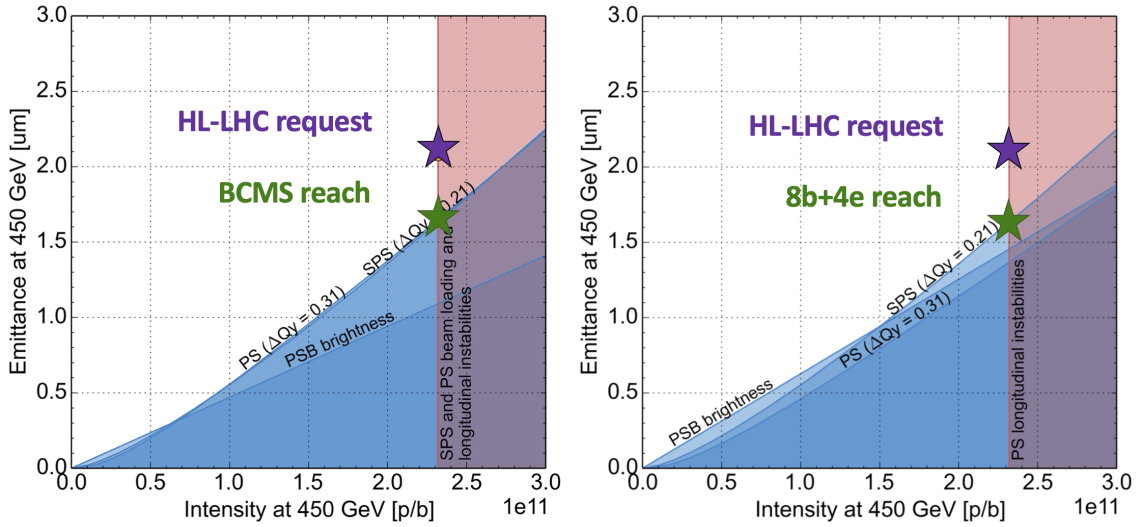


Figure 60. Limitation diagrams for LHC BCMS and 8b+4e 25 ns beam. The single bunch characteristics even exceed the HL-LHC target (purple star), but the number of bunches in LHC is reduced for both schemes.

and mitigation of space charge at RF capture in LEIR, the intensity extracted from LEIR more than doubled over Run 2 and eventually exceeded the LIU target value by about 20 %, as displayed in figure 61. Besides, in the SPS the overall transmission was also improved thanks to working point, RF and transverse feedback optimisation, and the batch spacing at injection could be successfully reduced to 150 ns by optimising the kicker switch settings and by deploying the transverse damper for ions. In 2018, only 9 trains spaced by 150 ns, each train made of 4 bunches spaced by 100 ns, were injected from the SPS to LHC. The remaining LIU item to be implemented for post-LS2 ion operation is the momentum slip stacking in the SPS [126, 127]. With this process, the 56 bunches grouped in 14 trains of four bunches spaced by 100 ns and 150 ns between trains, which can be accumulated over 14 injections in the SPS, will be longitudinally compressed into 7 trains spaced by 100 ns, each train being made of 8 bunches spaced by 50 ns, to be transferred to the LHC. This will be achieved by independently controlling two groups of 7 trains with two different RF cavities, which allows slipping them longitudinally and merging them when the bunches are exactly at 50 ns spacing. In this configuration, the total number of bunches that can be injected into the LHC can be increased from 648 to 1240. The momentum slip stacking in the SPS depends on the full deployment of new Low-Level Radio Frequency (LLRF) system capabilities for the 200 MHz RF system, expected to be ready in the last quarter of 2021, and its feasibility has been proved in simulations.

Furthermore, an alternative filling scheme for LHC was set up and operationally used in the 2018 Pb-Pb run, based on the production of three bunches in LEIR and on batch compression to 75 ns before the PS extraction. This scheme has the advantage of being able to pack a higher number of bunches in the LHC (733 instead of 648), each with 10 % higher population. To be noted that the potential 33 % gain in bunch population is partly lost due to strongly nonlinear transmission through the SPS, which exhibits much higher losses for more intense bunches. Both the larger population per bunch and the overall larger number of bunches result in larger total numbers of ions in LHC, and therefore a higher integrated luminosity in LHC. In fact, as also demonstrated in the 2018 run, the 3

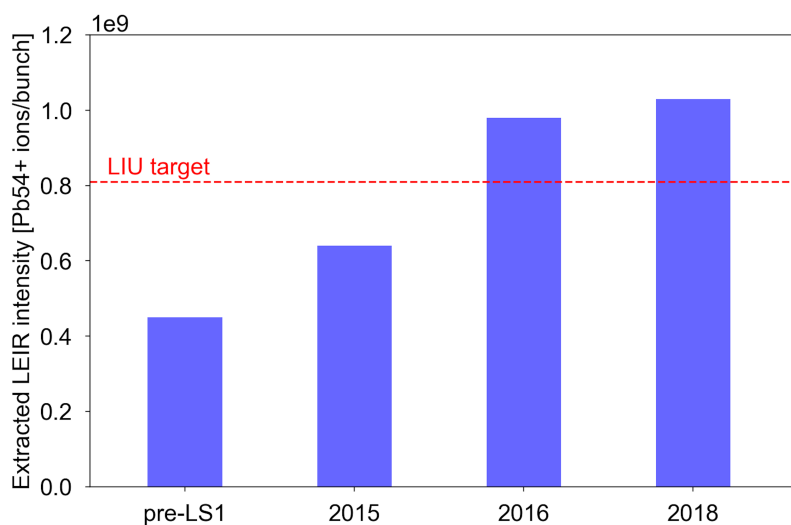


Figure 61. Evolution of the extracted bunch population from LEIR since 2013. The LIU target value is also displayed as a dashed line.

bunch scheme has the potential to achieve 70% of the HL-LHC integrated luminosity target, which was estimated beforehand from calculations [128, 129], and is therefore a valid fallback scenario if the momentum slip stacking in the SPS is delayed or does not perform as expected.

4.2.5 LIU beam commissioning plan in Run 3

After the end of the LS2 equipment installation and testing phase without beam, all the upgraded injector synchrotrons sequentially resumed operation between December 2020 and March 2021 and moved into the stand-alone beam commissioning phase. Linac 4 already restarted operation in July 2020, after it had already undergone a number of reliability and beam quality runs in 2017–2019, including a half sector test, at the end of 2017, designed to verify the basic functionalities of the future H^- charge exchange injection into the PSB. Thanks to this preparation, Linac 4 was ready to become injector for the PSB in 2020, and in fact, the PSB received its first beam from Linac 4 in December 2020. The beam from the PSB was then sent downstream to the PS in March 2021. The SPS restarted operation with beam in mid April 2021. Linac 3 and LEIR were back to production of Pb ion beams in April and June 2021, respectively.

The current timeline for the commissioning of the LIU beams in Run 3 is sketched in figure 62 and it is based on the idea that we will gradually learn how to operate the upgraded injectors and we will gain performance stepwise during Run 3 [130].

The main goal for the 2020–2021 recommissioning has been the recovery of the pre-LS2 beam performance. However, the brightness in the SPS injectors has been already improved beyond the original plans. In particular the target PSB brightness line has been already achieved early in 2021, and then further improved with optimised Linac 4-to-PSB transfer, β -beating correction during collapse of the injection bump and resonance compensation implemented in the operational cycle (see figure 63). These LHC beams have been already systematically fed to the accelerators downstream. In the PS, the LIU target of 2.6×10^{11} ppb, which was already achieved in 2018, has

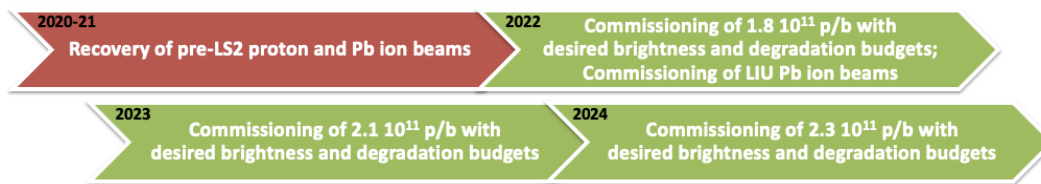


Figure 62. Gradual intensity ramp-up to the LIU beam parameters over Run 3.

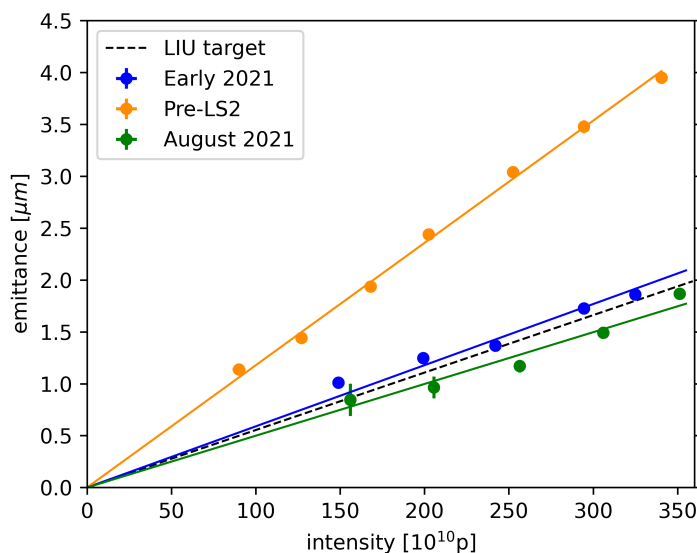


Figure 63. Brightness line of the PSB: pre-LS2 (orange), early 2021 (blue), August 2021 (green), LIU target (dashed black).

been successfully recovered within a normalised transverse emittance at extraction of about $2.7 \mu\text{m}$, i.e. less than $1 \mu\text{m}$ above the optimal LIU value, as shown in figure 64. Having already reached these targets of brightness and population in the PSB and PS lays an excellent basis for the successful continuation of the LIU beam performance ramp-up in the following years.

Conditioning of new equipment and general machine scrubbing after the LS2 venting has been needed in the SPS to successfully circulate and accelerate LHC beams in the SPS. Unfortunately the full pre-LS2 performance of these beams could not be fully recovered due to the vacuum interlock at the location of a newly installed non-conform dump kicker (MKDV1), which limited to 1.1×10^{11} ppb the bunch population of the beam accelerated in 4 trains to 450 GeV. At the same time, single or double trains with bunch population up to 2×10^{11} ppb were successfully injected into the SPS during machine studies. The maximum population achieved at flat top with less than 10 % losses over the cycle and stable beams in both longitudinal and transverse planes, has been 1.75×10^{11} ppb in two trains of 48 bunches or 1.65×10^{11} ppb in one train of 72 bunches, well above the previous record of 1.35×10^{11} ppb achieved only during machine development prior to LS2 for any train of more than 12 bunches. This means that the basic functionalities of the upgraded systems have, in general, been demonstrated and there are good indications that the SPS will be able to continue the LIU performance ramp-up as of 2022, after the MKDV1 will be exchanged and the related limitation will

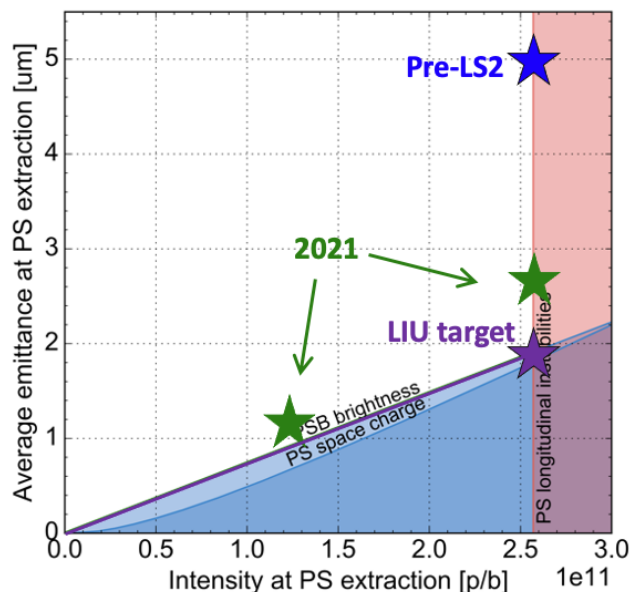


Figure 64. Limitation diagram at PS extraction and 2021 points.

be removed. During 2021, the state of the machines after LS2 has also been successfully assessed versus expectations by conducting reference measurements of physical aperture and impedance, and comparing the new data with those acquired pre-LS2.

The general injector operation in 2021 has been very challenging due to the fact that all major new LIU systems had to be commissioned with beam and operationally integrated (though not fully exploited), e.g. the new H^- charge exchange injection into the PSB, the new PSB main power supply and RF system, the PSB-PS transfer at higher energy, the upgraded 200 MHz RF system in the SPS (both for power and LLRF), the new SPS beam dump. In addition to all of this, the 2018 Pb ion beam performance had to be recovered (both 4 and 3 bunch schemes) and the first part of the commissioning of the momentum slip stacking in the SPS took place in the last months of 2021 in preparation of the 2022 LHC Pb-Pb ion run. In this respect, the functionalities of the LLRF system to perform slip stacking have been demonstrated with up to 12 trains of 4 nominal population bunches, which have been successfully stabilised along the cycle by means of the 800 MHz RF system. As from 2022, the real intensity ramp-up of the LHC proton beams can begin.

During 2022, one can expect a combined intensity and brightness ramp-up, with the bunch population at the SPS extraction progressively increased from the pre-LS2 1.35×10^{11} ppb to 1.8×10^{11} ppb while the transverse emittance is tentatively decreased from $2.5 \mu\text{m}$ to $1.7 \mu\text{m}$ (see figure 64) after including a further 10% beam loss and emittance growth in the SPS. New territory will be explored in terms of beam parameters. In fact, although intensities up to 2.6×10^{11} ppb were already produced up to PS extraction and even tested at SPS injection during Run 2, beams with bunch population exceeding 1.5×10^{11} ppb need the upgraded SPS main RF system to be accelerated in trains longer than 12 bunches. The SPS will have to be scrubbed for this new range of intensities and the already encountered horizontal and longitudinal instabilities at 25 GeV will have to be overcome in order to ensure beam losses within 10% in the SPS, as required for operational deployment. Therefore, a stabilisation strategy will have to be developed, tested and demonstrated. It should be mentioned that,

although the LIU ramp-up plan will focus on the LHC standard beam, which is the one required for the HL-LHC run, priority will be given in 2022 to the deployment of the operational beams required by LHC (e.g. BCMS or 8b+4e with population and brightness consistent with the LIU ramp-up plan).

In 2023–2024 the injected population into the SPS will have to be further ramped-up from 2 to 2.6×10^{11} ppb at constant brightness, thus expecting the extracted population to go from 1.8 to 2.3×10^{11} ppb — possibly in two steps, see figure 62. Apart from the needed additional SPS scrubbing, new and yet unknown limitations might emerge when moving into this parameter range, and require additional actions to achieve the target beam parameters. Addressing these limitations and implementing measures to overcome them is part of the scope of the subject treated in the next subsection. These high intensity beams, though unlikely to be requested already for operation during Run 3, might be of interest for LHC Machine Development sessions to explore possible limitations.

4.2.6 Run 3 hardware options beyond the LIU baseline

In the course of the LIU project, several additional items were considered at different stages for the achievement of the LIU beam parameters, but were then dropped from the baseline because of low benefit over cost ratio. A complete inventory of these options can be found in [131] with details in the references therein. However, some of them could still be revived to respond to some potential performance limitations. In the following we will list the main items, to be kept in mind during Run 3, should any of the associated failure scenarios indeed occur.

Impedance reduction of the extraction kickers in the PSB. Horizontal instabilities occurring along the PSB cycle are caused by the unmatched terminations of the extraction kickers and are cured by the transverse feedback in routine operation. Future operation might suffer due to the 160 MeV injection, which is a critical energy for the instability, and the acceleration of higher intensity beams for ISOLDE. Although this limitation is expected to be mitigated by the upgraded transverse feedback system, an impedance reduction scheme for the kicker exists and has been proved effective both in electromagnetic and beam dynamics simulations.

Landau RF system in the PS. While the LIU beam intensity has been already demonstrated at PS extraction, the implementation of a Landau RF system would increase the stability margin and give more potential to decrease the longitudinal emittance out of the PS, which might directly benefit the SPS losses at injection energy if they are too high. A conceptual design of this additional RF system has been performed and its efficiency has been demonstrated in simulations.

A-C coating of the dipole chambers in the SPS. Beam induced scrubbing has been shown to work for high intensity in the SPS, however large tune shifts along the batches and instabilities have been also observed, which might be due to electron cloud and limit future operation. If an active measure to suppress the electron cloud in the most critical elements of the SPS will have to be implemented, the logistics for in-situ a-C coating of selected SPS chambers will be ready and widely tested during YETS and LS2.

Further SPS impedance reduction. In addition to the shielding of the QF flanges and further suppression of the HOMs in the 200 MHz cavities, the SPS might benefit from reducing the impedance of the injection kickers (both for equipment heating and longitudinal stability) as well as from

shielding the defocusing quadrupole (QD) transitions and the vacuum valves (mainly for longitudinal stability). The benefit of these measures has been shown in beam dynamics simulations. Concerning the impedance reduction of the MKP-L module of the injection kickers, a solution with longitudinal serigraphy has been found and is planned to be implemented in one of the first YETS after LS2, because it has been calculated that the heating of this element would strongly limit scrubbing and machine development for the LIU intensities during Run 3 and later routine operation in the HL-LHC era.

Wideband feedback system for the SPS. A prototype system was installed in the SPS and proved to work against vertical instabilities both in single and multi-bunch operation. An upgraded version of this system could be used against potential future vertical instabilities caused by persisting electron cloud, or a similar system could be developed ex-novo in the horizontal plane to be used against the horizontal instabilities observed in high intensity operation. In fact, the wideband feedback system in either transverse plane is a powerful means against any type of unpredicted beam instability that could rise in high intensity operation and for which the source cannot be easily suppressed.

Collimation system in the SPS. A two-stage collimation system has been designed for the SPS to intercept large momentum particle losses. Such a system could turn out to be necessary in operation with the LIU parameters and higher loss regime to reduce machine equipment irradiation and activation.

4.3 Understanding of the observed heat-load in the Sectors during Run 2, upgrade of the instrumentation and expectations

In the cryogenic arcs of the LHC, the beam vacuum system is surrounded by the superconducting coils which are maintained at 1.9 K during operations. To minimise the heat input to the 1.9 K helium circuit, a beam-screen [1, 2, 132, 133] (co-laminated copper on stainless steel) operating between 4.6 K and 20 K, is inserted into the cold bore to intercept the beam-induced heat-loads due to synchrotron radiation, impedance and electron-cloud effects. The resulting design is shown in figure 65. Pumping slots punched into the top and bottom faces of the beam-screen allow the pumping of the gas at the cold bore surface where the gas molecules are then protected from electrons, ions or photons impact. Pumping slot shields clipped onto the helium cooling capillaries of the beam-screen intercept electrons from the cloud which could escape the beam-screen by the pumping slots.

At the interconnections between the cryo-magnets, Plug-In Modules (PIM) consisting of bellows shielded by sliding contact fingers, allow for thermal expansion and compensation of mechanical and alignment tolerances between consecutive beam-screens [2] while guaranteeing electrical continuity for beam-induced image currents.

This section discusses the beam-induced heat-loads deposited on the beam-screens which operate between 4.6 K and 20 K. Figure 66 shows a typical beam-screen cooling loop with two circuits in parallel (circuits a and b) controlled by a common valve located at the cooling-loop outlet. In this configuration, the heat-loads per half-cell Q can be globally assessed by an enthalpy (H) balance:

$$Q = m \times (H_{\text{out}} - H_{\text{in}}) \quad (4.1)$$

The corresponding mass-flow m is indirectly obtained by using the flow-coefficient, the characteristics, and the opening percentage of the outlet valve. By this method, the uncertainty on

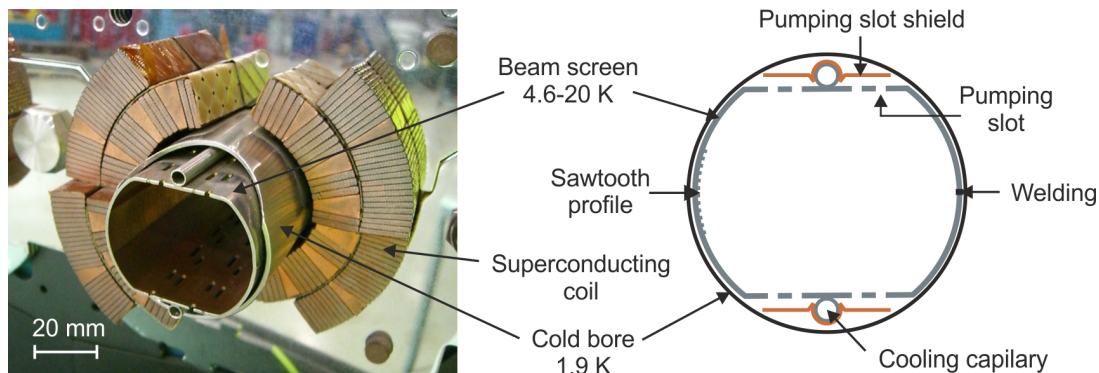


Figure 65. LHC vacuum system for one beam in a LHC arc cryo-dipole: view of one beam vacuum line (left) and corresponding schematic (right).

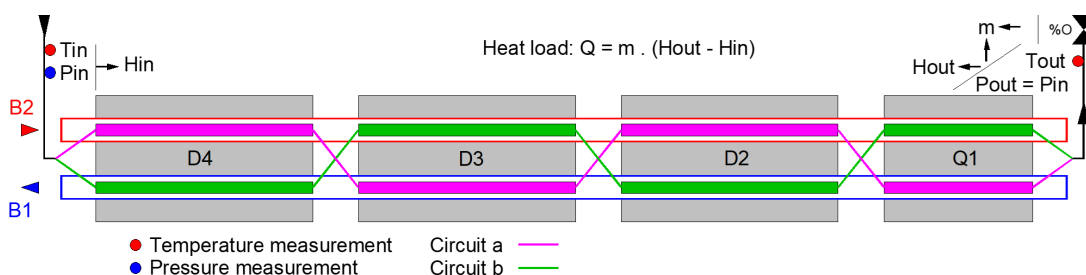


Figure 66. Typical beam-screen cooling loop of a half-cell (~ 53 m) hosting one main quadrupole (Q1) and three main dipoles (D2, D3 and D4). T , P and H refer to the temperature, pressure and enthalpy, respectively, at the inlet (in) and outlet (out) locations, while m corresponds to the helium mass-flow.

the calculation of the half-cell heat-load is between 10 and 15 %, mainly driven by the uncertainty in determining the mass-flow [134].

During LS1, three half-cells in sector 45 (13R4_947, 33L5_947 & 13L5_943, corresponding respectively to the half-cells containing the quadrupoles Q12R4, Q33L5 and Q13L5) were instrumented by adding temperature measurements in some interconnects. During the EYETS 2016–2017, in the shadow of a magnet exchange in the sector 12, an additional half-cell (31L2_943), containing the quadrupole Q32L2, was also instrumented. Figure 67 shows the beam-screen cooling loop of these 4 instrumented half-cells. These additional temperature measurements allow assessing the heat-load per beam-screen. However, in case of a significant heat-load imbalance between circuits and apertures, the flow shared between the two circuits is also unbalanced and the uncertainty on the heat-load calculation of a single beam-screen increases.

4.3.1 Observed heat-load distribution during Run 2

Run 2 marked an important milestone for the LHC as it was only in Run 2 that the nominal bunch spacing of 25 ns was used routinely for p-p physics operation. With such a shorter bunch spacing the heat loads in some of the arcs reached levels close to the design cooling capacity of 160 W/half-cell as shown in figure 68. In all sectors, the heat-loads were significantly larger than expected from impedance and synchrotron radiation and large differences were present among the eight arcs though they are identical by design [135–137].

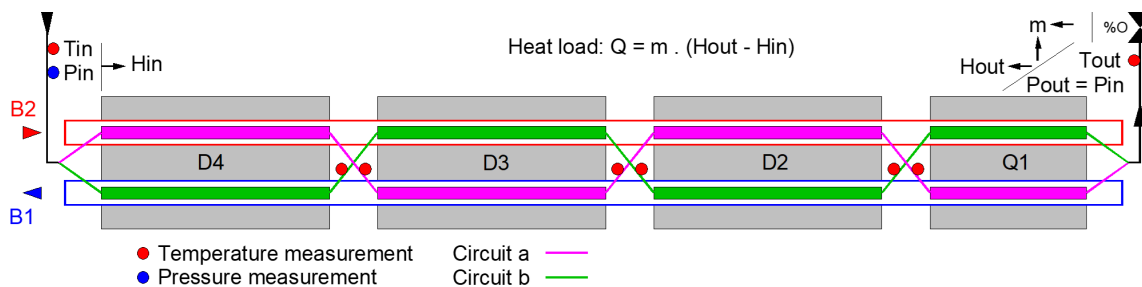


Figure 67. Beam-screen cooling loop of an instrumented half-cell (with additional temperature measurements on some interconnects).

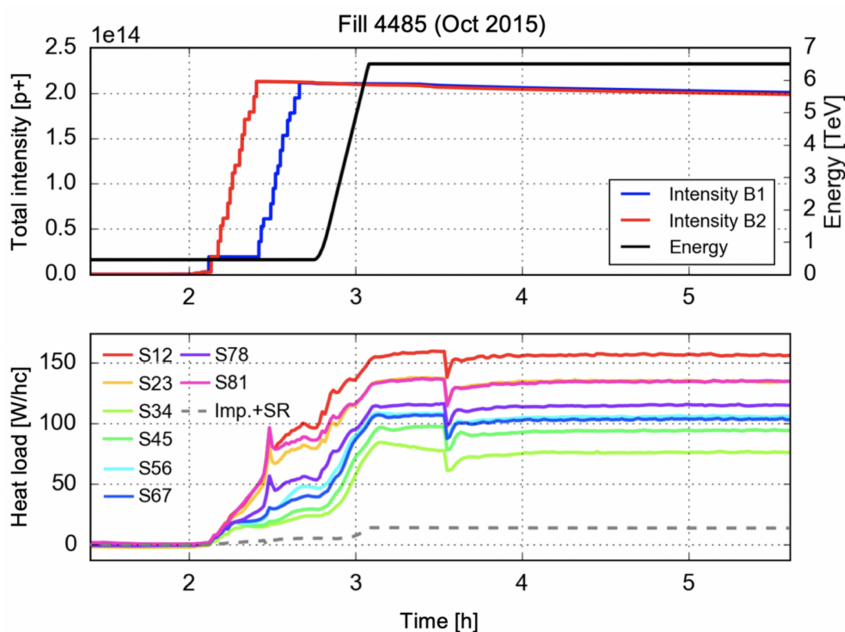


Figure 68. One of the physics fills during which the highest heat-loads on the arc beam-screens were observed. Top: intensity and energy of the circulating beams. Bottom: heat-loads measured in the eight arcs (average per half-cell). The expected power deposited by impedance and synchrotron radiation is indicated by the dashed line.

Surface conditioning provided a significant mitigation of the heat-loads. Figure 69 shows the heat-loads measured in the eight sectors normalized to the circulating beam population, for all the physics fills of Run 2 that were performed with 25 ns bunch spacing and with more than 600 bunches. A strong reduction of the heat-loads, driven by surface conditioning, is observed in 2015 and in the first part of 2016. After that the heat-loads remained practically constant, and the observed differences among sectors remained unaffected.

Figure 70 shows the typical distribution of the half-cell heat-loads along the LHC during the Run 2 (Fill #6675 at a beam population of 2.8×10^{14} protons per beam and at a beam energy of 6.5 TeV). The sectors can be classified in two families: the low-load sectors (S34, S45, S56 and S67) located in the north part of the LHC, and the high-load sectors (S78, S81, S12 and S23) located in the south part of the LHC. Figure 71 shows the distribution of the half-cell heat-loads

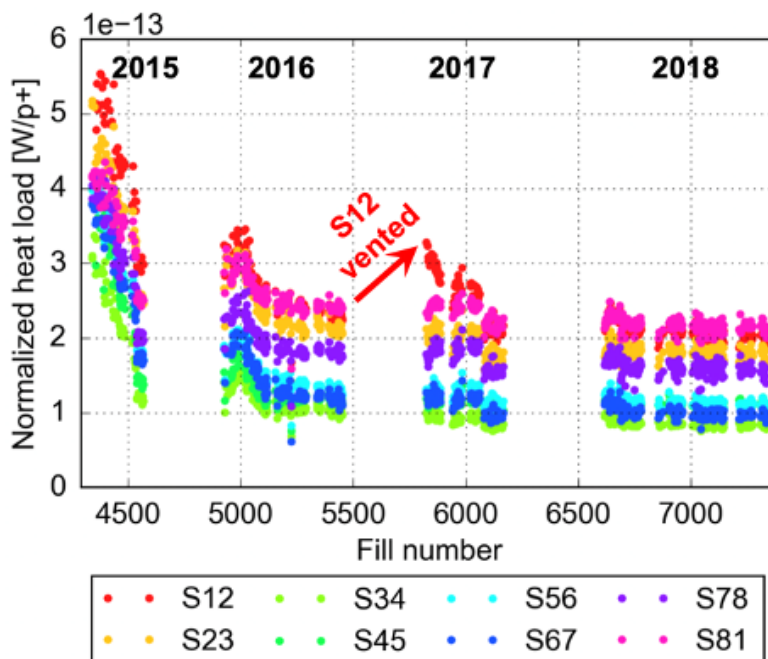


Figure 69. Evolution of the heat-loads normalized to the circulating beam population in the eight LHC arcs during Run 2 (average over the arc half-cells). Data measured at 6.5 TeV for physics fills performed with 25 ns bunch spacing and more than 600 bunches.

on the LHC, on the high-load (south) and the low-load (north) sectors. The spread of the half-cell heat-load values in the high-load sectors is very broad: the heat-load per half-cell varies from 25 W to 260 W i.e., by a factor of about 10 (121 W r.m.s.). Some spread in the heat-load is also visible in the low-load sectors but limited to a factor 6 (from 25 W to 170 W — 71 W r.m.s.). The peak of the distribution is located at about 60 W per half-cell both in the high-load and low-load sectors.

Figure 72 shows the heat-load distribution in two instrumented half-cells (31L2_943 (left chart) and 33L5_947 (right chart)). The beam-screens of the D3 cryo-dipole of the half-cell 31L2_943 in sector 12 exhibit high heat-loads (12 to 16 W per beam-screen) which are 2 to 10 times higher than the heat-loads calculated in the adjacent beam-screens in the D2 and D4 cryo-dipoles: a large spread of the heat-load is observed even within a half-cell.

Differences among sectors, half-cells and magnets are very reproducible and were observed in all 25 ns fills over the entire Run 2 (see for example figure 69 comparing the eight sectors). Nevertheless these differences were not always present. A test period with 25 ns beams took place at the end of Run 1, in 2012. The heat-loads measured during this period can be directly compared against Run 2 data, as the measurement system was largely unchanged and the beam conditions were very similar. A comparison between similar fills performed before and after LS1 is shown in figure 73. It is evident that the differences among sectors appeared only after the LS1, during which all arcs were warmed up to room temperature and exposed to air. Table 12 compares the average half-cell heat-loads for the different sectors. In Run 2, the average heat-loads per half-cell have increased by factors of 1.2 to 3.1 as compared to Run 1.

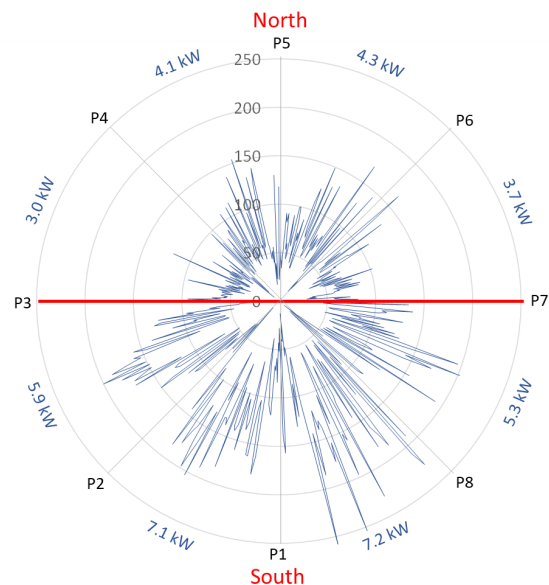


Figure 70. Spread of half-cell heat-loads along the LHC (Fill #6675). The numbers indicated in the circumference are to the total heat-loads of the corresponding sectors.

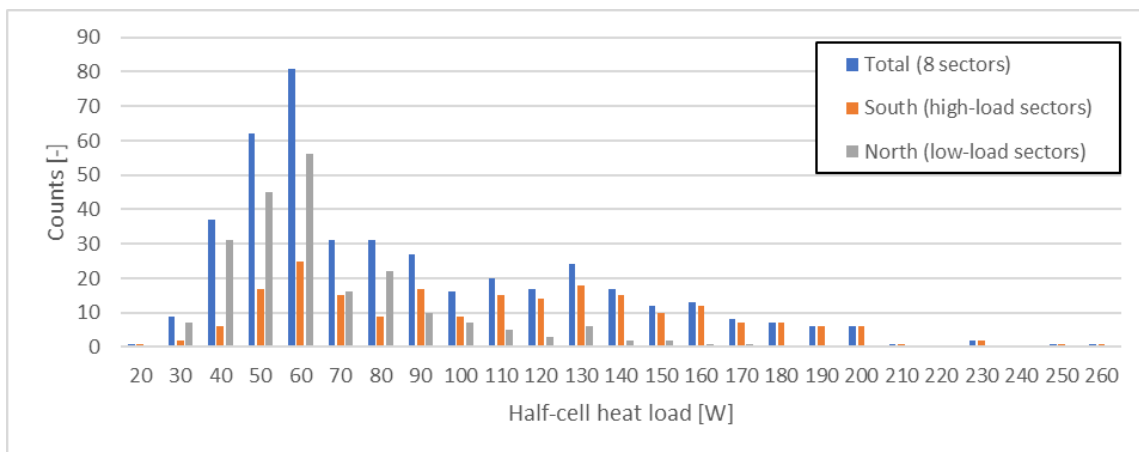


Figure 71. Distribution of half-cell heat-loads along the LHC.

Table 12. Average half-cell beam-induced heat-load comparison for a total beam population of 2.05×10^{14} protons per beam.

Sector	Average half-cell heat-load [W]		Ratio	Classification
	2012 Fill #3438	2017 Fill #5814		
S34	20	24	1.2	Run 2 low-load sectors
S67	23	30	1.3	
S45	26	33	1.3	
S56	23	36	1.6	
S78	23	46	2.0	Run 2 high-load sectors
S12	22	62	2.9	
S23	25	62	2.5	
S81	25	77	3.1	

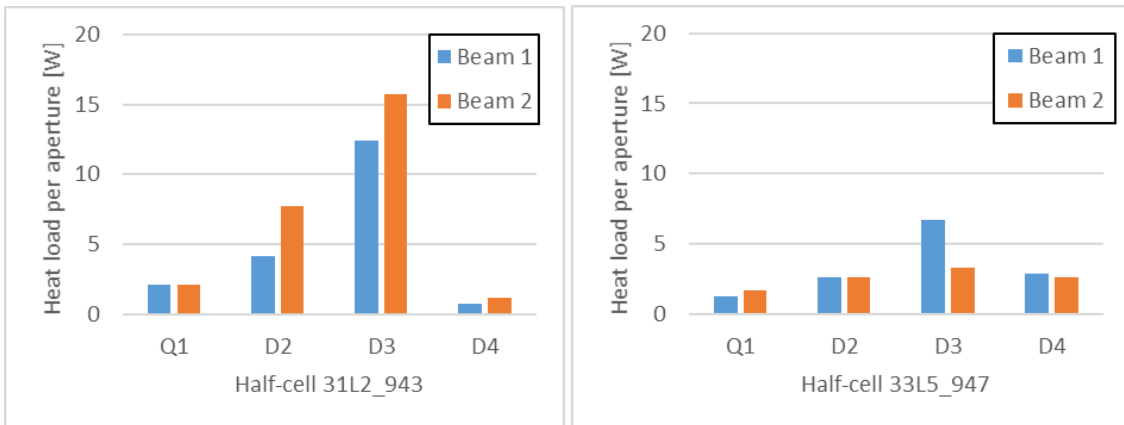


Figure 72. Heat-load distribution within instrumented half-cells (Fill #6255).

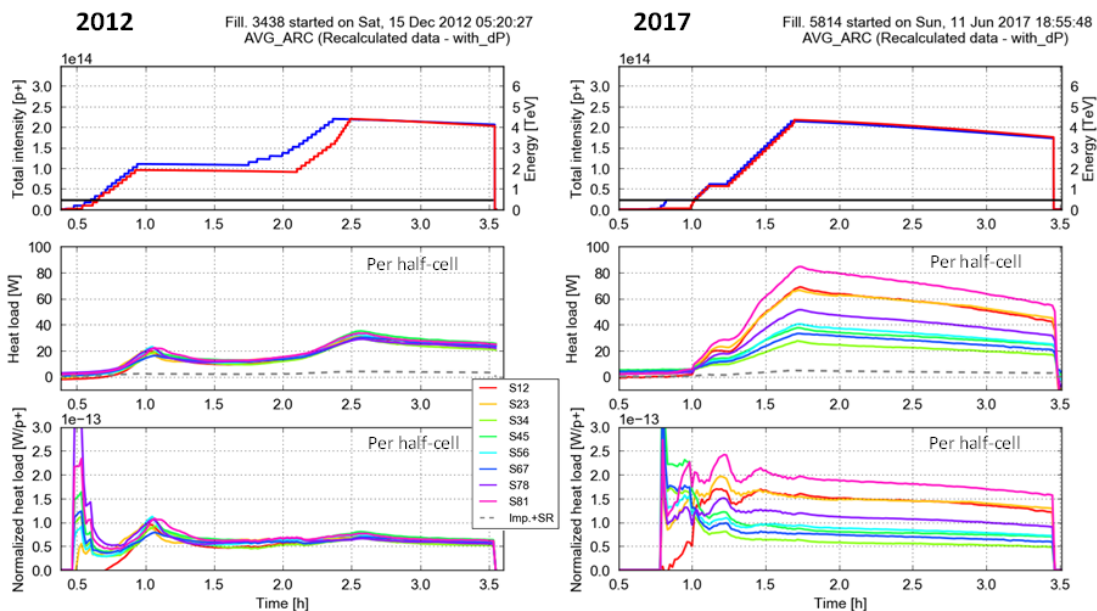


Figure 73. Evolution of the beam-induced heat-load during the 2012 and 2017 scrubbing campaigns with trains of 72 proton bunches and a bunch spacing of 25 ns.

4.3.2 Underlying mechanism

The most characteristic features of the observed heat-loads are the following [138]:

- Measured heat-loads are significantly larger than those expected from impedance and synchrotron radiation, in addition differences among the eight sectors are very pronounced during operation with the 25 ns bunch spacing but disappear when the 50 ns bunch spacing is employed.
- Heat-load measurements taken with 25 ns beams at different bunch populations show a threshold around 0.4×10^{11} ppb.

- For a fixed bunch population the heat-loads are proportional to the number of circulating bunch trains.
- Large heat-loads and differences among sectors are already present at injection energy (450 GeV) and increase only moderately during the energy ramp.

Based on these features and on the analysis of the heat-load measurement technique, it is possible to exclude that the observed differences result from measurement artifacts.

Experimental observations both from physics fills and from dedicated tests provide important information on the source of the heat-loads and in particular of the observed differences among sectors [135, 138].

Different heating mechanisms were considered as possible sources of head loads:

Losses of beam particles. The hypothesis that the differences in heat-loads are generated by protons lost on the beam-screen can be easily discarded since the total power associated to beam losses (calculated from beam intensity measurements) only amounts to less than 10 % of the measured heat-loads.

Synchrotron radiation. The possibility that the observed heat-loads are deposited by photons radiated by the beam can also be excluded. In fact, the power from synchrotron radiation is proportional to the beam intensity and independent of the bunch spacing, which is inconsistent with the experimental data. Finally a strong dependence on the beam energy would be expected, while only a small increase is observed during the energy ramp.

Electromagnetic coupling. The hypothesis that the energy is transferred through electromagnetic coupling between the beam and the surrounding structures is incompatible with the observations as well. The measured dependence of the heat-load on the bunch population is not quadratic and heating due to impedance cannot justify the large differences observed between 25 ns and 50 ns beam.

Electron-cloud build-up. The hypothesis that the energy deposition comes from electron-cloud (electrons impacting on the beam pipe) is not in conflict with any of the mentioned observations and it has been further investigated by numerical simulations and experiments, as discussed in the following.

In order to compare the measured heat-loads against electron-cloud simulations, we have assumed that the differences observed among sectors and among half-cells are caused by non-identical surface properties of the beam-screens resulting in a different SEY parameter (also called δ_{\max} in literature). The electron-cloud build-up process has been simulated using the PyECLOUD code [139] as a function of the SEY parameter for all the elements of the LHC arc half-cell [140, 141]. The total simulated heat-load as a function of the SEY is shown in figure 74 for the two circulating 25 ns beams at 6.5 TeV for the beam intensity corresponding to a fill during which the heat-load was measured. By comparing the simulated heat-loads against the measured ones, it is possible to infer the SEY of the beam-screen surface. According to the heat-load spread observed in the LHC (from 25 to 260 W per half-cell, see figure 71), the SEY (here assumed to be constant within a half-cell) should vary from 1.1 up to 1.47. At the peak of the heat-load distribution (60 W), the corresponding SEY is 1.21.

Figure 75 shows the simulation of the expected heat-load on a dipole beam-screen as a function of the bunch population for different surface SEY. With respect to the heat-load distribution within

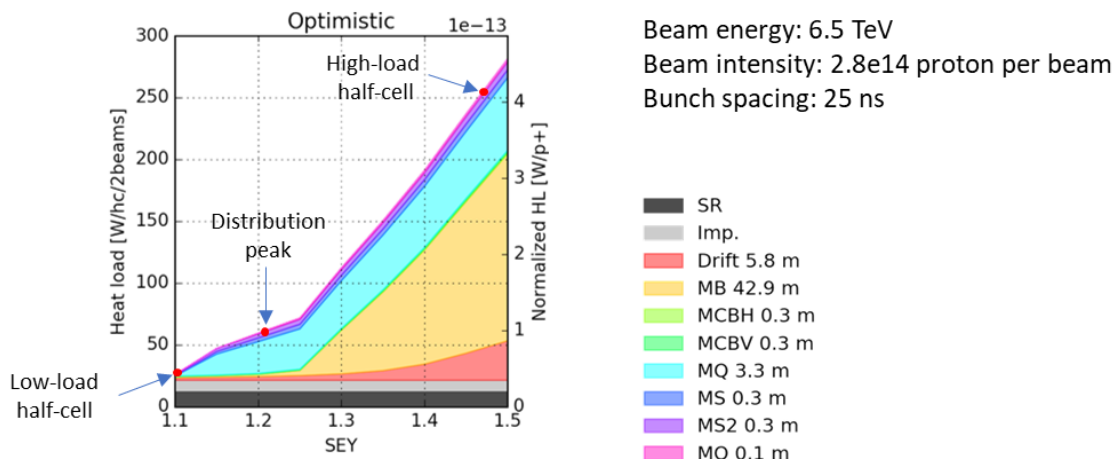


Figure 74. Half-cell heat-load simulation versus SEY.

the instrumented half-cell of sector 12 (see figure 72), the SEY of the different beam-screen surfaces vary from 1.05 to 1.4.

An extensive campaign of measurements and simulations took place in the last part of Run 2 in order to validate the simulation models with experimental data [138]. Heat-load measurements were collected with different filling patterns and bunch populations both at injection and at collision energies. Although in Run 2 the LHC injectors could not produce long bunch trains with bunch populations larger than 1.2×10^{11} ppb, it was possible to probe higher bunch populations using short bunch trains. This was particularly relevant in view of the increase of the bunch population foreseen for Run 3 and for the HL-LHC upgrade.

Figure 76 shows the comparison of the collected data against simulations for one of the high-load arcs. One beam configuration (corresponding to the point circled in red in figure 76) is used to infer the SEY for the arc half cells. Simulations are performed for the inferred SEY values to obtain the expected heat-loads for the other populations and configurations for which experimental data is available. The results of such simulations are represented by the curves in figure 76. Very good agreement is found between simulations and data, which provides an important validation of the simulation model and confirms that the electron-cloud build-up due to different values of the SEY of the beam-screen surface is at the origin of the observed heat-load.

4.3.3 Beam-screen surface analyses

Several LHC cryo-magnets presenting non-conform internal splices were exchanged during the LS2. Within this set of cryo-magnets, two cryo-dipoles of particular interest have been identified:

- the B31L2 cryo-dipole located in the half-cell 31L2 of sector 12 containing two beam-screens exhibiting high heat-loads (D3 dipole in figure 72);
- the C21R6 cryo-dipole, which is included in a low-load half-cell of sector 67 and which contains two beam-screens exhibiting low heat-loads.

After their warm-up, the beam pipes of the two concerned sectors had been vented with high-purity nitrogen and oxygen (79 %-21 %). After the cryo-dipole disconnection and the PIM

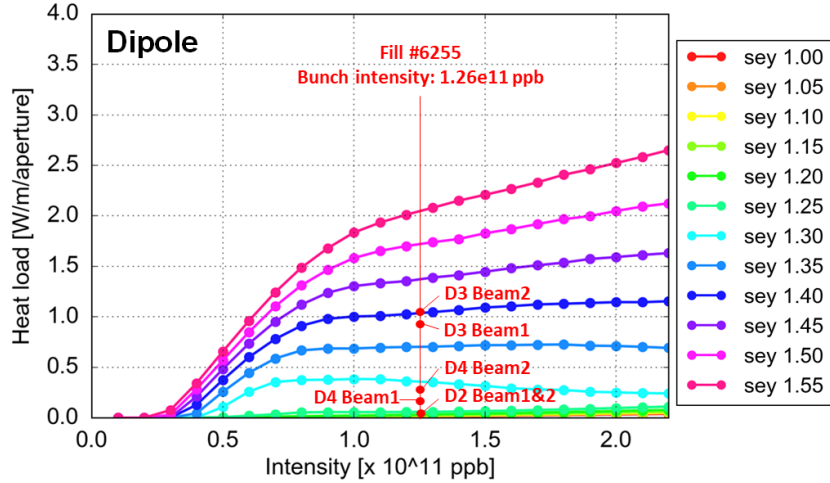


Figure 75. Heat-load of the 31L2_943 beam-screens for a bunch population of 1.26×10^{11} ppb and comparison against simulated heat-loads on an arc dipole magnet beam-screen.

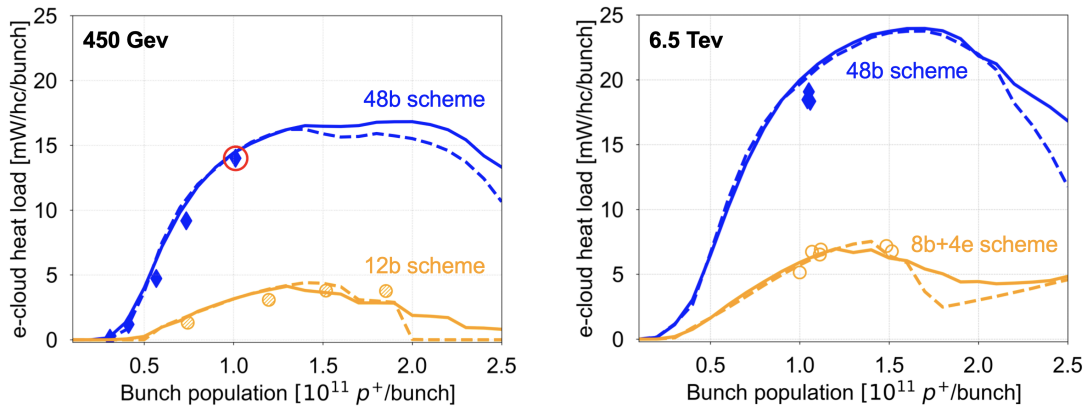


Figure 76. Heat-load as a function of the bunch population as obtained from simulations using a different SEY for each half-cell (continuous lines), simulations using the same SEY for all half-cells in the arc (dashed lines), experimental data from the LHC Run 2 (dots). The data point circled in red is used to infer the SEY used in the simulations.

extraction, the ends of the beam-screens were protected with cleaned leak-tight aluminium flanges. The beam-screens were extracted from the cold bores, then cut in parts 2 m long and stored in 4 chambers under static vacuum to avoid any modifications of their surface conditions beyond those provoked by the unavoidable air exposure during opening [142]. In total four 15 m long beam-screens (two high-load and two low-load ones) were available for analyses. First visual inspections of the high-load beam-screen did not reveal specific issues. The internal beam-screen surface is clean and shiny (see figure 77). The print of the beam-screen pumping slots are visible on the pumping slot shield in some places (see figure 78). This observation is a sign of beam-induced electron multipacting, i.e. of electron-cloud build-up.

Following visual inspections, X-ray Photo-electron Spectroscopy (XPS) was performed on different low-load and high-load samples of beam-screen to analyse their surface composition [143].



Figure 77. Photographs obtained during visual inspection of the B31L2 beam-screens (B1 left, B2 right).

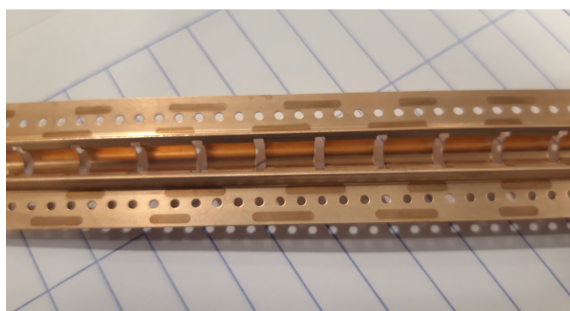


Figure 78. Print of the beam-screen pumping slots on the pumping slot shield.

These samples were collected from locations where a dipole field was applied and from field-free locations (close to interconnects). Figure 79 shows the result of XPS analyses of a high-load and a low-load sample. While the native Cu_2O copper oxide [144] is dominant at the surface of the low heat-load beam-screen samples, the presence of CuO , a non-native surface copper oxide, is observed in the high heat-load samples. In addition, the high-load sample exhibits a very low atomic concentration of carbon (~ 10 at.%).

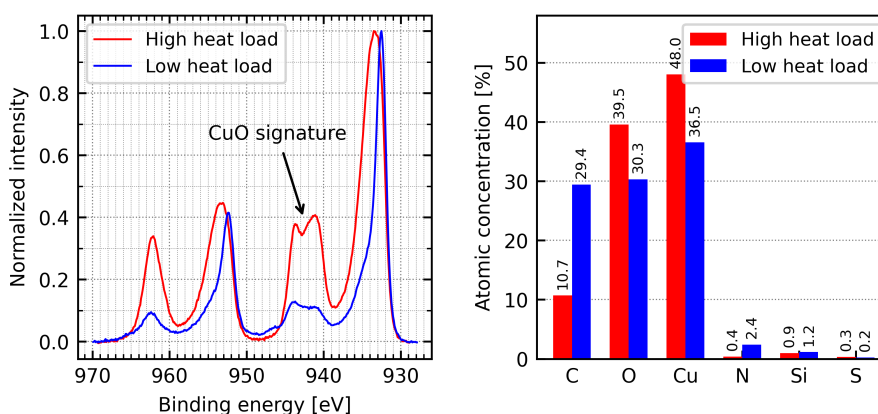


Figure 79. XPS analyses of beam-screen samples.

Samples of the extracted beam-screens were conditioned in the laboratory at room temperature by irradiation with electrons at 250 eV and their conditioning was compared with that of a sample taken

from a spare beam-screen [143] (see figure 80). The conditioning of the low-load samples reaches the expected SEY level at the expected dose for cleaned beam-screen copper. The conditioning of the high-load samples does not reach the expected level at the expected dose. After a dose three times larger than the usually required one, the SEY is still as high as 1.2.

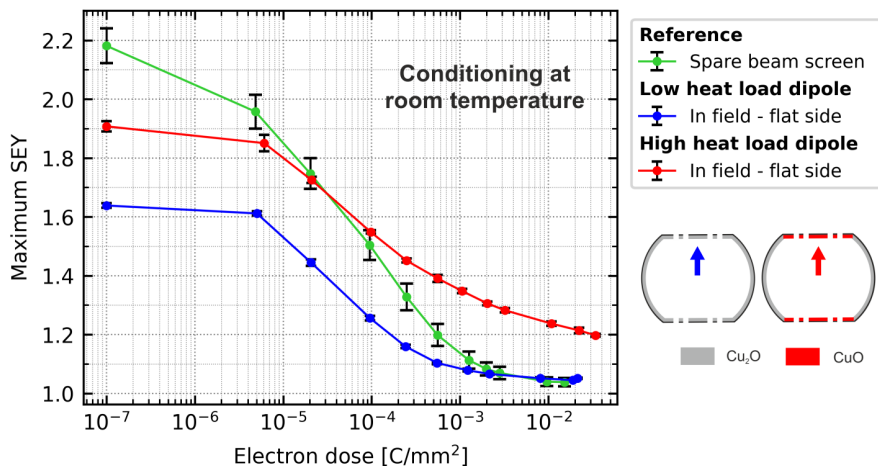
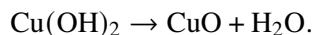


Figure 80. Variation of the maximum SEY during conditioning of beam-screen samples.

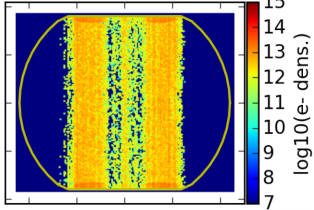
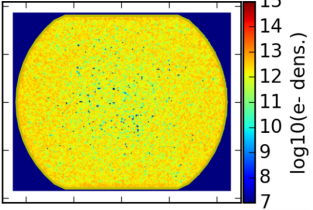
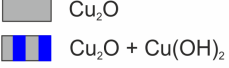
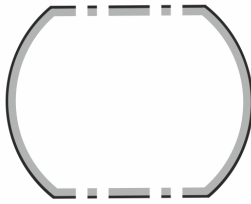
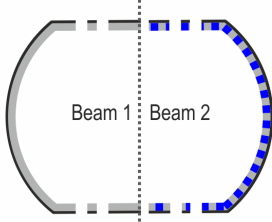

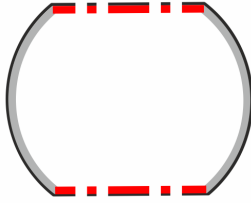
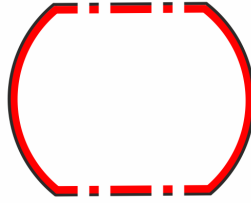
Table 13 gives the summary of the surface analyses. They indicate a strong correlation of high-load beam-screens with the presence of CuO on the surface. In addition, the location and the concentration of CuO is correlated with the electron density distribution expected from simulations in the dipole-field and field-free regions. A very low atomic concentration of carbon is also observed at all azimuths on the high-load beam-screens. The carbon depletion observed at the surface of the high-load beam-screen also hinders the surface conditioning [145–147].

As CuO is a non-native surface copper oxide, mechanisms for CuO build-up were investigated. CuO can be produced in the laboratory by copper exposure to ozone generated by an UV lamp in air at room temperature [148], by copper exposure to oxygen plasma at room temperature [149] and by electron irradiation of a thick layer of water condensed on copper at 11 K. However, in the LHC beam pipe, the residual gas density is too low to induce the observed CuO build-up through the above mechanisms [143]. Airborne copper-hydroxide ($\text{Cu}(\text{OH})_2$) has also the necessary oxygen atoms to generate CuO. The formation of CuO would require dehydration of $\text{Cu}(\text{OH})_2$ to occur during electron bombardment, that is the occurrence of the following reaction in the LHC environment:



The dehydration of airborne $\text{Cu}(\text{OH})_2$ layers and formation of CuO has never been observed in electron bombardment experiments at room temperature, where typically the airborne $\text{Cu}(\text{OH})_2$ layer is reduced to Cu_2O [147]. However, at cryogenic temperature, when surface and bulk diffusion processes are significantly hindered, the dehydration of airborne $\text{Cu}(\text{OH})_2$ could be possible. To limit the diffusion at room temperature, thick $\text{Cu}(\text{OH})_2$ layers have been produced by an electro-chemical process. By irradiating at room temperature these thick $\text{Cu}(\text{OH})_2$ layers with electrons at 250 eV, CuO appears after a dose of about $1 \times 10^{-5} \text{ C mm}^{-2}$. Figure 81 shows the test sample before and

Table 13. Surface analysis summary.

Location		In-field	Field-free
Expected electron density (simulations)			
Low-load samples (C21R6)	Dominant copper oxidation product 		
	Carbon concentration	29 atomic%	29 atomic%
	SEY after conditioning	1.05	1.05
High-load samples (B31L2)	Dominant copper oxidation product 		
	Carbon concentration	11 atomic% (azimuthally uniform)	11 atomic% (azimuthally uniform)
	SEY after conditioning	1.2	1.2

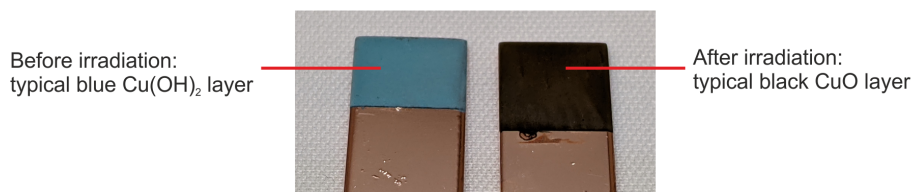


Figure 81. Cu(OH)₂ test samples before and after irradiation with 250 eV electrons.

after irradiation. The initial layer of Cu(OH)₂ with a typical blue colour has been transformed into CuO with a typical black colour. Consequently, the hypothesis that CuO built up from Cu(OH)₂ in the machine remains possible and should be confirmed by tests at cryogenic temperature.

4.3.4 New laboratory diagnostic tools

An experimental set-up was built at CERN in order to perform combined SEY and XPS measurements on a sample at cryogenic temperature (down to 10 K), to investigate the CuO build-up mechanisms, to perform conditioning of beam-screen samples at cryogenic temperature and to validate curative

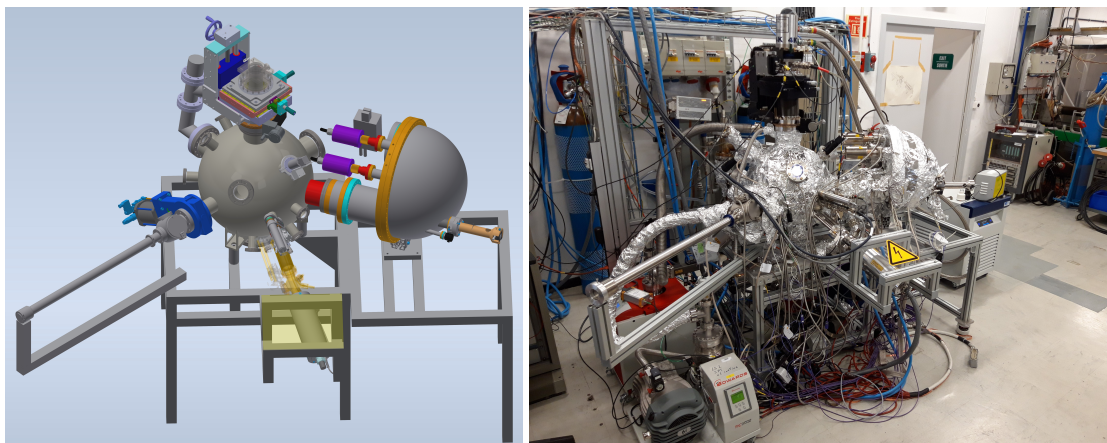


Figure 82. New experimental set-up for SEY and XPS analyses at cryogenic temperatures.

solutions. Figure 82 shows the experimental set-up which is crucial for determining the underlying surface processes in the LHC beam-screens and is currently under commissioning.

4.3.5 New LHC diagnostic instrumentation

The existing instrumentation allows assessing the global heat-load deposited on the beam-screen circuits of a half-cell with an accuracy of 10–15%. However, this instrumentation does not allow measuring the share of this global heat-load on the different beam-screens, especially in case of unbalanced heating which creates unbalanced mass-flow distribution in-between the two circuits a and b (see figures 66 and 67). Consequently, the upgrade of the instrumentation of 10 half-cells (see figure 83) during the LS2 [150] has been proposed:

- 6 high-load half-cells (31L2_943, 15R2_943, 33R2_947, 33L5_947, 17L6_943 & 27L8_947, corresponding respectively to the half-cells containing the quadrupoles Q32L2, Q15R2, Q32R2, Q33L5, Q17L6 and Q28L8). Despite its low heat-load, the half-cell 33L5_947 is here considered as a high heat-load one, due to the significant heat-load of its D3 dipole (see figure 72);
- 2 low-load half-cells (13R4_947 & 13L5_943, corresponding respectively to the half-cells containing the quadrupoles Q12R4 and Q13L5);
- 1 half-cell with a high-field dipole (11 T cryo-dipole) (09R7_947, corresponding to the half-cell containing the quadrupole Q8R7);
- 1 half-cell with a field-free connection cryostat (11R2_947, corresponding to the half-cell containing the quadrupole Q10R2).

The instrumentation upgrade consists of adding temperature sensors at each beam-screen interconnect (up to 9 temperature sensors per half-cell) and mass-flowmeters at the inlet of each cooling circuit (2 mass-flowmeters per half-cell). Figure 84 shows the beam-screen cooling loop of these upgraded half-cells. This upgraded instrumentation will allow to assess the heat-load on each beam-screen by local enthalpy balances. As the installation of the 11 T cryo-dipoles was postponed,

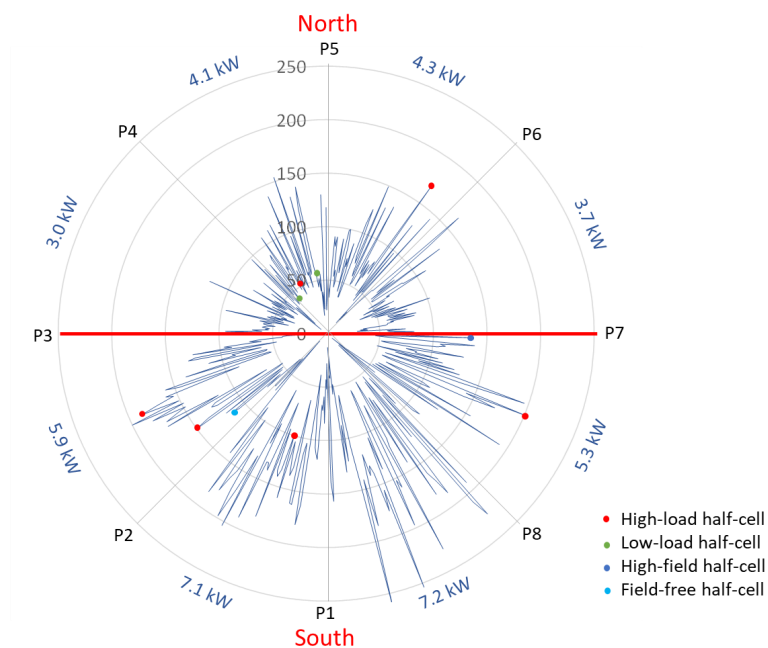


Figure 83. Location of the upgraded half-cells.

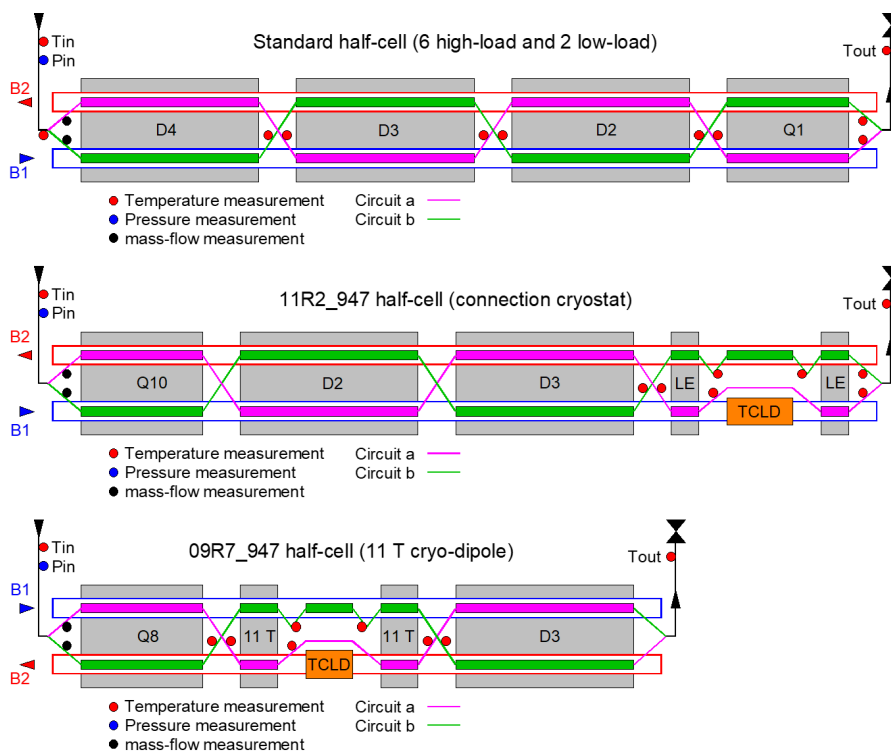


Figure 84. Beam-screen cooling loop of upgraded half-cells.

the corresponding half-cell has been partially upgraded with the installation of the mass-flowmeters only. To complete the local diagnostic capabilities, additional temperature sensors were added on PIMs: three sensors on a high-load PIM of the half-cell 31L2_943, two sensors on a high-load PIM of the half-cell 33L5_947 and one sensor on a low-load PIM of the half-cell 13L5_943.

This new instrumentation will also allow assessing the temperature profile i.e., the heat deposition profile along a beam-screen. Following a beam dump, the beam-induced heating disappears, and the beam-screens are re-cooled down to about 6 K. During this process, the measurements of the helium mass-flow and of the inlet and outlet temperatures allow calculating the required cooling power and by mathematical integration the energy which is required to re-cool down the beam-screens. A simulation tool has been developed to calculate the different initial temperature profiles which are compatible with the re-cooldown energy [151].

To perform global diagnostics at the sector level, mass-flowmeters have been added on the main return lines (Line D and Warm Recovery Line — WRL) of the refrigerators of two high-load sectors (S12 and S23) and of one low-load sector (S56). Figure 85 shows a simplified sector cooling scheme. The mass flows of the beam-screen cooling loop are collected in Line D in addition to the mass flows needed to cool the standalone magnets. Then the Line D mass flow is used to cool the resistive part of the HTS current leads (m_{WRL}) and the remaining part (m_{D}) returns to the refrigerator. By assuming that the heat-loads of the standalone magnets and of the heat intercepts remain constant or negligible during the beam injection, the mass-flow variations of ($m_{\text{D}} + m_{\text{WRL}}$) are produced by the beam-induced heating of the beam-screens and will allow assessing the corresponding heat-load by a global enthalpy balance.

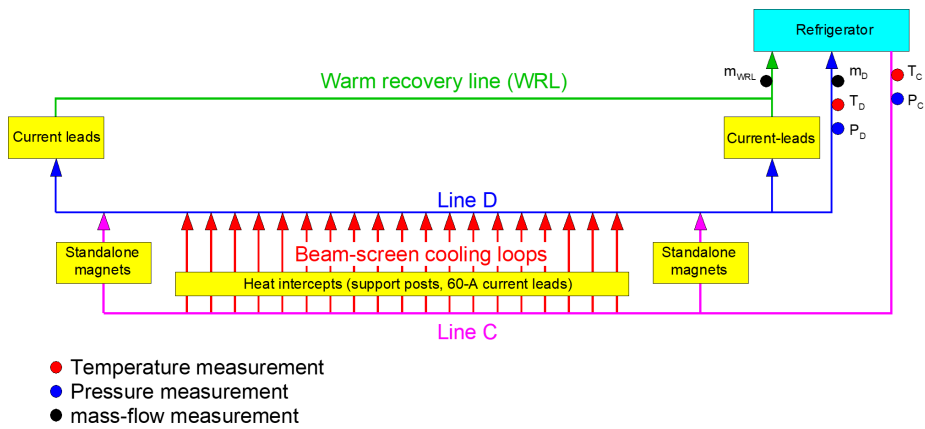


Figure 85. Simplified sector cooling scheme with additional mass-flowmeters.

4.3.6 Expected limitations

Based on the present observed deterioration of the beam-screen surface SEY, figure 86 shows the simulations of the heat-load evolution in the most critical sector 81 as a function of the bunch population, as obtained from PyECLLOUD simulations. At nominal HL-LHC bunch population, this sector will need a cooling capacity of about 10 kW. Table 14 gives the available cooling capacity per sector and the expected heat-load for the beam-screen cooling in Run 3 and Run 4, considering the HL-LHC cryogenic system upgrade in Point 1 and Point 5 during LS3. The cooling margin varies

from -3% for sector 12 in Run 3 (value within the error bars of the estimate) to 100% for the sector 56 in Run 4. The high-load sectors will be close to or at the limit of the cooling capacity without margin. Consequently, any further deterioration of the beam-screen surface in these sectors will jeopardize the nominal HL-LHC operation. Special care has been taken during LS2 to avoid the formation of additional $\text{Cu}(\text{OH})_2$ during the beam-vacuum venting by using a high-purity N_2/O_2 gas mixture and by reducing as much as possible the air exposure time. In case further degradation will be observed, methods are being investigated to treat the surface of the beam-screens and re-establish a low SEY.

As the treatments of half-cells will not be possible before the LS3, short-term (Run 3) mitigations have been investigated to minimize the performance loss, which are based on hybrid filling schemes composed of 25 ns bunch trains combined with 8b+4e bunch trains (see section 4.2.3).

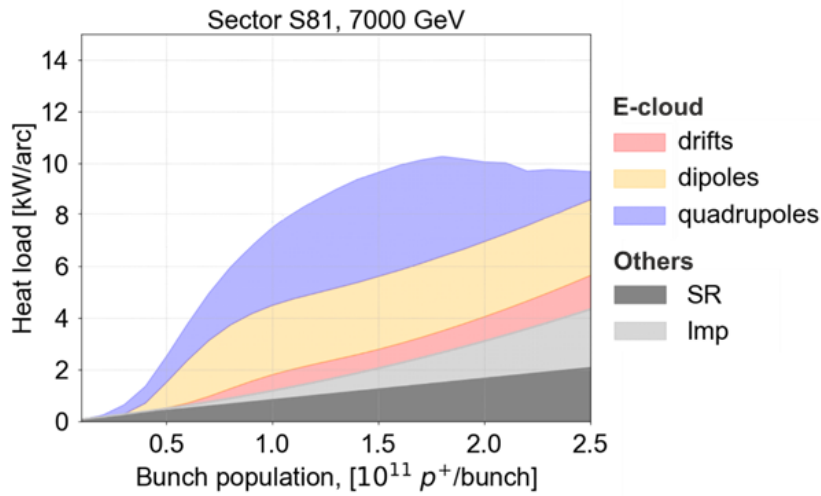


Figure 86. Expected heat-loads in sector 81 during Run 3 and HL-LHC operation.

Table 14. Available cooling capacity and cooling margin (for the standard filling scheme) of sector refrigerators.

Sector	Available cooling capacity [kW]		Expected heat-load [kW]		Cooling margin [%]	
	Run 3	Run 4	Run 3	Run 4	Run 3	Run 4
S12	9.5	10.6	9.8	9.6	-3	10
S23	10.3	10.3	8.6	8.6	20	20
S34	11.0 (6.5*)	11.0 (6.5*)	5.7	5.7	92 (12*)	92 (12*)
S45	9.5	10.6	6.8	6.7	40	60
S56	12.7	13.8	7.0	6.9	81	100
S67	9.3	9.3	6.4	6.4	46	46
S78	9.3	9.3	8.0	8.0	16	16
S81	12.2	13.3	9.9	9.7	24	37

* Without taking into account the capacity upgrade of sector 34 refrigerator during LS2

Remedies against high heat-load are under investigation to implement a curative treatment in the LHC during LS3 if high-intensity beams in Run 3 confirm the heat-load predictions. Five different strategies are under investigation:

- Treatment by ion etching [152] and copper re-oxidation to Cu_2O in air. In laboratory, this treatment removes efficiently CuO by etching (100 nm) and the surface is partially re-oxidized to Cu_2O during the venting. For an air exposed surface, the maximum SEY reaches 1.15 after full conditioning at room temperature in the laboratory. This maximum SEY would be below the threshold for electron-cloud build-up in the dipoles; but above it in the quadrupoles. Moreover, venting of the treated beam-screens would possibly not ensure the same level of airborne carbon contamination, which is necessary to reach the low SEY limit of 1.15 [147] and a second step in the treatment might be necessary. The implementation of the complete treatment in the machine would require the insertion of a sputtering device in the beam-screen aperture across the interconnections.
- Treatment by thermal reduction of the CuO beam-screen surface [153, 154]. Efficient reduction of CuO is obtained at 120°C under vacuum for 60 h. However, 120°C exceeds the maximum acceptable temperature of the machine elements. The maximum SEY reaches 1.15 after full conditioning at room temperature. This maximum SEY would be below the threshold for electron-cloud build-up in the dipoles; but above it in the quadrupoles. Additional tests are ongoing by adding forming (reducing) gas to try to lower the reduction temperature [155]. This treatment could be non-intrusive if the beam-screen cooling channels are used to heat the beam-screens.
- Treatment by Vacuum-Ultra-Violet (VUV) light [156–158]. VUV light exposure in forming gas environment at room temperature seems efficient to reduce CuO . Oxides are partially reduced to metallic copper during this treatment. The implementation of this treatment in the machine would require the insertion of a device in the beam-screen aperture across the interconnections. This method efficiently reduces surface oxides as well as hydrocarbon surface adsorbates. Therefore, in a subsequent step, the re-adsorption of carbon species must be verified to achieve proper conditioning.
- Treatment by a cold atmospheric pressure plasma using a reactive, reducing operation gas [159, 160]. The chemical reduction of CuO strongly depends on process conditions, with some inhomogeneity in between treated samples. Further tests are scheduled in glove box using inert environment. The implementation of the complete treatment in the machine would require the insertion of a plasma device in the beam-screen aperture across the interconnections. This method efficiently reduces surface oxides as well as hydrocarbon surface adsorbates. Therefore, in a subsequent step, the re-adsorption of carbon-species must be verified to achieve proper conditioning.
- Treatment by covering the CuO surface with CH_x to favour the formation of a graphitic layer. This layer would erase the memory of the underlying CuO along the conditioning of the machine. In the SPS, a treatment was applied during LS2 to cover some beam pipes with a thin film of amorphous-carbon (a-C) produced by magnetron sputtering [161]. A similar

in-situ treatment was also applied to the beam-screens of a LHC standalone magnet during LS2. However, this treatment is not compatible with the aperture verifications performed after each sector warm-up to detect PIM RF-finger buckling [162]. Candidate molecules for such a CH_x coverage have not been explored yet.

For all treatment methods, conditioning of treated surfaces, the possible need to recover carbon contamination and the robustness of the treatment against new CuO build-up during the subsequent Runs and Long Shutdowns of the LHC must be assessed at cryogenic temperature in the new cryogenic experimental set-up.

The deployment of the surface treatments discussed in this section will most likely not be possible before the end of Run 3. In case issues are encountered already in Run 3, for example further degradation from LS2, issues with cryogenics performance, or worse than expected dependence of the heat-loads on bunch population, the heat-loads will need to be mitigated using the 8b+4e filling pattern. “Mixed filling schemes” featuring 8b+4e trains and 25 ns trains within the same scheme can also be used to maximize the number of bunches without exceeding the heat-load limit defined by the cryo-plant performance [140].

4.4 LHC configuration and operational scenario for Run 3: protons

The restart of the LHC for Run 3 coincides with the completion of the LIU project [7], offering to the LHC the opportunity and the challenge to operate with up to two times higher beam brightness, pending the complete installation of the HL-LHC [9], which should take place in LS3. In this context, Run 3 is clearly a transition between the LHC and the HL-LHC, with key ingredients which will be made available, either gradually (LIU beam) or immediately (ATS optics [31]). Run 3 shall therefore be exploited not only for performance, but also as a full scale demonstrator of the HL-LHC in terms of beams, optics and beam manipulation (e.g. β^* levelling over a very large dynamic range). To this aim, the so-called LHC configuration, namely the optics, needs to be adapted in order to cope or mitigate constraints of different nature, from beam brightness limitations due to the machine impedance, to specific desiderata of some LHC experiments. After reviewing these constraints, including the intensity limitations coming from the existing hardware, the beam parameters targeted for the LHC in Run 3 are given. A possible solution for the machine configuration will then be described, and analyzed from various perspectives, which should not limit the machine performance over the full Run 3, and should enable to more than double the integrated luminosity delivered so far to the two high luminosity insertions of the LHC.

4.4.1 Beam parameters targeted for Run 3

During the third exploitation period of the LHC, an unprecedented ramp-up of the beam intensity will take place in the LHC injector chain, thanks to the completion of the LIU project. Assuming a BCMS [122] beam structure, possibly combined with a few 8b+4e [123] bunch train inserts in order to mitigate the heat-load due to electron cloud (see section 4.3.6), the forecast by the LIU project are summarised in table 15 (see section 4.2). In 2022, a bunch population N_b of up to 1.8×10^{11} ppb within a transverse normalised emittance $\epsilon_n = 1.30 \mu\text{m}$ is planned to be demonstrated in dedicated studies. This beam, however, will only be operational beginning of 2023. Later on, the bunch population will continue to be pushed while operating at the beam brightness limit in the injectors,

namely up to 2.1×10^{11} ppb (within $\epsilon_n = 1.55 \mu\text{m}$) at the end of 2023, and meeting the HL-LHC target of 2.3×10^{11} ppb (within $\epsilon_n = 1.70 \mu\text{m}$) at the end of 2024.

Table 15. Beam parameters expected at SPS extraction in Run 3 for BCMS (or 8b+4e) proton beams. The intensity ramp-up is planned to be conducted at constant transverse emittance during the first year, till reaching the beam brightness limit in the injector towards the end of 2022: 1.8×10^{11} ppb within $\epsilon_n = 1.30 \mu\text{m}$. The bunch population limit mentioned in each year will be targeted in dedicated machine studies only. In particular, an operational beam with 1.8×10^{11} ppb will a priori be available for the LHC only as of 2023.

Parameters	2022	2023	2024
Bunch population N_b [10^{11} ppb]	1.40 \rightarrow 1.80	1.80 \rightarrow 2.10	2.10 \rightarrow 2.30
Norm. transverse emittance ϵ_n [μm]	1.30	1.30 \rightarrow 1.55	1.55 \rightarrow 1.70

On the other hand, the LHC will have to wait until Run 4 in order to fully profit from the LIU beam, with a bunch population of at most 1.8×10^{11} ppb allowed in Run 3 due to intensity limitations in several LHC sub-systems, which are not planned to be upgraded (or only partially) before LS3, namely:

- The injection system, more precisely the beam induced heating of the MKI which should limit the bunch population to 1.45×10^{11} ppb in 2022 (for a r.m.s. bunch length $\sigma_z = 8.2$ cm), and to 1.8×10^{11} ppb (for $\sigma_z = 10.1$ cm) after the replacement of the MKI-8C kicker by an upgraded one in the YETS 2022–2023 (see [163] for more details). This estimate however stands in permanent regime, with 2808 equidistant bunches circulating continuously in the LHC ring with constant population. In a more realistic case, taking into account intensity reduction during luminosity production and the inevitable turnaround time without beam between the end of a physics fill and injection of the high-intensity beams for the next fill, a somewhat reduced bunch length could still be sustained without exceeding the MKI temperature limit, but for a few hours, depending upon the temperature of the ferrite yoke at the start of the fill. Accordingly, the r.m.s. bunch length at top energy has been chosen to $\sigma_z = 9.0$ cm for the entire Run 3, compared to 7.5 cm in Run 2, but might need to be adjusted depending on the needs and observations in Run 3, in particular in the 2023–2025 period, when this parameter could become critical from the MKI heating perspective.
- The 400 MHz RF system of the LHC, for which the limitation comes from the available klystron power at injection. The klystrons are rated to deliver 300 kW of RF power, but in operation the observed readings reveal a saturation at 250–280 kW, although with large error bars. In Run 2, several machine development studies [164] have been performed in order to identify the optimal settings, both to improve the SPS-LHC matching and to reduce the power required for the LIU beams. A beam with bunch population of 1.8×10^{11} ppb can be injected in the LHC by setting the RF voltage at 6.4 MV, while guaranteeing a good RF capture in the LHC using the SPS Q20 optics [165]. During the ramp and at flat top energy, RF power requirements can be made independent of the beam current thanks to the full-detuning beam-loading compensation scheme [166, 167]. At flat-top energy, the present system is fully able to operate at the required 16 MV total voltage for $\sigma_z = 9$ cm. Even slightly longer bunches at the End of Ramp (EoR), e.g. to mitigate the MKI heating, would be acceptable for the RF system.

- The LHC main dump system (body, upstream and downstream windows) for which operation with a bunch population of 1.8×10^{11} ppb still needs to be confirmed (see on-going validation plan described in section 2.3.4).
- The TCDQ absorbers for which operation with a bunch population of 1.8×10^{11} ppb [168] is compatible with the optics functions at that location taking into account orbit and misalignment tolerances.
- The TCDS absorbers, protecting the beam-dump Lambertson septum magnets, have been designed for a bunch population of 1.7×10^{11} ppb [169] (with a maximum of 40 consecutive bunches possibly hitting the TCDS in case of asynchronous dump). The above limit corresponds to the onset of plastic deformation for the $\text{Ti}_6\text{Al}_4\text{V}$ blocks at the end of the second TCDS module. It is expected that the induced distortion of the titanium-alloy block remains acceptable in case of asynchronous beam dumps with 1.8×10^{11} ppb. Another set of simulations was also recently conducted to study the other TCDS blocks, made of CFC and graphite [170]. The studies were based on updated material properties, which were obtained in a new material characterization campaign. The results indicate that the CFC and graphite blocks of the TCDS can also sustain the impact of bunches with 1.8×10^{11} ppb in Run 3. In all cases, a series of checks and measurements, with and without beam, has been defined to assess the integrity of both the TCDS (and TCDQ), before restarting operation after the occurrence of an asynchronous beam dump [171]. Moreover, an endoscopic inspection could be performed during the following YETS to evaluate the actual status of the critical TCDS absorbing blocks.

Except for the upstream window of the TDE (see section 2.3), all the intensity limitations summarized above are rather independent of the beam emittance.

A bunch population of 1.8×10^{11} ppb also corresponds to a worst case for the heat-load in the arcs due to the electron cloud (see section 4.3), which is slightly above the arc cryo-cooling capacity limit in the high heat-load sector 12 for bunch trains of 72 bunches, slightly below the limit for BCMS beams, and possibly further reduced using instead an hybrid filling scheme, with 8b+4e [123] bunch train inserts, at a cost of about 10 % less bunches for the eventual recovery of 25 % missing cryo-cooling capacity or, said differently, of an unexpected heat-load excess by 33 % (see figure 87). This consideration clearly favours the BCMS beam structure, with respect to the standard one, for Run 3, along with the considerably smaller injected emittance for BCMS bunch trains (which should maximize the beam transmission to flat top energy), and at a cost of only a marginal reduction in terms of total number of bunches (2748 vs. 2760 bunches).

Combining all the above concerns, together with the expected intensity ramp-up of the LIU beam, a challenging but still realistic intensity target for operating the LHC in Run 3 is a bunch population of 1.4×10^{11} ppb in 2022, pushed to a maximum of 1.8×10^{11} ppb in 2023 onward, within an injected emittance of $1.3 \mu\text{m}$ (for BCMS beams). Due to Intra-Beam Scattering (IBS) effects, this emittance should rise up to $1.65 \mu\text{m}$ after 40 minutes spent on the injection plateau before the start of the ramp (see figure 88). Considering an emittance growth budget in between 10 % and 50 % in the ramp, the transverse emittance at the start of Stable Beams (SB) period should then range in between $1.8 \mu\text{m}$ and $2.5 \mu\text{m}$. To be noted that an overall emittance growth budget of 50 % is still

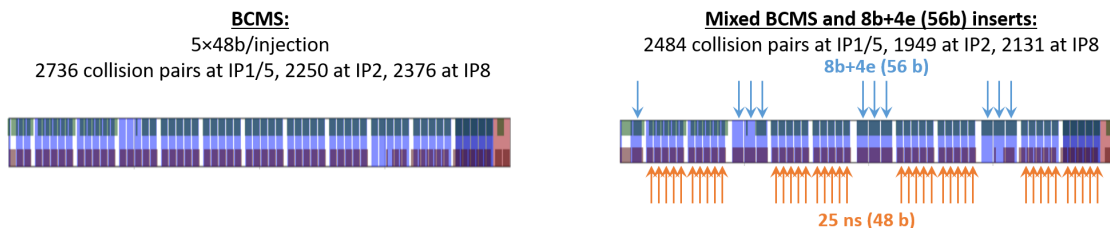


Figure 87. Possible filling schemes considered for the LHC operation in Run 3. The first one is a pure BCMS beam, resulting in 2736 collision pairs in the two high luminosity experiments. The second one is a hybrid filling scheme, consisting of a BCMS beam structure mixed with 8b+4e inserts, in order to restore margin in the cryo-cooling capacity of the LHC arcs by mitigating the electron cloud induced heat-load. A margin of 2.5 kW/arc (i.e. 25 %) results into a ~ 10 % reduction of the total number of bunches, corresponding to 2484 collision pairs at IP1/5 and 1949/2131 at IP2/8 (vs. 2736 and 2250/2376, respectively, for a pure BCMS scheme). (Courtesy of G. Iadarola, CERN).

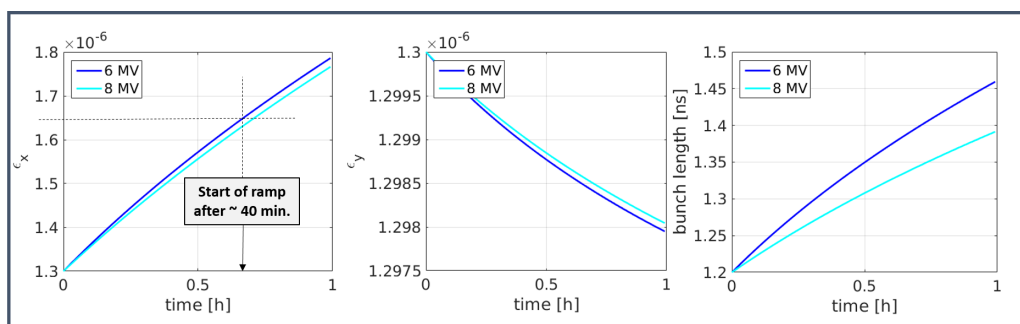


Figure 88. Transverse and longitudinal emittance growth due to IBS on the injection plateau at 450 GeV, assuming a bunch population of 1.8×10^{11} ppb, an injected transverse emittance of $1.3 \mu\text{m}$, and $\sigma_z = 9$ cm, for two possible settings of the RF voltage.

compatible with the unexplained emittance extra blow-up observed during the ramp (but also at injection) in Run 2 [172]. Finally, based on the above discussion on possible cryo-cooling limitations in Run 3, the total number of bunches should range in between 2736 (+12 non-colliding) bunches in 2022, possibly down to 2484 (+12) bunches in case of heat-load limitation at high intensity in 2023 onward. This range of beam parameters is summarized in table 16, at start of SB, assuming no beam loss from injection to flat top energy. Unless specified differently, the best beam parameters will be assumed in all the rest of the paper, namely a bunch population of 1.4×10^{11} ppb and 1.8×10^{11} ppb in 2022 and 2023 onward, respectively, within a transverse emittance of $1.8 \mu\text{m}$ and $\sigma_z = 9$ cm at start of SB, with 2736, 2376 and 2250 colliding bunch pairs at IP1/5, IP8 and IP2, respectively. For performance estimate (see section 4.4.2), the recently confirmed beam energy of 6.8 TeV (see section 4.1) will be assumed, while a beam energy of 7.0 TeV has been used for the tracking studies reported in section 4.4.3.

4.4.2 LHC experiment requirements versus machine constraints

ATLAS and CMS. The main constraints from the ATLAS and CMS experiments lie in the fact that $\langle \mu \rangle$ should be less than 60, within a luminous region in between 32 mm r.m.s. (as in Run 2)

Table 16. Beam parameter range at start of SB in Run 3, taking into account the LIU beam intensity ramp-up and various limitations in the LHC. The uncertainty on the number of bunches in 2023–2025 should be clarified in 2022 based on heat-load measurements. The uncertainty on the beam emittance at start of SB depends on the emittance control in the ramp which will be demonstrated in Run 3. Finally, a small uncertainty still exists on the minimum achievable bunch length at flat-top energy depending on the MKI heating control at high intensity.

Calendar Year	2022	2023 / 2024 / 2025
# bunches	2748	2748 → 2496
# colliding bunch pairs at IP1/5	2736	2736 → 2484
# colliding bunch pairs at IP2	2250	2250 → 1949
# colliding bunch pairs at IP8	2376	2376 → 2131
Bunch population N_b [10^{11} ppb]	1.40	1.80
r.m.s. bunch length σ_z [cm]	9.0	9.0 (→ 10.1)
Norm. transverse emittance ϵ_n [μm]		1.80 → 2.50

and ~ 50 mm, above which the inner tracker could be blind to a small fraction (percent level) of the vertices [173].

Regardless of the number of colliding bunch pairs at IP1 and IP5 in the two extreme cases considered so far (namely 2484 or 2736, see table 16), the PU constraint is automatically fulfilled with a luminosity levelled to $2 \times 10^{34} \text{ cm}^{-2}\text{s}^{-1}$ (limited by the cryo-cooling capacity of the inner triplet [174]), with the worst case of 2484 collisions corresponding to an average number of PU events of about $\langle \mu \rangle = 57$ per bunch crossing. Concerning an appropriate choice of the optics parameters at start of SB (and the resulting luminous region), Figure 89 shows a color plot of the peak luminosity as a function of the bunch population and of the transverse emittance, for two different values of β^* (namely 60 cm and 1.2 m), assuming in both cases a beam energy of 6.8 TeV and 2736 collisions at IP1 and IP5, with a half crossing-angle of $160 \mu\text{rad}$ as in 2018. Considering the beam intensity projection for 2022 (1.4×10^{11} ppb) and as of 2023 (1.8×10^{11} ppb), and assuming a good emittance preservation in the ramp ($\epsilon_n \sim 1.8 \mu\text{m}$ at flat-top energy), it is rather clear that the choice of β^* at start of luminosity levelling has to be modified in between the first year of Run 3 and the rest of the run. $\beta^* = 60$ cm seems to be an appropriate choice for the 2022 run, while an initial β^* as large as 1.2 m could be needed in 2023 onward assuming that a good emittance control in the ramp would have been demonstrated in 2022.

The choice of crossing angle at start of SB for 2022 is a compromise between an as small as possible β^* -levelling range for the first year of Run 3 (only a factor of 2 from 60 cm down to 30 cm), and a further reduction of the Piwinski angle, namely $\phi_w \propto \Theta_c \sigma_z / \sqrt{\beta^*}$, with respect to the 2018 run ($\beta^* = 30$ cm with $\Theta_c/2 = 160 \mu\text{rad}$ and $\sigma_z = 7.5$ cm [5]), in order to minimise the risk of beam instabilities when the two beams are put in collision [175]. Even for a bunch population of 1.8×10^{11} ppb at start of levelling in 2023 onward, a half crossing-angle as large as $160 \mu\text{rad}$ is oversized in order to mitigate the BBLR interactions at $\beta^* = 1.2$ m. Such a crossing angle remains however preferable, again to minimise the β^* dynamic range in SB (a factor of 4 from 1.2 m down to 30 cm in 2023 onward), and might be appropriate in order to avoid extra-losses during the first hour of SB, as observed in Run 2 [176]. Then, later on in SB, operating at the so-called BBLR

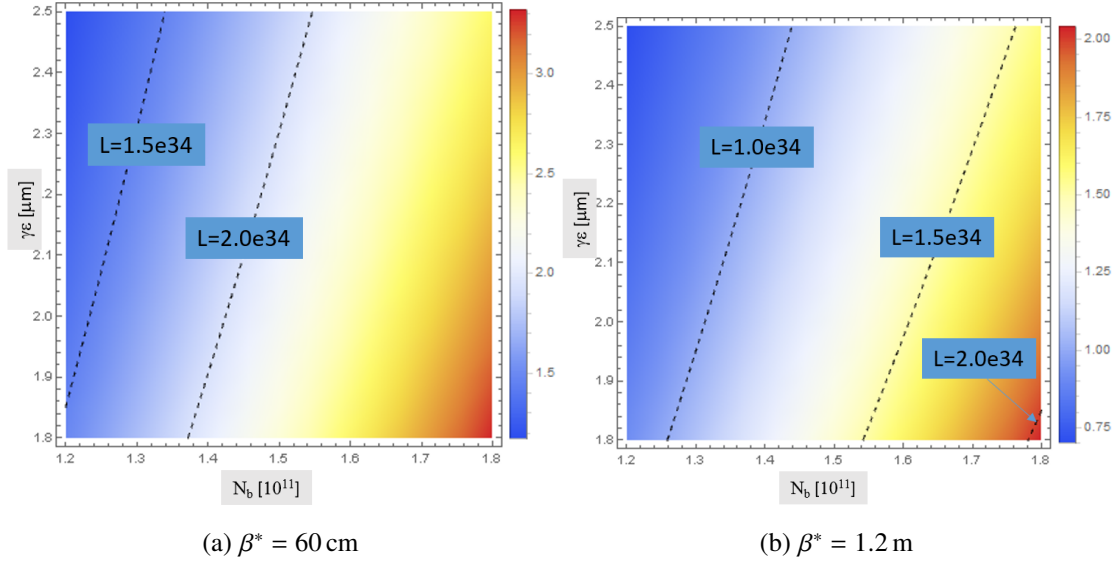


Figure 89. Peak luminosity in ATLAS and CMS as a function of the bunch population and transverse emittance for two different values of β^* , taking an half crossing-angle $\Theta_c/2 = 160 \mu\text{rad}$ in both cases. 2736 colliding bunch pairs are assumed at IP1 and IP5 at a c.o.m. energy of $2 \times 6.8 = 13.6 \text{ TeV}$. The r.m.s. bunch length is set to 9 cm.

limit, i.e. at the minimum possible crossing angle allowed by the BBLR interactions, becomes an interesting option for two main reasons of completely different nature, namely: (i) mitigate the radiation dose taken by the inner triplet, and (ii) optimize the physics conditions for the CMS-PPS forward physics experiment [177] in IR5 (H crossing), where the dispersion is maximized at the RP locations when the horizontal crossing angle is minimized.

The so-called BBLR limit is a complex function of β^* , depending on the beam parameters (bunch charge and emittance), and on the actual levelled luminosity in ATLAS and CMS (so as well on the total number of bunches). In practice, it is estimated numerically by tracking for the initial and final β^* , with the initial and final beam parameters, imposing a typical target of 6σ [2] for the Dynamic Aperture (DA) at start of levelling (high intensity), then in the range of $5.0\text{--}5.5\sigma$ at the end of levelling based on Run 2 experience and including the contribution of the other LHC experiments to beam-beam effects such as LHCb, which will run at higher luminosity in Run 3 (see section 4.4.3). The normalised crossing angle (namely $\Theta_{\text{norm}} = \Theta_c / \sqrt{\epsilon/\beta^*}$, where ϵ is the beam physical emittance), obtained this way at the start and end of β^* -levelling, is then interpolated linearly as a function of the bunch population for intermediate β^* . Plugging this linear function into the luminosity formula, and working at a given prescribed levelled luminosity, the bunch population can be extracted as a function of β^* and, finally, the requested parametric variations of the physical crossing angle Θ_c with β^* can be obtained. This parametric function is shown in figure 90, considering the worst case beam parameters of table 16, namely only 2484 collisions at IP1 and IP5, and a poor emittance preservation in the ramp (i.e. $\epsilon_n = 2.5 \mu\text{m}$ at start of SB, assumed to stay constant in this case). At the prescribed levelled luminosity of $2 \times 10^{34} \text{ cm}^{-2}\text{s}^{-1}$, the BBLR limit at the start of β^* -levelling corresponds to a half crossing-angle of $145 \mu\text{rad}$ and $135 \mu\text{rad}$, in 2022 (with $N_b = 1.4 \times 10^{11}$ ppb and $\beta^* = 60 \text{ cm}$) and as of 2023 (with $N_b = 1.8 \times 10^{11}$ ppb and $\beta^* = 1.2 \text{ m}$), respectively, and to $160 \mu\text{rad}$ at the end

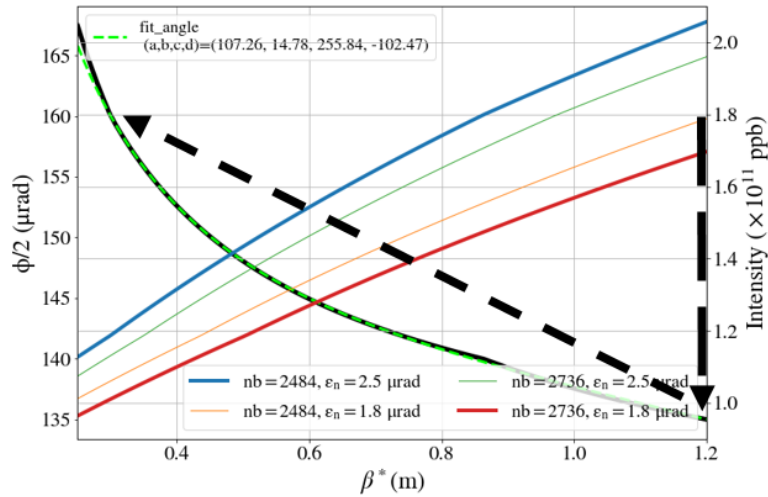


Figure 90. Parametric variations of the crossing angle with β^* in Run 3 calculated for the worst case beam parameters (namely with 2484 collisions at IP1 and IP5 and a poor emittance conservation in the ramp leading to $\epsilon_n = 2.5 \mu\text{m}$ from start to end of SB). Fixing this crossing angle function as input, the evolution of the bunch population is shown during β^* -levelling at the prescribed levelled luminosity of $2 \times 10^{34} \text{cm}^{-2}\text{s}^{-1}$, for the 4 possible beam parameter sets considered in table 16. The dashed arrows indicate schematically the two phases of the luminosity levelling beam process.

of the levelling (with $N_b \sim 1.2 \times 10^{11}$ ppb and $\beta^* = 30$ cm, which typically corresponds to the optics and beam parameters in 2018 at start of SB).

The luminosity levelling beam process will therefore contain two well distinct periods, namely:

- a first luminosity levelling period, rather short, acting on the crossing angle at constant β^* till reaching the BBLR limit,
- and a second period of β^* -levelling with concomitant variations of the crossing angle following the BBLR limit.

At the start of the second period, the gain in dispersion at the CMS-PPS Roman Pots is expected to be around 15% in 2023 onward ($\Theta_c/2 = 135 \mu\text{rad}$ instead of $160 \mu\text{rad}$), leading to an improvement in the same proportion for the minimum mass detection threshold. Operating the machine at the BBLR limit should also mitigate by at least 3–4% (0.5 MGy) the integrated radiation dose which will be taken by the triplet over the whole Run 3 [178], w.r.t. to a scenario where the luminosity would be delivered at a strictly constant crossing angle of $\Theta_c/2 = 160 \mu\text{rad}$.

In order to minimize the complexity in 2022 (where the luminosity production will be anyway marginal with respect to the entire run), it has however been decided to operate at constant crossing angle $\Theta_c/2 = 160 \mu\text{rad}$ during this re-commissioning year, and to implement the above crossing-angle management plan only in 2023 onward.

Beam-beam simulation studies (DA) have been performed in order to successfully validate this running scenario, and will be reported in section 4.4.3. For a typical fill of 2022 ($N_b = 1.4 \times 10^{11}$ ppb) and 2023–2025 ($N_b = 1.8 \times 10^{11}$ ppb), the profiles of the various quantities (β^* , half crossing-angle,

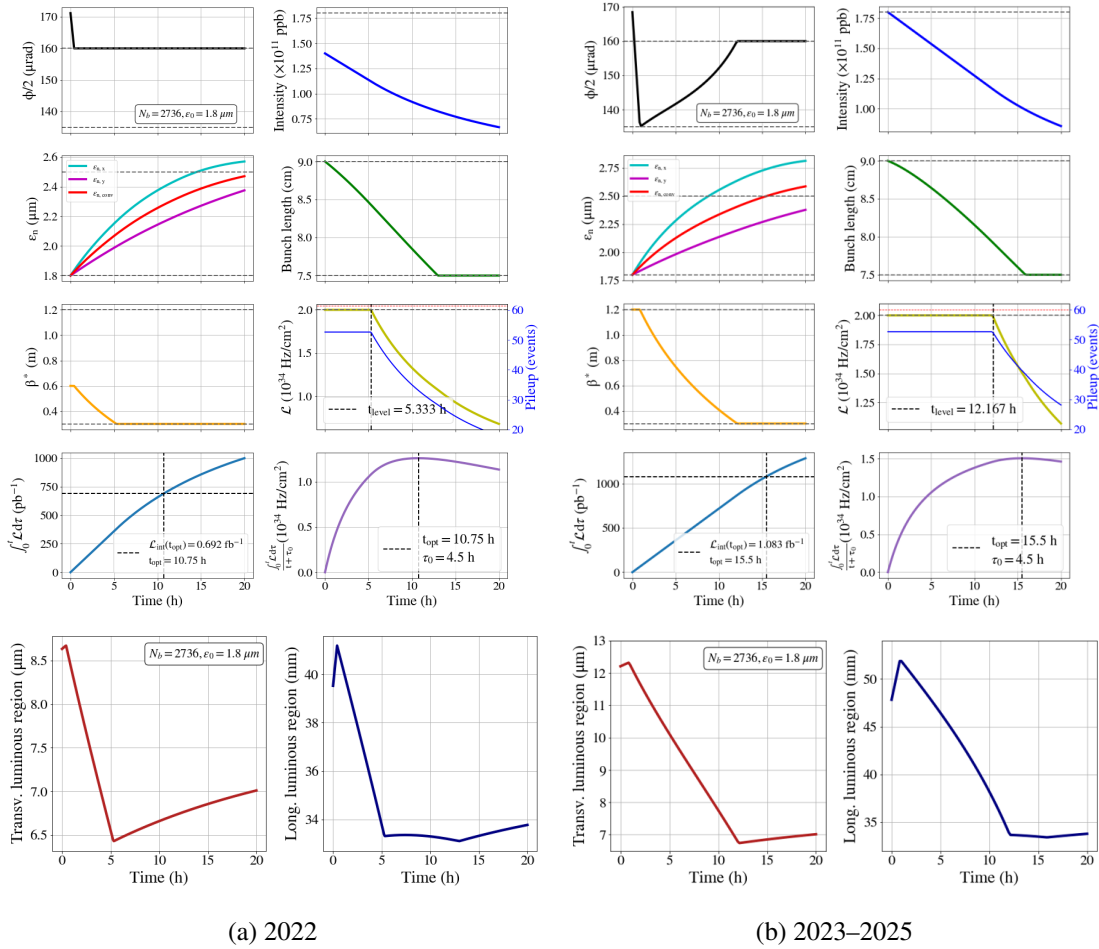


Figure 91. Typical variations of beam and optics parameters in SB at 6.8 TeV in 2022 and as of 2023, together with luminosity, pile-up and integrated luminosity profiles, and evolution of the r.m.s. size of the transverse and longitudinal luminous regions (bottom pictures). Finite β^* steps are neglected in these plots. The luminosity levelling is assumed to be conducted based on the ATLAS peak luminosity which is more penalized than CMS (H crossing) by the horizontal emittance growth due to IBS. The evolution of the longitudinal luminous region contains 4 distinct parts, related to the variations of the loss factor $1/\sqrt{1+\phi_w^2}$ (with ϕ_w denoting the Piwinski angle), first from the crossing angle at constant β^* , then from the β^* -levelling proper, then from the bunch length shrinkage (from SR) at constant optics, and finally from the transverse emittance growth at constant optics and constant bunch length.

bunch length, bunch charge, emittance and luminosity at IP1 and IP5) are plotted in figure 91, together with the evolution of the transverse and longitudinal luminous regions, assuming 2736 collisions and a good emittance preservation in the ramp (i.e. $\epsilon_n = 1.8 \mu\text{m}$ at flat-top energy). The emittance and bunch length variations in SB have been simulated considering IBS and Synchrotron Radiation (SR) effects at 6.8 TeV, and considering an additional empirical transverse emittance growth rate of $0.05 \mu\text{m}/\text{h}$ and $0.1 \mu\text{m}/\text{h}$ in the horizontal and vertical planes, respectively, as observed in Run 2 [176]. It is assumed that continuous longitudinal emittance blow-up by RF phase modulation is applied when the r.m.s. bunch length reaches 7.5 cm to level at this value. If really needed,

Table 17. Performance estimate at 6.8 TeV for 2022, 2023, 2024, and 2025, considering various possible beam parameters in the 2023–2025 period, assuming a turnaround time of 4.5 h, 105 days of p-p run in 2022 and 130 days per year later on, and an effective cross-section of 100 mb. The impact of the finite β^* steps during β^* -levelling (see section 4.5.1) is neglected, degrading at the percent level or less the performance of each year (e.g. corresponding to a reduction of the 2022 and 2023–2025 yearly performance by 0.3–0.4 fb⁻¹ and 1.1–1.2 fb⁻¹, respectively, assuming a β^* step of the order of 5 %, see [179] for more details).

Calendar Year	2022	2023 / 2024 / 2025			
Machine efficiency	20 %	40 %			
Number of OP days	105	130			
Bunch population N_b [10^{11} ppb] at FT	1.4	1.8			
Collisions at IP1 and IP5	2736	2736		2484	
Norm. emittance at FT ϵ_n [μm]	1.8	1.8	2.5	1.8	2.5
Levelling time [h]	5.3	12.1	11.4	10.2	9.3
Optimal fill length [h]	10.7	15.5	15.0	13.7	13.3
Integrated luminosity/year [fb ⁻¹]	32.5	87.2	86.9	86.3	85.8

solutions can be found to cure the small excursion above 50 mm which can be observed in figure 91 at start of SB for the longitudinal luminous region in 2023 onward (e.g. by playing one or a few β^* -levelling steps at constant crossing angle, before reducing it down to the BBLR limit).

The performance estimate per year is reported in table 17, for the various beam configurations of table 16, assuming 130 days of p-p physics per year (only 105 days for 2022), a turnaround time of 4.5 h, a fraction of 20 % and 40 % in SB mode for 2022 and the 2023–2025 period, respectively, and an effective cross section of $\sigma_{\text{eff}} = 100$ mb (for proton burn-off calculation) to be compared with the inelastic cross section $\sigma_{\text{inel}} \sim 85$ mb at 7.0 TeV. As shown in table 17, the integrated luminosity delivered in Run 3 will possibly reach, and could even slightly exceed 290 fb⁻¹, in addition to the 190 fb⁻¹ integrated so far by each of the two ATLAS and CMS experiments. The total (~ 480 fb⁻¹) is well beyond the target initially fixed to 300 fb⁻¹ before triplet exchange, and corresponding to an estimate of the triplet damage dose limit of 30 MGy. In practice, however, this dose is deposited at specific locations and azimuthal angles in the coils of the inner triplet, namely (see figure 92):

- at the entry of Q2A in IR1 with vertical crossing, and at an azimuthal angle 90 or 270 degrees depending on the polarity of the crossing angle,
- and at the exit of Q2B in IR5 with horizontal crossing, inwards in all cases, since the sign of the crossing angle is fixed by the ring geometry in IR5.

De facto, a careful management of the crossing-angle polarity in IR1 becomes a vital ingredient for Run 3, as already proposed and implemented in Run 2 [178]. The present situation and proposal for Run 3 is summarized in table 18. Restarting the machine in 2022 with a negative crossing angle for ATLAS (Beam 1), waiting for 2024 to flip the sign, and eventually inserting a second polarity reversal during the 2025 run (depending on the luminosity integrated till then), will maximize the triplet lifetime in IR1. In this scenario, at the end of 2024 (~ 400 fb⁻¹), the peak doses deposited in the triplets of ATLAS and CMS become very similar [178], estimated to 23 MGy and 24 MGy in the Q2A of IR1 and Q2B of IR5 (at 6.8 TeV), respectively. The crossing-angle polarity reversal inserted

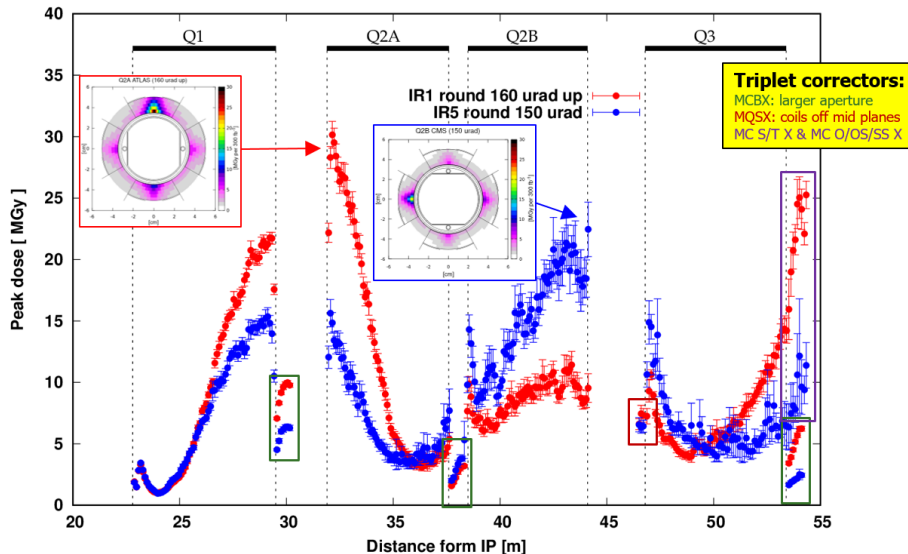


Figure 92. Peak dose deposited in the inner coils of the triplet in IR1 (vertical crossing) and IR5 (horizontal crossing) after 300 fb^{-1} . The most critical magnet is Q2A in IR1 where the peak dose reaches 30 MGy, deposited upwards or downwards depending of the polarity of the crossing angle. These simulations were done for a beam energy of 7.0 TeV. (Courtesy of F. Cerutti, CERN).

Table 18. Integrated luminosity and crossing angle polarity gymnastics in ATLAS to mitigate the peak dose deposited in the inner triplet after $\sim 480 \text{ fb}^{-1}$.

Integrated luminosity [fb^{-1}]	Run 1 + 2	2022 (-)	2023 (-)	2024 (+)	2025 (+/-)	Total
Crossing angle up	115	0	0	86	39	240
Crossing angle down	75	32	86	0	47	240
Total	190	32	86	86	86	480

in the 2025 run should then allow not to exceed the 30 MGy limit in the Q2A magnets hosted in IR1 (with this limit being reached as well for the Q2B magnets of IR5).

Forward physics experiments ATLAS Forward Proton (AFP) and CMS-PPS. As in Run 2, the forward physics experiments AFP [180] and CMS-PPS [177] (hosted in IR1 and IR5, respectively) will keep running in parallel with the ATLAS and CMS physics data taking. These two experiments rely on Roman Pots installed in the matching section between Q5 and Q6. With the large dynamic β^* -range expected in Run 3 (a factor of 2 in 2022, and up to 4 in 2023 onward), the transport matrix from the IP to the RP's would however change drastically in SB if standard optics squeezing techniques were used to vary β^* , i.e. by acting on the IR1 and IR5 matching quadrupole settings, which would add a substantial level of complexity for the detector calibration. This complexity can however be overcome if the β^* -levelling beam process is performed in telescopic mode [31], that is at constant settings in the matching quadrupoles of IR1 and IR5, and by acting on IR8 and IR2, and on IR4 and IR6, in order to modify β^* at IP1 and IP5, respectively.

The choice of the (constant) matching quadrupole settings in IR1 and IR5 during β^* -levelling corresponds to a constant pre-squeezed β^* , namely β_{Pre}^* , while the dynamic variations in SB of the

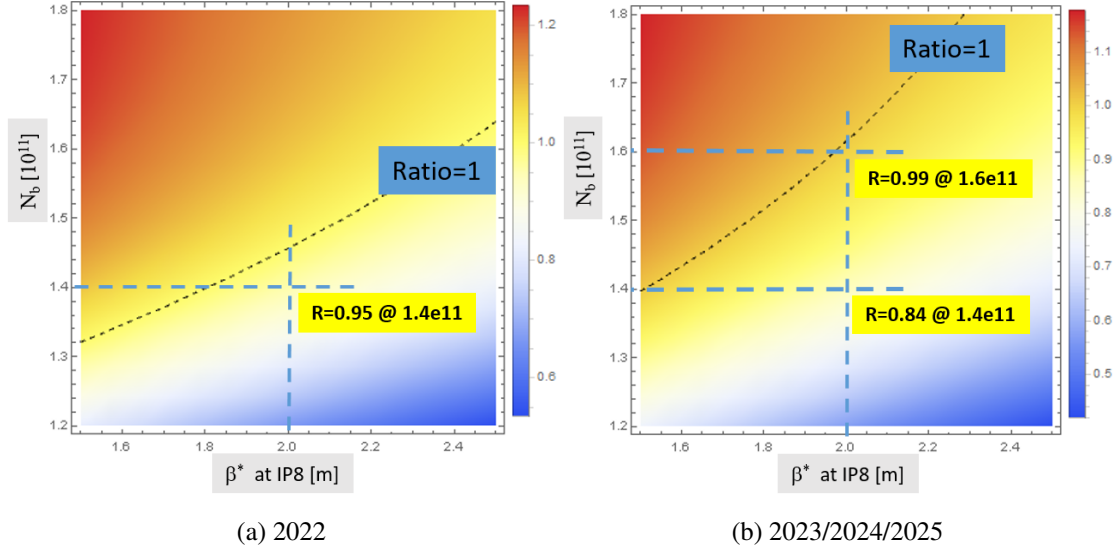


Figure 93. Ratio between LHCb levelling time and optimal fill length for ATLAS and CMS as a function of β^* at IP8 and of the bunch population at start of SB. The LHCb luminosity is assumed to be levelled at $1.5 \times 10^{33} \text{ cm}^{-2}\text{s}^{-1}$ in 2022 (left picture), and set to its Run 3 target value of $2.0 \times 10^{33} \text{ cm}^{-2}\text{s}^{-1}$ for the rest of the run. The beam energy is 6.8 TeV. The assumptions made on the other parameters can be found in the text.

IR2, IR4, IR6 and IR8 quadrupole settings modify the actual of β^* value at IP1 and IP5, as follows:

$$\beta^* \equiv \beta_{\text{Pre}}^* / r_{\text{Tele}}, \quad (4.2)$$

where r_{Tele} is an optics parameter referred to as the so-called telescopic index. The telescopic index, or its inverse $1/r_{\text{Tele}}$, also corresponds to the relative increase of the peak β -function induced by this gymnastics in the four arcs adjacent to IR1 and IR5. In order to minimise this optics perturbation during the telescopic β^* -levelling beam process, the initial collision optics (at start of SB) shall be anti-telescopic ($r_{\text{Tele}} \leq 1$), while the final collision optics shall be telescopic ($r_{\text{Tele}} \geq 1$). Furthermore, the pre-squeezed β^* shall be chosen as the geometric mean of the initial and final β^* values, namely:

$$\beta_{\text{Pre}}^* = \sqrt{\beta_{\text{start}}^* \times \beta_{\text{end}}^*} = 60 \text{ cm for 2023–2025.} \quad (4.3)$$

In order to maximize the synergy in terms of optics between 2022 and the rest of the run, the same pre-squeezed β^* will be chosen for 2022. In order words, the β^* -levelling range in 2022, from 60 cm down to 30 cm will correspond to a telescopic index range from 1 to 2 (compared to 1.6 at 25 cm in 2018 [5]), while the β^* -range in 2023 onward, from 1.2 m down to 30 cm, will be achieved by a change of the telescopic index from 0.5 to 2 in SB.

ALICE. The collision optics parameters for ALICE will not change with respect to Run 2, namely keeping $\beta^* = 10 \text{ m}$ with an external vertical half crossing-angle of $200 \mu\text{rad}$ at IP2, which is deemed to be acceptable for halo collision at an instantaneous luminosity of $6 \times 10^{30} \text{ cm}^{-2}\text{s}^{-1}$ [181] (corresponding to an interaction rate of 0.5 MHz), to be compared to $2.5 \times 10^{30} \text{ cm}^{-2}\text{s}^{-1}$ in Run 2.

LHCb. The LHCb luminosity was stably levelled at $0.4 \times 10^{33} \text{ cm}^{-2}\text{s}^{-1}$ throughout the whole of Run 2 and a good fraction of Run 1, using the parallel separation at IP8. Following the LHCb upgrade phase I which took place in LS2 [182], the LHCb luminosity is planned to be levelled at $2 \times 10^{33} \text{ cm}^{-2}\text{s}^{-1}$ for the production years 2023–2025, but at a somewhat lower value in 2022, which is considered as a commissioning year for the upgraded detector. Taking into account the above performance ramp-up schedule, together with the request that the levelling time at LHCb should be similar or larger than the optimal fill length for ATLAS and CMS, namely

$$\mathcal{R} \equiv \frac{T_{\text{Lev}}^{(\text{LHCb})}}{T_{\text{Opt}}^{(\text{ATLAS,CMS})}} \gtrsim 1, \quad (4.4)$$

a collision β^* of 2 m at IP8 seems to be an appropriate choice over the whole of Run 3 (to be compared with $\beta^* = 10$ m in 2015/2016, and then $\beta^* = 3$ m in 2017–2018). Indeed, in order to justify this choice, a color plot of the \mathcal{R} ratio is shown in figure 93, as a function of β^* and of the bunch population at start of SB, assuming an emittance of $\epsilon_n = 2.5 \mu\text{m}$ at the end of fill, 2736 and 2376 collisions at IP1/5 and IP8 (see table 16), respectively, a turnaround time of 5.0 h, and an effective cross-section of 110 mb⁴. For 2022 (commissioning year for the new detector) shown in figure 93(a), this ratio has been calculated assuming a levelled luminosity of $1.5 \times 10^{33} \text{ cm}^{-2}\text{s}^{-1}$, and a horizontal external half-crossing-angle of 200 μrad , corresponding to an internal half-crossing-angle of 339 μrad at 6.8 TeV for the worst polarity of the LHCb spectrometer. For the rest of the run (see figure 93(b)), the levelled luminosity is set to its target value of $2.0 \times 10^{33} \text{ cm}^{-2}\text{s}^{-1}$, and the external half-crossing-angle of 200 μrad is assumed to be deployed in the vertical plane (see later), corresponding to an internal (tilted) angle of 243.5 μrad at 6.8 TeV, regardless of the polarity of the LHCb spectrometer. As illustrated in figure 93 for $\beta^* = 2$ m at IP8, the \mathcal{R} ratio is expected to be very close to 1 in 2022 ($\mathcal{R} = 0.95$ for $N_b = 1.4 \times 10^{11}$ ppb and a levelled luminosity of $1.5 \times 10^{33} \text{ cm}^{-2}\text{s}^{-1}$), and should comfortably exceed 1 in 2023 onward (for $N_b = 1.8 \times 10^{11}$ ppb) at the target luminosity of $2.0 \times 10^{33} \text{ cm}^{-2}\text{s}^{-1}$.

A second demand from the LHCb experiment in Run 3 is to keep similar physics conditions at the IP, regardless of the spectrometer polarity. When the external crossing angle is horizontal, typically in the range of $\Theta_c/2 = -200 \mu\text{rad}$ (for Beam 1), the internal half-crossing-angle indeed drastically changes by $\pm 139 \mu\text{rad}$ (at 6.8 TeV) depending on the polarity of the spectrometer. In this respect a vertical external crossing angle will be implemented in Run 3, using a dedicated rotation beam process recently designed, which is independent from the LHCb spectrometer polarity, and will be inserted at the EoR, just before the squeeze. The evolution of the crossing bump knobs during this beam process is shown in figure 94, where the EoR internal crossing angle passes from the horizontal plane to a skewed plane [$(p_x^*, p_y^*) = (-200 \pm 139 \mu\text{rad}, 0) \rightarrow (\pm 139 \mu\text{rad}, 200 \mu\text{rad})$ for Beam 1], and the parallel separation, initially in the vertical plane, becomes horizontal at the IP at the end of the beam process. The crossing knob functions during this process are optimized in order to maximize the radial beam-beam separation at the BBLR encounters (with a target of 20σ for the

⁴For the sake of robustness study, in the present purpose, a turnaround time of 5.0 h and an effective cross-section of 110 mb were chosen, because they lead to slightly worse predictions for the \mathcal{R} factor compared to the ones that would be obtained by taking the values of 4.5 h and 100 mb which were used to estimate the ATLAS and CMS performance in table 17.

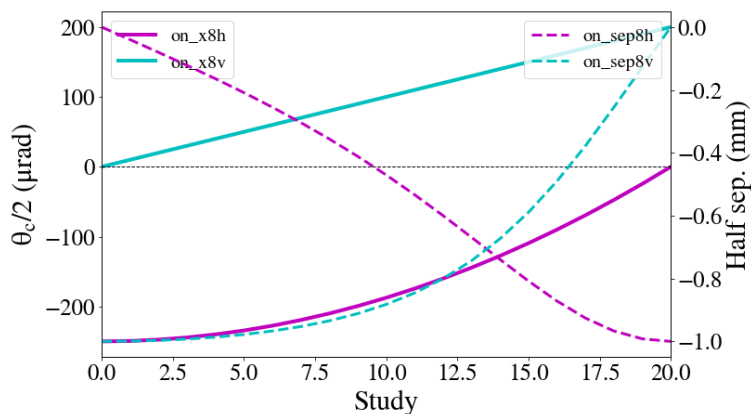


Figure 94. Evolution of the crossing knobs at IP8 to rotate the external crossing angle from the horizontal to the vertical plane. The abscissa monitors the ramp-up of the external vertical crossing angle from 0 to 200 μrad . This beam process is planned to be implemented in 2023 onward, at the end of the ramp, just before the squeeze.

worst separation for either polarity of the LHCb spectrometer). Although this gymnastics is found to be transparent for the dynamic aperture (see later in section 4.4.3), such a beam manipulation has never been run so far at high intensity. Hence, the beam process will only be implemented as of 2023, after having been demonstrated in 2022 in a dedicated machine study program. In the presence of electron cloud, the main concern is indeed a possible lifetime dip during the rotation, when the beams cross at 45° the high electron-density lines facing the magnetic poles of the inner triplet quadrupoles.

Summary. The main collision optics parameters discussed above are summarized in table 19, but keeping in mind all the uncertainties still existing on the beam parameters for Run 3, in terms of management (e.g. heat-load from electron cloud) and preservation (e.g. emittance in the ramp) in the LHC, which may impact the final choice.

4.4.3 Beam physics considerations and LHC hypercycle in Run 3

With the machine configuration defined in collision (see section 4.4.2), and the beam parameter range specified for 2022 and 2023 onward (see table 16), the LHC hypercycle can be designed and correctly calibrated in order not to limit the machine performance over these two consecutive periods, while taking care of maximizing the synergies in terms of optics evolution over Run 3.

Injection optics. The 2017–2018 injection optics will be kept over the whole Run 3, in particular with $\beta^* = 11/10/11/10$ m at IP1/2/5/8, and a half crossing-angle of 170 μrad in the four experimental insertions. Indeed, tracking studies performed at injection show that the dynamic aperture remains quite insensitive to the BBLR effect up to a bunch population of 1.8×10^{11} ppb, even using the pessimistic assumption of a transverse emittance of 2.5 μm (see figure 95). Based on these simulations, the main degradation of the dynamic aperture actually comes from the linear chromaticity and the Landau octupoles (MO), the settings of which are not expected to change at

Table 19. Main optics parameters in collision for the four LHC experiments in Run 3.

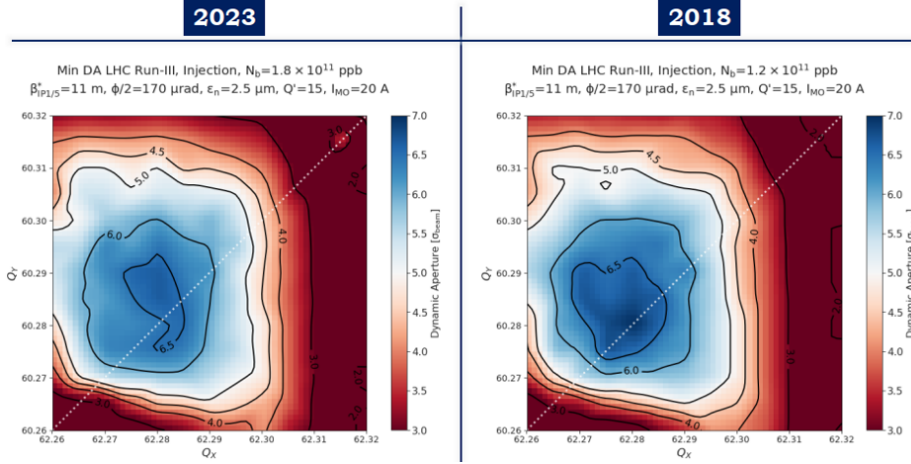
Optics Parameters	2022	2023/2024/2025
ATLAS and CMS		
β^* [m] at the start of collision	0.60	1.20
β^* [m] at the end of levelling	0.30	0.30
Pre-squeezed β^* [m]	0.60	0.60
Telescopic index variations in SB	1.0 \rightarrow 2.0	0.5 \rightarrow 2.0
Half crossing-angle [μ rad] (start of collision)	160	160
Half crossing-angle [μ rad] (start of β^* -levelling)	145	135
Half crossing-angle [μ rad] (end of β^* -levelling)	160	160
ALICE		
β^* [m]	10.0	10.0
Half crossing-angle [μ rad]	200 (V)	200 (V)
LHCb		
β^* [m]	2.0	2.0
Half crossing-angle [μ rad]	200 (H)	200 (V)

injection with respect to Run 2 (within a possible re-scaling with emittance of the MO current in order to work at constant tune spread [183]).

Energy ramp. In order to minimise the turnaround time, most of the optics manipulations should be performed in the ramp, with the aim to arrive at flat-top energy with an optics configuration which is the one, or very close to the one, targeted for the start of SB. In this respect, a so-called combined ramp and squeeze was deployed in Run 2, bringing β^* as low as 1 m at the end of the 2017 and 2018 nominal ramp, compared to $\beta^* = 11$ m at injection and 30 cm at start of SB (see e.g. [5]). With the machine aperture to be revalidated after LS2, such an EoR β^* is however deemed to be too aggressive for 2022. It is therefore proposed to slightly relax the EoR β^* to 1.33 m for 2022. This is possible at a marginal cost for the squeeze duration in 2022, which will take place at flat top energy in order to bring β^* down to the prescribed value of 60 cm at start of SB (see table 19). As of 2023, the idea is then to further push the pre-squeezed β^* down to $\beta_{\text{Pre}}^* = 1$ m at the EoR (as in 2017–2018), but also to deploy in parallel the anti-telescopic squeeze, such as to arrive at flat top energy with a tele-index of $r_{\text{Tele}} = 0.5$ (corresponding to the telescopic conditions at the start of collisions in 2023 onward, see table 19), i.e. leading to $\beta^* \equiv \beta_{\text{Pre}}^*/r_{\text{Tele}} = 2$ m at the EoR. In addition to the beneficial impact on the turnaround time, this combined ramp and telescopic squeeze has the advantage of building up some margin in terms of Landau octupole settings for a bunch population of 1.8×10^{11} ppb (see the expected octupole thresholds in table 20).

Ideally, the 2023–2025 ramp should push β^* down to 1.2 m (see table 19), i.e. $\beta_{\text{Pre}}^* = 60$ cm at a tele-index of $r_{\text{Tele}} = 0.5$, in order to strictly get rid of any optics squeeze period at flat-top energy. On the other hand, the 60 cm pre-squeezed optics is matched with a very low current for the Q6 matching quadrupoles in IR1 and IR5 (~ 200 A at $\beta_{\text{Pre}}^* = 60$ cm, vs. ~ 750 A at $\beta_{\text{Pre}}^* = 1$ m), in order to offer optimal beam conditions to the AFP and CMS-PPS forward physics experiments (with a maximized normalized dispersion at the Roman Pots). With the existing single-quadrant power

Tune Scan @ $I_{MO} = 20$ A



Tune Scan @ $I_{MO} = 40$ A

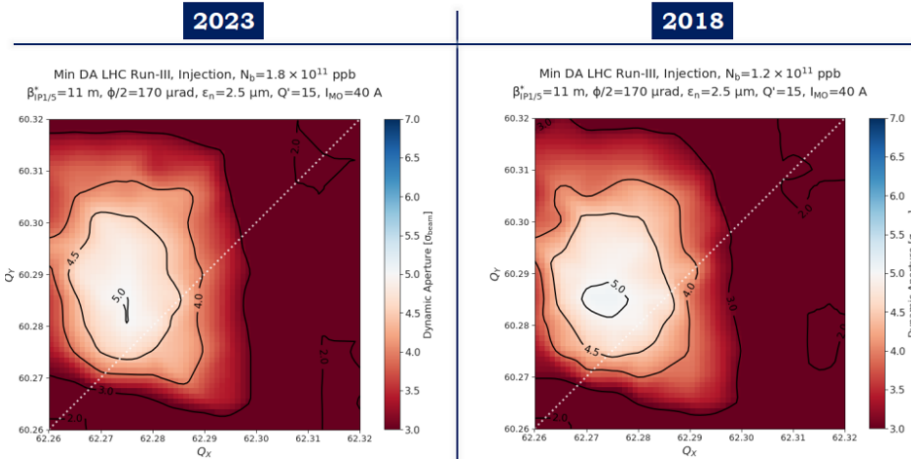


Figure 95. Tune scan at injection using the 2017–2018 LHC injection optics for a bunch population of 1.8×10^{11} ppb (2023) and 1.2×10^{11} ppb (2018), for two possible settings of Landau octupole currents (20 A and 40 A for the top and bottom pictures, respectively), and a linear chromaticity set to $Q' = 15$ units. A transverse normalised emittance of $\epsilon_n = 2.5$ μ m is assumed in both cases. BBLR effects do not seem to have a significant impact on the dynamic aperture at higher bunch population.

supplies feeding the Q6 magnets, such a reduction of the Q6 current only relies on the natural decay time of the circuit, of the order of 2 min. As a result, the ramp would be too short to accommodate this last optics transition, in addition to all the above mentioned optics manipulations, such that a mini-squeeze ($\lesssim 4$ min) cannot be avoided for the 2023–2025 period of Run 3.

The main features of the 2022 and 2023–2025 ramps are summarized below.

- Both for 2022 and 2023–2025, the optics variation starts at an energy of ~ 1.7 TeV, as for the nominal LHC ramp in 2017–2018.
- The pre-squeeze of the optics down to $\beta^* = 2$ m at IP1, IP5 and IP8 is completed at an energy of ~ 4.5 TeV, while keeping a constant β^* of 10 m at IP2, but reducing the normalised strength

Table 20. Expected octupole thresholds [A] at 7 TeV for 1.8×10^{11} ppb for various telescopic index reached at the end of the ramp, for the beam emittance range targeted in Run 3 at flat-top energy, and assuming all MO circuits perfectly working (see [184] for the degradation in case of failure of one or several circuits). The maximum allowed octupole current is 590 A. Run-2-type settings are assumed for the collimators, the new low-impedance collimators installed in LS2 are taken into account in the impedance model, and an empirical factor of 2 is added between strict prediction from the model and expectation, as observed in Run 2 [185]. If the beam energy is not exactly 7 TeV at flat-top for Run 3, these thresholds should be re-scaled by $E^{5/2}$. (Courtesy of N. Mounet, CERN).

Scenario	$r_{\text{Tele}} = 1.0$	$r_{\text{Tele}} = 0.6$	$r_{\text{Tele}} = 0.5$	$r_{\text{Tele}} = 0.4$
$\epsilon_n = 1.8 \mu\text{m}$	550	480	430	360
$\epsilon_n = 2.5 \mu\text{m}$	400	350	310	260

of the IR2 triplets to reach a 7 TeV-equivalent-gradient of 205 T m^{-1} vs. 222 T m^{-1} for the injection optics, which is needed to correctly adjust the phase advances between the injection kicker MKI and the injection protection elements (TDIS and TCLI), and to protect the machine against injection failure at 450 GeV.

- The ramp then continues at constant optics in IR2 and IR8 and IR1 and IR5 are squeezed to 1.33 m in 2022, while, in 2023 onward, the anti-telescope is deployed at constant β^* to reach a telescopic index of $r_{\text{Tele}} = 0.5$ at the end of the ramp, corresponding to a pre-squeezed β^* of $\beta_{\text{Pre}}^* \equiv r_{\text{Tele}} \times \beta^* = 1 \text{ m}$ at IP1 and IP5.

As soon as the optics is changing (as of 1.7 TeV and beyond), the main challenge is to maintain the normalised aperture of the triplet as large as possible during the ramp. Keeping in mind that the telescopic squeeze can only be deployed when the pre-squeezed β^* is of the order of 2 m or below (when appropriate left and right betatron phase advances can be matched in IR1 and IR5 [31]), and that sufficient time should be left for the telescopic gymnastics in the remaining part of the ramp in order to reach a tele-index of 0.5 on arrival at flat-top, the 2 m pre-squeezed optics shall be placed at an energy of 4.5 TeV (or slightly beyond for a ramp compatibility with 6.8 TeV instead of 6.5 TeV at flat-top energy). At this energy, the normalised triplet aperture is minimal, but is shown to be still quite comfortable as of the order of 16σ (see figure 96).

Crossing angle rotation in LHCb. As discussed in section 4.4.2, following dedicated machine studies performed in 2022, a special beam process will be placed right after the end of the ramp in order to rotate the external crossing angle in IR8, from horizontal ($p_x^* = -200 \mu\text{rad}$ at the EoR for Beam 1) to vertical with $p_y^* = 200 \mu\text{rad}$ for Beam 1 (see table 19 for 2023–2025). This gymnastics is found to be transparent for the dynamic aperture for both polarities of the LHCb spectrometer (see figure 97).

Squeeze. As in Run 2, an optics squeeze beam process will follow, at constant telescopic index, and still using the injection tunes $Q_{x,y} = (62.270, 60.295)$, namely:

- from $\beta^* = 1.33 \text{ m}$ down to $\beta^* = 60 \text{ cm}$ at $r_{\text{Tele}} \equiv 1$ in 2022,
- and from $\beta^* = 2 \text{ m}$ down to $\beta^* = 1.2 \text{ m}$ at $r_{\text{Tele}} \equiv 0.5$ in 2023 onward, i.e. $\beta_{\text{Pre}}^* = 1 \text{ m} \rightarrow 60 \text{ cm}$.

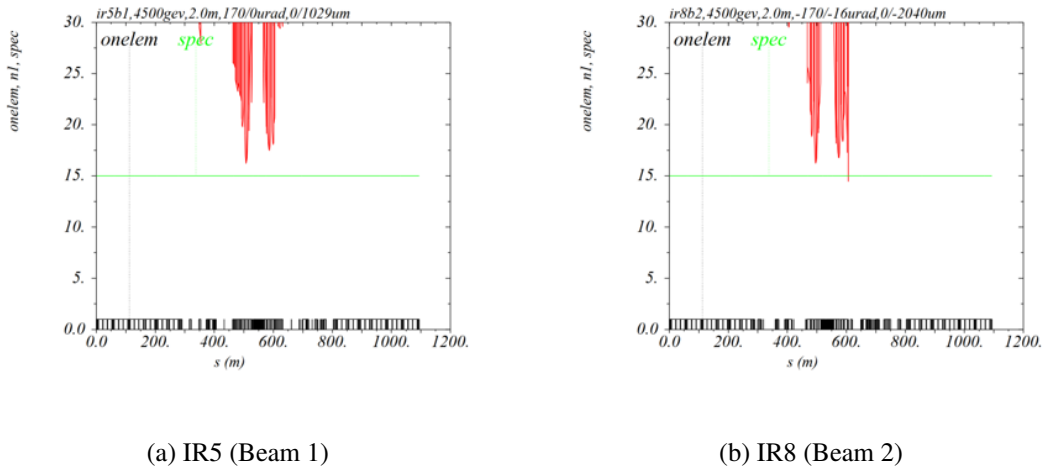


Figure 96. Normalised triplet aperture [σ] in IR1/5 (left) and IR8 (right) at a beam energy 4.5 TeV, with $\beta^* = 2.0$ m and a half crossing-angle of $170 \mu\text{rad}$, and for a reference normalised emittance of $\epsilon_n = 3.5 \mu\text{m}$. The tolerance budget for the closed orbit, β -beating, normalised spurious dispersion and momentum error is assumed to be 2 mm, 21 %, 14 % and 0.86×10^{-3} , respectively (taking the value specified in table 4 of [186], but with a doubled budget for the β -beating). The only slight aperture restriction is found in IR8, for Beam 2 only, in the horizontal plane at the TCDDM (D1 mask): 0.5σ are missing with respect to a target of 15σ , which is deemed to be acceptable.

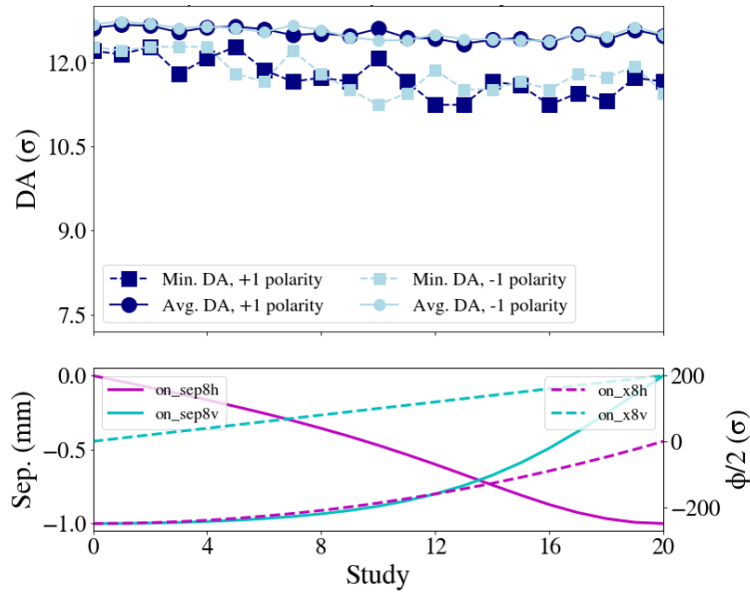


Figure 97. Minimum and average DA (over phase space angle) during the rotation of the external crossing angle in IR8, for both possible polarities of the LHCb spectrometer. This beam process is run at EoR with the injection tune $Q_{x,y} = (62.270, 60.295)$. The beam energy was set to 7.0 TeV for these simulations, assuming a bunch population of 1.8×10^{11} ppb within an emittance of $\epsilon_n = 2.5 \mu\text{m}$ (worst case compared to $\epsilon_n = 1.8 \mu\text{m}$). The abscissa monitors the ramp-up of the external vertical crossing angle from 0 to $200 \mu\text{rad}$.

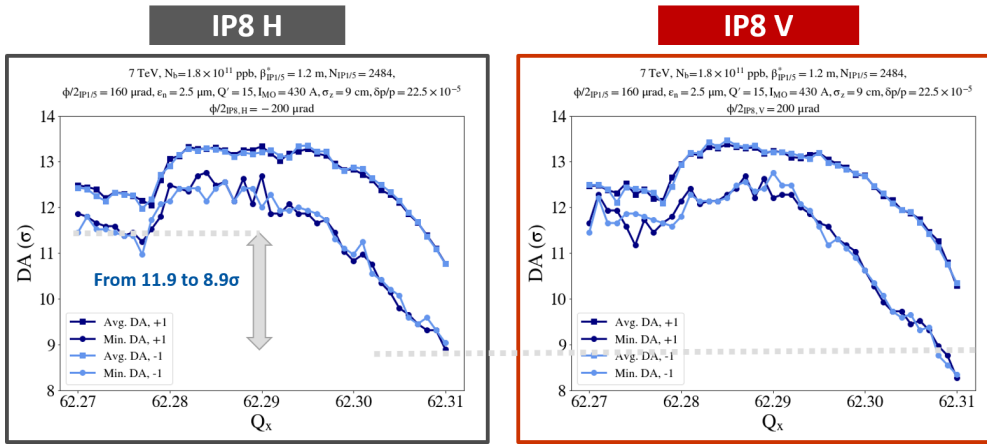


Figure 98. Minimum and average DA (over phase space angle) during the Q-change beam process, for both possible polarities of the LHCb spectrometer, and both possible configurations of the external crossing angle (H or V). This beam process is run after the squeeze to move the working point from the injection tunes $Q_{x,y} = (62.270, 60.295)$ to the collision tunes $Q_{x,y} = (62.310, 60.320)$. The beam energy was set to 7.0 TeV for these simulations, assuming a bunch population of 1.8×10^{11} ppb within an emittance of $\epsilon_n = 2.5 \mu\text{m}$ (worst case compared to $\epsilon_n = 1.8 \mu\text{m}$).

The squeeze duration is estimated to be only 4 min long in 2023 onward, (“mini-squeeze”), and about 2.5 min more in 2022, limited by the decay time of the Q6 current in IR1 and IR5 (see also the previous discussion on the combined ramp and squeeze).

Tune change. The so-called “Q-change”, which brings the working point onto the collision tune $Q_{x,y} = (62.310, 60.320)$, is conducted after the squeeze, just before putting the beam into collision. This strategy, validated during ATS optics machine development sessions (as it also offered more margin for linear coupling), represents a change with respect to Run 2, where this beam process was actually played right after the energy ramp. Indeed, in the absence of head-on beam-beam tune shift, the collision working point was found to be far from optimal for the dynamic aperture in Run 3 (see figure 98).

Adjust. The parallel separation is then completely collapsed to establish head-on collision at IP1 and IP5, and tuned for a given prescribed levelled luminosity at IP2 and IP8. This, so-called adjust, beam process should last about 60 s in Run 3, i.e. twice less than in Run 2, assuming that no or only a small residual IP shift will be requested by the ALICE and CMS experiments (compared to -2 mm in 2017–2018), thanks to the ALICE detector and LSS5 realignment campaigns which took place in LS2. This beam process is combined with an additional fine tuning of the working point which depends on the actual crossing bump configuration in IR8 and, to a marginal extent, on the transverse beam emittance at flat-top energy. At the end of this beam process, and as illustrated in figure 99, the dynamic aperture is still well above 6σ in the case of a horizontal external crossing angle at IP8 (taking $Q_{x,y} = (62.316, 60.321)$ as the best working point at start of SB in this case), while the 6.0σ target is just met in the case of a vertical crossing angle (choosing $Q_{x,y} = (62.313, 60.318)$ for this configuration). The degradation of dynamic aperture in the second case comes from the fact that the best working point for this configuration is shifted closer to the diagonal when the external

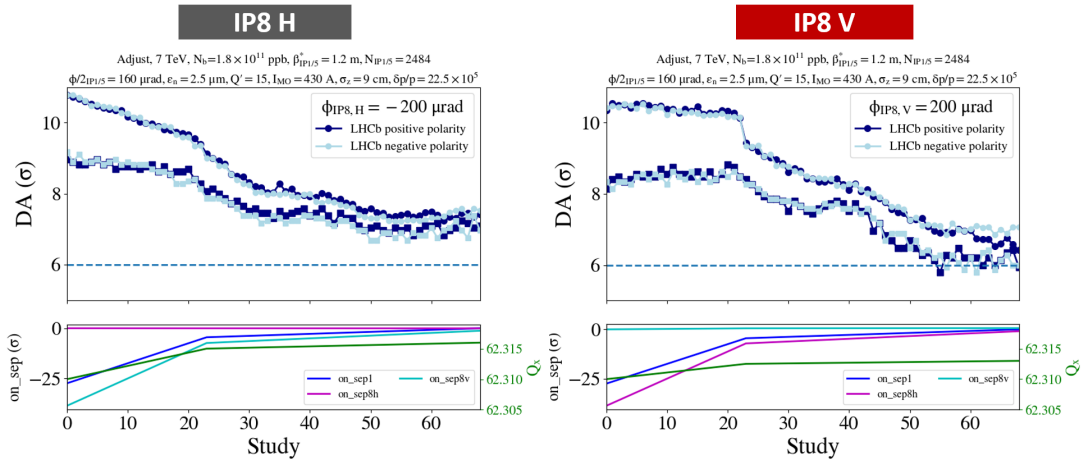


Figure 99. Minimum and average dynamic DA (over phase space angle) during the adjust beam process, where fully head-on collisions are established at IP1 and IP5, while the parallel separation at IP8 and IP2 is tuned for a levelled luminosity of $2 \times 10^{33} \text{ cm}^{-2} \text{ s}^{-1}$ for LHCb, and to $6 \times 10^{30} \text{ cm}^{-2} \text{ s}^{-1}$ for ALICE. Both possible polarities of the LHCb spectrometer, and both possible configurations for the external crossing angle in IR8 (H or V) have been looked at. This beam process is run after the Q-change, and combined with an additional fine-tuning of the working point, depending on the actual configuration of the crossing bumps in IR8 and, marginally, on the beam emittance (see details in the text). The abscissa monitors the ramp-down of the parallel separation at IP1, by step of 1σ for large separation and reduced granularity for small separation, with all the other quantities depending linearly on this parameter. The beam energy was set to 7.0 TeV for these simulations, assuming a bunch population of 1.8×10^{11} ppb within an emittance of $\epsilon_n = 2.5 \mu\text{m}$.

crossing angle is vertical in IR8 (see figure 100). The above degradation can be mitigated by a reduction of the linear coupling whose feasibility remains to be demonstrated [187].

Luminosity levelling. The strategy for luminosity levelling at IP1 and IP5 has been described in section 4.4.2. Due to the large variations of the head-on beam-beam tune shift during β^* -levelling (up to $\Delta Q_{\text{bb}} \sim 0.02$), coming from the proton burn-off, the emittance blow up, and from the bunch length and optics parameter changes in SB (see figure 91), the working point shall also be varied with β^* (see details on figure 101).

As shown in figure 101 at the end of luminosity levelling, i.e. for $\beta^* = 30 \text{ cm}$, the dynamic aperture is in the range of $5\text{--}5.5\sigma$, basically corresponding to the Run 2 situation in terms of beam and optics parameters at start of SB, for which the machine is known to be well-behaved. At start of levelling, the 6σ target is then fully or nearly met (depending on the crossing bump configuration at LHCb). As for the previous beam processes, all the simulations were done keeping quite a lot of margin in terms settings for the linear chromaticity ($Q' = 15$) and octupole settings (430 A, see table 20).

Summary. The sequence of beam processes from injection to collision is summarized in figure 102, both for 2022 and the period 2023–2025. The latest versions of the corresponding LHC optics can be found in [188] and [189], for the 2022 and 2023–2025 proton runs, respectively.

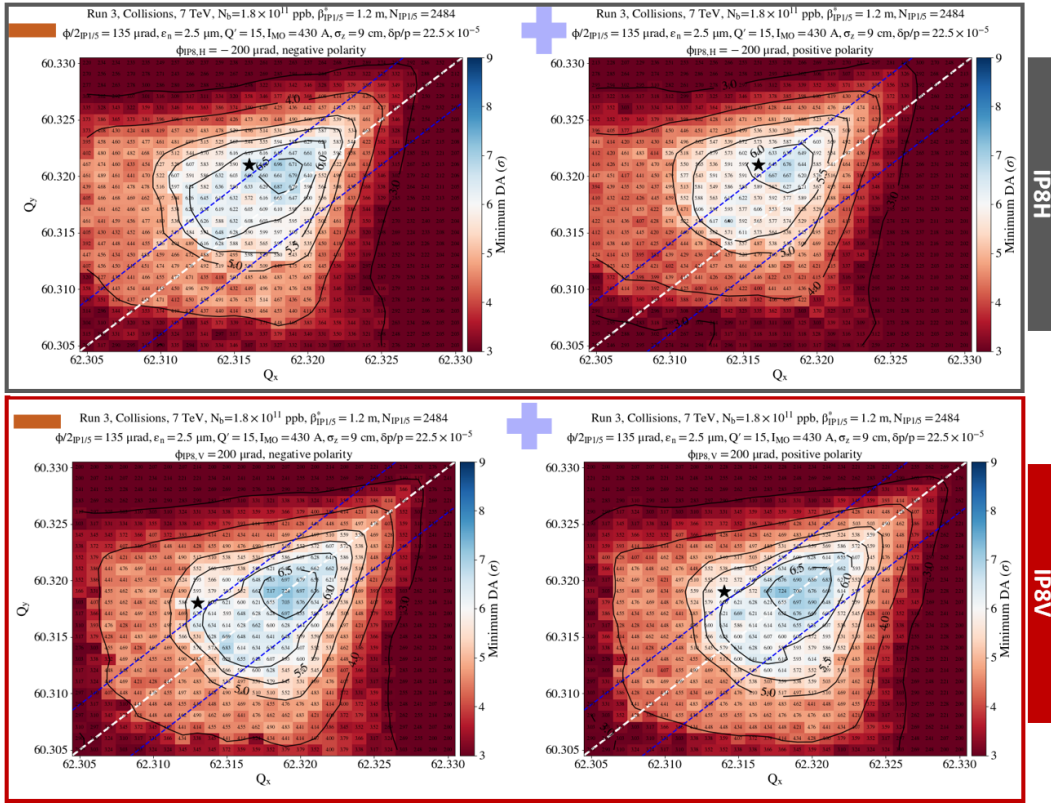


Figure 100. Tune scan (i.e. dynamic aperture versus working point) in collision assuming a horizontal (top) or a vertical (bottom) external crossing angle in IR8, with negative (left) or positive (right) polarity for the LHCb spectrometer. The beam energy was set to 7.0 TeV for these simulations, assuming a bunch population of 1.8×10^{11} ppb within an emittance of $\epsilon_n = 2.5 \mu\text{m}$. The other parameters are specified on the top of each picture. On each picture, the dotted lines indicate a fractional tune split of ± 0.004 ($q_y = q_x \pm 0.004$), and the star symbols correspond to the best working point for the dynamic aperture while imposing a distance of at least 0.005 with respect to the diagonal (where the control of the linear coupling might become challenging). For a vertical external crossing angle, the best DA island is pushed onto the diagonal compared to the other configuration.

4.4.4 Summary and outlook

The completion of the LIU project, one full run in advance with respect to the installation of the HL-LHC, offers a great opportunity to the LHC, both in order to gain experience with high intensity beams, but also to double the luminosity integrated so far by the ATLAS and CMS experiments, while continuing to maximize the beam conditions delivered to the other experiments, including the forward physics experiments. In this context, a beam intensity target of 1.8×10^{11} ppb for p-p runs in 2023 onward (and 1.4×10^{11} ppb for 2022) seems to be appropriate, being of course challenging, but a priori not out of reach, for the existing equipment of the LHC ring which are not planned to be upgraded in Run 3. With this target in mind, the machine configuration can be established and correctly calibrated in order not to be a limitation to the machine performance over the full Run 3. The main ingredients and novelties are

- the full deployment of luminosity levelling with β^* for the ATLAS and CMS experiments, operating at the triplet cryo-cooling capacity limit ($\mathcal{L} \sim 2 \times 10^{34} \text{ cm}^{-2} \text{ s}^{-1}$),

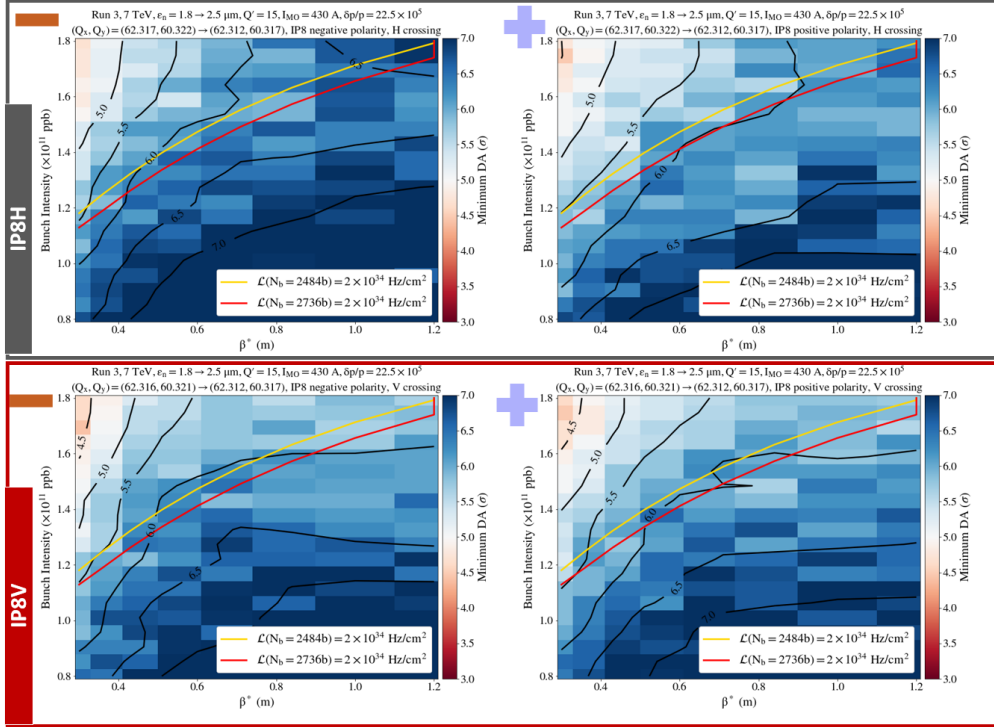


Figure 101. Dynamic aperture as a function of β^* (with the crossing angle adjusted to the BBLR limit defined in figure 90) and of the bunch population, assuming a horizontal (top) or a vertical (bottom) external crossing angle in IR8, with negative (left) or positive (right) polarity of the LHCb spectrometer. The yellow and red contour lines indicate the evolution of the bunch population with β^* , assuming 2484 and 2736 bunches (see table 16), respectively, when levelling at the prescribed luminosity of $2 \times 10^{34} \text{ cm}^{-2} \text{ s}^{-1}$ at IP1 and IP5. The beam energy was set to 7.0 TeV for these simulations, with an emittance varying from $\epsilon_n = 1.8 \mu\text{m}$ at start of levelling ($\beta^* = 1.2 \text{ m}$), up to $\epsilon_n \sim 2.5 \mu\text{m}$ at the end of levelling ($\beta^* = 30 \text{ cm}$) (see 2023–2025 model in figure 91). The best working points determined by tracking at the start and end of levelling (and slightly depending on the LHCb configuration at start of levelling) are interpolated linearly at intermediate β^* keeping a distance of 0.005 with respect to the diagonal (see the details on the top of each picture).

- the exclusive usage of telescopic optics squeezing techniques to vary β^* at IP1 and IP5 (together with the crossing angle in option), over a quite large dynamic range (within a factor of 2 in 2022, and up to a factor of 4 in 2023 onward),
- the deployment of anti-telescopic optics in the ramp as of 2023,
- a careful crossing angle management in IR1 and IR5 in order to maximize the triplet luminosity lifetime, with a total radiation dose deposited in the triplet which is expected in the range of $\sim 25 \text{ MGy}$ at the end of 2024 ($\sim 400 \text{ fb}^{-1}$), and just reaching the 30 MGy limit at the end of 2025 ($\sim 480 \text{ fb}^{-1}$) [178], but provided an additional inversion of the crossing angle polarity in ATLAS during the last year of Run 3.
- dedicated crossing angle gymnastics in IR8 (as of 2023), implemented right after the ramp, in order to rotate the external crossing angle from horizontal to vertical, as requested by the LHCb experiment.

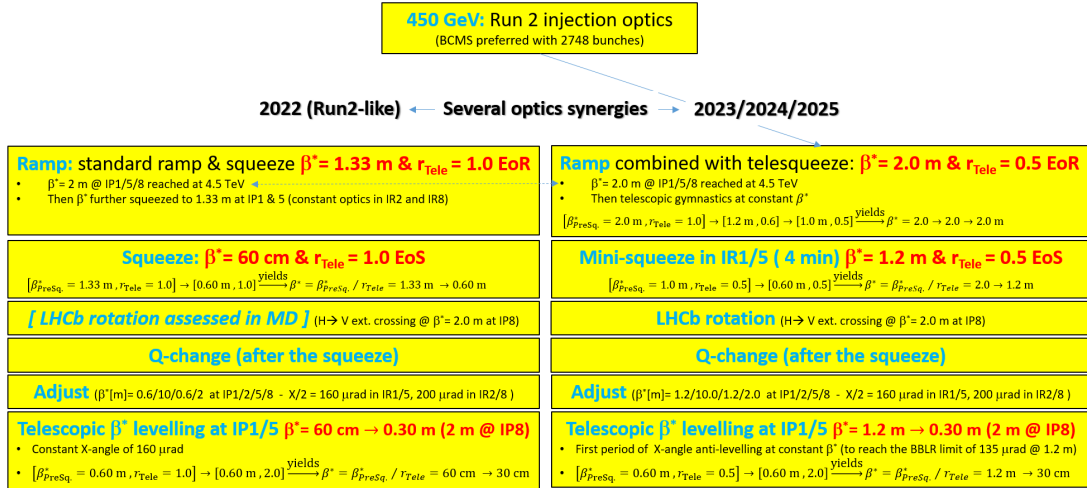


Figure 102. Template for the LHC hypercycle in Run 3, for 2022 (left) and 2023–2025 (right).

Some uncertainties however still remain concerning the compatibility of the 1.8×10^{11} ppb target with the existing beam dump of the LHC (see section 2.3.4). Some challenges are also ahead in order to safely and reliably deploy these techniques in operation at high intensity, in particular the new combined ramp and telescopic squeeze foreseen in 2023 onward (which will deserve dedicated machine studies in 2022), and the above-mentioned telescopic β^* -levelling over a β^* -range of 2 to 4. In this respect, first studies on the optics commissioning strategy already showed that only two collision optics will necessitate an accurate correction in 2022 (at $\beta^* = 60 \text{ cm}$ and 30 cm) for a good control of the β -beating for intermediate optics, and to keep the possible luminosity unbalance between ATLAS and CMS to the percent level during the β^* -levelling process [190]. Experience gained in 2022 will of course be crucial to fine-tune this estimate for the larger β^* -range expected as of 2023, and, in general and if needed, to re-calibrate the overall plan for the rest of Run 3.

4.5 Levelling techniques

Since the beginning of the first LHC run, the luminosity was levelled by separation in the two low-luminosity experiments, ALICE and LHCb. Separation levelling uses 4-corrector orbit bumps around the IPs to introduce a beam separation at the IP, perpendicular to the crossing angle. While the involved orbit bumps are small and operationally easy to control, the separation deteriorates the beam stability due to the loss of Landau damping of the head-on collisions [175, 185], in particular when used in all IPs simultaneously with large levelling factors.

For LHC Run 3, as outlined in section 4.4.2, luminosity levelling by crossing angle and by β^* is a necessity to control the pile-up and to minimize the radiation to the triplets around the high-luminosity experiments, ATLAS and CMS. During LHC Run 2, these two novel levelling techniques were commissioned during machine development campaigns [191, 192] and later introduced in day-to-day operation [193]. In preparation for Run 3, they are further upgraded to allow for levelling by β^* over an extended range, optionally also changing the crossing angle during the β^* squeeze. A schematic overview of the 3 levelling techniques is shown in figure 103.

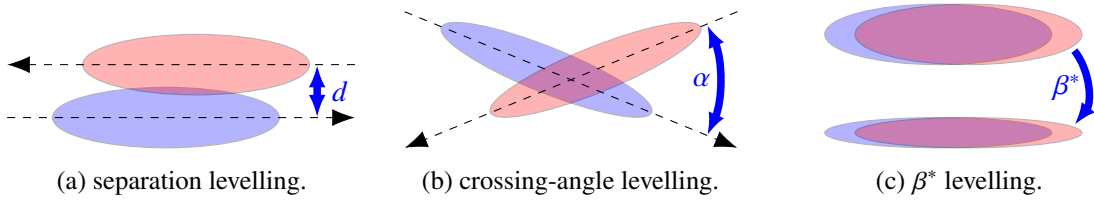


Figure 103. Schematic overview of the luminosity levelling techniques for LHC Run 3.

4.5.1 β^* levelling in IP1 and IP5

Setup. The β^* -levelling for IP1 and IP5 in Run 3 is done in predefined finite steps, with equal β^* in the two IPs. The steps are spaced such that the change in luminosity between steps is within the acceptable tolerance of 5 % for ATLAS and CMS. This requires 10 steps ($\beta^* = 60$ cm to 30 cm) for the initial 2022 operational scenario, and 21 steps ($\beta^* = 1.2$ m to 30 cm) as of 2023 [179] (see 4.4.2).

As for the traditional LHC squeeze, optics are pre-matched for each β^* -levelling step [188, 189]. The pre-matched optics are uploaded to the LHC settings management system (LHC Software Architecture — LSA, [194]) and smooth magnet strength functions linking these *matched points* are generated in a *Beam Process* (BP) in LSA. These pre-generated settings can then be played in steps during the levelling process to transition from one matched optics to the next.

To ensure the protection of the machine and experiment apertures during the levelling, the tertiary collimators (TCTs) around the IPs need to move to account for the change in beam size and orbit. The collimator positions and gaps are guarded by interlock thresholds that define a safe envelope for a given machine configuration [195]. When levelling over a wide range of β^* and crossing angles, as in LHC Run 3, the interlock thresholds also need to change during the levelling. As Machine Critical Settings (MCS) [196] with digital signatures, these functions can not be split once they are generated. Therefore, separate TCT interlock threshold function slices are pre-generated, signed, and stored in LSA for each β^* -levelling step [197].

During the initial machine commissioning, the optics are measured at the matched points and corrections are applied as necessary [190]. Also, collimator positions and limits are established and validated over the full levelling range. All settings and their corrections are stored in the β^* -levelling beam process in LSA.

Levelling logic. The β^* -levelling is controlled by the *LHC Luminosity Server* [198], and can run either in “manual” or in “automatic” mode.

In “manual” mode, the operator in the control room triggers each β^* -squeeze step via a Graphical User Interface (GUI). This mode of operation was used in Run 2 (figure 104), and will be used in Run 3 for commissioning and testing of the system.

For Run 3, an additional “automatic” mode will be introduced. In automatic mode, a luminosity target (e.g. $2 \times 10^{34} \text{ cm}^{-2}\text{s}^{-1}$) and a tolerance (e.g. ± 2.5 %) is programmed. The levelling logic acquires the measured luminosity of ATLAS and CMS, and automatically triggers a β^* step when the average of the two luminosity signals is lower than the tolerance band. During the acquisition period, separation levelling in IP2 and IP8 (section 4.5.2) and continuous luminosity optimization in IP1 and IP5 (section 4.5.3) are allowed to run. Once the acquisition shows that a β^* -levelling step is required, these tasks are paused to avoid interference. They are resumed after the step has been applied.



Figure 104. The operational GUI for β^* -levelling in “manual” mode, as used in Run 2 to reduce the β^* from 30 cm to 25 cm in two steps towards the end of a fill (example from fill #6714). The left part shows the available LSA beam processes and matched optics for β^* -levelling.

β^* Step execution. For a smooth optics transition while keeping the beams in collisions, the magnet Power Converters (PCs), the TCTs and the power converter software interlock system (PCInterlock) need to move in a synchronized, self-consistent manner. Also, the Orbit FeedBack system (OFB) must be used to correct orbit transients during the process. In 2018, the Singular Value Decomposition (SVD) algorithm applied for orbit correction by the OFB proved to effectively suppress orbit transients with a gain setting of 3.0 and 200 eigenvalues per plane (figure 105) [191].

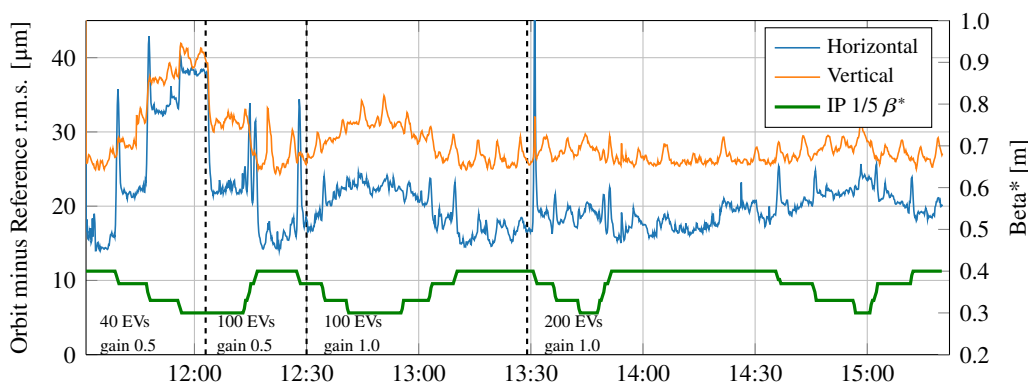


Figure 105. Luminosity and orbit evolution during a β^* -levelling test (MD #2427) for different OFB settings. Orbit transients are suppressed well by the OFB with a gain setting of 1.0 and 200 SVD eigenvalues (EV). During 2018 operation, the gain was gradually increased to 3.0 to further reduce the transients, mainly in the horizontal plane.

The traditional way to play the LHC squeeze using pre-programmed sequences requires a static management of all machine settings (in particular any orbit corrections and closed orbit bumps), which makes it unsuitable for use in physics conditions with colliding beams and frequently changing corrections, e.g. from luminosity optimization or separation levelling.

Therefore the Luminosity Server uses novel mechanics for executing β^* -levelling steps. It reads the required settings from the β^* -levelling beam process, and orchestrates all involved equipment during the transition by performing the following steps:

1. Prepare the settings for the transition:
 - Find the matched point in the used BP corresponding to the actual machine configuration.
 - Slice the settings in the BP to extract the segments between the actual and the target matched point.⁵ Orbit, tune and chromaticity functions are treated as relative corrections to the actual settings in the machine, while the start points of the lattice quadrupole functions are required to match the actual machine settings [191].
 - Find and extract the pre-generated TCT interlock limit function slices corresponding to the β^* -levelling step, and their digital signatures.
2. Calculate the expected orbit response resulting from the change of magnet strengths and optics during the levelling step.
3. Update the active OFB reference to provide a starting point which includes all local orbit bumps currently present in the machine (e.g. from separation levelling in IP2 and IP8). This step is important as during the transition, the OFB will do an aggressive orbit correction that would suppress any bumps not included in the reference. There are two alternative approaches to achieve this:
 - (a) Get all orbit bumps introduced or changed since the active feedback reference orbit was established. Build an updated reference orbit including these changes and send it to the OFB.
 - (b) Acquire the orbit reading and use it as a new OFB reference.

Both options are available in the software and will be tested during the commissioning.
4. Arm the orbit feedback system for the transition with:
 - the reference orbit evolution from the calculated orbit response (step 2),
 - a gain function to run at increased feedback gain during the transition, and restore it to the value for stable conditions at the end,
 - the orbit response matrix evolution to account for the optics change, and to run a correction with an increased number of eigenvalues during the transition.
5. Arm the TCTs for the transition with:
 - the jaw positions from the calculated orbit response (step 2) and the programmed gap functions (step 1),
 - the interlock limits from the pre-signed function segments prepared in step 1.
6. Arm the magnet power converters with the function slices calculated in step 1.

⁵In Run 3 physics operation, only steps from one matched point to the next will be made. However, the software is more flexible, allowing to move between any two matched points of a BP, including skipping intermediate points, and going backwards (de-squeeze). This extra flexibility is used for commissioning and machine development.

7. Update the active optics information in LSA to make sure LSA and all other LHC applications are aware of the change of optics.
8. Create an event table in the LHC timing system to trigger the OFB changes, the TCTs movement and interlock limit changes, the power converters and PCInterlock reference changes synchronously, and to update the optics information distributed via the timing system once a new matched point is reached.
9. Start the timing table and wait for the power converters to reach their new currents. Since all systems involved are moved synchronously, they will reach their targets at the same time.

If any of the above steps fails or the new settings would violate any operational limits, the transition is cancelled and all changes are reverted. The error is propagated to the β^* -levelling logic that initiated the step, which will stop any further steps and report the error to the operator.

4.5.2 Separation levelling in IP2 and IP8

Separation levelling has been used for IP2 and IP8 throughout LHC Run 1 and 2 [198–200], using local 4-corrector orbit bumps around the IPs to introduce a beam separation in the “separation plane”, perpendicular to the crossing angle. This allows to control the luminosity at each IP fully independently.

The LHC Luminosity Server implements a feedback loop based on the luminosity measurement of the experiment concerned. The experiments can request their individual target luminosity and levelling step size online. The levelling task on the LHC side ensures that the values are within safe limits for the machine, and applies the requested step once the luminosity measurement is outside of the target band (figure 106).

To avoid exceeding the target luminosity significantly at the start of collisions, an initial beam separation in IP2 and IP8 is established during the commissioning. This effectively prevents the separation bumps that are present throughout the cycle before collisions from fully collapsing, keeping the initial luminosity below the target.

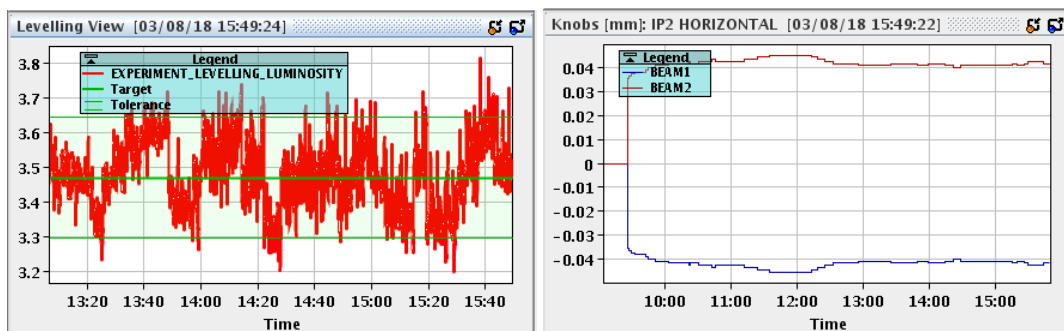


Figure 106. Separation levelling in IP2 during fill #7017. Left: measured luminosity and target band from ALICE. Right: orbit bumps applied in the separation plane.

4.5.3 Luminosity optimization

Due to the small transverse beam sizes at the IPs ($\sigma \approx 9 \mu\text{m}$ at $\beta^* = 30 \text{ cm}$), luminosity is strongly affected by orbit drifts. After the collapse of the separation bumps, and regularly over the course of a fill, the positions of the beams at the IPs need to be optimized to ensure head-on collisions.

In IP1 and IP5, both transverse planes are optimized. In IP2 and IP8, optimization is limited to the crossing plane, while the separation plane is used for luminosity levelling (section 4.5.2).

On-demand optimization. Throughout Run 2, the optimization was triggered manually by the operator. The optimization task scans the separation at an IP (in one or both transverse planes) to maximize the luminosity signal from the experiment [198]. Multiple IPs can be scanned in parallel. After all peaks are found, the results are displayed to the operator for confirmation before they are applied.

This on-demand optimization will continue to be used for Run 3, in particular for the initial optimization at the start of collisions, but also for periodic checks of the optimization by the operator.

Continuous optimization. To correct the orbit drifts observed at IP1 and IP5 in the first hours of collisions more promptly, and to minimize interference with automatic β^* -levelling, a novel continuous optimization logic was implemented for Run 3.

This “optimization autopilot” continuously applies small orbit bump steps ($0.05\text{--}0.1\sigma$) in one of the transverse planes. After each step, it acquires the luminosity over a long integration time (30–60 s) to minimize the statistical errors, then compares the acquisition to the previous step. If a reduction in luminosity is observed, the step is reverted, the scanning direction is changed until an optimum is found, then the optimization continues in the other transverse plane.

In simulations, this simple algorithm was effective to counteract drifts in one or both transverse planes over several hours, with a typical oscillation of $\sim 0.2\sigma$ around the optimum position (figure 107).

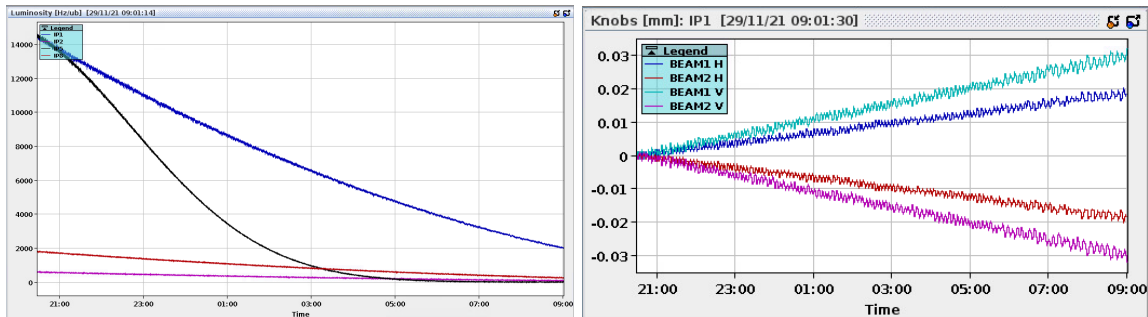


Figure 107. Continuous optimization in simulation mode. In addition to the intensity decay, a separation drift of $3 \mu\text{m h}^{-1}$ in horizontal $5 \mu\text{m h}^{-1}$ in vertical was simulated. The continuous optimization was running on IP1, while IP5 was left uncorrected. Left: luminosity evolution. Right: orbit bumps applied in IP1.

4.6 Beam beam long range compensation

One of the main limitations of LHC and HL-LHC beam lifetime in collision are BBLR interactions occurring around the IPs, where the two beams come closer to each other and share the same vacuum chamber. Following past conceptual and simulation studies [201–205] and in order to

prove experimentally the mitigation of the BBLR effect, four BBLR wire compensators embedded in tertiary collimators have been installed in the LHC, on Beam 2 only. After the first clear demonstration of such a compensation during the LHC Run 2 [206–208], two of the four wire demonstrators have been moved from Beam 2 to Beam 1 in order to fully exploit the potential of the compensators, during operation in Run 3 (see section 3.1.7).

As wire demonstrators are embedded in both jaws of tertiary collimators, the transverse beam-wire distance and thereby the effect is constrained. By connecting the two wires of both jaws in series, the “octupole-like” effect of the wire is doubled, as for all even multipoles, while the others are cancelled. This allows an appreciable compensation effect even if the physical transverse distance from the beam is relatively large. During LHC Run 3, the wires are planned initially to be powered at the end of each fill, after the foreseen β^* -levelling (β^* of 30 cm) with wire collimators opened at 8.5σ (see section 3.1).

The linear tune shifts induced by the wires can reach $\approx 10^{-2}$ and should be locally compensated, in order to avoid also any induced β -beating. During the LHC Run 2 this feed-forward system was using the Q4 and Q5 nearby quadrupoles. During the LHC Run 3, using the two Q4 quadrupoles, located on each side of the IP is considered. Since the phase advance between the two is about π , the β -beating induced by the correction is limited and confined to the region between the two Q4 magnets. As an example, the impact of this compensation in terms of tune and chromatic effects as function of wire current is presented in figure 108, for Beam 1. Both tunes and chromaticities are within acceptable limits, i.e. $\approx 10^{-4}$ and below 1 unit, respectively.

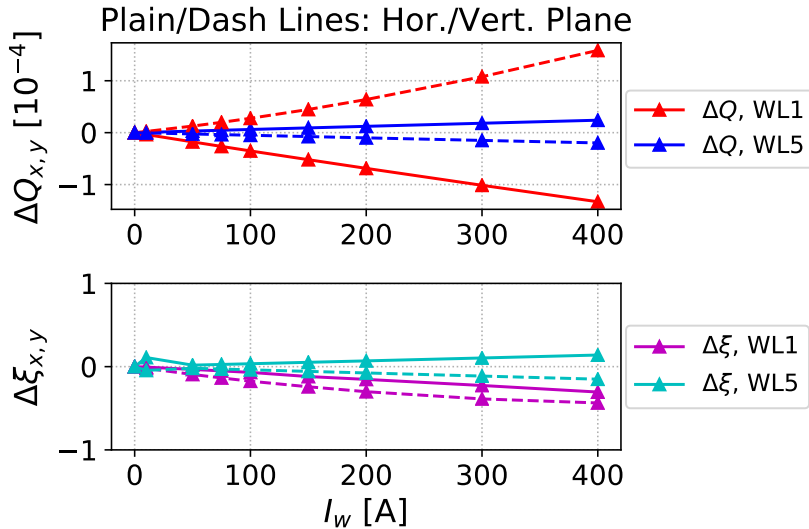


Figure 108. Tune feed-forward for the wire compensators during the LHC Run 3 (Beam 1). The notation “WL n ” corresponds to “Wire Left”, followed by the IP number.

During the nominal operation of the LHC, the transverse beam-wire distance is set by the collimator openings, as defined by machine protection considerations. The physical beam-wire distances for Beam 1 (Beam 2 being symmetric) are reported in table 21 for the two considered collimator openings, with 8.5σ being the nominal and 7.5σ , a tighter setting which could be used and validated during machine studies.

Table 21. Transverse distances between the wires center and the beam center, as a function of the collimators opening ($\beta^* = 30$ cm).

Collimator opening [σ]	Wire L1 (Vert.)	Wire L5 (Hor.)
7.5	8.39 mm	11.15 mm
8.5	9.1 mm	12.23 mm

The impact of different wire and machine parameters on the average DA is presented in figure 109. The simulations reproduce an end-of-fill configuration, at the end of β^* -levelling, with $\beta^* = 30$ cm and a crossing angle of $158 \mu\text{rad}$. The bunch population is set to 1.1×10^{11} ppb, and the nominal octupole current is set to $+350$ A (unless varied).

Figure 109(a) shows the dependency of the average DA on the wire currents. An improvement of about 0.4σ is observed, in particular in the case of the wires in IR1 since the ones in IR5 are further away from the beam (see table 21). For I_{w1} set to 350 A and I_{w5} set to 300 A or 50 A the DA improvement is maximized, where I_{w1} and I_{w5} are the currents of the wires L1 and L5 acting on Beam 1, respectively.

The nominal tunes of the LHC at collision are $Q_x = 62.31$ and $Q_y = 60.32$, but it has been shown that the DA can be improved by moving the tunes away from this nominal working point [209]. The impact of the wire compensators as a function of the working point (Q_x , Q_y) is studied in figure 109(b). In this respect, the DA variation is presented between a configuration with the wires powered ($I_{w1} = 350$ A and $I_{w5} = 300$ A, upper right triangle) and a configuration without them (lower left triangle), as a function of the horizontal and vertical tunes. The wires improve the DA mostly in between the nominal working point (green asterisk) and the diagonal. This creates a larger working point area to accommodate additional non-linear effects such as a bunch-by-bunch parameters spread due to beam-beam interactions or electron cloud effects.

The octupoles powered at $+350$ A, ensure sufficient tune spread so that the beams remain stable, even when separated (no Head-On collision). However, it has been shown experimentally that with the ATS optics and high tele-indexes, strong negative octupoles can also mitigate the BBLR interactions effects, while ensuring beam stability [210]. Figure 109(c) shows the average DA dependency on the wire currents (assumed to be equal in IR1 and IR5) and the octupole currents. Taking into consideration the contributions of the BBLR interactions, the octupoles and the wires, it is possible to overlap the DA scan with the iso-detuning lines corresponding to the direct and cross terms of the linear detuning with amplitude (green, red and blue lines of the plot) [211, 212]. A negative polarity of the octupoles current can contribute to the mitigation of the BBLR interactions. The configurations where the octupole-like detuning vanishes (in particular the vertical one) seem to improve DA. For instance, a gain of 0.7σ is observed for the wires powered with 175 A and the octupole current set to -300 A.

Figure 110(a) shows the DA dependency on the crossing angle and the bunch population, without the use of the wire compensators. For a bunch population of 1.1×10^{11} ppb, a crossing angle of $158 \mu\text{rad}$ is the limit for which the DA remains above 5σ . However, the luminosity levelling goal of $2 \times 10^{34} \text{ cm}^{-2}\text{s}^{-1}$ stands far from this limit (the iso-luminosity line is computed assuming 2736 collisions in IP1 and IP5). The wires could improve the machine performance reach by allowing smaller crossing angles for the same bunch population.

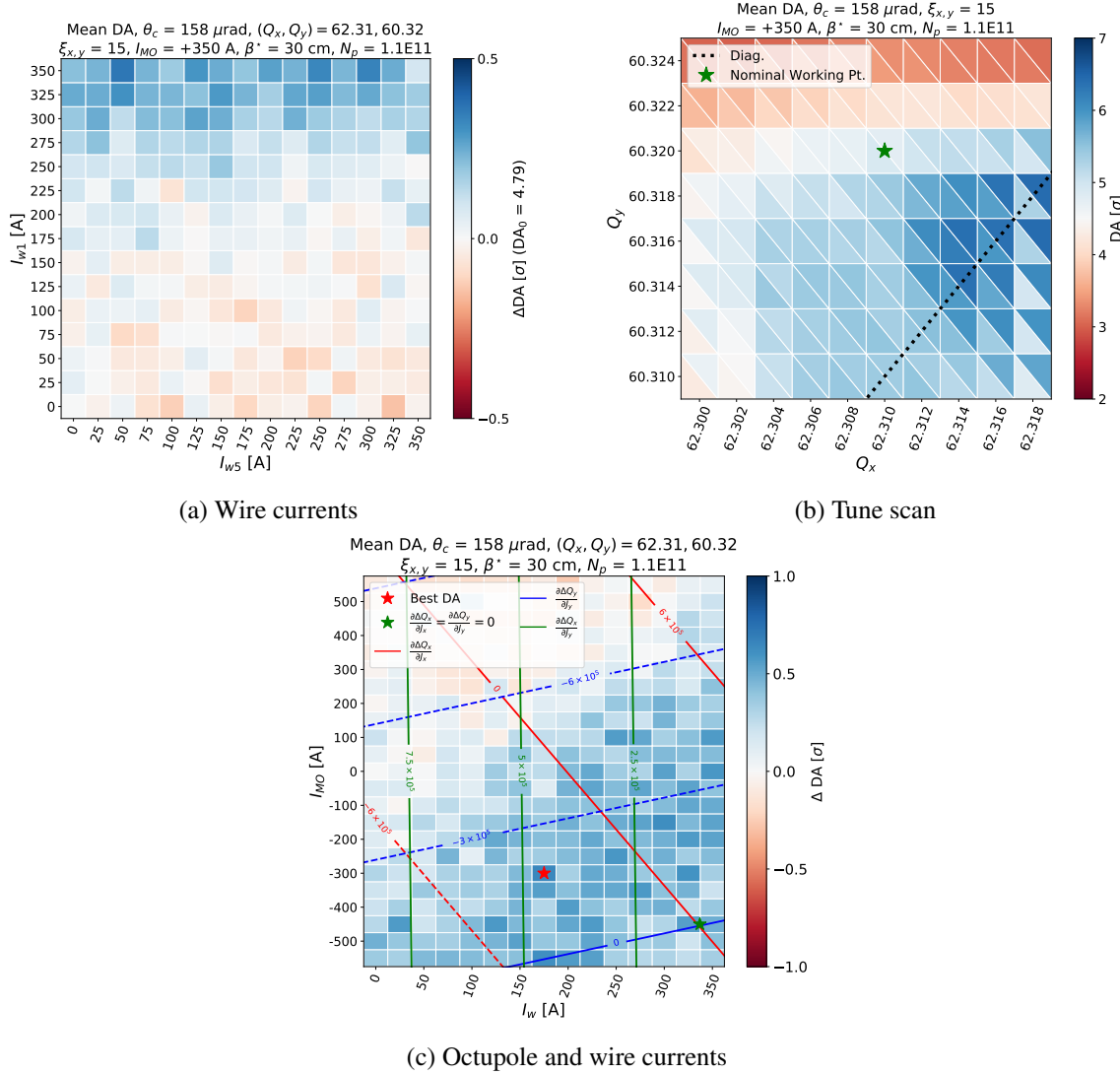


Figure 109. Average DA variation as a function of (a) wire current, (b) the horizontal and vertical tunes, and (c) octupole and wire currents for the nominal collimator settings of 8.5σ .

Figure 110(b) shows the same DA study, with the wires in IR1 and IR5 powered at 350 and 300 A, respectively and the octupoles set at +350 A, as in the nominal configuration. One can observe that the wires could allow for a reduction of crossing angle of about 5 to 10 μrad after the β^* -levelling. As expected, the luminosity gain would be marginal. However, the main objective of the systematic powering of the compensator is to gain experience in operating such devices during luminosity production.

Considering a smaller gap in the wire collimators (from 8.5 to 7.5 σ , see table 21), and by a global optimization of the wire currents and the octupole settings, the best DA configuration (absolute gain of about 1σ) can be found by powering the wires in IR1 with 125 A and the wires in IR5 with 200 A. Figure 110(c) then shows the DA dependency on the bunch population and the crossing angle, using this configuration. In that case, and for a bunch population of 1.1×10^{11} ppb, it is possible to further reduce the crossing angle down to 145 μrad , keeping the DA around 5σ . In operation, one

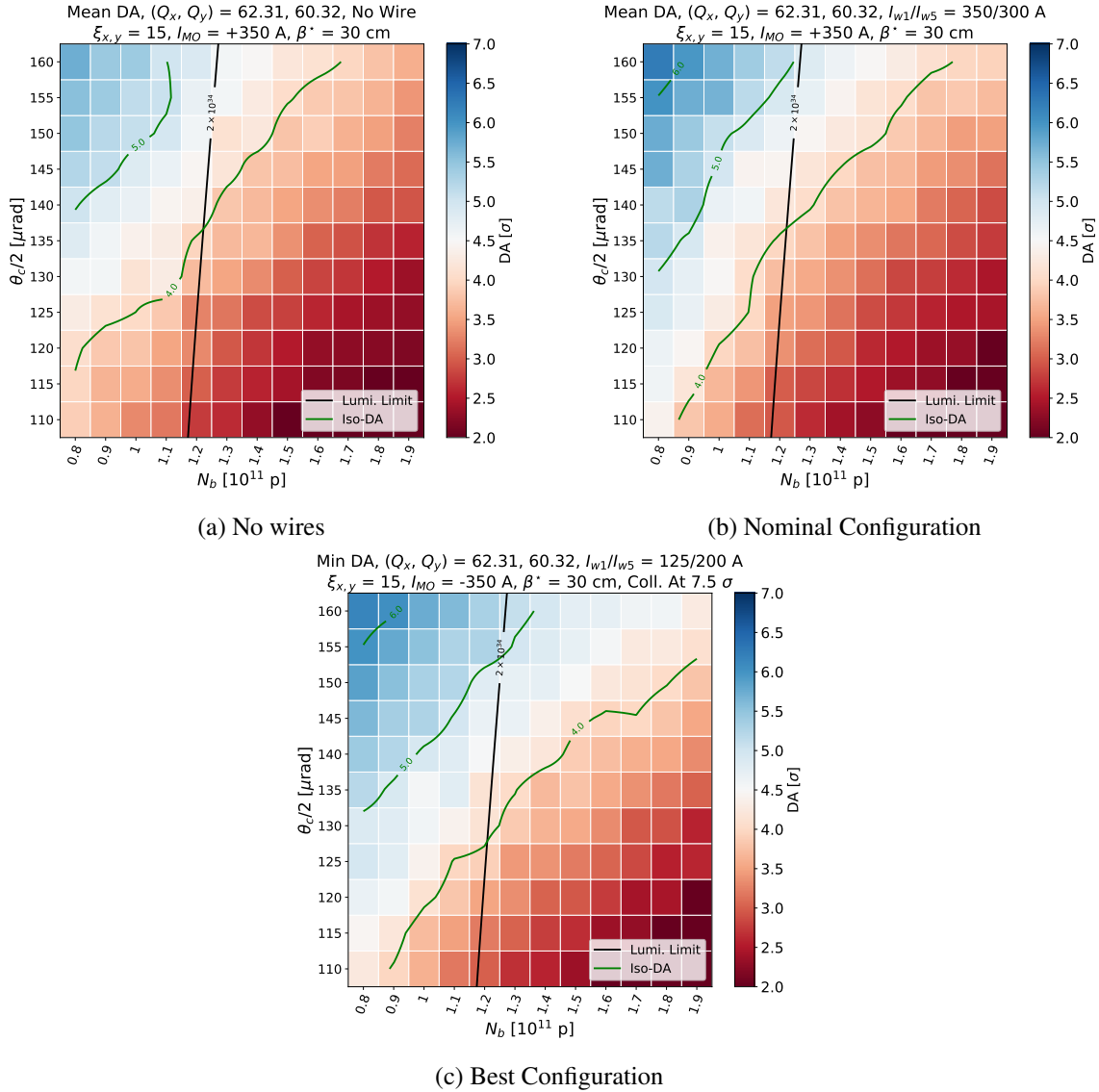


Figure 110. Average DA as a function of the bunch population and the crossing angle. The luminosity is computed assuming 2736 colliding bunches, an energy of 7 TeV, normalized emittances of $3.5 \mu\text{m}$ and a bunch length of 7.5 cm.

could then consider operating a crossing angle anti-levelling, keeping the instantaneous luminosity constant for an additional couple of hours. This could lead to an increase of the integrated luminosity by about 2% over the year.

4.7 LHC configuration and operational scenario for Run 3: ions

This section presents the plans for LHC heavy-ion operation in Run 3, summarizing the results presented in [213, 214] with an update of the beam energy. We give first a brief history and background to the heavy-ion programme, after which we discuss the expected future beam parameters, machine configuration, and performance.

4.7.1 LHC heavy-ion operation

Apart from the main physics programme with proton collisions, the LHC has been designed to collide also heavy ions. The heavy-ion operation was implemented very successfully in Run 1 [215] and Run 2 [216–218] (see also section 1), with typical operational periods of about one month per year. So far four Pb-Pb runs have been performed (in 2010, 2011, 2015, and 2018), and over time all the LHC experiments (ALICE, CMS, ATLAS, LHCb and, occasionally, LHCf) have requested heavy-ion collisions. A total integrated luminosity of about 1.5 nb^{-1} has been collected at ALICE, specialized in heavy-ion collisions, thus exceeding the LHC design target of 1 nb^{-1} target. About 2.5 nb^{-1} was delivered to the general-purpose experiments ATLAS and CMS, since they could run at higher luminosity [219]. The ALICE luminosity had to be levelled at $1 \times 10^{27} \text{ cm}^{-2}\text{s}^{-1}$ in order not to saturate the detector. LHCb, which was the last experiment to request heavy-ion collisions, collected about 0.25 nb^{-1} in Run 2.

Furthermore, a new operational mode with proton-Pb collisions has been put into operation [220–223]. An initial one-day pilot run took place in 2012, which was followed by one-month p-Pb physics runs in 2013 and 2016. ATLAS and CMS collected about 220 nb^{-1} of integrated luminosity, while ALICE collected 75 nb^{-1} .

It is planned to continue the heavy-ion programme in Run 3 and Run 4, typically with annual one-month runs with Pb-Pb or p-Pb operation. The overall physics goals of the Run 3–4 heavy-ion programme were given initially in [224] and later refined in [225]. The requests include a total of 13 nb^{-1} of integrated Pb-Pb luminosity at ALICE, ATLAS, and CMS, as well as 2 nb^{-1} at LHCb. For p-Pb, the goals are to collect 1200 nb^{-1} at ATLAS and CMS, and 600 nb^{-1} at ALICE and LHCb. These goals are very ambitious compared to the luminosity collected so far, and several upgrades have been implemented in LS2. No further upgrades for ions are foreseen for LS3, meaning that the expected performance in Run 3 and Run 4 is similar.

4.7.2 Beam parameters

Several upgrades and improvements for Pb operation have been performed in the LHC injector chain within the LIU project [8], resulting already in significantly increased Pb beam intensity in past runs. The only remaining upgrade for Run 3 is the momentum slip-stacking in the SPS [8], which relies on a new low-level RF system installed in LS2 (see section 4.2.4). The slip-stacking interleaves bunch trains through RF manipulations, which halves the bunch spacing of affected bunch trains with a 100 ns bunch spacing. This results in an increase in the number of bunches injected in the LHC from 733, as in 2018 using a 75 ns bunch spacing, to 1240 bunches spaced by 50 ns in Run 3 [213, 214]. The predicted beam parameters at injection and collision are shown in table 22, together with the 2018 parameters and the LHC design. The 75 ns scheme used in 2018 remains available as a backup, in case of, e.g., delays in the commissioning of the slip-stacking.

Based on the 50 ns beam structure, a number of filling patterns have been developed [213], with different distributions of collisions between the experiments. Typically a larger number of collisions at LHCb come at the expense of fewer collisions at the other experiments, due to the small displacement of the LHCb interaction point by 15 RF buckets (i.e. 37.5 ns) away from the symmetry point at $7/8^{\text{th}}$ of the LHC ring. Therefore, to achieve collisions at LHCb, trains with 50 ns beams must be displaced longitudinally away from a perfect quadrant symmetry, reducing the

Table 22. Pb beam parameters at injection and at top energy at the start of collision, from the LHC design report [2], as achieved in 2018 [218, 219], and as foreseen for Run 3 and HL-LHC [226]. The injection parameters quoted for 2018 are directly at injection, before any blowup on the flat bottom, where no reliable measurements of the transverse emittance with 75 ns beams are available.

	LHC design	2018	Run 3/HL-LHC
Total # of bunches	592	733	1240
Bunch spacing [ns]	100	75	50
# of bunches per injection	54	42	56
Beam energy at injection [Z TeV]	0.45	0.45	0.45
Beam energy at collision [Z TeV]	7	6.37	6.8/7
Ion bunch population at injection [10^7 ppb]	7	23	19
Ion bunch population at collision [10^7 ppb]	7	21	18
Normalized transverse emittance at injection [μm]	1.4	n.a.	1.5
Normalized transverse emittance at collision [μm]	1.50	2.33	1.65

number of collisions at the other experiments, which are all placed at symmetry points of the LHC circumference. As a side note, this is not constraining proton operation, where 25 ns beams are used. A final baseline filling pattern has not yet been selected among the proposed ones.

We assume the same Pb beam parameters (shown in table 22) for p-Pb operation and that the proton beam has a 50 ns bunch spacing, as the Pb beam, and normalized emittances around $2.5 \mu\text{m}$ as for p-p operation. The proton intensities are *chosen* to be about 3×10^{10} protons per bunch. Higher proton intensities would accelerate the degradation of the Pb beam as a result of the fast luminosity burn-off at the unlevelled experiments, ATLAS and CMS, while the resulting short beam lifetime and fill duration would be unfavourable for the levelled experiment ALICE. An alternative running scenario is being investigated, with larger proton bunch populations, and also ATLAS and CMS levelled, which could potentially provide more luminosity to all experiments.

4.7.3 LHC machine configuration

The optics used for heavy-ion operation, different from what is used for protons, includes $\beta^* = 0.5$ m at ALICE, ATLAS, and CMS, and $\beta^* = 1.5$ m at LHCb. The gain from squeezing to very small β^* is smaller with heavy ions than with protons, since the burn-off is anyway very fast due to the high total cross section of 515 b [214]. Nevertheless, some gain could be realized with smaller β^* , and the feasibility will be investigated in the future.

The net crossing-angle at the IPs has contributions from both the so-called external crossing-angle bump, which should ensure sufficient separation at the parasitic beam-beam encounters, and the spectrometer compensation bumps present at ALICE and LHCb. We assume an external half crossing-angle of $\pm 170 \mu\text{rad}$ at all IPs, which, after accounting for the spectrometer bumps, gives net crossing-angles of $100 \mu\text{rad}$ and $-305 \mu\text{rad}$ at ALICE and LHCb respectively.⁶ We assume the same optics and crossing-angles for p-Pb as for Pb-Pb.

For simplicity, it is assumed that luminosity levelling is done dynamically varying the parallel beam separation at the IP, as opposed to the β^* -levelling used for protons. The luminosity needs to be

⁶ALICE will operate with both spectrometer polarities, while LHCb will only operate with one polarity.

levelled at about $6.4 \times 10^{27} \text{ cm}^{-2}\text{s}^{-1}$ at ALICE, in order not to saturate the detector [224, 227–229]. This is an improvement by more than a factor 6 compared to previous runs, thanks to an upgraded detector. We assume the same levelling target at ATLAS and CMS, although these experiments could potentially accept a higher luminosity. At LHCb, we assume levelling at $1 \times 10^{27} \text{ cm}^{-2}\text{s}^{-1}$ to avoid quenches from BFPP, as explained in section 3.1.4. The 281 b BFPP cross-section accounts for more than half of the total one (cross sections for the most relevant processes are listed in [214]), and for a luminosity of $6.4 \times 10^{27} \text{ cm}^{-2}\text{s}^{-1}$ the power of the secondary BFPP beam is about 165 W. The induced heat is high enough to quench the impacted magnets at a luminosity around $2.3 \times 10^{27} \text{ cm}^{-2}\text{s}^{-1}$, as shown experimentally downstream of CMS in 2015 [65]. At ALICE, ATLAS, and CMS, these losses are mitigated for the luminosities considered for Run 3 and Run 4 through orbit bumps, or a combination of orbit bumps and new collimators (see details in section 3.1.4). At LHCb, orbit bumps alone are not enough and no collimator installation is presently foreseen, implying that the luminosity must be levelled at a lower value.

The collimation of the ion beam halo is another potential performance limitation. A multi-stage collimation system is installed in the LHC [2, 33, 35, 37], which should clean the unavoidable halo, localise losses, provide passive machine protection [43, 195], and reduce experimental backgrounds [40, 41]. However, the collimation system is about two orders of magnitude less efficient with heavy-ion beams than with protons [66, 67], and it has been shown experimentally that large ion beam losses risk to quench the magnets in the DS downstream of the collimators [230]. Therefore, an upgrade was needed in order to cope with the higher beam intensity in Run 3–4. Otherwise, there would be a significant risk of quenching magnets, or prematurely dumping the beam, in case of any large halo losses. The upgrade, discussed in detail in section 3.1.5 and 3.1.6, relied initially on the installation of new collimators in the DS. To make space for them, shorter and stronger magnets (11 T dipoles) were foreseen. However, this installation was postponed due to performance issues of the new magnets. Instead, a backup solution will be used in Run 3, relying on a novel collimation technique using bent crystals acting as primary collimators and channeling the beam halo onto a standard secondary collimator used as absorber. This promises a significant gain in cleaning efficiency.

4.7.4 Predicted performance

In this section, we show the estimated performance in future Pb-Pb and p-Pb operation using the beam and machine configuration discussed in previous sections. We simulate a typical fill in terms of the inter-linked time evolution of the intensities and emittances, as well as the resulting luminosity, under the influence of a number of beam physics processes (most importantly burn-off from luminosity, IBS and radiation damping). Two different simulation codes are used: Collider Time Evolution (CTE) [214, 231], which tracks macro-particles, and the Multi-Bunch Simulation (MBS) [214, 232], which is based on a set of coupled differential equations for bunch populations and beam phase space moments.

Figure 111 shows the simulated evolution from CTE of key parameters during a typical future Pb-Pb fill for the range of filling patterns detailed in [213]. Various 50 ns schemes are included, for which we assume the predicted beam parameters from the injectors in table 22, as well as the backup 75 ns scheme for which we assume the achieved 2018 beam parameters. A total burn-off cross-section of 515 b is assumed [214], as well as a 100 h non-collisional beam lifetime as observed in 2018 [213].

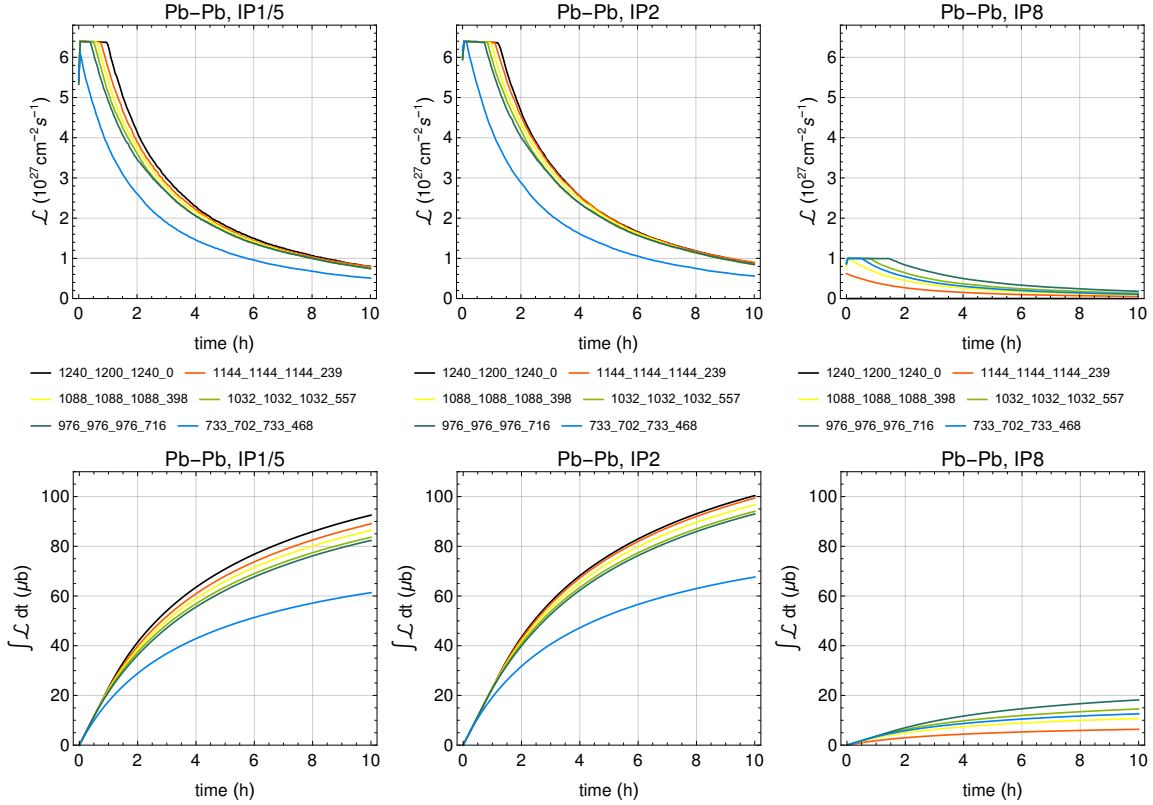


Figure 111. The simulated instantaneous luminosity (top) and integrated luminosity (bottom) in a typical future Pb-Pb fill from CTE at 6.8Z TeV, for the different filling patterns from [213]. The naming indicates the total number of bunches (b) followed by the number of collisions at ATLAS/CMS, ALICE, and LHCb, respectively.

As can be seen, the luminosity levelling time at ATLAS, ALICE, and CMS is up to about 1.5 h, with ALICE having a slightly longer levelling time because of its smaller crossing-angle. At LHCb, with a lower luminosity due to fewer collisions, and larger β^* and crossing-angle, not all of the filling patterns require levelling. Here the integrated luminosity improves dramatically for the filling patterns with more collisions at IP8, at the expense of a small reduction for the other experiments.

Based on the simulated evolution in a single fill, we estimate the total integrated luminosity in a typical one-month run, in which we assume that 24 days are available for data-taking after the initial commissioning. We first calculate the so-called optimum fill time $T_{f,\text{opt}}$, i.e. the time after which the beam should be dumped in order to maximize the time-averaged luminosity \mathcal{L}_{avg} , as in [214]. We assume a turnaround time between fills of 200 min [229]. We can then estimate the integrated luminosity \mathcal{L}_{int} in a one-month run as

$$\mathcal{L}_{\text{int}} = \mathcal{L}_{\text{avg}}(T_{f,\text{opt}}) \times T_{\text{run}} \times \eta, \quad (4.5)$$

where T_{run} is the total time allocated to the physics run and η is the so-called operational efficiency, accounting for downtime and unavailability of the machine, premature fill aborts, occasional longer turnaround times and, most importantly, the performance ramp-up to the ideal during the few weeks of the run. As for HL-LHC proton operation [233], we assume conservatively $\eta = 0.5$. Higher

values of η , as achieved in the 2015 heavy-ion run and as assumed in some calculations for injector upgrades [234], would result in proportionally higher integrated luminosity.

Table 23 shows the calculated one-month integrated luminosity for each experiment and filling pattern. The filling pattern naming is defined with a convention indicating the total number of bunches (b) followed by the number of collisions at ATLAS/CMS, ALICE, and LHCb, respectively. Results are shown based on both simulation codes: the numbers without brackets are based on CTE, while the numbers in square brackets are based on MBS. It can be seen that the two simulation codes agree very well, although they are based on fundamentally different models. This strengthens our confidence in the results.

At ALICE, ATLAS and CMS, \mathcal{L}_{int} varies in the range 2.1–2.8 nb⁻¹ for the 50 ns schemes, while 20–30% lower values are found for the 75 ns backup scheme (last row in table 23). At LHCb, \mathcal{L}_{int} is strongly dependent on the filling pattern, going up to a maximum of about 0.5 nb⁻¹. These values for a single one-month run are close to, or even exceed, the total data collected during the first 10 years of LHC operation with heavy ions (see sections 1 and 4.7.1). Some 50 ns filling patterns have higher luminosity at all experiments than the 75 ns backup, so a 50 ns scheme is preferred, if available. It should be noted that these projections could be on the conservative side, e.g. if the operational efficiency or injected bunch population would be higher. A smaller β^* , smaller crossing-angles, or modified filling schemes could be other ways to increase the integrated luminosity.

Table 23. Projected integrated luminosity (in nb⁻¹) [214] during a one-month Pb-Pb run at each experiment for the filling schemes from [213] at 6.8 Z TeV. The values in square brackets are based on MBS simulations, while the values without are based on CTE.

Filling scheme	\mathcal{L}_{int} IP1/5	\mathcal{L}_{int} IP2	\mathcal{L}_{int} IP8
1240b_1240_1200_0	2.5 [2.6]	2.7 [2.8]	0 [0]
1240b_1144_1144_239	2.4 [2.4]	2.6 [2.7]	0.17 [0.21]
1240b_1088_1088_398	2.3 [2.3]	2.6 [2.6]	0.29 [0.33]
1240b_1032_1032_557	2.2 [2.2]	2.5 [2.5]	0.38 [0.43]
1240b_976_976_716	2.2 [2.1]	2.4 [2.5]	0.46 [0.50]
733b_733_702_468	1.7 [1.8]	1.9 [1.9]	0.34 [0.36]

Similar studies for p-Pb operation have been performed, assuming a similar Pb beam as for Pb-Pb and 50 ns proton beam with 3×10^{10} ppb, for which new filling schemes have been matched. A slightly higher performance could be reached by colliding the 50 ns Pb beam with a 25 ns proton beam, although the feasibility of this remains to be studied. The luminosity at ALICE is levelled at 5×10^{29} cm⁻²s⁻¹ to avoid detector saturation, while the other experiments are not levelled. Therefore, the predicted \mathcal{L}_{int} in a one-month run at ALICE is around 320 nb⁻¹, while the projections show values in the range of 470–630 nb⁻¹ for ATLAS and CMS, and up to 170 nb⁻¹ at LHCb. The projected data in a one-month run typically surpass significantly the total data collected so far in LHC p-Pb operation. A potential performance improvement under study to further increase the collected data is to significantly increase the proton intensity and use nominal proton beams.

Acknowledgments

This paper is certainly an incomplete summary of the dedicated effort of all the teams involved in the activities that took place in the LHC and its Injectors during LS2 and in the definition of the Run 3 operational scenarios. We are indebted to their commitment and contributions.

A Acronyms

a-C	amorphous Carbon
AFP	ATLAS Forward Proton
ALARA	As Low As Reasonably Achievable
ATS	Achromatic Telescopic Squeeze
BBLR	Beam-Beam Long Range
BCMS	Bunch Compression Merging and Splitting
BETS	Beam Energy Tracking System
BFPP	Bound-Free Pair Production
BIS	Beam Interlock System
BLM	Beam Loss Monitor
BP	Beam Process
BPM	Beam Position Monitor
CF	Con-Flat
CFC	Carbon Fiber Composite
CMS-PPS	CMS-Precision Proton Spectrometer
c.o.m.	centre of mass
CTE	Collider Time Evolution
D1	separation Dipole
D2	Recombination dipole
DA	Dynamic Aperture
DISMAC	Diode Insulation and Superconducting MAgnets Consolidation
DOF	Degree Of Freedom
DS	Dispersion Suppressor
EoR	End of Ramp
ECT	End-Cap Toroid
EFB	Earth Fault Burner
EMD	Electro-Magnetic Dissociation
EPDM	Ethylene Propylene Diene Monomer
EYETS	Extended Year End Technical Stop
GUI	Graphical User Interface
hBN	hexagonal Boron Nitride
HEL	Hollow Electron Lens
HL-LHC	High Luminosity – Large Hadron Collider
HO	Head-On

HOM	High Order Mode
HWC	Hardware Commissioning
IBS	Intra-Beam Scattering
IP	Interaction Point
IR	Insertion Region
IT	Inner Triplet
JFC	Forward Cylindrical Shielding
JTT	ATLAS Toroidal Tube Shielding
LEIR	Low Energy Ion Ring
LHC	Large Hadron Collider
LIU	LHC Injectors Upgrade
LLRF	Low Level Radio Frequency (system)
LS	Long Shutdown
LSA	LHC Software Architecture
LSS	Long Straight Section
LVDT	Linear Variable Differential Transformer
MB	Main Dipole cold mass
MBS	Multi-Bunch Simulation
MCS	Machine Critical settings
MDI	Machine-Detector Interface
MKDV	SPS Beam Dump Kicker
MKI	Magnet Kicker Injection — LHC Injection Kicker
MKP-L	SPS Injection Kicker Long (module)
MO	LHC Landau Octupoles
MoGr	Molybdenum Carbide-Graphite
MQ	Lattice Quadrupole in the arc
NEG	Non-Evaporable Getter
OFB	Orbit Feedback System
PC	Power converter
PIM	Plug-In Module
PM	Post Mortem
ppb	protons per bunch or particles per bunch
PS	Proton Synchrotron
PSB	Proton Synchrotron Booster
PU	Pile-up — inelastic events occurring in the same bunch crossing
QA	Quality Assurance
QC	Quality Control
QD	Defocussing Quadrupole
QF	Focussing Quadrupole
QSRA	Surface 4.5 K Refrigeration Cold Box
QURA	Underground 4.5 K Refrigeration Cold Box
QXL	Cryogenic Distribution Line
RB	Main Dipole Circuit

RF	Radio-Frequency
RP	Roman Pot
SB	Stable Beams — Machine mode for experiment data taking
SEY	Secondary Electron Yield
SEM	Scanning Electron Microscopy
SMACC	Superconducting Magnets and Circuits Consolidation
SMP	Safe Machine Parameter
SPS	Super Proton Synchrotron
SR	Synchrotron Radiation
SSS	Short Straight Section
SVD	Singular Value Decomposition
TAN	Target Absorber Neutrals (for neutral particles leaving the IP)
TANB	Target Absorber Neutral for IR8
TAS	Target Absorber Secondaries (for particles leaving the IP at large angles)
TAXN	New HL-LHC Target Absorber Neutrals
TAXS	New HL-LHC Target Absorber Secondaries
TCAP	Target Collimator Absorber Passive
TCAPM	Target Collimator Absorber Passive Mask
TCDDM	Target Collimator Dipole D1 Mask — protection mask for the D1 separation dipole
TCDQ	Target Collimator Dump Quadrupole — movable one-sided collimator positioned upstream of superconducting quadrupole Q4 in IR6
TCDS	Target Collimator Dump Septum — fixed diluter block protecting the beam dump septum
TCL	Target Collimator for physics debris
TCLA	Target Collimator Long Absorber
TCLD	Target Collimator Dispersion Suppressor
TCLI	Target Collimator Long Injection — Injection Protection Collimator
TCP	Target Collimator Primary
TCPC	Target Collimator Primary — Crystal, Crystal Collimator
TCPPM	Target Collimator Primary, with BPM pick-up (P), low-impedance (M)
TCS	Target Collimator Secondary
TCSG	Target Collimator Secondary, carbon-fibre composite jaw
TCSPM	Target Collimator Secondary, with BPM pick-up (P), low-impedance (M)
TCTP	Target Collimator Tertiary, with BPM pick-up (P)
TCTW	Target Collimator Tertiary, with Wire
TDE	Target Dump External
TDI	Target Dump Injection — LHC Injection dump
TDIS	New LHC Injection Dump
TED	Target Extraction Dump
TI2	SPS to LHC Transfer Line (clockwise rotating beam)
TI8	SPS to LHC Transfer Line (anti-clockwise rotating beam)
UFO	Unidentified Flying Object

UHV	Ultra-High Vacuum
VAX	Vacuum Assembly for eXperimental areas
VT	ATLAS Vacuum Toroidal chamber
VUV	Vacuum-Ultra-Violet
WRL	Warm Recovery Line
XPS	X-ray Photo-electron Spectroscopy
YETS	Year-End Technical Stop
ZDC	Zero Degrees Calorimeter

References

- [1] Ph. Bryant and L. Evans, eds., *LHC Machine*, 2008 *JINST* **3** S08001.
- [2] O.S. Brüning, P. Collier, P. Lebrun, S. Myers, R. Ostojic, J. Poole et al., *LHC Design Report Vol.1: The LHC Main Ring*, Tech. Rep. CERN-2004-003-V1, CERN, Geneva (2004) [[DOI:10.5170/CERN-2004-003-V-1](https://doi.org/10.5170/CERN-2004-003-V-1)].
- [3] R. Alemany-Fernandez et al., *Operation and Configuration of the LHC in Run 1*, Tech. Rep. [CERN-ACC-NOTE-2013-0041](https://arxiv.org/abs/1307.6545), CERN, Geneva (2013).
- [4] F. Lackner et al., *Consolidation of the 13-kA Superconducting Magnet Circuits of the LHC at CERN*, *IEEE Trans. Appl. Supercond.* **25** (2015) 4802305.
- [5] J. Wenninger, *Operation and Configuration of the LHC in Run 2*, Tech. Rep. [CERN-ACC-NOTE-2019-0007](https://arxiv.org/abs/1907.0007) CERN, Geneva (2019).
- [6] R. Bruce et al., *Review of LHC Run 2 Machine Configurations*, <https://cds.cern.ch/record/2750415>, CERN, Geneva (2019).
- [7] H. Damerou et al., *LHC Injectors Upgrade, Technical Design Report*, Tech. Rep. [CERN-ACC-2014-0337](https://arxiv.org/abs/1407.6545) CERN, Geneva (2014) [[DOI:10.17181/CERN.7NHR.6HGC](https://doi.org/10.17181/CERN.7NHR.6HGC)].
- [8] J. Coupard et al., *LHC Injectors Upgrade, Technical Design Report*, Tech. Rep. [CERN-ACC-2016-0041](https://arxiv.org/abs/1607.0041), CERN, Geneva (2016) [[DOI:10.17181/CERN.L6VM.UOMS](https://doi.org/10.17181/CERN.L6VM.UOMS)].
- [9] I. Zurbano Fernandez et al., *High-Luminosity Large Hadron Collider (HL-LHC): Technical design report*, Tech. Rep. CERN-2020-010 CERN, Geneva (2020) [[DOI:10.23731/CYRM-2020-0010](https://doi.org/10.23731/CYRM-2020-0010)].
- [10] J.-P. Tock et al., *The Second LHC Long Shutdown (LS2) for the Superconducting Magnets*, in the proceedings of the 9th International Particle Accelerator Conference, Vancouver, BC, Canada, 29 April–4 May 2018, pp. 240–243 [[DOI:10.18429/JACoW-IPAC2018-MOPMF056](https://doi.org/10.18429/JACoW-IPAC2018-MOPMF056)].
- [11] A. Perillo-Marcone et al., *LHC Dump Assembly — Operational Feedback and Future Prospective*, in the proceedings of the 9th LHC Operations Evian Workshop, Evian Les Bains, France, 30 January–1 February 2019, pp. 135–138.
- [12] E. Todesco et al., *Training Behavior of the Main Dipoles in the Large Hadron Collider*, *IEEE Trans. Appl. Supercond.* **27** (2017) 4702807.
- [13] E. Todesco et al., *Training of the Main Dipoles Magnets in the Large Hadron Collider Toward 7 TeV Operation*, *IEEE Trans. Appl. Supercond.* **28** (2018) 4006905.
- [14] M.J. Bednarek et al., *Design, Assembly and Use of a Device to Eliminate Earth Faults Caused by Metallic Debris in the LHC Main Dipole Circuits*, *IEEE Trans. Appl. Supercond.* **28** (2017) 4005805.

- [15] R. Denz et al., *Upgrade of the Protection System for Superconducting Circuits in the LHC*, in the proceedings of the 23rd Particle Accelerator Conference, Vancouver, Canada, 4–8 May 2009, p. 244–246.
- [16] C. Scheuerlein et al., *Specification for the Consolidation of the LHC Dipole Diode Busbar Insulation*, Tech. Rep. [LHC-DQD-ES-0003](#), CERN, Geneva (2018).
- [17] F.R. Mateos et al., *Voltage Withstand Levels for Electrical Insulation Tests on Components and Busbar Cross Sections for the Different LHC Machine Circuits*, Tech. Rep. [LHC-PM-ES-0001 rev. 2.0](#), CERN, Geneva (2004).
- [18] R. Versaci, F. Cerutti and V. Vlachoudis, *Absorbed radiation dose on LHC interconnects*, Tech. Rep. [CERN-ATS-Note-2011-072 TECH](#), CERN, Geneva (2011).
- [19] J.-C. Garnier et al., *Smooth Migration of CERN Post Mortem Service to a Horizontally Scalable Service*, in the proceedings of the 15th International Conference on Accelerator and Large Experimental Physics Control Systems, Melbourne, Australia, 17–23 October 2015, pp. 806–809 [[DOI:10.18429/JACoW-ICALEPCS2015-WEPGF047](#)].
- [20] A.A. Gorzawski et al., *The AccTesting Framework: An Extensible Framework for Accelerator Commissioning and Systematic Testing*, in the proceedings of the 14th International Conference on Accelerator and Large Experimental Physics Control Systems, San Francisco, CA, U.S.A., 6–14 October 2013, p. 1250–1253.
- [21] *STEAM*, <https://www.cern.ch/STEAM>.
- [22] J. Uythoven et al., *Interlock System Upgrades at the CERN Accelerator Complex During Long Shutdown 2*, in the proceedings of the 12th International Particle Accelerator Conference, Campinas, SP, Brazil, 24–28 May 2021, pp. 3316–3319 [[DOI:10.18429/JACoW-IPAC2021-WEPAB284](#)].
- [23] R. Schmidt et al., *Protection of the CERN Large Hadron Collider*, *New J. Phys.* **8** (2006) 290.
- [24] J. Spasic et al., *An Enhanced Quench Detection System for Main Quadrupole Magnets in the Large Hadron Collider*, in the proceedings of the 9th International Particle Accelerator Conference, Vancouver, BC, Canada, 29 April–4 May 2018, pp. 2032–2035 [[DOI:10.18429/JACoW-IPAC2018-WEPAF081](#)].
- [25] K.H. Mess, G.-J. Coelingh and K. Dahlerup-Petersen, *Results from Commissioning of the Energy Extraction Facilities of the LHC Machine*, in the proceedings of the 11th European Particle Accelerator Conference, Genoa, Italy, 23–27 June 2008, p. 1383–1385.
- [26] J. Maestre et al., *Design and behaviour of the Large Hadron Collider external beam dumps capable of receiving 539 MJ/dump*, *2021 JINST* **16** P11019 [[arXiv:2110.08783](#)].
- [27] J. Maestre et al., *LHC External Beam Dumps (TDE) Modifications and upgrades during LS2 for Run3*, CERN, Geneva (2021), <https://doi.org/10.5281/zenodo.8365957>.
- [28] J.M. Martin Ruiz et al., *Practical Challenges of the LHC Main Beam Dump Upgrades*, Tech. Rep. [CERN-ACC-NOTE-2021-0027](#), CERN, Geneva (2021).
- [29] J. Maestre Heredia et al., *Sigraflex® Studies for LHC CERN Beam Dump: Summary and Perspective*, in the proceedings of the 12th International Particle Accelerator Conference, Campinas, SP, Brazil, 24–28 May 2021, pp. 3571–3574 [[DOI:10.18429/JACoW-IPAC2021-WEPAB368](#)].
- [30] L. Rossi, *LHC Upgrade Plans: Options and Strategy*, in the proceedings of the 2nd International Particle Accelerator Conference, San Sebastian, Spain, 4–9 September 2011, p. 908–912.

- [31] S. Fartoukh, *Achromatic telescopic squeezing scheme and application to the LHC and its luminosity upgrade*, *Phys. Rev. ST Accel. Beams* **16** (2013) 111002.
- [32] G. Arduini et al., *Beam parameters at LHC injection*, Tech. Rep. [CERN-ACC-2014-0006](#), CERN, Geneva (2014).
- [33] R.W. Assmann, *Collimators and beam absorbers for cleaning and machine protection*, in the proceedings of the *LHC Project Workshop 14th Chamonix Workshop*, Chamonix, France, 17-21 January 2005, pp. 54–60.
- [34] G. Robert-Demolaize, *Design and Performance Optimization of the LHC Collimation System*, Ph.D. thesis, Université Joseph Fourier, Grenoble, France (2006).
- [35] R. Assmann et al., *The final collimation system for the LHC*, *Conf. Proc. C* **060626** (2006) 986.
- [36] C. Bracco, *Commissioning Scenarios and Tests for the LHC Collimation System*, Ph.D. thesis, EPFL, Lausanne, Switzerland (2008).
- [37] R. Bruce et al., *Simulations and measurements of beam loss patterns at the CERN Large Hadron Collider*, *Phys. Rev. ST Accel. Beams* **17** (2014) 081004 [[arXiv:1409.3123](#)].
- [38] G. Valentino et al., *Final implementation, commissioning, and performance of embedded collimator beam position monitors in the Large Hadron Collider*, *Phys. Rev. Accel. Beams* **20** (2017) 081002.
- [39] S. Redaelli, *Beam Cleaning and Collimation Systems*, in the proceedings of the *Joint International Accelerator School: Beam Loss and Accelerator Protection*, Newport Beach, U.S.A., 5–14 November 2014, p. 403–437 [[DOI:10.5170/CERN-2016-002.403](#)] [[arXiv:1608.03159](#)].
- [40] R. Bruce et al., *Sources of Machine-Induced Background in the ATLAS and CMS Detectors at the CERN Large Hadron Collider*, *Nucl. Instrum. Meth. A* **729** (2013) 825.
- [41] R. Bruce et al., *Collimation-induced experimental background studies at the CERN Large Hadron Collider*, *Phys. Rev. Accel. Beams* **22** (2019) 021004.
- [42] B. Salvachua et al., *LHC collimation cleaning and operation outlook*, in the proceedings of the *4th Evian Workshop on LHC beam operation*, Evian-les-Bains, France, 17–20 December 2012, pp. 155–160.
- [43] R. Bruce et al., *Reaching record-low β^* at the CERN Large Hadron Collider using a novel scheme of collimator settings and optics*, *Nucl. Instrum. Meth. A* **848** (2017) 19.
- [44] S. Redaelli, R. Bruce, A. Lechner and A. Mereghetti, *Chapter 5: Collimation system*, *CERN Yellow Rep. Monogr.* **10** (2020) 87.
- [45] G. Azzopardi et al., *LHC Collimation Controls System for Run III Operation*, in the proceedings of the *18th International Conference on Accelerator and Large Experimental Physics Control Systems*, online, 18–22 October 2021, p. 888–893.
- [46] O. Brüning, *HL-LHC project status*, presented at the *11th HL-LHC Collaboration Meeting*, CERN, Geneva, Switzerland, 19-22 October 2021, <https://indico.cern.ch/event/1079026/contributions/4544715/>.
- [47] S. Redaelli, *Collimation Upgrade — installations in LS2 and outstanding plans for LS3* presented at the *11th HL-LHC Collaboration Meeting*, CERN, Geneva, Switzerland, 19-22 October 2021, <https://indico.cern.ch/event/1079026/contributions/4544742/>.
- [48] S.A. Antipov et al., *Transverse beam stability with low-impedance collimators in the High-Luminosity Large Hadron Collider: Status and challenges*, *Phys. Rev. Accel. Beams* **23** (2020) 034403 [[arXiv:1910.09974](#)].

- [49] A. Bertarelli, *Beam-Induced Damage Mechanisms and their Calculation*, in the proceedings of the *2014 Joint International Accelerator School: Beam Loss and Accelerator Protection*, Newport Beach, U.S.A., 5–14 November 2014, p. 159–227 [DOI:10.5170/CERN-2016-002.159] [arXiv:1608.03056].
- [50] G. Arduini et al., *Chapter 2: Machine layout and performance*, *CERN Yellow Rep. Monogr.* **10** (2020) 17.
- [51] Brevetti Bizz, <https://www.brevettibizz.com>
- [52] J. Guardia-Valenzuela et al., *Development and properties of high thermal conductivity molybdenum carbide — graphite composites*, *Carbon* **135** (2018) 72.
- [53] C. Accettura et al., *Ultra-high vacuum characterization of molybdenum-carbide graphite for HL-LHC collimators*, in the proceedings of the *10th International Particle Accelerator Conference*, Melbourne, Australia, 19–24 May 2019, pp. 1078–1081 [DOI:10.18429/JACoW-IPAC2019-MOPTS093].
- [54] N. Simos et al., *Proton irradiation effects in Molybdenum-Carbide-Graphite composites*, *J. Nucl. Mater.* **553** (2021) 153049.
- [55] G. Gobbi et al., *Novel LHC collimator materials: High-energy Hadron beam impact tests and nondestructive postirradiation examination* *Mech. Adv. Mater. Struct.* **27** (2020) 1518.
- [56] M. Pasquali et al., *Dynamic Response of Advanced Materials Impacted by Particle Beams: The MultiMat Experiment*, *J. Dynamic Behavior Mater.* **5** (2019) 266.
- [57] C. Accettura et al., *Resistivity Characterization of Molybdenum-Coated Graphite-Based Substrates for High-Luminosity LHC Collimators*, *Coatings* **10** (2020) 361.
- [58] S. Redaelli et al., *Staged implementation of low-impedance collimation in IR7: plans for LS2*, Tech. Rep. CERN-ACC-NOTE-2019-0001 CERN, Geneva (2019).
- [59] C. Bahamonde Castro et al., *Improved Protection of the Warm Magnets of the LHC Betatron Cleaning Insertion*, in the proceedings of the *8th International Particle Accelerator Conference*, Copenhagen, Denmark, 14–19 May 2017, pp. 72–75 [DOI:10.18429/JACoW-IPAC2017-MOPAB004].
- [60] S.R. Klein, *Localized beam pipe heating due to e^- capture and nuclear excitation in heavy ion colliders*, *Nucl. Instrum. Meth. A* **459** (2001) 51 [physics/0005032].
- [61] J.M. Jowett, J.B. Jeanneret and K. Schindl, *Heavy ion beams in the LHC*, *Conf. Proc. C* **030512** (2003) 1682.
- [62] J.M. Jowett et al., *Limits to the performance of the LHC with ion beams*, in the proceedings of the *9th European Particle Accelerator Conference*, Lucerne, Switzerland, 5–9 July 2004, pp. 578–580.
- [63] R. Bruce et al., *First observations of beam losses due to bound-free pair production in a heavy-ion collider*, *Phys. Rev. Lett.* **99** (2007) 144801 [arXiv:0706.2292].
- [64] R. Bruce, S. Gilardoni, J.M. Jowett and D. Bocian, *Beam losses from ultra-peripheral nuclear collisions between $^{208}\text{Pb}^{82+}$ ions in the Large Hadron Collider and their alleviation*, *Phys. Rev. ST Accel Beams* **12** (2009) 071002 [arXiv:0908.2527].
- [65] M. Schaumann et al., *Bound-free pair production from nuclear collisions and the steady-state quench limit of the main dipole magnets of the CERN Large Hadron Collider*, *Phys. Rev. Accel. Beams* **23** (2020) 121003 [arXiv:2008.05312].
- [66] P.D. Hermes et al., *Measured and simulated heavy-ion beam loss patterns at the CERN Large Hadron Collider*, *Nucl. Instrum. Meth. A* **819** (2016) 73.

- [67] N. Fuster-Martínez et al., *Simulations of heavy-ion halo collimation at the CERN Large Hadron Collider: Benchmark with measurements and cleaning performance evaluation*, *Phys. Rev. Accel. Beams* **23** (2020) 111002 [[arXiv:2008.03234](https://arxiv.org/abs/2008.03234)].
- [68] A. Lechner et al., *Validation of energy deposition simulations for proton and heavy ion losses in the CERN Large Hadron Collider*, *Phys. Rev. Accel. Beams* **22** (2019) 071003.
- [69] V. Previtali, *Performance evaluation of a crystal-enhanced collimation system for the LHC*, Ph.D. thesis, EPFL, Lausanne, Switzerland (2010).
- [70] D. Mirarchi, *Crystal collimation for LHC*, Ph.D. thesis, Imperial College, London, U.K. (2015).
- [71] R. Rossi, *Experimental Assessment of Crystal Collimation at the Large Hadron Collider*, Ph.D. thesis, University of Rome, Rome, Italy (2017).
- [72] M. D’Andrea, *Applications of Crystal Collimation to the CERN Large Hadron Collider (LHC) and its High Luminosity Upgrade Project (HL-LHC)*, Ph.D. thesis, University of Padova, Padova, Italy (2021).
- [73] M. Butcher, A. Giustiniani, R. Losito and A. Masi, *Controller design and verification for a rotational piezo-based actuator for accurate positioning applications in noisy environments*, in the proceedings of the 41st Annual Conference of the IEEE Industrial Electronics Society, Yokohama, Japan, 9–12 November 2015, pp. 3887–3892 [[DOI:10.1109/iecon.2015.7392706](https://doi.org/10.1109/iecon.2015.7392706)].
- [74] P. Serrano Gálvez, M. Butcher and A. Masi, *A Dual-Interferometer-Based Angular Measurement System With Absolute Angle Recovery Method*, *IEEE Trans. Instrum. Measur.* **68** (2019) 864.
- [75] P.S. Galvez, *Modelling and Control of Piezoactuators for High Precision Positioning Systems Used in Radioactive Environments*, Ph.D. thesis, Polytechnic University of Madrid, Madrid, Spain (2019).
- [76] W. Scandale et al., *Observation of nuclear dechanneling length reduction for high energy protons in a short bent crystal*, *Phys. Lett. B* **743** (2015) 440.
- [77] S. Redaelli et al., *First observation of ion beam channeling in bent crystals at multi-TeV energies*, *Eur. Phys. J. C* **81** (2021) 142.
- [78] M. D’Andrea et al., *Crystal Collimation of 20 MJ Heavy-Ion Beams at the HL-LHC*, in the proceedings of the 12th International Particle Accelerator Conference, Campinas, SP, Brazil, 24–28 May 2021, pp. 2644-2647 [[DOI:10.18429/JACoW-IPAC2021-WEPAB023](https://doi.org/10.18429/JACoW-IPAC2021-WEPAB023)].
- [79] D. Mirarchi et al., *Reducing Beam-Related Background on Forward Physics Detectors Using Crystal Collimation at the Large Hadron Collider*, *Phys. Rev. Appl.* **14** (2020) 064066.
- [80] A. Poyet et al., *MD3263: Beam-Beam Long-Range Compensation using DC Wires in the LHC*, Tech. Rep. [CERN-ACC-NOTE-2019-0053](https://arxiv.org/abs/1905.0053), CERN, Geneva (2019).
- [81] A. Poyet, *Beam-Beam Long-Range Wire Compensation For Enhancing CERN LHC Performance. Compensation des interactions faisceau-faisceau pour améliorer les performances du Grand Collisionneur de Hadrons du CERN*, Ph.D. thesis, Université Joseph Fourier, Grenoble, France (2021).
- [82] L. Ducimetiere, M.J. Barnes, N. Garrel and G.D. Wait, *The LHC Injection Kicker Magnet*, in the proceedings of the 20th Particle Accelerator Conference, Portland, OR, U.S.A., 12–16 May 2003, pp. 1162–1164.
- [83] V.K. Verena Kain, *Machine Protection and Beam Quality during the LHC Injection Process*, <http://cds.cern.ch/record/902813>.
- [84] A. Lechner et al., *TDI — past observations and improvements for 2016*, in the proceedings of the 6th Evian Workshop on LHC beam operation, Evian Les Bains, France, 15–17 December 2015, p. 123–130.

- [85] C. Bracco et al., *Angular Alignment of the LHC Injection Protection Stopper*, in the proceedings of the *3rd International Particle Accelerator Conference*, New Orleans, LA, U.S.A., 20–25 May 2012, pp. 2056–2058.
- [86] G. Valentino et al., *Semiautomatic beam-based LHC collimator alignment*, *Phys. Rev. ST Accel. Beams* **15** (2012) 051002.
- [87] A. Masi and R. Losito, *LHC Collimators low level control system*, *IEEE Trans. Nucl. Sci.* **55** (2008) 333.
- [88] N. Voumard, *The LHC Beam Energy Tracking System for the TDI and MS*, Tech. Rep. [EDMS 1322845](#), CERN, Geneva (2020).
- [89] J.M. Jowett, *ALICE's ZDC Requirements*, talk given at the *8th TREX meeting*, Geneva, Switzerland, 27 August 2015.
- [90] T. Jin, *Update on TDIS Impedance Studies*, talk given at the *HL-LHC WP14 Technical Meeting #3*, Geneva, Switzerland, 2 October 2015.
- [91] B. Salvant and N. Biancacci, *TDIS Impedance Update*, talk given at the *HL-LHC WP14 Technical Meeting #5*, Geneva, Switzerland, 14 January 2016.
- [92] N. Biancacci, *Update on TDIS Impedance and Stability Studies*, talk given at the *81st HL-LHC WP2 meeting*, Geneva, Switzerland, 24 November 2016.
- [93] G. Mazzacano, *Impact of NEG and aC Coatings on Cu/Ti TDIS Jaws*, talk given at the *TDIS coating treatments meeting*, Geneva, Switzerland, 10 January 2018.
- [94] G. Mazzacano, *Update on TDIS Impedance Simulations: Jaw Coatings, Flanges Coating, Anti-Scratching Glassy-Carbon Sheet*, talk given at the *Impedance meeting*, Geneva, Switzerland, 2018.
- [95] D.C. Perez, *WP14 TDIS Beam Absorber for Injection*, Tech. Rep. [1905241](#), CERN, Geneva (2020).
- [96] G. Skripka and G. Iadarola, *Electron cloud studies for the LHC TDI and HL-LHC TDIS*, Tech. Rep. [CERN-ACC-NOTE-2018-0060](#) CERN, Geneva (2018).
- [97] B. Lindstrom et al., *Dynamics of the interaction of dust particles with the LHC beam*, *Phys. Rev. Accel. Beams* **23** (2020) 124501.
- [98] C. Scheuerlein, B. Henrist, N. Hilleret and M. Taborelli, *The Secondary electron yield of TiZr and TiZrV nonevaporable getter thin film coatings*, *Appl. Surf. Sci.* **172** (2001) 95.
- [99] A. Infantino, *Radiation Protection estimates for LS3 activities in LSS1 and LSS5*, Tech. Rep. [EDMS 2435122](#), CERN, Geneva (2021).
- [100] E. Hoyer and B. Elliott, *LHC IP1/IP5 Front Quadrupole Absorbers (TAS)*, Tech. Rep. [EDMS 111998](#), LBNL, Berkeley, CA, U.S.A. (2002).
- [101] F.S. Galan, *Functional Specification of TANB*, Tech. Rep. [EDMS 1960537](#), CERN, Geneva (2018).
- [102] N. Grada, *TANB-System Safety Assessment*, Tech. Rep. [EDMS 1937016](#), CERN, Geneva (2020).
- [103] H.G. Gavela, *TANB-End of Manufacturing Review*, Tech. Rep. [EDMS 2305097](#), CERN, Geneva (2020).
- [104] *The ATLAS Forward Shielding*, <http://atlas.web.cern.ch/Atlas/GROUPS/Shielding/shielding.htm#part5>.
- [105] *KUKA Robotics*, <https://www.kuka.com>.

- [106] J. Sestak and P. Gebolis, *Modification of the VT retractable support system in the ATLAS experiment*, Tech. Rep. [EDMS 1961919](#), CERN, Geneva (2018).
- [107] M. Huhtinen, *Optimization of the CMS forward shielding*, Tech. Rep. [CMS-NOTE-2000-068](#), CERN, Geneva (2000).
- [108] J. Sestak and C. Di Paolo, *Upgrade of the IP5.X Beam Vacuum Sector*, Tech. Rep. [EDMS 1967199](#), CERN, Geneva (2019).
- [109] *FLUKA*, <https://fluka.cern/>.
- [110] F. Cerutti and A. Tsinganis, *Update on D2 protection with TANB in IR8 for the LS2 LHCb upgrade*, talk given at the 54th HL-LHC WP8 meeting, 6 July 2017, <https://edms.cern.ch/document/1961050/1>.
- [111] M.L. Diogo Dos Santos, *TANB — Thermomechanical FEA*, Tech. Rep. [EDMS 1752658](#), CERN, Geneva (2018).
- [112] M.L. Diogo Dos Santos et al., *Weplate WP8 6DOF Alignment Platform*, Tech. Rep. [CERN-ACC-NOTE-2019-0035](#) CERN, Geneva (2019).
- [113] M.L. Diogo Dos Santos, *Prototype Alignment Plate 6DOF Test Results*, Tech. Rep. [EDMS 2068040](#), CERN, Geneva (2019).
- [114] S. Fartoukh, *Machine configuration in Run3 (pp runs)*, talk given at the Chamonix 2022 Workshop on LHC Performance, Chamonix, France, 24–27 January 2022, <https://indico.cern.ch/event/1097716/contributions/4618693/>.
- [115] P. Pugnât and A. Siemko, *Review of Quench Performance of LHC Main Superconducting Magnets*, *IEEE Trans. Appl. Superconduct.* **17** (2007) 1091.
- [116] A. Verweij et al., *Retraining of the 1232 Main Dipole Magnets in the LHC*, *IEEE Trans. Appl. Supercond.* **26** (2016) 4000705.
- [117] A. Verweij, *Training the dipoles*, in the proceedings of the Chamonix 2009 Workshop on LHC Performance, Chamonix, France, 2–6 Feb 2009, pp. 25–28, <http://cds.cern.ch/record/1172379>
- [118] A. Verweij, *Outcome of Risk Analysis for Target Energy of 7 TeV* talk given at the 424th LHC Machine Committee meeting, CERN, Geneva, Switzerland, 15 September 2021, <https://indico.cern.ch/event/1075568/contributions/4523214/>.
- [119] R. Tomás et al., *Beam parameter requirements from HL-LHC*, talk given at the LHC Injectors Upgrade (LIU) Workshop, Montreux, Switzerland, 13–15 February 2019, <https://indico.cern.ch/event/774181/contributions/3218339/>.
- [120] M. Benedikt and F. Sonnemann, *Summary of Session 7: Accelerator and non-LHC Experimental Areas Consolidation up to LS3*, in the proceedings of the Chamonix 2014 Workshop on LHC Performance Chamonix, France, 22–25 September 2014, pp. 31–32 <http://cds.cern.ch/record/2031177> [DOI:10.5170/CERN-2015-002.31].
- [121] A. Lombardi, *Linac4: From Initial Design to Final Commissioning*, in the proceedings of the 8th International Particle Accelerator Conference, Copenhagen, Denmark, 14–19 May 2017, pp. 1217–1222 [DOI:10.18429/JACoW-IPAC2017-TUYA1].
- [122] R. Garoby, *New RF Exercises Envisaged in the CERN-PS for the Antiprotons Production Beam of the ACOL Machine*, *IEEE Trans. Nucl. Sci.* **NS-32** (1985) 2232.

- [123] B. Goddard and F. Zimmermann, *RLIUP: Review of LHC and Injector Upgrade Plans*, in the proceedings of the *RLIUP: Review of LHC and Injector Upgrade Plans*, Archamps, France, 29–31 October 2013, pp. 139–144 [DOI:10.5170/CERN-2014-006].
- [124] H. Bartosik et al., *Injectors Beam Performance Evolution during Run 2*, presented at the *9th LHC Operations Evian Workshop*, Evian, France, 30 January–1 February 2019, <https://indico.cern.ch/event/751857/contributions/3259375/>.
- [125] N. Karastathis et al., *Report from the Run 3 configuration working group*, presented at the *9th LHC Operations Evian Workshop*, Evian, France, 30 January–1 February 2019, <https://indico.cern.ch/event/751857/contributions/3259414/>.
- [126] D. Quartullo, *Simulations of RF beam manipulations including intensity effects for CERN PSB and SPS upgrades*, Ph.D. thesis, Istituto Nazionale di Fisica Nucleare (INFN) and “Sapienza” Università di Roma, Rome, Italy (2019), CERN-THESIS-2019-006.
- [127] E. Shaposhnikova et al., *Longitudinal beam quality and stability in the SPS (protons and ions)*, presented at the *LHC Injectors Upgrade Workshop*, Montreux, Switzerland, 13–15 February 2019, <https://indico.cern.ch/event/774181/timetable/#20190213.detailed>.
- [128] H. Bartosik et al., *LIU-SPS: Protons and Ions*, presented at the *LHC Performance Workshop Chamonix 2018*, Chamonix, France, 29 January–1 February 2018, <https://doi.org/10.5281/zenodo.8370633>.
- [129] H. Bartosik et al., *Transverse beam quality and stability in the SPS (protons and ions)*, presented at the *LHC Injectors Upgrade Workshop*, Montreux, Switzerland, 13–15 February 2019, <https://indico.cern.ch/event/774181/timetable/#20190213.detailed>.
- [130] G. Rumolo, H. Bartosik, V. Kain and M. Meddahi, *What to expect from the injectors during Run 3*, presented at the *9th LHC Operations Evian Workshop*, Evian, France, 30 January–1 February 2019 https://indico.cern.ch/event/751857/contributions/3259375/attachments/1820780/2997635/Evian2019_injectors.pdf.
- [131] H. Bartosik and G. Rumolo, *Beyond LS2: Possible injector upgrades to reach the LIU parameters*, Tech. Rep. EDMS 2400331, CERN, Geneva (2020).
- [132] O. Grobner, *Technological problems related to the cold vacuum system of the LHC*, *Vacuum* **47** (1996) 591.
- [133] O. Grobner, *Overview of the LHC vacuum system*, *Vacuum* **60** (2001) 25.
- [134] B. Bradu, K. Brodzinski and G. Ferlin, *How does a cryogenic system cope with e-cloud induced heat load?*, *CERN Yellow Rep. Conf. Proc.* **7** (2020) 73.
- [135] G. Iadarola et al., *Electron Cloud and Heat Loads in Run 2*, in the proceedings of the *9th LHC Operations Evian Workshop*, Evian, France, 30 January–1 February 2019, pp. 221–232.
- [136] G. Skripka et al., *Comparison of electron cloud build-up simulations against heat load measurements for the LHC arcs with different beam configurations*, in the proceedings of the *10th International Particle Accelerator Conference*, Melbourne, Australia, 19–24 May 2019, pp. 3366–3369 [DOI:10.18429/JACoW-IPAC2019-WEPTS051].
- [137] G. Iadarola et al., *Progress in Mastering Electron Clouds at the Large Hadron Collider*, in the proceedings of the *12th International Particle Accelerator Conference*, Campinas, SP, Brazil, 24–28 May 2021, pp. 1273–1278 [DOI:10.18429/JACoW-IPAC2021-TUXA03].

- [138] G. Iadarola et al., *Beam-induced heat loads on the LHC arc beam screens with different beam and machine configurations: experiments and comparison against simulations*, Tech. Rep. [CERN-ACC-NOTE-2019-0057](#) CERN, Geneva (2019).
- [139] G. Iadarola et al., *Evolution of Python Tools for the Simulation of Electron Cloud Effects*, in the proceedings of the 8th *International Particle Accelerator Conference*, Copenhagen, Denmark, 14–19 May 2017, pp. 3803–3806 [[DOI: 10.18429/JACoW-IPAC2017-THPAB043](#)].
- [140] G. Skripka and G. Iadarola, *Beam-induced heat loads on the beam screens of the HL-LHC arcs*, Tech. Rep. [CERN-ACC-NOTE-2019-0041](#) CERN, Geneva (2019).
- [141] P. Dijkstal, G. Iadarola, L. Mether and G. Rumolo, *Simulation studies on the electron cloud build-up in the elements of the LHC Arcs at 6.5 TeV*, Tech. Rep. [CERN-ACC-NOTE-2017-0057](#) CERN, Geneva (2017).
- [142] V. Petit et al., *Impact of deconditioning on the secondary electron yield of Cu surfaces in particle accelerators*, *Phys. Rev. Accel. Beams* **23** (2020) 093101.
- [143] V. Petit et al., *Beam-induced surface modifications as a critical source of heat loads in the Large Hadron Collider*, *Commun. Phys.* **4** (2021) 192.
- [144] S.K. Chawla, B.I. Rickett, N. Sankarraman and J.H. Payer, *An X-ray photo-electron spectroscopic investigation of the air-formed film on copper*, *Corrosion Sci.* **33** (1992) 1617.
- [145] C. Scheuerlein et al., *An AES study of the room temperature conditioning of technological metal surfaces by electron irradiation*, *Appl. Surf. Sci.* **202** (2002) 57.
- [146] R. Cimino et al., *Nature of the Decrease of the Secondary-Electron Yield by Electron Bombardment and its Energy Dependence*, *Phys. Rev. Lett.* **109** (2012) 064801.
- [147] V. Petit et al., *Role of the different chemical components in the conditioning process of air exposed copper surfaces*, *Phys. Rev. Accel. Beams* **22** (2019) 083101.
- [148] S. Bok, G.-H. Lim and B. Lim, *UV/Ozone treatment for adhesion improvement of copper/epoxy*, *J. Ind. Eng. Chem.* **46** (2017) 199.
- [149] W. Hu, K. Manabe, T. Furukawa and M. Matsumura, *Lowering of operational voltage of organic electroluminescent devices by coating indium-tin-oxide electrodes with a thin CuOx layer*, *Appl. Phys. Lett.* **80** (2002) 2640.
- [150] B. Bradu et al., *Beam induced heat load instrumentation installed in LHC during the Long Shutdown 2*, *IOP Conf. Ser. Mater. Sci. Eng.* **1240** (2022) 012043.
- [151] B. Bradu et al., *Heat load profile estimates on LHC beam screens by thermal transient analysis*, *IOP Conf. Ser. Mater. Sci. Eng.* **502** (2019) 012116.
- [152] G. Panzner, B. Egert and H.P. Schmidt, *The stability of CuO and Cu₂O surfaces during argon sputtering studied by XPS and AES*, *Surf. Sci.* **151** (1985) 400.
- [153] S.Y. Lee et al., *Copper oxide reduction through vacuum annealing*, *Appl. Surf. Sci.* **206** (2003) 102.
- [154] J.A. Rodriguez et al., *Reduction of CuO in H₂: In situ time-resolved XRD studies*, *Catal. Lett.* **85** (2003) 247.
- [155] S. Poulston, P.M. Parlett, P. Stone and M. Bowker, *Surface Oxidation and Reduction of CuO and Cu₂O Studied Using XPS and XAES*, *Surf. Interf. Anal.* **24** (1996) 811.
- [156] T.H. Fleisch, G.W. Zajac, J.O. Schreiner and G.J. Mains, *An XPS study of the UV photoreduction of transition and noble metal oxides*, *Appl. Surf. Sci.* **26** (1986) 488.

- [157] J.-X. Li and A.-H. Liu, *Reduction of Copper Oxide Induced by 172 nm Vacuum Ultraviolet Radiation at Ambient Temperature*, *J. Electron. Mater.* **40** (2011) 2105.
- [158] T.H. Fleisch and G.J. Mains, *Reduction of copper oxides by UV radiation and atomic hydrogen studied by XPS*, *Appl. Surf. Sci.* **10** (1982) 51.
- [159] J. Lee, T.S. Williams and R.F. Hicks, *Atmospheric pressure plasma reduction of copper oxide to copper metal*, *J. Vacuum Sci. Technol. A* **39** (2021) 023001.
- [160] Y. Sawada et al., *The reduction of copper oxide thin films with hydrogen plasma generated by an atmospheric-pressure glow discharge*, *J. Phys. D* **29** (1996) 2539.
- [161] W. Vollenberg et al., *Amorphous Carbon Coating in SPS*, in the proceedings of the *12th International Particle Accelerator Conference*, Campinas, SP, Brazil, 24–28 May 2021, pp. 3475–3478 [DOI:10.18429/JACoW-IPAC2021-WEPAB338].
- [162] O.R. Jones et al., *Aperture Restriction Localisation in the LHC Arcs using an RF Mole and the LHC Beam Position Measurement System*, in the proceedings of the *11th European Particle Accelerator Conference*, Genova, Italy, 23–27 June 2008, p. 2644–2646.
- [163] F.M. Velotti et al., *LHC injection system along run II*, in the proceedings of the *9th LHC Operations Evian Workshop*, Evian, France, 30 January–1 February 2019, pp. 103–111.
- [164] H. Timko et al., *LHC Longitudinal Beam Dynamics in Run-II*, in the proceedings of the *9th LHC Operations Evian Workshop*, Evian, France, 30 January–1 February 2019, pp. 245–251.
- [165] H. Timko, E. Chaponnikova and K. Turaj, *Estimated LHC RF system performance reach at injection during Run III and beyond*, Tech. Rep. CERN-ACC-NOTE-2019-0005 CERN, Geneva (2018).
- [166] D. Boussard, *RF power requirements for a high intensity proton collider*, *Conf. Proc. C* **910506** (1991) 2447.
- [167] T. Mastoridis, P. Baudrenghien and J. Molendijk, *Cavity voltage phase modulation to reduce the high-luminosity Large Hadron Collider rf power requirements*, *Phys. Rev. Accel. Beams* **20** (2017) 101003.
- [168] J.M. Heredia et al., *TCDQ thermo-mechanical analysis for the HL-LHC*, presented at the *7th LHC LHC Run-III Configuration Working Group Meeting*, CERN, Geneva, Switzerland, 9 November 2018.
- [169] B. Goddard, L. Massidda, A. Presland and W.J.M. Weterings, *Dynamic Stresses in the LHC TCDS Diluter from 7 TeV Beam Loading*, in the proceedings of the *10th European Particle Accelerator Conference*, Edinburgh, U.K., 26–30 June 2006, pp. 1511–1513.
- [170] J.M. Heredia et al., *TCDQ/S simulation results*, presented at the *HL-LHC WP14 Meeting*, CERN, Geneva, Switzerland, 30 June 2021.
- [171] C. Bracco et al., *Beam Based Measurements to Check Integrity of LHC Dump Protection Elements*, in the proceedings of the *7th International Particle Accelerator Conference*, Busan, Korea, 8–13 May 2006, pp. 3908–3910 [DOI:10.18429/JACoW-IPAC2016-THPOR051].
- [172] S. Papadopoulou et al., *What do we understand on the emittance growth?*, in the proceedings of the *9th LHC Operations Evian Workshop*, Evian, France, 30 January–1 February 2019, pp. 199–205.
- [173] B. Petersen, *Experiment Desiderata*, in the proceedings of the *10th LHC Operations Workshop*, Geneva, Switzerland, 23–25 November 2021, to be published.
- [174] G. Ferlin et al., *Cryogenics experience during Run2 and impact of LS2 on next run*, in the proceedings of the *9th LHC Operations Evian Workshop*, Evian, France, 30 January–1 February 2019, pp. 85–90.

- [175] X. Buffat et al., *Strategy for Landau damping of head-tail instabilities at top energy in the HL-LHC*, Tech. Rep. [CERN-ACC-NOTE-2020-0059](#) CERN, Geneva (2020).
- [176] S. Papadopoulou et al., *Monitoring and Modelling of the LHC Emittance and Luminosity Evolution in 2018*, *J. Phys. Conf. Ser.* **1350** (2019) 012011.
- [177] M. Albrow et al., *CMS-TOTEM Precision Proton Spectrometer*, Tech. Rep. [CERN-LHCC-2014-021](#) CERN, Geneva (2014).
- [178] F. Cerutti et al., *Triplet luminosity lifetime*, in the proceedings of the 10th LHC Operations Workshop, Geneva, Switzerland, 23–25 November 2021, to be published.
- [179] S. Fartoukh and S. Kostoglou, *Latest Run 3 optics versions with requested β^* granularity*, presented at the 22th LHC Run-III Configuration Working Group Meeting, CERN, Geneva, Switzerland, 08 October 2021.
- [180] ATLAS collaboration, *The AFP Project*, *Acta Phys. Polon. B* **42** (2011) 1615 [[arXiv:1104.1858](#)].
- [181] ALICE collaboration, *Future high pp programme with ALICE*, Tech. Rep. [CERN-LHCC-2020-018](#), CERN, Geneva (2020).
- [182] LHCb collaboration, *Framework TDR for the LHCb Upgrade: Technical Design Report*, Tech. Rep. [CERN-LHCC-2012-007](#) CERN, Geneva (2012).
- [183] G. Iadarola, *Electron cloud instabilities at injection*, presented at the 14th LHC Run-III Configuration Working Group Meeting, CERN, Geneva, Switzerland, 03 April 2021.
- [184] S. Fartoukh, *Impact and possible mitigation measures in case of failure of lattice sextupole and octupole circuits in Run 3*, Tech. Rep. [CERN-ACC-NOTE-2020-0057](#) CERN, Geneva (2020).
- [185] X. Buffat et al., *Transverse Instabilities*, in the proceedings of the 9th LHC Operations Evian Workshop, Evian, France, 30 January–1 February 2019, pp. 233–243.
- [186] R. Bruce et al., *Updated parameters for HL-LHC aperture calculations for proton beams*, Tech. Rep. [CERN-ACC-2017-0051](#), CERN, Geneva (2017).
- [187] E. Høydaalsvik and T.H.B. Persson, *Reaching the Sub Per Mil Level Coupling Corrections in the LHC*, in the proceedings of the 12th International Particle Accelerator Conference, Campinas, SP, Brazil, 24–28 May 2021, pp. 3752–3755 [[DOI:10.18429/JACoW-IPAC2021-THPAB001](#)].
- [188] S. Fartoukh, *Latest version of the LHC Optics for the 2022 pp Run*, http://proj-lhc-optics-web.web.cern.ch/proj-lhc-optics-web/OpticsSourceAllVersions.link/runIII/RunIII_dev/2021_V6/PROTON/ (2021).
- [189] S. Fartoukh, *Latest version of the LHC Optics for the 2023 and 2024 pp Runs*, http://proj-lhc-optics-web.web.cern.ch/proj-lhc-optics-web/OpticsSourceAllVersions.link/runIII/RunIII_dev/2022_V5/PROTON/ (2021).
- [190] T. Persson and E.J. Høydaalsvik, *Linear optics commissioning scenarios*, presented at the 21th LHC Run-III Configuration Working Group Meeting, CERN, Geneva, Switzerland, 18 June 2021.
- [191] M. Hostettler et al., *β^* levelling using the LHC Lumi Server (MD 2427)*, Tech. Rep. [CERN-ACC-NOTE-2018-0001](#) CERN, Geneva (2020).
- [192] A. Calia et al., *Start collisions at 1m β^* (MD 3349)*, Tech. Rep. [CERN-ACC-NOTE-2022-0006](#) CERN, Geneva (2021).
- [193] M. Hostettler, *LHC Luminosity Performance*, Ph.D. thesis, University of Bern, Bern, Switzerland (2018), <https://cds.cern.ch/record/2319396/CERN-THESIS-2018-051>.

- [194] C. Roderick and R. Billen, *The LSA Database to Drive the Accelerator Settings*, in the proceedings of the 12th International Conference On Accelerator And Large Experimental Physics Control Systems, Kobe, Japan, 12–16 October 2009, p. 417–419.
- [195] R. Bruce, R.W. Assmann and S. Redaelli, *Calculations of safe collimator settings and β^* at the CERN Large Hadron Collider*, *Phys. Rev. ST Accel. Beams* **18** (2015) 061001.
- [196] W. Sliwinski, P. Charrue, V. Kain and G. Kruk, *Management of Critical Machine Settings for Accelerators at CERN*, in the proceedings of the 12th International Conference On Accelerator And Large Experimental Physics Control Systems, Kobe, Japan, 12–16 October 2009, p. 594–596.
- [197] M. Hostettler, *TCT interlock thresholds during β^* levelling*, presented at the 260th LHC Collimation Working Group Meeting, CERN, Geneva, Switzerland, 11 October 2021, <https://doi.org/10.5281/zenodo.8363800>.
- [198] M. Hostettler et al., *Online luminosity control and steering at the LHC*, in the proceedings of the 16th International Conference on Accelerator and Large Experimental Physics Control Systems, Barcelona, Spain, 8–13 October 2017, pp. 989–993 [DOI:10.18429/JACoW-ICALEPCS2017-TUSH201].
- [199] F. Follin, R. Alemany-Fernandez and R. Jacobsson, *Online Luminosity Optimization at the LHC*, in the proceedings of the 14th International Conference on Accelerator and Large Experimental Physics Control Systems, San Francisco, CA, U.S.A., 6–11 October 2013, p. 1351–1354.
- [200] G. de Cataldo et al., *An upgraded luminosity leveling procedure for the ALICE Experiment*, *IEEE Trans. Nucl. Sci.* **66** (2019) 763.
- [201] Y. Papaphilippou and F. Zimmermann, *Diffusive Aperture due to Long-Range Beam-Beam Interaction*, in the proceedings of the 7th European Particle Accelerator Conference, Vienna, Austria, 26–30 June 2000, pp. 1217–1219.
- [202] Y. Papaphilippou and F. Zimmermann, *Estimates of diffusion due to long-range beam-beam collisions*, *Phys. Rev. ST Accel. Beams* **5** (2002) 074001.
- [203] J.-P. Koutchouk, *Principle of a correction of the long-range beam-beam effect in LHC using electromagnetic lenses*, Tech. Rep. LHC-PROJECT-NOTE-223, CERN, Geneva (2000).
- [204] J.-P. Koutchouk, *Correction of the Long-Range Beam-Beam Effect in LHC Using Electro-Magnetic Lenses*, in the proceedings of the Particle Accelerator Conference, Chicago, IL, U.S.A., 18–22 June 2001, pp. 1681–1683.
- [205] S. Fartoukh, A. Valishev, Y. Papaphilippou and D. Shatilov, *Compensation of the long-range beam-beam interactions as a path towards new configurations for the high luminosity LHC*, *Phys. Rev. Accel. Beams* **18** (2015) 121001.
- [206] G. Sterbini et al., *First results of the compensation of the beam-beam effect with DC wires in the LHC*, in the proceedings of the 10th International Particle Accelerator Conference, Melbourne, Australia, 19–24 May 2019, pp. 2262–2265 [DOI:10.18429/JACoW-IPAC2019-WEYYPLM3].
- [207] A. Poyet et al., *Numerical simulations of the DC wire prototypes in the LHC for enhancing the HL-LHC performances*, in the proceedings of the 10th International Particle Accelerator Conference, Melbourne, Australia, 19–24 May 2019, pp. 566–569 [DOI:10.18429/JACoW-IPAC2019-MOPMP052].
- [208] K. Skoufaris et al., *Numerical optimization of dc wire parameters for mitigation of the long range beam-beam interactions in High Luminosity Large Hadron Collider*, *Phys. Rev. Accel. Beams* **24** (2021) 074001.
- [209] D. Pellegrini et al., *Multiparametric response of the LHC Dynamic Aperture in presence of beam-beam effects*, *J. Phys. Conf. Ser.* **874** (2017) 012006.

- [210] S. Fartoukh et al., *Round telescopic optics with large telescopic index*, Tech. Rep. [CERN-ACC-2018-0032](#), CERN, Geneva (2018).
- [211] N. Mounet, *The LHC Transverse Coupled-Bunch Instability*, Ph.D. thesis, EPFL, Lausanne, Switzerland (2012) <http://infoscience.epfl.ch/record/174672> [DOI:10.5075/EPFL-THESIS-5305].
- [212] Y. Papaphilippou, *Proposal for the experimental scenario*, presented at the *Workshop on Simulations and Measurements of Long Range Beam-Beam Effects in the LHC*, Lyon, France, 30 November–1 December 2015, <https://indico.cern.ch/event/456856/contributions/1968793/>.
- [213] R. Bruce et al., *HL-LHC operational scenarios for Pb-Pb and p-Pb operation*, Tech. Rep. [CERN-ACC-2020-0011](#), CERN, Geneva (2020).
- [214] R. Bruce et al., *Performance and luminosity models for heavy-ion operation at the CERN Large Hadron Collider*, *Eur. Phys. J. Plus* **136** (2021) 745 [arXiv:2107.09560].
- [215] G. Arduini et al., *First Run of the LHC as a Heavy-ion Collider*, *Conf. Proc. C* **110904** (2011) 1837.
- [216] J.M. Jowett et al., *The 2015 Heavy-Ion Run of the LHC*, in the proceedings of the *7th International Particle Accelerator Conference*, Busan, Korea, 8–13 May 2016, pp. 1493–1496 [DOI:10.18429/JACoW-IPAC2016-TUPMW027].
- [217] J.M. Jowett, *Colliding Heavy Ions in the LHC*, in the proceedings of the *9th International Particle Accelerator Conference*, Vancouver, BC, Canada, 29 April–4 May 2018, pp. 584–589 [DOI:10.18429/JACoW-IPAC2018-TUXGBD2].
- [218] J.M. Jowett et al., *The 2018 heavy-ion run of the LHC*, in the proceedings of the *10th International Particle Accelerator Conference*, Melbourne, Australia, 19–24 May 2019, pp. 2258–2261 [DOI:10.18429/JACoW-IPAC2019-WEYYPLM2].
- [219] J.M. Jowett et al., *Overview of ion runs during Run 2*, in the proceedings of the *Evian Les Bains*, France, 30 January–1 February 2019, pp. 15–25
- [220] J.M. Jowett and C. Carli, *The LHC as a proton nucleus collider*, *Conf. Proc. C* **060626** (2006) 550.
- [221] J.M. Jowett et al., *Proton-nucleus Collisions in the LHC*, in the proceedings of the *4th International Particle Accelerator Conference*, Shanghai, China, 12–17 May 2013, pp. 49–51.
- [222] R. Versteegen et al., *Operating the LHC Off-momentum for p-Pb Collisions*, in the proceedings of the *4th International Particle Accelerator Conference*, Shanghai, China, 12–17 May 2013, pp. 1439–1441.
- [223] J.M. Jowett et al., *The 2016 Proton-Nucleus Run of the LHC*, in the proceedings of the *8th International Particle Accelerator Conference*, Copenhagen, Denmark, 14–19 May 2017, pp. 2071–2074 [DOI:10.18429/JACoW-IPAC2017-TUPVA014].
- [224] ALICE collaboration, *Upgrade of the ALICE Experiment: Letter Of Intent*, *J. Phys. G* **41** (2014) 087001.
- [225] Z. Citron et al., *Report from Working Group 5: Future physics opportunities for high-density QCD at the LHC with heavy-ion and proton beams*, *CERN Yellow Rep. Monogr.* **7** (2019) 1159 [arXiv:1812.06772].
- [226] H. Bartosik, M. Meddahi and G. Rumolo, *LIU baseline for ions*, presented at the *LHC Performance Workshop Chamonix 2017*, Chamonix, France, 23–27 January 2017.
- [227] ALICE collaboration, *Technical Design Report for the Upgrade of the ALICE Inner Tracking System*, *J. Phys. G* **41** (2014) 087002.

- [228] J.M. Jowett, *HL-LHC heavy-ion beam parameters at LHC injection*, Tech. Rep. *CERN EDMS 1525065*, CERN, Geneva (2015).
- [229] J.M. Jowett, R. Alemany, M. Schaumann, P. Hermes and T. Mertens, *HL-LHC beam parameters and performance with heavy ions — an update*, presented at the *LHC Performance Workshop Chamonix 2017*, Chamonix, France, 23–27 January 2017.
- [230] P.D. Hermes et al., *LHC Heavy-Ion Collimation Quench Test at 6.37Z TeV*, Tech. Rep. [CERN-ACC-NOTE-2016-0031](#) CERN, Geneva (2016).
- [231] R. Bruce, J.M. Jowett, M. Blaskiewicz and W. Fischer, *Time evolution of the luminosity of colliding heavy-ion beams in BNL Relativistic Heavy Ion Collider and CERN Large Hadron Collider*, *Phys. Rev. ST Accel. Beams* **13** (2010) 091001 [[arXiv:1009.1562](#)].
- [232] M.A. Jebramcik, *Beam dynamics of proton-nucleus collisions in the large hadron collider*, Ph.D. thesis, Johann Wolfgang Goethe-Universität, Frankfurt am Main, Frankfurt, Germany (2020).
- [233] E. Metral et al., *Update of the HL-LHC operational scenarios for proton operation*, Tech. Rep. [CERN-ACC-NOTE-2018-0002](#) CERN, Geneva (2018).
- [234] H. Bartosik et al., *LIU beam parameters specifications for ions at the exit of the SPS*, Tech. Rep. [LIU-PM-ES-0005](#), CERN, Geneva (2016).